University of Southampton

Faculty of Engineering and Physical Sciences

School of Chemistry

PEROVSKITE OXYNITRIDES OF TANTALUM, TITANIUM AND NIOBIUM AND THEIR SOLID SOLUTIONS AS SELF-CLEANING COATINGS

by

Antonio Iborra Torres

Thesis for the Degree of Doctor of Philosophy

September 2020

University of Southampton

Abstract

Faculty of Engineering and Physical Sciences

School of Chemistry

Thesis for the degree of Doctor of Philosophy

PEROVSKITE OXYNITRIDES OF TANTALUM, TITANIUM AND NIOBIUM AND THEIR SOLID SOLUTIONS AS SELF-CLEANING COATINGS

Antonio Iborra Torres

Metal oxynitrides adopting the perovskite structure have shown to be active photocatalysts. In this work we established a route for the synthesis of $CaTaO_2N$, $SrTaO_2N$, $BaTaO_2N$, $LaTaON_2$, $EuTaO_2N$, $SrNbO_2N$, $LaNbON_2$ and $LaTiO_2N$ as powders as well as thin films, and an assessment on their photocatalytic activities. Their synthesis was achieved using the polymeric precursor method (Pechini method), which makes use of citric acid and propylene glycol to form a polymeric resin containing the metal cations homogeneously distributed. For the thin film deposition, alumina and quartz substrates were dip-coated into the polymeric gel to form an amorphous oxide precursor film, followed by ammonolysis. Prior to ammonolysis, both, powder and thin film precursors were annealed in air at 800˚C to obtain the oxide precursor. Perovskite oxynitride phases were synthesised in the temperature range of 850-1000 ˚C, a flowing rate of 250 ml min^{-1}, a heating ramp of 3˚C min^{-1} and reaction time of 10-54 hours. Phase purity was confirmed by XRD and Rietveld/Le Bail analysis and diffuse reflectance spectra were recorded for each sample. Optical band gaps were calculated from the Tauc plot derived from the Kubelka-Munk function and were found in the range of 1.7-2.4 eV. A cobalt oxide co-catalyst (CoO_x) was deposited onto each film by drop casting and the photocatalytic activity was assessed under visible light using dichlorophenolindophenol (DCIP) dye degradation in the presence of a sacrificial oxidant. The light source used was a solar simulator equipped with a 400 nm cut-off filter. The dye degradation test demonstrated photocatalytic activity in all samples except $EuTaO_2N$ and $BaTaO_2N$. The three most active samples $SrTaO_2N$, $CaTaO_2N$ and $SrNbO_2N$ showed initial rate constants of $5.0(1) \times 10^{-4}$ min^{-1}, $24.3(5) \times 10^{-4}$ min^{-1} and $64(5) \times 10^{-4}$ min^{-1}, respectively. The co-catalyst loading was investigated at nominal surface concentrations of 0.04-0.46 μg cm^{-2}, however, for all samples, a co-catalyst loading of 0.3 μg cm^{-2} resulted in being the optimal one, providing an

equilibrium between sufficient active sites for the degradation to occur without blocking the light from reaching the underlying photocatalyst.

The three most active samples $SrTaO_2N$, $CaTaO_2N$ and $SrNbO_2N$ were assessed on their self-cleaning abilities using the stearic acid test, demonstrating full degradation of an organic contaminant under a visible light source. The protocol for the mineralisation of stearic acid required transparent substrates. In this context, quartz substrates were protected by a layer of Al_2O_3 deposited via Aerosol-Assisted Chemical Vapour Deposition (AACVD). This method allowed to dip-coat the polymeric gels onto the quartz substrates, preventing side reactions on the perovskite phase with the quartz during the ammonolysis. The pure oxynitride phase was obtained using the conditions optimised for the perovskite oxynitrides deposited onto alumina tiles. For the photocatalytic test, the three samples $SrTaO_2N$, $CaTaO_2N$ and $SrNbO_2N$ were decorated with 0.3 μg cm^{-2} cobalt atoms, and the degradation of stearic acid was monitored by FTIR. The rate constants for the mineralisation of the stearic acid were determined and gave values of 14(2) × 10^{-4} min^{-1} for $SrNbO_2N$, 8(1) × 10^{-4} min^{-1} for $SrTaO^2N$, and 7.8(6) × 10−4 min^{-1} for $CaTaO^2N$. In line with the results from the DCIP dye testing, the $SrNbO_2N$ thin film was the most active sample.

Finally, we reported a method for the preparation of a materials library using manual ink-jet printing and subsequent screening of the photocatalytic activities of the different constituting compositions. This method was applied for the synthesis of a materials library containing nine different compositions of alkaline (Na, K) and alkaline earth (Mg) doped $SrNbO_2N$.

Table of Contents

List of Tables

List of Figures

Research Thesis: Declaration of Authorship

I, **Antonio Iborra Torres,** declare that this thesis and the work presented in it are my own and has been generated by me as the result of my own original research.

Perovskite Oxynitrides of Tantalum, Titanium and Niobium and their Solid Solutions as Self-cleaning Coating

I confirm that:

1. This work was done wholly or mainly while in candidature for a research degree at this University;
2. Where any part of this thesis has previously been submitted for a degree or any other qualification at this University or any other institution, this has been clearly stated;
3. Where I have consulted the published work of others, this is always clearly attributed;
4. Where I have quoted from the work of others, the source is always given. With the exception of such quotations, this thesis is entirely my own work;
5. I have acknowledged all main sources of help;
6. Where the thesis is based on work done by myself jointly with others, I have made clear exactly what was done by others and what I have contributed myself;
7. Parts of this work have been published as:

Demonstration of Visible Light-Activated Photocatalytic Self-Cleaning by Thin Films of Perovskite Tantalum and Niobium Oxynitrides. Antonio Iborra-Torres, Alexander N Kulak, Robert G Palgrave, and Geoffrey Hyett**.** *ACS Applied Materials & Interfaces* **2020** *12* (30), 33603-33612**.** DOI: 10.1021/acsami.0c05008

Signature: Date: 20/09/2020

Acknowledgements

I would like to express my most sincere gratitude to all those who have supported me during my PhD at the University of Southampton.

Firstly, I would like to express my gratitude to my supervisor Dr. Geoffrey Hyett for giving me the opportunity of working in his research group. Moreover, I would like to thank him for his generous guidance and assistance throughout the duration of my PhD. Thank you for the enthusiasm, advice and for boosting my confidence to effectively communicate in English. It has been a real pleasure to work and learn from you. Additionally, thanks to the Engineering and Physical Sciences Research Council (EPSRC) for the provided funding.

I am very grateful to all the group members from my lab for their help during these amazing but challenging four years. Thanks to Dr. Limburn for his friendship, support and great memories shared inside the lab. Also, thank you to Dr. Kyriazi for your friendship, for being supportive inside and outside the lab, for your dedication and for all those unforgettable moments shared together in Southampton.

Y sobre todo a mi familia, en especial a mi tía Matilde, a quien dedico toda mi formación y este doctorado. Por su apoyo incondicional y cariño cuando más lo he necesitado, y que ha sido fundamental para llegar hasta aquí. A mi hermana Carla, por nuestras confidencias, por su apoyo también incondicional y por sus consejos. Extiendo los agradecimientos a mi padre y a mi madre, así como mi tía Elisa, por creer en mi siempre y por su apoyo durante esta desafiante y a la vez gratificante experiencia. En general, a toda mi familia, por transmitirme unos valores que me han formado como persona y de los que estoy muy agradecido.

Finalmente, también me gustaría agradecer a mis amigos de Valencia, a mis UNDICI, y a mis amigas de Southampton, Dr. Ureña y Dr. Aguirregabiria por su apoyo en el día a día, tanto dentro como fuera del laboratorio, y por todas nuestras aventuras en el Reino Unido.

A todos, gracias, gràcies, thank you!

Definitions and Abbreviations

AACVD	Aerosol-Assisted Chemical Vapour Deposition
CVD	Chemical Vapour Deposition
DCIP	2,6-dichlorophenolindophenol
EDX	Energy Dispersive X-ray Diffraction
FQY	Formal Quantum Yield
L-H	Langmuir-Hinshelwood
RhB	Rhodamine B
SEM	Scanning Electron Microscopy
UV	Ultraviolet

Chapter 1 Visible Light Photocatalysts (VLPC): A Brief Perspective

1.1 Introduction to Visible Light Photocatalysis (VLPC)

Photocatalysis is the process by which a compound – the photocatalyst – is excited by ultraviolet (UV) or visible light, producing a change in the rate of the reaction partners without being altered or consumed during the process. Nowadays, concerns related to the future scarcity of fossil-fuels for energy production and air contamination are increasing and one of the challenges of the twenty-first century, chemistry has to replace fossil fuels by solar fuels, using catalysts and sunlight as the energy source.[1-2,3]

The use of fossil fuels and air/water contamination are closely related.[4] Volatile Organic Compounds (VOCs) are the organic molecules (usually chain of less than 12-C atoms containing elements such as O, S, F, Cl, Br and N) with high vapor pressure at room temperature. VOCs are an important class of air pollutants with an anthropogenic origin (transportation, fossil fuels, evaporation or organic solvents, *etc.*). VOCs, together with nitrogen oxides and catalysed by visible light, are responsible for the formation of tropospheric ozone, which accumulates at the ground level causing severe respiratory problems. Other environmental effects include, destruction of the ozone layer by chlorofluorocarbons (CFCs) and the formation of ultra-fine particles ($PM_{2.5}$), a component of smog that affects climate and air quality.[4,5]

Furthermore, scarcity of fossil fuels has led to the development of new techniques which are able to convert abundant low-energy molecules to energy-rich molecules by means of visible-light driven photocatalysis. Among these techniques we find water splitting for the production of hydrogen (energy-rich molecule) and CO_2 photoreduction (energy-poor molecule) to methanol (energy-rich molecule), among others.[6,7] Hydrogen is a solar fuel, however, commercial hydrogen is mainly obtained from steam reforming of hydrocarbons (fossil fuels). Thus, water splitting using visible light photocatalysts paves a way for environmentally friendly H_2 generation.[8]

Growing environmental concerns make it necessary to seek solutions that make use of green technologies. In this context, semiconductor photocatalysts have received considerable attention because of their promising potential for solving the problems of environmental pollution and use as solar fuels.[9]

The development of heterogeneous photocatalysis was pioneered by Honda and Fujishima. In 1972, both reported the first overall photocatalytic water splitting using TiO_2 upon UV illumination.[10] Titanium dioxide is a low cost, naturally occurring mineral and widely available material. It has multiple uses such as whitening agent in food industry and cosmetics, and as active sunscreen ingredient due to its ability to reflect and scatter both, UVA and UVB radiation.[11–13] Since its photoactivity discovery , extensive work has been carried out focusing on the production of hydrogen (which is an eco-friendly fuel) *via* water splitting as a means of solar energy conversion.[11]

Over the last twenty-five years, the number of publications containing the key words heterogeneous photocatalysis and visible light photocatalyst have grown exponentially as seen in Figure 1.

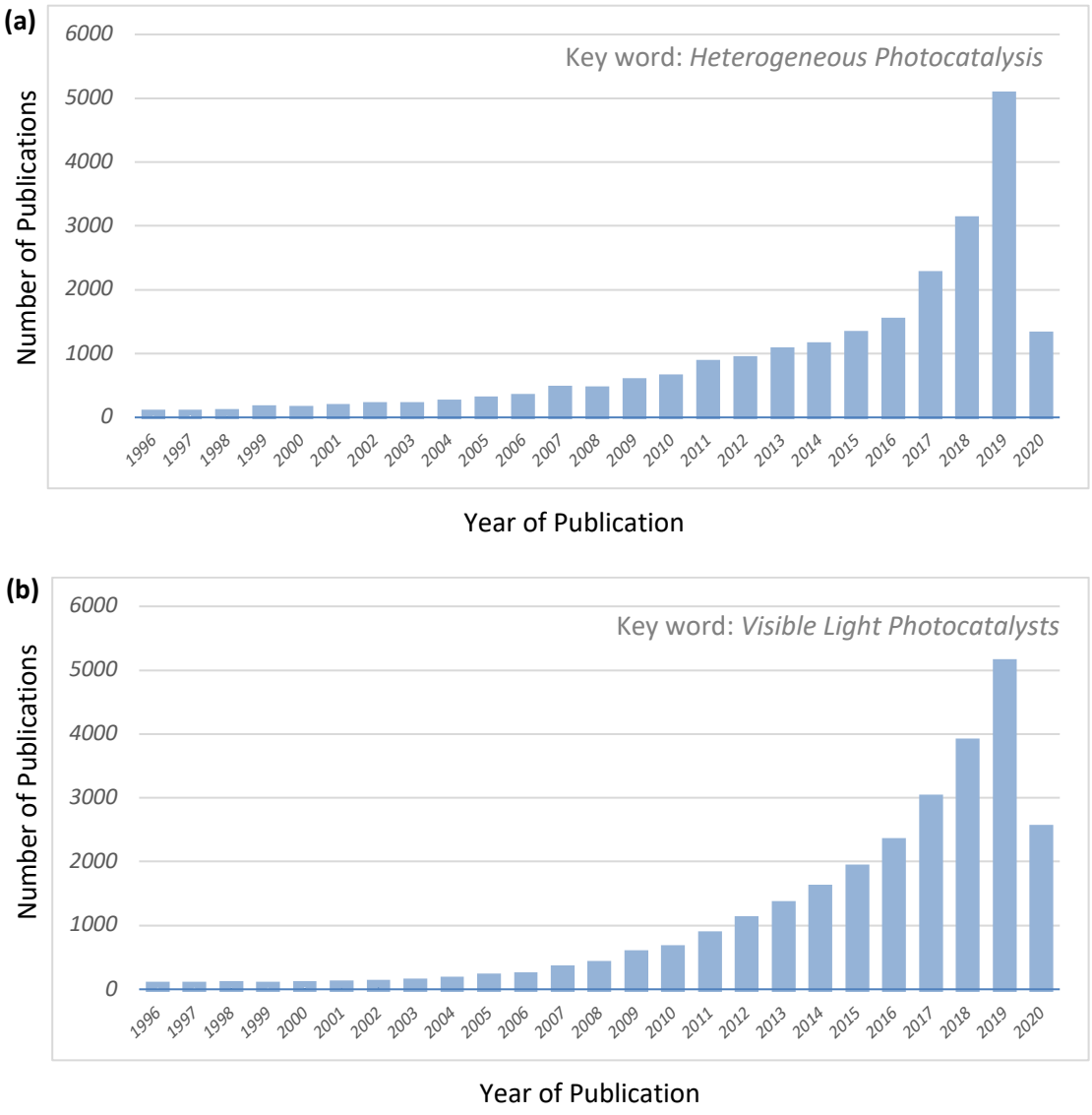

Figure 1. Evolution of the number of publications related to **(a)** heterogeneous photocatalysis and **(b)** visible light photocatalyst over the last twenty-five years. Data: Web of Science [14].

As a consequence of this increased interest for the photocatalytic processes, new applications making use of TiO_2 as a photocatalyst have been expanded in recent decades.[15] Certainly, this is mainly due to its ability to degrade organic molecules under UV radiation. The applications can be translated into thin films showing self-cleansing applications such self-cleansing glass, as the already commercialised Pilkington Activ™ or small-scale air/water purification systems.[16,17] Nevertheless, the use of UV light is neither viable nor economical for the degradation of industrial amounts of pollutants since UV light barely comprises 4 % of the solar spectrum. Alternatively, a visible light photocatalyst can make more efficient use of the solar radiation, since visible light makes up 46% of the solar spectrum.

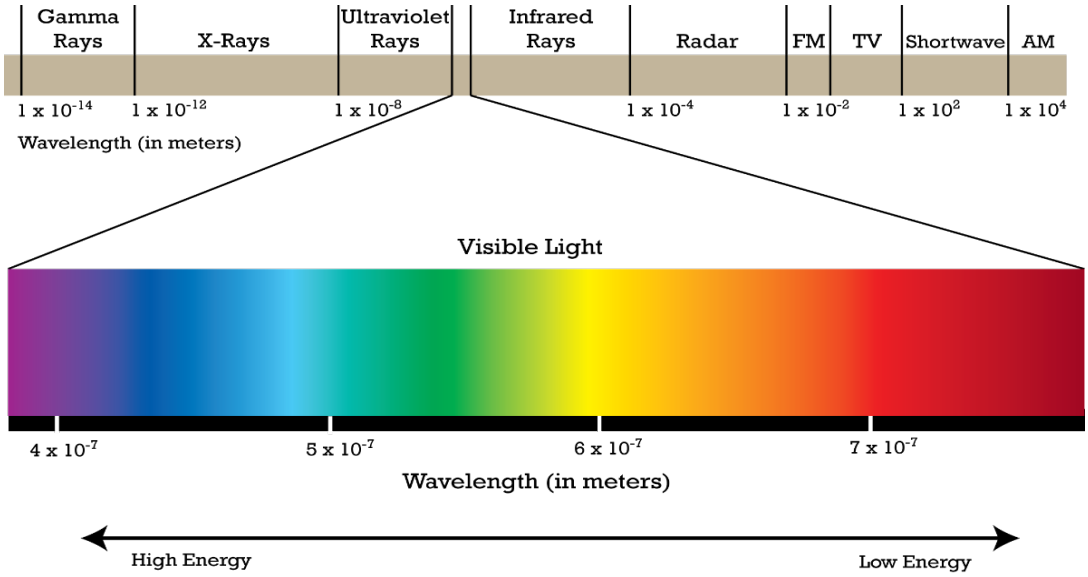

Figure 2. Sections of the electromagnetic spectrum. Adapted from Ref.[18]

Visible-light driven photocatalysis makes possible the use of a primary source of visible radiation that is both inexhaustible and sustainable. The photocatalytic mechanism is based on irradiating the surface of a semiconductor with light of sufficiently short wavelength, giving rise to the photo-generation of electron-hole pairs that can be used in redox reactions such as the formation of Reactive Oxygen Species (ROS) at the photocatalysts surface level.[15,19]

The most well-known example of a photocatalyst making use of visible light in nature is the photosynthesis of plants through the use of chlorophyll, whose range of absorption in the visible is located in the blue portion of the electromagnetic spectrum, allowing plants to absorb energy from the sun. Attempting to emulate nature, chemists have focused their work on the synthesis of semiconductors that are able to fully exploit sunlight potential in order to provide viable solutions to pollution problems.[20,21] In this context, different types of visible-light photocatalyst ranging from magnetic composites[22], TiO_2-based[16], ZnO-based[23], Carbon-based[24], MOFs[25], perovskite materials[26] *etc.* have been assessed for a series of photocatalytic reactions described in the following section.

1.1.1 Overview of Photocatalytic Reactions

1.1.1.1 Photocatalytic Water Splitting

Photocatalytic water splitting into H_2 offers a promising approach toward fulfilling the need of production of clean energy while reducing the environmental impact associated with fossil fuels. In this context, hydrogen is a zero-emission fuel that could be used as a green alternative to fossil fuels, offering many potential applications including its use in commercial fuel cell vehicles or as a fuel for spacecraft propulsion.[2,27] The problem remains that thermodynamically, the overall water-splitting reaction of water is uphill, requiring an applied voltage of at least 1.23 eV as a driving force for its dissociation into molecular hydrogen and oxygen (Gibbs energy).[27–29]

$$H_2O \longrightarrow H_2 + \tfrac{1}{2}\, O_2 \qquad \Delta G = 237\ kJ/mol$$

Generally, the photocatalytic water-splitting reaction involves three major steps: (i) the photocatalyst (a semiconductor) is excited when photons with an energy higher than the band gap hit the semiconductor generating an electron-hole pair, (ii) the photogenerated electron-holes that did not recombine migrate towards the surfaces of the semiconductor, (iii) and finally, the photogenerated electron-holes are consumed in electron transfer reactions . Usually, a co-catalyst (typically a noble metal (i.e. Pt, Rh) or a transition metal (i.e. CoO_x, NiO_x) is loaded onto the surface to promote the H_2 evolution. The photogenerated holes oxidise H_2O molecules absorbed in the surface of the semiconductor to O_2, while the surface-absorbed H^+ ions are reduced by the photogenerated electrons to produce molecular hydrogen. However, for redox reactions to take place, the photocatalyst must have a suitable valence band (VB), where its highest energy level must be more positive than the water oxidation value $E(O_2/H_2O)$ = 1.23 eV *vs.* NHE and the lowest energy level of the CB must be more negative than the H_2 evolution potential $E(H_2/H_2)$, o V *vs.* NHE.[2,29,30]

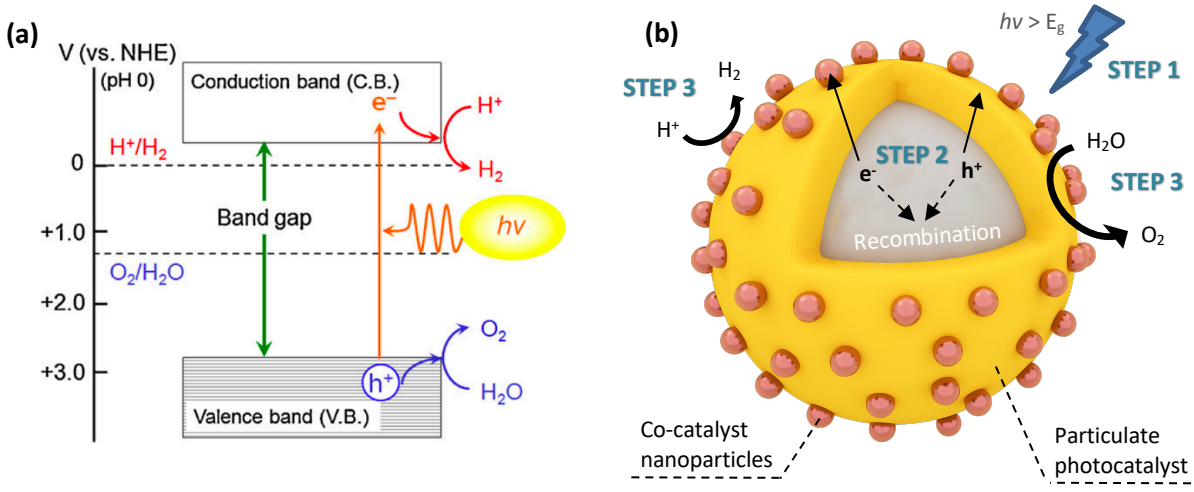

Figure 3. **(a)** Mechanisms of photocatalytic water-splitting on a semiconductor-based photocatalyst and **(b)** basic steps involved in photocatalytic water-splitting.[(a)] Adapted from ref [9].

1.1.1.2 Photocatalytic Reduction of CO_2

Excessive anthropogenic CO_2 emissions have been proved to be one of the main causes of global warming[31], and at the same time they are implicated in phenomena such as acid rain.[32,33] An approach that would make use of the CO_2 produced by most industries has gained popularity since its publication by Halmann in 1978, and it is the photocatalytic reduction of CO_2 to high-energy compounds (fuels) such as methanol or methane, among others.[34–36] Generally, in the photoreduction of CO_2, two different configurations are adopted. In the first one, the photochemical reduction of CO_2 can be achieved either using a homogeneous or heterogeneous system.[36,37] The last one makes use of a powdered photocatalyst suspended in the solution (Figure 4a). Here, the particles interact with the dissolved CO_2 in the solution, purely driven by solar light. However, both the oxidation and reduction reactions occur at different reaction sites on the surfaces of the particle, resulting in the mixing of all the reaction products. Consequently, the reduced CO_2 species can be re-oxidised by the generated molecular oxygen if a hole scavenger is not used.[38] Additionally, the semiconductor must have a suitable band gap small enough to absorb visible light, with a VB more positive that the water oxidation potential and a CB more negative than the CO_2 reduction potential. In last four decades, extensive research has been conducted towards the development of suitable semiconductors that can be used as photocatalysts for the photochemical reduction of CO_2, however, due to the mentioned requirements, the number of successful candidates is still low.[31,35]

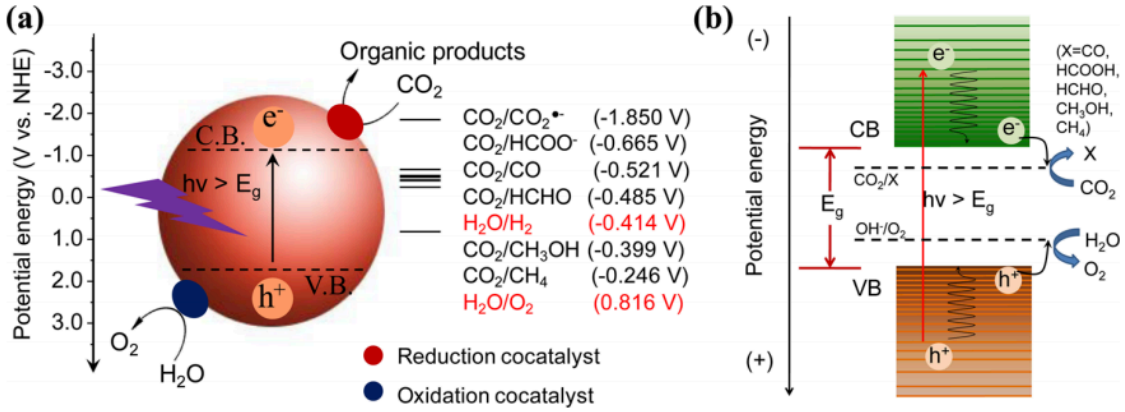

Figure 4. (a) Schematic illustration of the mechanism and **(b)** relative energy levels of the photochemical reduction of CO_2. Adapted from ref [39].

The second method, known as photoelectrochemical cell (PEC) system (Figure 5b) consists of a half-cell containing a photocathode, a p-type semiconducting photocatalyst coated on a conductive substrate and usually a reference electrode. The second half-cell contains a counter

electrode. Both cells are separated by a proton membrane (Nafion) which allows for proton exchange and prevents the re-oxidation of the reduction products.[6,35]

The mechanism comprises the irradiation of the photocathode with visible light, resulting in the generation of electron-holes pairs. The photogenerated electrons are utilized in the reduction of CO_2 on the surface of the photocathode while the photogenerated holes migrate to the counter electrode, taking part in oxidation reactions. Efficiency can be enhanced compared to the photochemical system since an external bias can be applied to promote separation of charge carriers. Product selectivity is mainly determined by the selection of a semiconductor with a suitable energy levels of the VB and CB and the additional energy supplied by external bias potential.[6]

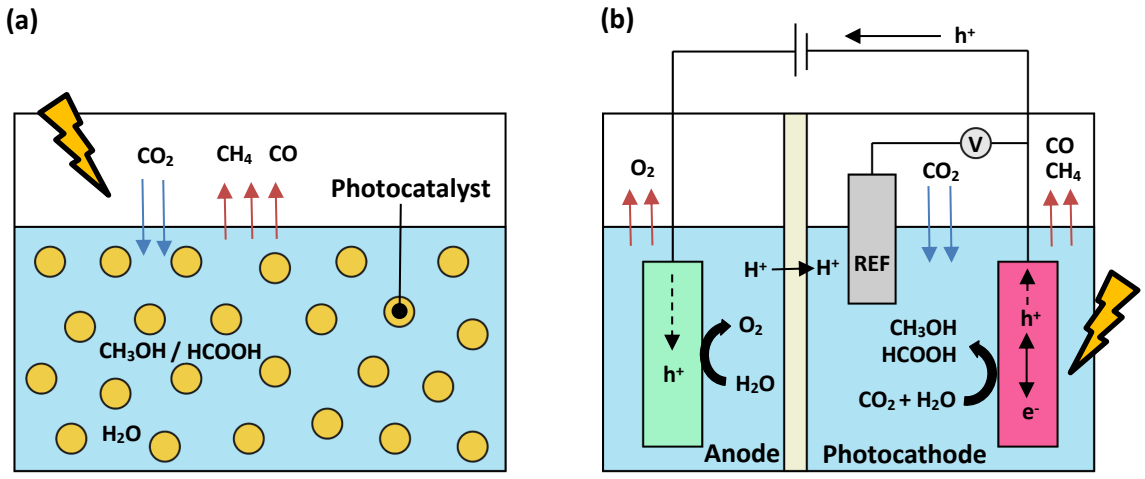

Figure 5. **(a)** Photo-reduction of CO_2 using photochemical system (PC) and **(b)** photoelectrochemical cell (PEC) system for photo-reduction of CO_2.

1.1.1.3 Photodegradation of Organic Molecules and Self-cleaning Surfaces

The industrialization process in most countries has led to environmental pollution due to the emission of toxic gases to the atmosphere which contribute to global warming and the uncontrolled release of industry by-products, which contaminate water bodies and soils. In this context, one of the most promising solutions and a green way to control the toxic molecules presented in wastewater is the photodegradation of organic compounds. Different classes of organic pollutants such as dyes (azo dyes, synthetic dyes, cationic/anionic dyes, *etc.*), drugs (antibiotics, pesticides, *etc.*) and fine chemicals (benzo compounds, phenolic compounds, *etc.*) have been successfully degraded under visible light.[40–44]

The typical mechanism for the photodegradation of organic molecules is like the one proposed previously for water splitting and CO_2 reduction. Firstly, the photocatalyst is irradiated

with photons with energy equal to and more than the band gap energy of the semiconductor, leading to the photogeneration of electron-hole pairs. The photogenerated electron-holes can either recombine or migrate to the surface of the semiconductor where they participate in redox reactions with the absorbed molecules. The photogenerated holes react with surface-bound H_2O and OH^- to produce hydroxyl radicals ($^{\bullet}OH$) while the photogenerated electrons react with oxygen dissolved in the solution to generate superoxide radical anions. These radicals are also known as Reactive Oxygen Species (ROS) and it has been suggested that they are the primary oxidising species responsible for the mineralisation of the organic molecules to CO_2 and H_2O. However, the photocatalytic process depends on the operational parameters such as pH of the solution, temperature, initial concentration of the dye, photocatalyst amount and form and irradiation intensity.[42,45]

The photodegradation of dyes is a feasible approach widely used to assess the photocatalytic activity of powders and thin films and it will be discussed in detail in Chapter 2 and 5.

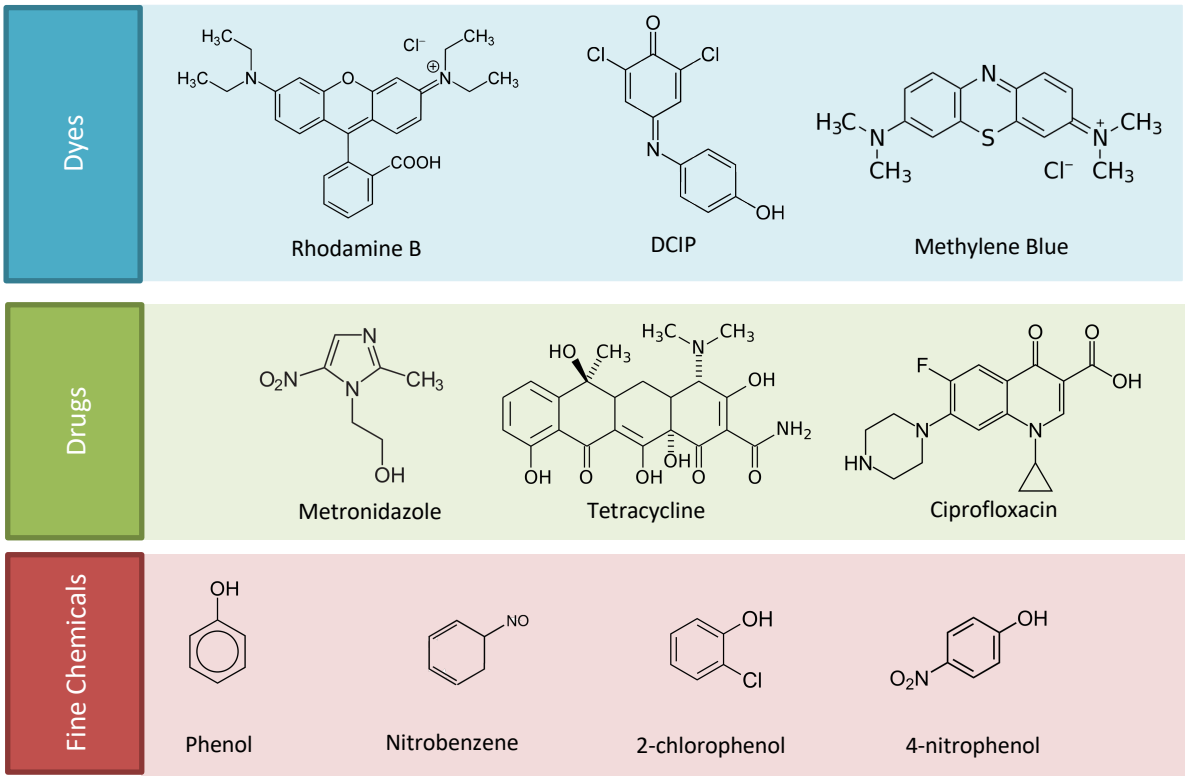

Figure 6. Classification of organic pollutants and examples that have been successfully degraded under visible light and a suitable photocatalyst in an aqueous solution. Dyes: Rhodamine B[46], DCIP[47] and Methylene Blue[48]. Drugs: Metronidazole[28], Tetracycline[50] and Ciprofloxacin [51]. Fine chemicals: phenol[52], nitrobenzene[43] , 2-chlorophenol[53] and 4-nitrophenol[44].

- *Photocatalytic Self-Cleaning*

The discovery of the light-induced wettability change on TiO_2 thin films and its ability to undergo oxidative decomposition of organic pollutants under UV radiation by Fujishima et al. over two decades ago led to the understanding of the structure-function relationship and subsequently, the development of self-cleaning materials.[54,55] In his work, Fujishima highlighted the ability to control the surface wettability (surface engineering) of TiO_2-coated substrates by using UV radiation. The prepared TiO_2 (anatase) polycrystalline films were deposited onto glass substrates and showed a water-contact angle of 72° before and 0° after UV irradiation, resulting in the water droplets spread out on the films surface. Moreover, TiO_2-coated substrates, regardless of their photocatalytic activities, showed cleaner surfaces after six months outdoors when compared to those uncoated. UV radiation from sunlight was able to maintain the amphiphilic surface on the films, being the oleophilic and hydrophilic contaminants on the surface easily washed away by rain. Besides the self-cleaning properties, Fujishima also showed a remarkable antifogging effect on the thin films when the TiO_2-coated glass was exposed to water vapor. Under UV irradiation, the fogged thin films became transparent, showing again the photoinduced wettability of the TiO_2-coated glass.[54] However, the wide band gap of TiO_2 ($\sim$ 3.2 eV) limits its light absorption to the UV regions, which comprises a small percentage of the visible spectrum, reducing the overall photocatalytic efficiency. Besides of absorbing light in the visible spectra, the novel candidates must exhibit significant low toxicity, chemical and physical stability, easy availability and excellent photocatalytic activity.

In the self-cleaning process of a hydrophilic surface, the generated ROS are responsible for oxidising the film of organic matter to CO_2 and water. When wet, the water droplets form a thin layer on the photocatalytic surface which causes to lift off the remaining contaminants. The self-cleaning properties are just not restricted to organic pollutants, the oxidising power of the ROS are also able to degrade the phospholipidic membrane in microbes (*Staphylococcus aureus*, *Escherichia coli*, *etc*), resulting in their inactivation.[19,56] The resulting surfaces with antimicrobial properties could be used indoors where hygiene is of crucial importance such as hospitals.

Oil contamination is a problem for self-cleaning surfaces since the access to O_2 and H_2O in the thin film surface can be hindered by a compact layer of grease. To overcome the mentioned problem, investigation has been focused towards the photocatalytic performance of TiO_2 thin films coated with a layer of oleic acid (stearic acid). Due to the nature of this grease (low volatility, temperature stability and double bond), it has been used a model compound to simulate grease stains on various substrates.[12,13] Consequently, the photodegradation of stearic acid is a feasible approach to assess the self-cleaning power of photoactive thin films and it will be discussed in detail in Chapters 2 and 5.

1.1.2 Overview of Visible-Light Photocatalyst (VLPCs)

Among all the photocatalysts, TiO_2 is still the most studied one, however, its wide band gap limits its use in visible-light driven photocatalysis. Certainly, most semiconductors do not have all the requisites needed to be effectively used in visible light photocatalyst such as optical and physical properties. Often, the photocatalytic efficiency of a single-component material is lowered due to the presence of defects acting as recombination centres for the photoinduced carriers. In this context, different methods have been reported in order to maximise these efficiencies investigated and include; (i) morphology optimization, (ii) doping, (iii) heterojunctions, and (iv) use of a co-catalyst.

Popular visible-light photocatalyst included magnetic composites, MOFs, Perovskites, Novel Composites as well as TiO_2, ZnO, bismuth and carbon-based materials.[39,57]

Table 1. Popular visible light photocatalyst, either as a single material or as parts of heterojunctions.

Type of VLPC	Examples
Bismuth-based	Ag-BiVO, BiOI/BiOBr microspheres, Er-Y-$BiVO_4$
Carbon-based	g- C_3N_4nanosheet, GO/g- C_3N_4, C_{70}/g-C_3N_4
Magnetic Composites	Fe_2O_3-AgBr, Ce-N-TiO_2/$NiFe_2O_4$/diatomite, $ZnFe_2O_4$
MOFs	MIL-101(Fe)-NH_2, MIL-125-NH_2
Novel Composites	NiO/Ag_3VO_4, α-$NiMoO_4$, CdS-nanospheres
Perovskites	$BaTiO_3$, $SrNbO_2N$, $CaTaO_2N$
TiO_2-based	Fluorinated N-TiO_2 NPs, Au/TiO_2, Cu-TiO_2 nanofibers
ZnO-based	F-ZnO, Au@Zn

Bismuth-based nanomaterials such as bismuth chalcogenides, bismuth oxyhalides (BiOX) and bismuth vanadates are considered of interest since they possess narrow band gaps and improved visible light absorption compared to undoped TiO_2 and ZnO. Monoclinic bismuth oxide nanorods (m-Bi_2O_4) have a band gap of 2.0 eV and inactivated water contaminated with *E.coli* after 120 minutes under visible light.[58] The heterojunction formed by BiOBr-Bismuth oxyhydrate (BHO) was able to remove Rhodamine B (RhB) in water (100 mg photocatalyst, 200 mL aqueous solution, [RhB] = 15 ppm) and acetophenone (100 mg photocatalyst, 200 mL aqueous solution, [AP] = 120 ppm) when irradiated with a 300 W Xe lamp (385–740 nm).[59]

In addition to conventional photocatalyst, **Metal-Organic Frameworks (MOFs)** have gained popularity in the photocatalyst field recently.[25,39] Chemically, a MOF is an organic-inorganic hybrid crystalline porous material with a large internal surface area, formed by organic linkers and transition-metal nodes. The photo-responsive properties arise from the ability of the organic linkers/metal nodes to absorb visible light. Thus, the photoexcited units in the MOFs are able to generate a ligand-to-metal electron-hole separation state that is translated into photocatalytic activity. MOFs have been reported in photocatalytic reaction on H_2 evolution and CO_2 reduction. For example, MOF-253-Pt has shown a hydrogen evolution rate (photoactivity) of 3000 μmol h^{-1} g^{-} when illuminated with a 300 W Xe lamp under solely visible light, while Au/NH_2-MIL-125 (Ti) has been reported for photocatalytic CO_2 reduction with a reported photoactivity of 9.06 μmol $HCOO^{-}$ under a 300W Xe lamp.[60, 61]

A different class of visible-light photocatalysts which have gained popularity in the recent years are the ones **based on carbon.** Graphitic carbon nitride g-C_3N_4 and graphene-based materials are among the most studied and reported carbon-based photocatalyst. g-C_3N_4 popularity is based due to its narrow band gap (2.7 eV) which allows for visible-light absorption. However, offers a lower stability when compared to TiO_2, as well as limited mobility of the photogenerated electrons due to its low conductivity and high electron-hole recombination rates. Researchers have explored the morphological optimization of g-C_3N_4 converting the bulk material to highly reactive nanosheets. Photoactive g-C_3N_4 nanosheets showed a 4-fold higher visible-light photocatalytic activity for *E. coli* degradation from water than the bulk g-C_3N_4. Graphene oxide/graphite carbon nitride (GO/g-C_3N_4) nanocomposites have also been developed for photocatalytic water disinfection. In particular, GO/g-C_3N_4 nanocomposite (100 μg mL^{-1}) inactivated 97.9 % of *E. coli* within 120 min under visible light (300 mW/cm^2).[24]

The construction of heterojunction photocatalysts has been addressed as an efficient way to overcome the efficiency problems, sometimes observed in single semiconductors, as previously mentioned. In this context, **magnetic composites** include Fe_2O_3-AgBr, g-C_3N_4/Fe_3O_4/$MnWO_4$, Ag_3PO_4/ZnO/Fe_3O_4 and have promoted easy separation and recyclability of the photocatalyst by magnetic force. The iron core from the composite accelerate charge transfer, delaying electron-hole recombination while the existence of Fe-OH can improve the adsorptive capacity of the photocatalyst. Fe_2O_3-AgBr composite was able to produce ROS which inactivated *E. coli* in water within 4 h of irradiation (100 mW/cm^2). $ZnFe_2O_4$/AgI composites have also been reported for dye degradation and microbial deactivation. $ZnFe_2O_4$/AgI induced 100% removal efficiency of *E. coli* in water under 80 minutes under solely visible light and 98.5 % removal rate of the dye Rhodamine B (RhB) in 40 minutes. Recyclability was tested by magnetic separation and four consecutive tests demonstrated the stability of the as-prepared $ZnFe_2O_4$/AgI magnetic composite.

Due to its many advantages, including abundance, cheap cost and stability, TiO_2 has traditionally been the archetypal photocatalyst. However, its limitation to effectively use visible light due to its wide band gap makes it necessary to seek solutions in order to extend the photocatalytic response of TiO_2 into the visible spectrum. **TiO_2-based** visible light photocatalyst have emerged as an alternative to phase pure TiO_2.[62–64] A common method to promote the visible absorption of TiO_2 is ion doping. The incorporation of transition metal cations or anions such as N and S induce changes in the band gap which increase the photoactivity under visible light while retaining the properties of TiO_2. Anatase-TiO_2 doped with Ti^{+3} allowed for an efficient absorption of visible light, showing a 100% degradation of an aqueous solution containing methyl orange (MO) under solely visible light (100 mg photocatalyst per 100 mL of MO aqueous solution 20 ppm). N, S doped TiO_2 was able to degrade a 100 mL solution containing 25 mg L^{-1} of tetracycline using 6 LED lamps as light source.[65] Titania has also been used together with carbon-based materials, and iron/silver compounds to form composites and these are summarised in Table 3.

Just like TiO_2, ZnO also has been extensively studied as photocatalyst due to its good quantum efficiency, stability, and non-toxicity. However, its wide band gap (3.37 eV) requires modification through doping or heterojunctions to be used under solely visible light. **ZnO-based** photocatalysts have attracted much attention as promising materials for degradation of organic pollutants in water. ZnO nanoparticles possess high surface areas and large number of active sites which can be used for redox reactions. Doping ZnO with noble metals (i.e. Ir, Rh, Pt) help to overcome the high degree of recombination of the photogenerated carriers observed in bulk ZnO, while narrowing its band gap. In/ZnO nanoparticles were able to fully oxidise a solution of methylene blue (100 ppm) in 30 minutes (1g/L of photocatalyst).[23]

Novel composites such as the heterojunction NiO-Ag_3VO_4, hydroxyapatite (HAp)-supported Ag_3PO_4 and Cu-MoS_2 have emerged as a new class of two-dimensional nanomaterials of interest among researchers.[66–68] Monoclinic Ag_3VO_4 has a suitable band gap for visible-light driven reactions, however, the high recombination rate of the photogenerated electron-holes makes it necessary to use it with another semiconductor (NiO). The composite NiO-Ag_3VO_4 has been proven to selectively degrade azo-dyes as well as antibacterial activity.[68,69]

However, among the large range of available visible-light photocatalysts reported so far, **perovskite** materials constitute a huge family of photocatalyst with multiple applications and an interesting structure, which needs to be explained in detail. The next section and the rest of this thesis will be focused on perovskite materials, specifically, **perovskite oxynitrides**.

Table 2. Summary of composites/MOFs reported for photocatalytic H_2 evolution and photocatalytic CO_2 reduction under visible light.

Composition	Photoactivity	Ref
Photocatalytic H_2 evolution		
Pt@MOF-1	3400 TON	[70]
MOF-253-Pt	3000 µmol	[60]
Pt-NH_2-UiO-66	2.8 mL	[71]
NH_2-UiO-66 (Zr/Ti)	3.5 µmmol g^{-1} h^{-}	[72]
RhB/UiO-66(Zr)-100*	33.9 µmol g^{-1} h^{-1}	[73]
Pt-UiO-66-30	37 µmol	[74]
Pt-Ti-MOF-$Ru(tpy)_2$	5.1 µmol	[75]
Fe_2O_3/TiO_2/Pt	0.8 µmol	[76]
Pt@CdS/MIL-101(Cr)	150 µmol h^{-1}	[77]
UiO-66/CdS/rGO	105 µmol h^{-1}	[78]
Pt/NH_2-MIL-125(Ti)	33 µmol	[79]
Pt(1.5)/NH_2-MIL-125(Ti)	15.5 µmol	[80]
Pt/ MIL-125(Ti)	38.68 µmol	[81]
Co@ NH_2-MIL-125(Ti)	37 µmol	[82]
Photocatalytic CO_2 reduction		
NH_2-MIL-125(Ti)	8.14 µmol $HCOO^-$	[83]
Au/NH_2-MIL-125(Ti)	9.06 µmol $HCOO^-$	[61]
Pt/ NH_2-MIL-125(Ti)	12.96 µmol $HCOO^-$	[61]
NH_2-UiO-66	13.2 µmol $HCOO^-$	[84]
NH_2-UiO-66 (Zr/Ti)	5.8 µmol $HCOO^-$	[84]
MIL-101(Fe)	59 µmol $HCOO^-$	[85]
NH_2- MIL-101(Fe)	178 µmol $HCOO^-$	[85]
MOF-253-$Ru(CO)_2Cl_2$	0.67 µmol $HCOO^-$	[86]
$Cu_3(BTC)_2$@TiO_2	Orthorhombic	[87]
CdS/Co-ZIF-9	0.67 µmol g^{-1} CH_4	[88]
g-C_3N_4 + Co-ZIF-9	20.8 µmol CO	[89]
ZIF-8/Zn_2GeO_4	0.67 µmol g^{-1} CH_3OH	[90]

Table 3. TiO_2-based visible light photocatalyst for bacteria deactivation with 100 % photodisinfection efficiency.

Composition	Bacteria	Photoactivity	Ref
g-C_3N_4/TiO_2 microspheres	*E. Coli* K-12 (1 x 10^7 CFU mL^{-1})	0.6 g L^{-1}, 180 min	91
P25 TiO_2/rGO composite	*E. Coli* (1 x 10^6 CFU mL^{-1})	0.5 g L^{-1}, 10 min	92
TiO_2/rGO composite	*E. Coli* (1 x 10^6 CFU mL^{-1})	18 mg L^{-1}, 180 min	93
P25/Ag_3PO_4r/GO	*S. aureus* (1 x 10^6 CFU mL^{-1})	< 100 ppm, 240 min	94
C- TiO_2	*L. monocytogenes* (1 x 10^5 CFU mL^{-1})	1 g L^{-1}, 150 min	95
N-TiO_2 NPs	*E. Coli* (2.7 x 10^4 CFU mL^{-1})	0.35 g L^{-1}, 420 min	96
F-N-TiO_2 NPs	*E. Coli* (4.1 x 10^6 CFU mL^{-1})	1 g L^{-1}, 60 min	97
Ce/B-TiO_2	*S. aureus* (1 x 10^6 CFU mL^{-1})	4 mg L^{-1}, 120 min	64
Cotton-TiO_2/1%Fe-N	*E. Coli* (1 x 10^7 CFU mL^{-1})	15 min	98
V/N-TiO_2	*E. Coli* (2 x 10^9 CFU mL^{-1})	1 mg L^{-1}, 120 min	99
Cu-TiO_2 nanofibers	*E. Coli* (1 x 10^3 CFU mL^{-1})	50 mg L^{-1}, 240 min	100
TiO_2/Ag_2O heterojunction	*E. Coli* (1 x 10^3 CFU mL^{-1})	1 mg L^{-1}, 60 min	94
TiO_2/Ag_3PO_4 heterojunction	*E. Coli* (1 x 10^7 CFU mL^{-1})	1 mg L^{-1}, 100 min	62
Au-TiO_2	*E. Coli* (6.5 x 10^7 CFU mL^{-1})	100 mg L^{-1}, 240 min	101

Table 4. Carbon-based visible light photocatalyst for bacteria deactivation with 100 % photodisinfection efficiency.

Composition	Bacteria	Photoactivity	Ref
g-C_3N_4 nanosheets	*E. Coli* (1 x 10^7 CFU mL^{-1})	1 g L^{-1}, 120 min	91
Porous g-C_3N_4 nanosheets	*E. Coli* (5 x 10^5 CFU mL^{-1})	0.4 mg mL^{-1}, 240 min	102
Co- C_{70}/g-C_3N_4	*E. Coli* (1 x 10^8 CFU mL^{-1})	0.5 mg mL^{-1}, 240 min	103
GO/g-C_3N_4 composite	*E. Coli* (1 x 10^7 CFU mL^{-1})	100 mg L^{-1}, 120 min	24
g-C_3N_4/EP	*E. Coli* (1 x 10^8 CFU mL^{-1})	6 g L^{-1}, 180 min	104
Ag-g-C_3N_4	S. aureus (1 x 10^6 CFU mL^{-1})	60 mg L^{-1}, 30 min	102
g-C_3N_4-AgBr composite	*E. Coli* (3 x 10^6 CFU mL^{-1})	100 mg L^{-1}, 60 min	105
g-C_3N_4-Ag_2WO_4 composite	*E. Coli* (1 x 10^7 CFU mL^{-1})	100 mg L^{-1}, 90 min	106
B-Ph-g-C_3N_4 nanosheets	*E. Coli* (5 x 10^5 CFU mL^{-1})	150 mg L^{-1}, 180 min	107
$AgVO_3$/g-C_3N_4	*Salmonella* (1 x 10^7 CFU mL^{-1})	75 mg L^{-1}, 10 min	108
VS_4/C composite	*E. Coli* (1 x 10^9 CFU mL^{-1})	100 mg L^{-1}, 30 min	110
Ag/g-C_3N_4 nanosheets	*E. Coli* (1 x 10^6 CFU mL^{-1})	60 mg L^{-1}, 30 min	42

1.2 Perovskite Materials

1.2.1 Perovskite Structure

The origin of the *perovskite* word dates back to the discovery of a mineral based on calcium titanate ($CaTiO_3$) by the German mineralogist Gustav Rose on the Ural Mountains in 1839, and named in honour of the Russian mineralogist L.A. Perovsky.[111] Nowadays, the term perovskite is universally used to describe a group of materials represented by a characteristic crystal structure (Figure 7) and the composition ABX_3 . Ideally, the ABX_3 composition is composed of three different ions (A, B and X) of which *A* denotes a voluminous cation with low charge such as an alkaline metal or rare/alkaline earth, the *B* cation corresponds to a transition metal and *X* is most often a non-metallic anion such as oxygen.

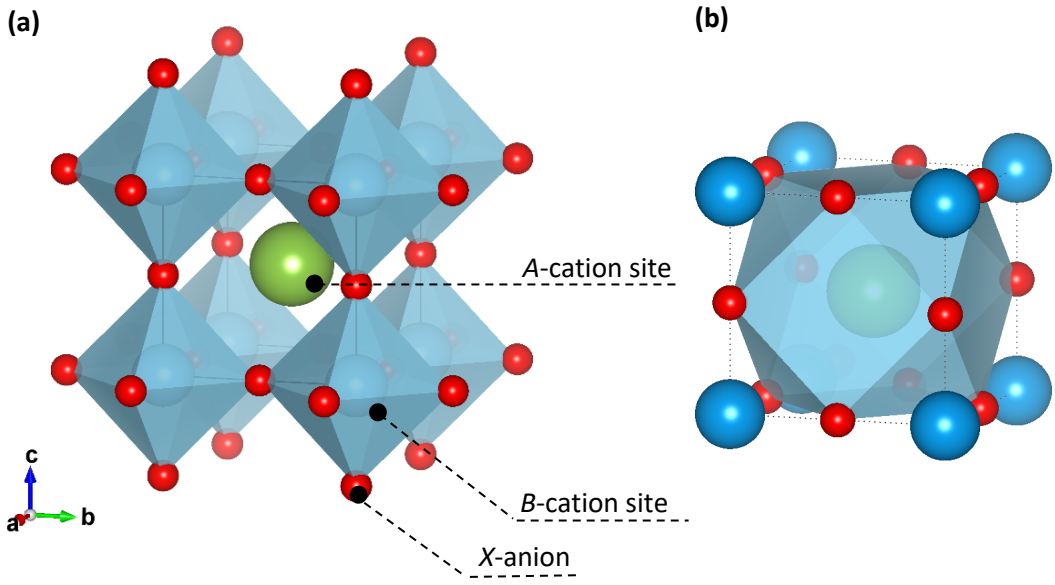

Figure 7. (a) Ideal perovskite non-distorted crystal structure (cubic *A* unit cell) and **(b)** 12-fold coordination (AO_{12}) of the *A*-site cation (cuboctahedron).

The larger *A*-cation locates in the centre of the unit cell and is coordinates twelve anions (X) located at the middle of the edge of the cubic *A*-centres unit cell at equidistance, resulting in a cuboctahedron. The smaller *B* cations occupy the eight corners forming a BX_6 octahedra with the adjacent oxygen (*X*) anions. Ideal perovskite structures self-organize into crystals with a cubic symmetry (space group of $Pm\bar{3}m$). Nevertheless, not all the perovskite compounds show an ideal cubic structure. The original mineral $CaTiO_3$ crystallizes with an orthorhombic distortion (*Pnma*) within the structure while $SrTiO_3$ exemplifies the archetypal ideal cubic perovskite structure ($Pm\bar{3}m$). These structural distortions are mainly based on two different mechanisms; cation displacements and tilting of the BX_6 octahedra, both of them are discussed in the following section.

1.2.2 Structural Distortions Occurring in Perovskite Materials

Deviations from the ideal symmetry of the cubic perovskite structure gives rise to compounds with tetragonal, orthorhombic, monoclinic or triclinic symmetries. When the cation *B* is relatively larger in comparison with the *A* cation, the value of the Goldschmidt's tolerance factor (τ) decreases ($\tau < 1$) involving the compression of the *B-X* bonds and the elongation of the *A-X* bonds. The resulting stress is relieved by means of the rotation of the BX_6 octahedra, reducing the symmetry of the structure and modifying their physical and electronic properties. On the contrary, if the *B*-site cation is too small ($\tau > 1$) the *B-X* bonds are subjected to stress whereas the *A-X* bonds are under compression. The presence of weak covalent bonds within the coordination polyhedron BX_6 leads to the displacement of the *B*-centred transition cation. This asymmetric behaviour denoted as the second order Jahn-Teller effect occurs in perovskites oxynitrides having high-valence transition metals (d^0 configuration) such as the Ti^{4+}, Ta^{5+} and Nb^{5+}.[112,113] The displacement of the *B*-site cations within the octahedron has been widely studied and plays an important role in the ferroelectric properties of some perovskite materials, $BaTiO_3$ being the most well-known ferroelectric example.[70]

1.2.2.1 Tilting of the BX_6 octahedra

The notation most used to describe the octahedral tilting in perovskites was described by Glazer (1970). This notation describes the different tilts using *a*, *b* or *c* for tilt axes parallel to three Cartesian axes x, *y* and *z*. The rotations about each axis are described by two parameters. The first parameter is a letter (*a*, *b* or *c*) which specifies the magnitude of the rotation about that axis, relative to the magnitude of rotation about x, *y* and *z*. For example, in the tilting system $a^+ a^+ a^+$, the rotation angle is the same for the three axes while in the tilting system $a^+ a^+ c^+$, the rotation angle around *z* is different from the axes x and *y*. The second parameters consist of a superscript which indicates the rotation of the octahedra in comparison with the adjacent octahedral layers. A positive sign (+) indicates rotation of the octahedra in the same direction than the adjacent layers, while a negative sign (-) indicates opposite rotation among the two neighbour octahedra. If the superscript is zero (0), there is not rotations about the axis.[114,115]

The Figure 8 shows a classic example which compares the two one-tilt systems $a^0 a^0 c^+$ *and* $a^0 a^0 c^-$. Each octahedron represents the B metal surrounded by six anions, such as oxygen(X). The remaining atoms represent the A metal. The repetition of the letters (*a*, *b* or *c*) indicates a repetition in the tilting. As observed, the tilting of the central octahedra forces the tilting of four of the six neighbouring octahedra, while the two remaining octahedra are not coupled the same way and they can rotate independently. Thus, the $a^0 a^0 c^+$ system occurs when the two adjacent octahedra

rotate in the same direction as the first octahedron while in the $a^0\ a^0\ c^-$ system the rotation occurs in the opposite direction.

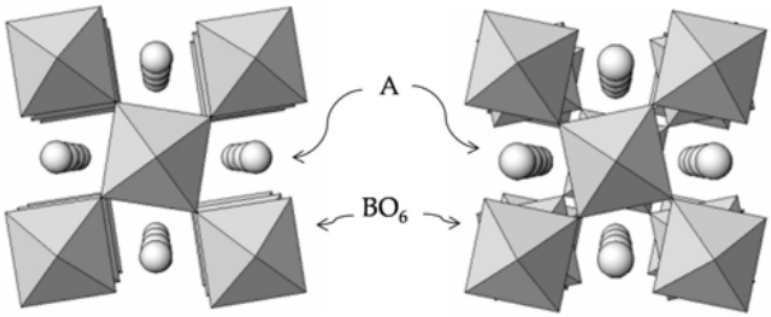

Figure 8. Scheme of the two one-tilt systems $a^0\ a^0\ c^+$ *and* $a^0\ a^0\ c^-$. View looking down the *z* axis. Adapted from ref.[114]

At the time, Glazer identified 23 tilting systems. However, in 1998 Howard and Stockes reported that five of the 23 glazer tilting systems were redundant and three others that were not able to occur in real crystals (i.e. $a^+\ b^+\ c^-$ (*Pmmm*), $a^+\ b^+\ b^-$ (*Pmmm*) and $a^+\ a^+\ a^+$ (*Pmmm*)).[116] Consequently, the number of tilting systems observed in real crystals can be reduced to 15, as shown in Table 5.

Table 5. Tilting systems, number of tilts, space groups and symmetry revised by Howard & Stokes.

Tilting system (Glazer)	Number of tilts	Space Group	Symmetry
$a^0\ a^0\ a^0$	0	$Pm\bar{3}m$	Cubic
$a^-\ a^-\ a^-$	3	$R\bar{3}c$	Rhombohedral
$a^0\ a^0\ c^-$	1	*I4/mcm*	Tetragonal
$a^0\ a^0\ c^+$	1	*P4/mbm*	Tetragonal
$a^0\ b^-\ b^-$	2	*Imma*	Orthorhombic
$a^-\ b^-\ b^-$	3	*C2/c*	Monoclinic
$a^+\ b^-\ b^-$	3	*Pnma*	Orthorhombic
$a^0\ b^-\ c^-$	2	*C2/m*	Monoclinic
$a^+\ a^+\ a^+$	3	$Im\bar{3}$	Cubic
$a^0\ b^+\ c^-$	2	*Cmcm*	Orthorhombic
$a^0\ b^+\ b^+$	2	*I4/mmm*	Tetragonal
$a^+\ a^+\ c^-$	3	$P4_2/nmc$	Tetragonal
$a^+\ b^+\ c^+$	3	*Immm*	Orthorhombic
$a^-\ b^-\ c^-$	3	*P-1*	Triclinic
$a^+\ b^-\ c^-$	3	$P2_1/m$	Monoclinic

1.2.3 Perovskite Oxynitrides

The main disadvantage of using perovskite oxides as visible light photocatalyst lies with the fact that they usually present wider band gaps which lead to inefficient use of the sunlight. A practical and common approach consists of modifying actual metal oxide semiconductors by narrowing their band gap via nitrogen doping in order to make them suitable for the absorption of visible light. Consequently, a class of novel materials with promising photocatalytic activity in the visible region has emerged, the perovskite oxynitrides.

Quaternary metal oxynitrides, with the general composition -$AB(O,N)_3$-, are a class of promising materials that combine the advantages of oxides and nitrides, such as greater stabilities in air and moisture than pure nitrides, while keeping small band gaps that make them suitable as visible light photocatalysts.[117] To the best of my knowledge, perovskite oxynitrides were first reported by Marchand et.al.[118] The published article, originally in French, discussed the preparation of *AB* (*A* = Ba, Sr, Ca and *B* = Ta, Nb) using oxide precursors and ammonia as nitriding source in the temperature range of 950-1000˚C. Since then, perovskite oxynitrides have attracted the attention of the researchers and the number of publications containing the key words "perovskite oxynitrides" keeps raising yearly.

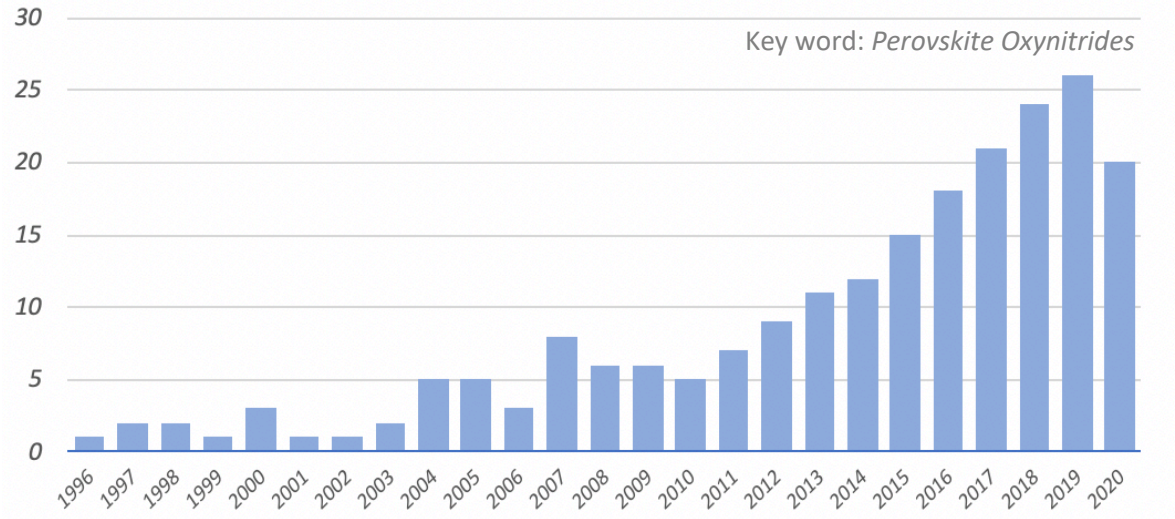

Figure 9. Evolution of the number of publications related to "perovskite oxynitrides" over the last twenty-five years. Data: Web of Science [14]

Partial substitution of stoichiometric amounts of oxygen by nitrogen into the anionic network of the oxide precursor makes it possible to narrow the band gaps to the visible region, while still retaining the photocatalytic ability common to ultraviolet (UV) absorbing oxides. These visible light photocatalysts can generate reactive oxygen species, such as the superoxide radical anion (O_2^-) and hydroxyl radicals (OH^-), both powerful oxidants. This means that they can be used indoors, under

ordinary illumination conditions for the degradation of organic pollutants and biological contaminants.

A better understating of the anion partial-substitution can be gained by taking a closer look at the difference between the ionic radii, Pauling´s electronegativity, electronic structure, and formal oxidation state between nitrogen (N^{3-}) and oxygen (O^{2-}). Firstly, the similarity of the ionic radii in between nitrogen (r = 1.50 Å) and oxygen (r = 1.40 Å) allows for the anionic substitution. Secondly, since nitrogen has a lower electronegativity than oxygen, the introduction of N^{3-} into the lattice structure induces a more covalent character to the *M-X* bond.

Perovskite oxynitrides are promising materials due to satisfying the following photocatalysis criteria:

- Stability: quaternary perovskite oxynitrides are insoluble in water/acid and corrosion resistant.
- Narrow band gaps allowing the absorption of visible light and generating the reactive oxygen species (ROS).
- Non-toxic: Perovskite oxynitrides have been suggested as eco-friendly alternatives to cadmium and lead pigments [yellow-orange-red Cd (S, Se)].

1.2.3.1 Formability of Perovskite Oxynitrides

The distortions in perovskite materials with the composition ABX_3 can be quantified by using the Goldschmidt's tolerance factor (τ) and octahedral factor (μ) (Equation 1 and 2, respectively). These parameters enable the prediction of a particular symmetry of a structure based on the ionic radius and can be used to evaluate the formability and stability of the perovskite phase.[119]

$$\tau = \frac{(r_A + r_X)}{\sqrt{2}(r_B + r_X)} \quad \text{Equation 1}$$

$$\mu = \frac{r_B}{r_X} \quad \text{Equation 2}$$

Where r_A and r_B being the cationic radii and r_X the anionic radius.

However, these equations cannot be used for the estimation of the tolerance and octahedral factors on perovskites oxynitrides –$AB(O,N)_3$- since the partial substitution of O^{2-} for N^{3-} makes necessary to take into the account the difference in ionic radii of the coordinated nitrogen and oxygen atoms (r_X).

Li et al. proposed a model based on the Goldschmidt's tolerance factor and the octahedral factor for assessing the formability of the perovskite structure in oxynitrides and for predicting new perovskite oxynitrides that have not been synthesized up to date.[119] The new approach considers a geometric average of the ionic radii of the oxygen/nitrogen (*X*) for the 6-fold coordinated *B*-site and the 12-fold coordinated *A*-site.[120]

In this context, tolerance and octahedral factors were formulated as:

$$\tau = \frac{(r_A + r_{AX12}^g)}{\sqrt{2}(r_B + r_{BX6}^g)} \quad \text{Equation 3}$$

$$\mu = \frac{r_B}{r_{BX6}^g} \quad \text{Equation 4}$$

Where r_A and r_B are the cationic radii as previously mentioned, and r_X^g is the geometric average of the anionic radii, express as:

$$r_X^g = \left[\prod_{i=1}^{CN}(r_x)\right]^{1/CN} \quad \text{Equation 5}$$

CN = coordination number.

- For ABO_2N: $r_{BX6}^{g} = (r_O^4 \times r_N^2)^{\frac{1}{6}}$ and $r_{AX12}^{g} = (r_O^8 \times r_N^4)^{1/12}$

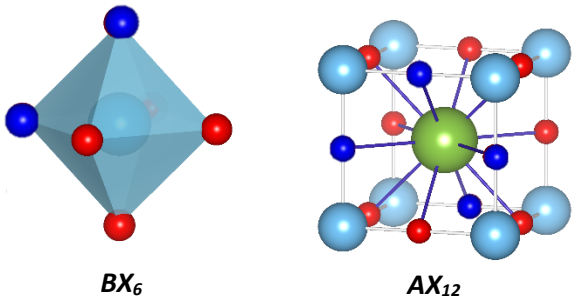

- For $ABON_2$: $r_{B-O/N}^{g} = (r_O^2 \times r_N^4)^{\frac{1}{6}}$ and $r_{A-O/N}^{g} = (r_O^4 \times r_N^8)^{1/12}$

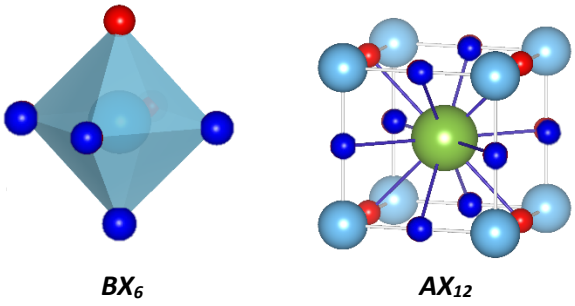

Figure 10. Occupancy of the anion-substituted perovskite oxynitrides on the $B(O,N)_6$ octahedra and the $A(O,N)_{12}$ cuboctahedron.

Anion-ordering still remains a matter of debate as described in Section 1.2.3.3. However, the model proposed by Li et al. considers disordered perovskite oxynitrides with a random nitrogen distribution, since nitrogen and oxygen are not distinguished in the structure. As mentioned before, the geometric average is used as recommended for distorted structures [120], however, Li et al. found that the difference between the arithmetic average and the geometric one is negligibly small. The final proposed equations for tolerance and octahedral factor are in summarised in the Table 6.

Table 6. Tolerance and octahedral factor equations for perovskite oxynitrides based on the ionic radii approximation.[119]

Perovskite	*Tolerance factor*	*Octahedral factor*
ABO_2N	$\frac{[(r_A + r_O)^8 (r_A + r_N)^4]^{1/12}}{\sqrt{2}[(r_B + r_O)^4 (r_B + r_N)^2]^{1/6}}$	$\frac{r_B}{(r_O^4 \times r_N^2)^{1/6}}$
$ABON_2$	$\frac{[(r_A + r_O)^4 (r_A + r_N)^8]^{1/12}}{\sqrt{2}[(r_B + r_O)^2 (r_B + r_N)^4]^{1/6}}$	$\frac{r_B}{(r_O^2 \times r_N^4)^{1/6}}$

Values of R_O (1.4 Å) and R_N (1.5 Å). Calculations make use of the standard Shannon radii data.[121]

When $\tau = 1$, the condition $r_A + \mathrm{r}^{\mathrm{g}}_{\mathrm{AX12}} = \sqrt{2}\,(r_B + r^{g}_{BX6})$ is obeyed, where $r_A + \mathrm{r}^{\mathrm{g}}_{\mathrm{AX12}}$ corresponds to the length of the cube's face diagonal and equals $\sqrt{2}$ times the edge of the cube, in agreement with the Pythagorean theorem. This value corresponds with the ideal cubic perovskite structure ($Pm\bar{3}m$).

$$\left(r_A + \mathrm{r}^{\mathrm{g}}_{\mathrm{AX12}}\right)^2 = \left(r_B + \mathrm{r}^{\mathrm{g}}_{\mathrm{BX6}}\right)^2 + \left(r_B + \mathrm{r}^{\mathrm{g}}_{\mathrm{BX6}}\right)^2$$

$$\left(r_A + r^{g}_{AX12}\right) = \sqrt{2\left(r_B + r^{g}_{BX6}\right)^2}$$

$$\left(r_A + r^{g}_{AX12}\right) = \sqrt{2}\left(r_B + r^{g}_{BX6}\right)$$

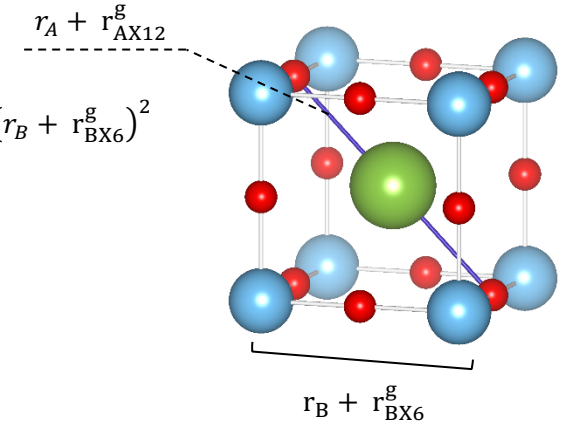

Figure 11. Relationship between the Goldschmidt's tolerance factor and the Pythagorean Theorem.

The crystal structures of a diverse range of novel perovskite oxynitrides have previously been reported from X-ray diffraction data along with crystal structure refinements and space group, which are listed Table 7.

Table 7. Target perovskite oxynitrides, crystal structures, space groups and tolerance and octahedral factors.

Sample	Crystal structure	Space Group	Tolerance factor[119]	Octahedral factor[119]
$BaTaO_2N$	Cubic [122]	$Pm\bar{3}m$	1.03	0.44
$CaTaO_2N$	Orthorhombic[122]	*Pnma*	0.94	0.44
$EuTaON_2$	Cubic[123]	$Pm\bar{3}m$	0.98	0.44
$LaNbON_2$	Orthorhombic[124]	*Pnma*	0.95	0.43
$LaTaON_2$	Monoclinic	*C2/m*	0.95	0.43
$LaTiO_2N$	Orthorhombic[125]	*Imma*	0.97	0.42
$NdTaON_2$	Orthorhombic[124]	*Pnma*	0.92	0.43
$PrTaON_2$	Orthorhombic[122]	*Pnma*	0.95	0.43
$SrNbO_2N$	Tetragonal[126]	*I4/mcm*	0.98	0.44
$SrTaO_2N$	Tetragonal[122]	*I4/mcm*	0.98	0.44

1.2.3.2 Electronic Band Structure

The electronic band structure of perovskite oxides is well established and the valence band and the conduction band of simple ABX_3 perovskites are based on the hybridisation of frontier orbitals from the metal (*M*) and the anion (*X*).[26]

In the case of oxide perovskites, the top valence band is mainly represented by the *O 2p* orbitals near the Fermi level, whereas the bottom conduction band is formed by the d-orbitals of the transition metals. However, the electronic structure is also influenced by the partial oxygen substitution with nitrogen in oxynitrides. The higher energy of the nitrogen *2p* frontier orbitals leads to the hybridisation of both the oxygen and nitrogen valence bands, effectively shifting the top of the valence band and resulting in a new valence band higher in energy. Consequently, smaller band gaps for perovskite oxynitrides compared to their oxide analogues can be expected.

It is noteworthy to mention that the energy difference between the O *2p* (-14.1 eV) and N *2p* (-11.4 eV) modifies the valence band edge positions and consequently, many of the complex oxynitrides containing Ta^{5+}, Nb^{5+} and Ti^{4+} have band gaps falling in the visible range (1.8 – 3.1 eV). Band-gap tuning through anionic substitution has fuelled the number of studies on oxynitride perovskites in the recent years.[127] Developments for their use as visible light-harvesting photocatalyst for water splitting, degradation of organic pollutants, CO_2 reduction as well as a non-toxic alternatives to some inorganic pigments show how perovskite oxynitrides have potential to take part in the solution of environmental issues.[26]

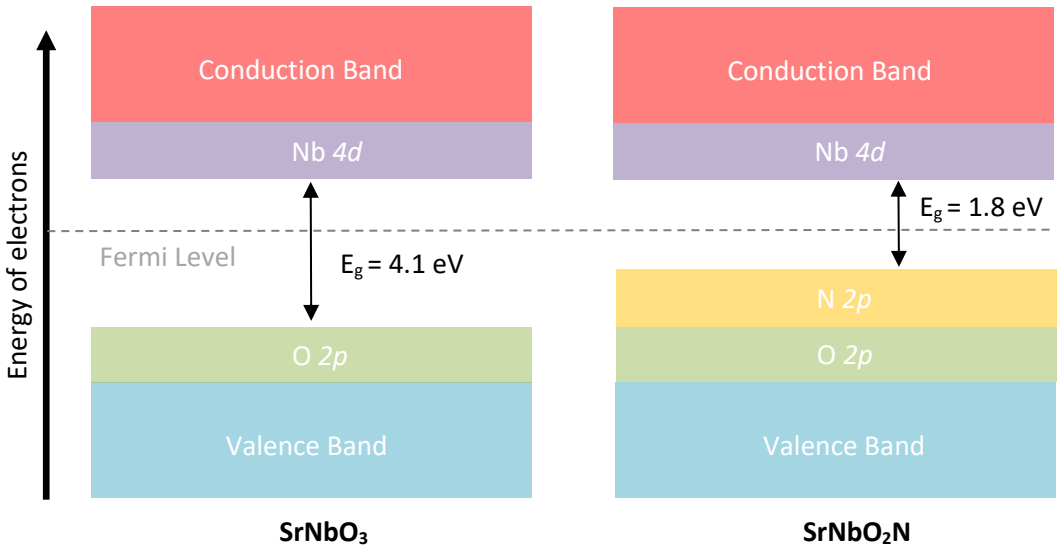

Figure 12. Schematic band structure for the Nb-perovskite oxide ($SrNbO_3$) and $SrNbO_2N$ oxynitride. The black arrow indicates the band gap energy (E_g).

1.2.3.3 Anion Ordering in Perovskite Oxynitrides

Properties of transition-metal oxynitrides with perovskite structure are sensitive to small structural changes within the unit cell. Structural distortions, that may arise from tilting or electronic deformations in the BX_6 octahedron are expected to have a strong influence of the physical properties of the final synthesised perovskite-type oxynitrides. Yang et al. reported an anion ordering investigation of two representative perovskite oxynitride compounds, $SrNbO_2N$ and $SrTaO_2N$, using variable-temperature neutron and electron diffraction.[128] Thus, oxide/nitride ordering is expected to have an impact in directing the metal cation (*B)* displacements in dielectric materials, being crucial with respect to their properties.

Theoretically, nitrogen atoms can adopt a random distribution or two different coordination: *cis-* or *trans-.*

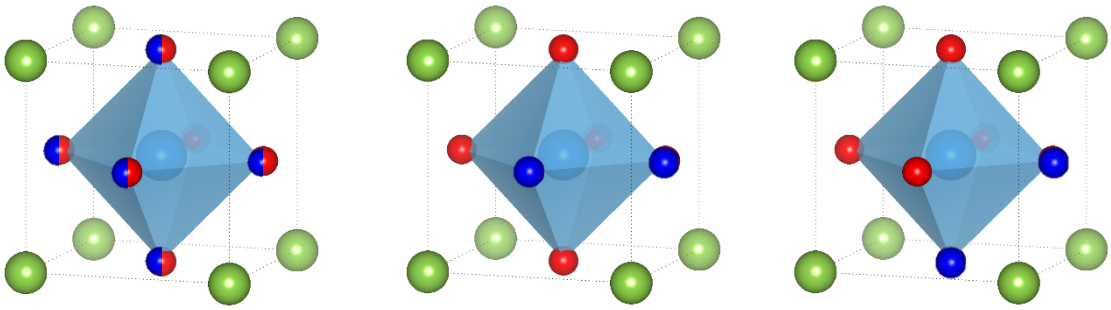

***random** configuration* **cis-** configuration ***trans-** configuration*

Figure 13. Cubic B unit cell showing the possible anion distributions in ABO_2N.

Neutron diffraction results showed that partial anion order in $SrBO_2N$ (*B* = Ta and Nb) perovskites is consistent with the adoption of a *cis-* configuration (90°) of the two nitrides in each octahedral unit (BO_4N_2) with regard to the central metal cation, maximising the $B(d_\pi)$ - $X(p_\pi)$ covalency.[129] This observed tendency is due to the difference in *B*-O and *B*-N covalent bond strength, being *B*-N bonded more strongly and thus, preferred. Hence, the favoured formation of the *cis-* configuration over the *trans-* (180°) is driven by covalent effects. The local *cis*-ordering results in the formation of cross-linked N-*B*-N chains in planes within the perovskite lattice.

An ideal anion order reflects a crystallographically perfect long-range arrangement of the O^{2-} and the N^{3-} along the a-b within the crystal lattice (Figure 14a). However, the N-*B*-N chains are intrinsically prone to disorder due to the 90° anion mobility, leading to six different N^{3-} arrangements within the *cis-* coordination. (Figure 14b and d). The use of high temperatures promotes anion mobility, the *B*-N chains being very susceptible to jumping to the adjacent planes, resulting in a complete random propagation of the chain in the three space directions. (Figure 14c)

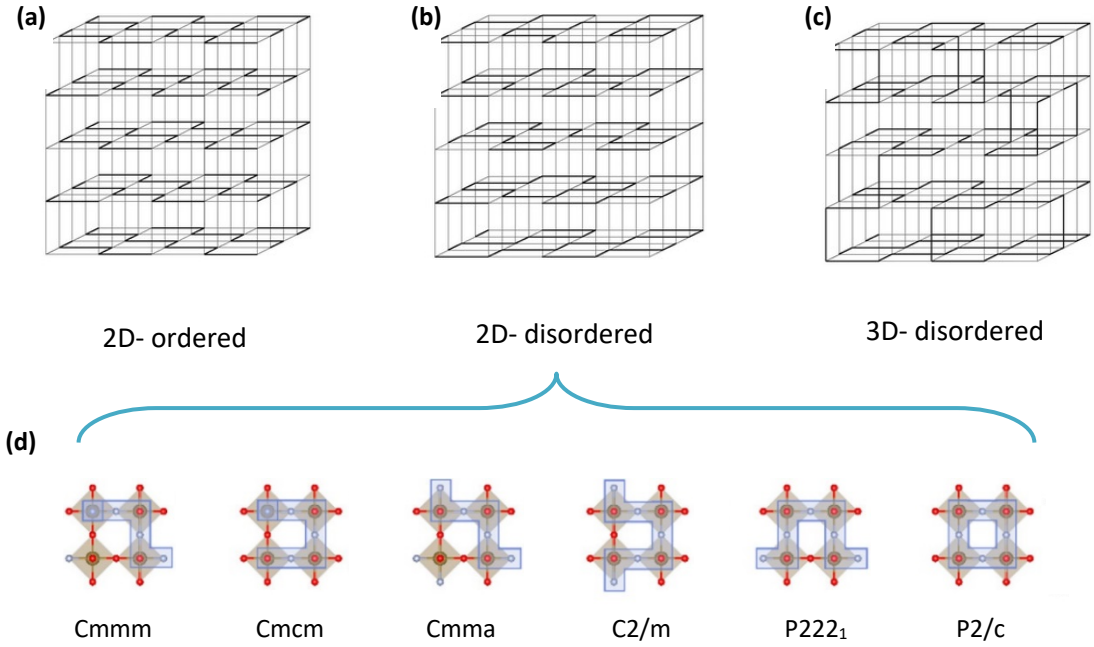

Figure 14. (a) Ideal two-dimensional ordered cubic-superstructure **(b)** 2-D structure showing anion disordered distribution along the plane a-b **(c)** Three dimensions disordered *B*-N chains[128] and **(d)** initial structures of each anion ordering.[129]

Since the valence band (VB) in perovskite oxynitrides is represented by the *2p* orbitals of the anions (O^{2-} and N^{3-}), an impact of the anion ordering on the band structure is evident. The research of Kubo et al. has been focused on clarifying the relationship between the band structure and anion ordering. Recently, theoretical research suggests anion order to be an approach to the tailorability of perovskite oxynitrides.[129] Anion-ordering principles remain a matter of debate and further research must be carried out in order understand the anion arrangements of O^{2-} and the N^{3-} in perovskite-type oxynitrides. The structural impact of the anion ordering on the photocatalytic activity still remains unclear due to the challenging task of controlling the anion-ordering experimentally. Thus, further work needs to be carried out to establish the influence of anion ordering on the structural and physical properties of perovskite oxynitrides.

1.2.3.4 Perovskite Oxynitrides Applications

As mentioned before, thorough research in metal oxynitrides has been carried out in recent years, not limited to the photocatalyst application. Emerging applications of the perovskite oxynitrides as LED devices[130], pigments[125] and magnetic and dielectric materials[131] have been described. For example, developing countries have established new regulations regarding the use of pigments containing of toxic/heavy metals such as Cd, Cr, Pb and Sn in order to protect human health. In this context, perovskite oxynitrides are an alternative as non-toxic inorganic pigments.

Jansen et al. reported the solid solutions of the perovskites $CaTaO_2N$ and $LaTaON_2$ as substitutes of inorganic yellow pigments without toxic metals.[132] In Figure 16, the $Ca_{(1+x)}La_xTaO_{(2-x)}N_{(1+x)}$ solid compositions (labelled as circles) are compared to commercial pigments (labelled as diamonds) such as (1) cadmium yellow, (2) cadmium orange, (3) cadmium red, (4) cadmium dark red, (5) Fe_2O_3 and (6) $(Al_{0.95}, Mn_{0.05})_2O_3$.[132]

Aguiar et al. compiled oxynitrides possessing a variety of colours and plotted them according to the colorimetry analysis in the *Lab* system (Figure 15b). The axes in the 3D graphic correspond to green (a^* (-)), red (a^* (+)), blue (b^* (-)), yellow (b^* (+)), and L^* dark-black (0) / white-light (100).[133]

All the samples the perovskite samples reported in both articles turned to be stable in air, water and in diluted acid, with no signs of decomposition at room temperature.

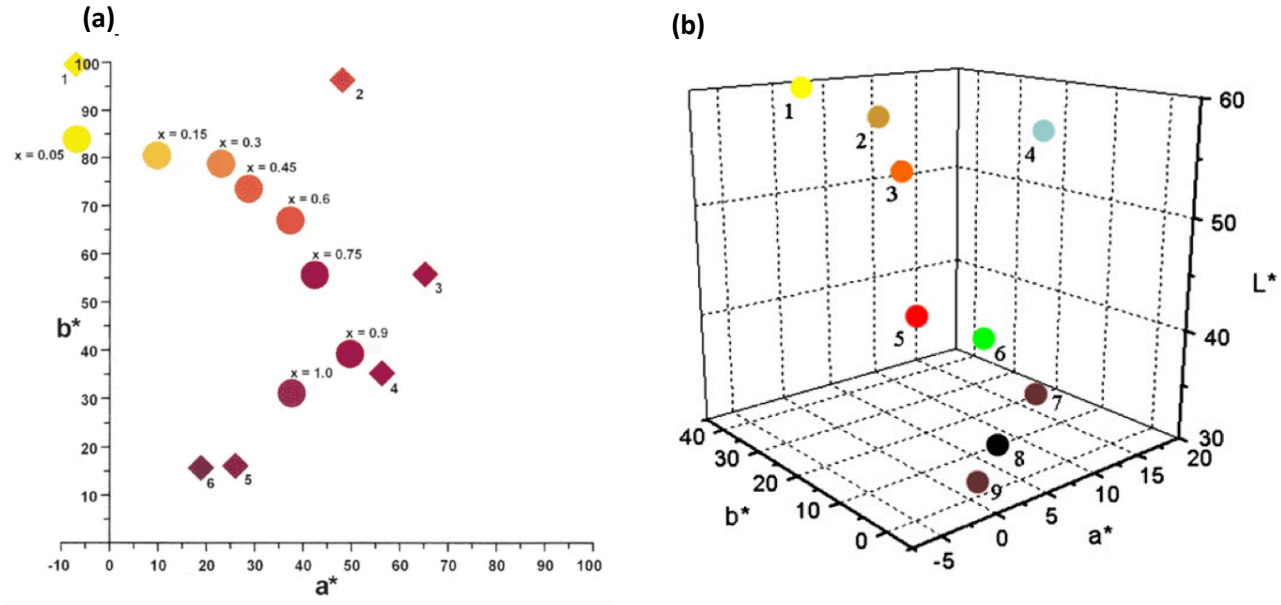

Figure 15. (a) Pigment colour coordinates of the $Ca_{(1+x)}La_xTaO_{(2-x)}N_{(1+x)}$ solid compositions and commercial pigments and **(b)** colorimetric graphic of some oxynitride perovskite pigments (1) $CaTaO_2N$, (2) $CaZr_{0.5}Ta_{0.5}O_{2.5}N_{0.5}$, (3) $SrTaO_2N$, (4) $SrTiO_2N$ (5) $BaTaO_2N$, (6) $Yb_2Ta_2O_5N_2$, (7) $LaTiO_2N$ (8) $BaTaO_2N$ and (9) $SrNbO_2N$. Adapted from ref (a) [132] and (b).[133]

1.3 Perovskite Materials as Photocatalyst

1.3.1 Perovskite Oxides

Perovskite oxides are of significant interest for numerous technologic applications due to properties such as piezoelectricity, multi-ferric behaviour[134] and photocatalytic activity.[91,135–137]

The table below compiles most of the promising perovskite-oxides photocatalyst, however, this section will be focused only in the description of the titanates, tantalates and niobates since the oxynitrides - $AB(N,O)_3$ – synthesised in this work contain Ti, Ta and Nb as the *B*-cation.

Table 8. Summary of the perovskite oxides with potential photocatalytic applications.

Perovskite-base oxide (ABO_3)		Band gap (eV)	Crystal structure	Ref
(ABO_3)	(*A*)			
ATiO_3	$SrTiO_3$	3.25	Cubic	91
	$BaTiO_3$	3.2	Cubic	70
	$CaTiO_3$	3.5	Orthorhombic	137
	$CoTiO_3$	2.28	Rhombohedral	138
	$NiTiO_3$	2.18	Rhombohedral	136
	$FeTiO_3$	2.8	Rhombohedral	139
	$CdTiO_3$	2.9	Rhombohedral	140
	$PbTiO_3$	2.75	Tetragonal	141
ATaO_3	$AgTaO_3$	3.30	Rhombohedral	142
	$KTaO_3$	3.6	Cubic or orthorhombic	127
	$NaTaO_3$	4	Orthorhombic, monoclinic, cubic	143
	$LiTaO_3$	4.9	Cubic or rhombohedral	144
ANbO_3	$AgNbO_3$	2.8	Orthorhombic	106
	$CuNbO_3$	2	Monoclinic	145
	$KNbO_3$	3.24	Cubic, orthorhombic, rhombohedral	146
	$LiNbO_3$	3.5 - 4.7	Rhombohedral	147
	$NaNbO_3$	3.4	Cubic, tetragonal, orthorhombic	148
	$SrNbO_3$	4.1	Cubic	149
AVO_3	$AgVO_3$	2.5	Monoclinic	150
	$BaVO_3$	3.2	Cubic	151
	$LaVO_3$	1.1	Orthorhombic	152
	$PbVO_3$	2.93	Cubic	153
	$SrVO_3$	3.22	Cubic	154
AFeO_3	$AlFeO_3$	2.1	Orthorhombic	155
	$GaFeO_3$	2.7	Orthorhombic	156
	$LaFeO_3$	2.1	Cubic or orthorhombic	157
ABiO_3	$AgBiO_3$	2.5	Trigonal	160
	$KBiO_3$	2.04	Cubic	160
	$LiBiO_3$	1.63	Orthorhombic	160
	$NaBiO_3$	2.53	Trigonal	160
ASbO_3	$AgSbO_3$	2.6	Cubic	161
ASnO_3	$BaSnO_3$	3.0	Cubic	162
	$SrSnO_3$	4.1	Orthorhombic	164

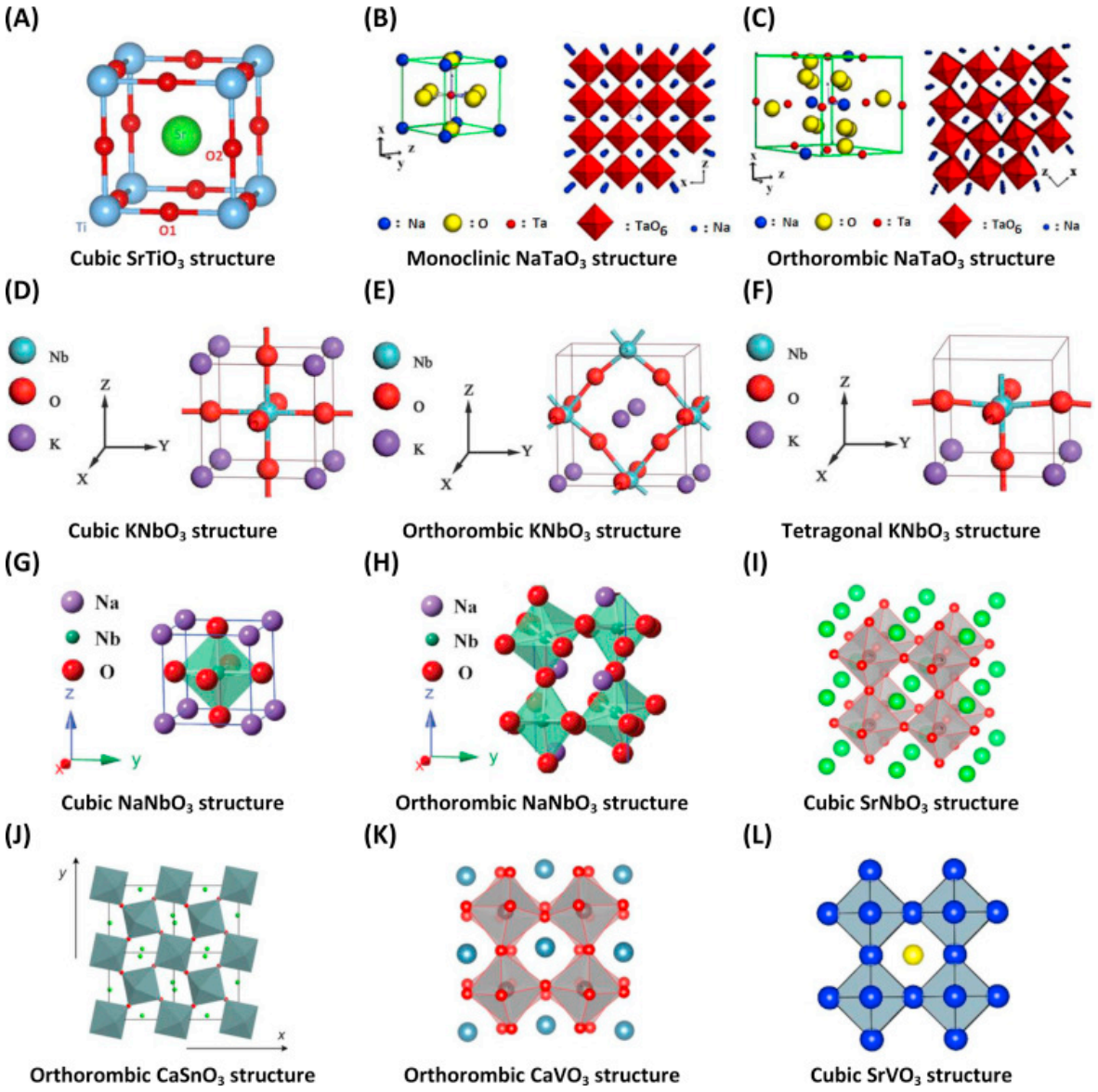

Figure 16. Crystal structures of selected perovskite oxides (ABO_3). Adapted from ref [148].

1.3.1.1 Titanium Oxide Perovskites

Titanate perovskites, $A TiO_3$ (*A* = Ba, Ca, Cd, Co, Fe, Mn, Ni, Pb, Sr) are a family of semiconductor materials with wide band gaps and interesting optic, electronic and magnetic properties as well as excellent photocatalytic activity under UV-Vis radiation. Titanates are promising materials for use in photocatalysis since they show high resistance to photo-corrosion and high temperature stability. Additionally, doping and/or loading with noble/transition metals are widely used techniques to narrow their band gaps and prevent electron hole-recombination, respectively, making them more suitable candidates for purely visible-light photocatalysis.

- *$SrTiO_3$*

Among the titanate perovskites, $SrTiO_3$ is the most promising and studied titanate. Chemically, $SrTiO_3$ is a simple cubic perovskite oxide ($Pm\bar{3}m$) with an indirect band gap of 3.25 eV. Due to its wide band gap, $SrTiO_3$ shows the same main disadvantage as TiO_2 since when undoped, both materials are only able to absorb energy in the UV regions. However, Lyu et al. showed that Al-doped $SrTiO_3$ (referred as $SrTiO_3$:Al) loaded with rhodium chromium oxide ($RhCrO_x$) acting as a co-catalyst was able to split water with an apparent quantum yield greater than 50% at 365 nm. The main problem found was the durability of the photocatalytic system during overall water splitting under sunlight. The activity loss was attributed to the oxidative dissolution of the Cr component in the co-catalyst. Co-loading with RuO_x/CoO_x as an oxygen evolution cocatalyst showed to be a feasible approach to overcome the oxidative problem.[91]

Moreover, Qin et al. investigated the effect of La doping on the photocatalytic properties of $CoO/SrTiO_3$. The photocatalytic activities of the $CoO/SrTiO_3$ system where enhanced with La-doping at different concentrations. The results showed that the rate of H_2 and O_2 evolution increased with the concentration of the doped La up to 0.03 mol%, and then decreased sharply.[135]

- *$BaTiO_3$*

Pristine $BaTiO_3$ has been experimentally confirmed to catalyse hydrogen production from water splitting under UV. However, the reaction cannot be driven under visible light due to its wide band gap (3.2 eV). Therefore, it is also necessary to modify $BaTiO_3$ in order to make it photocatalytically responsive to the visible spectrum. Doping of $BaTiO_3$ with 2.0 atom % Fe showed a shift of 0.39 eV in the UV-vis spectrum, allowing for visible light absorption and enhancing the photoelectrochemical activity. [134]

Maeda et al. reported the photocatalytic water reduction of rhodium-doped $BaTiO_3$ ($BaTiO_3$:Rh) under visible light ($\lambda > 420$ nm) in the presence of methanol as an electron donor. The

rate of H_2 was dependent on the loading amount of Rh. While $BaTiO_3$ exhibited little photocatalytic activity under visible light, $BaTiO_3$:Rh 1 mol% showed the highest rate, while the activity dropped when higher concentrations of Rh were used probably due to the excessive Rh in the surface which can act as recombination centres for the electron-hole pairs.[165]

- *$CaTiO_3$*

Calcium titanate ($CaTiO_3$), whose mineral name is perovskite, is along with $SrTiO_3$ one of the most studied and common perovskite materials. $CaTiO_3$ shows a wide band gap (3.5 eV) to absorb visible light. However, Cu doping has demonstrated to be effective at narrowing the band gap and enhancing hydrogen evolution under UV-vis light. In this context, $CaTiO_3$ doped with Cu^{2+} (2 mol%) and loaded with as a cocatalyst NiO_x has shown to be an effective photocatalyst for water splitting under visible light. $CaTi_{0.98}Cu_{0.02}O_3$ co-loaded with NiO_x showed a rate of H_2 evolution of 22.7 μmol h^{-1} g^{-1}.

Pei et al. described a simple method for the synthesis of nanosized $CaTiO_3$ powder with a hierarchical structure and an extended adsorption profile in the visible region. The band gap modification was achieved by creating defect states, such as oxygen vacancies (band gap engineering). Previous research has demonstrated that oxygen vacancies are able to generate isolated levels below the conductions band, thus, narrowing the band gap and making the semiconductor suitable for visible-light driven photocatalysis.[11,166] The synthesized hierarchical $CaTiO_3$ was able to split water into H_2 at a rate 14.19 μmol h^{-1} g^{-1}.[137]

- *$CoTiO_3$*

$CoTiO_3$ has a narrow band gap of 2.28 eV compared to its Ca and Sr analogues. $CoTiO_3$ nanorods have been reported with excellent photocatalytic performance; highest oxygen production yield up to 64.6 μmol h^{-1} in water oxidation under visible light radiation without any doping/cocatalyst.[138]

- *$NiTiO_3$*

Nickel titanate, with a narrow band gap of about 2.18 eV, possess a noticeable optical absorbance in the visible regions, indicating possible use in visible light driven photocatalytic test. $NiTiO_3$ nanorods showed excellent photocatalytic activity in the degradation of nitrobenzene as well as high stability and reproducibility.[136]

- *$FeTiO_3$*

$FeTiO_3$ possess a band gap of 2.8 eV, being able to absorb visible light. $FeTiO_3/TiO_2$ nanocomposites were able to degrade 97 % of a solution containing 2-propanol in gas phase and 13 % of an aqueous solution containing 4-chlorophenol after 2 h irradiation.[167]

- *$CdTiO_3$*

Hassan et al. reported for the first time $CdTiO_3$ nanofibers with a band gap of 2.8 eV as an effective photocatalyst (97 % of degradation efficiency) for the photodegradation of Rhodamine 6G.[140]

- *$PbTiO_3$*

Li et al. studied the spatial distribution of active sites on the ferroelectric $PbTiO_3$ photocatalyst (2.75 eV) for photocatalytic hydrogen production using a reduction cocatalysts (Pt) and oxidation cocatalyst (MnO_x) separated on the different surface sites of the semiconductor to reduce the probability of electron-hole recombination.[141]

Table 9. Compilation of promising reported titanate perovskites for its use in visible light driven photocatalytic reactions.

Material	Band gap (eV)	Photocatalytic Test	Ref
$RhCrO_x$-($SrTiO_3$:Al)	No data	Water splitting	91
CrO_x-($SrTiO_3$:La)	No data	Water splitting	135
$BaTiO_3$:Fe (2 % atom Fe)	2.81	Water Splitting	134
$BaTiO_3$:Rh	2.53	Water splitting	165
NiO_x-($CaTiO_3$:Cu)	3.6	Water splitting	137
$CoTiO_3$	2.28	Water splitting	138
$NiTiO_3$	2.18	Nitrobenzene degradation	136
$FeTiO_3/TiO_2$ composite	2.8	2-propenol/4-chlorophenol mineralization	167
$CdTiO_3$	2.81	Photodegradation of Rhodamine 6G	140
Pt-$MnO_x/PbTiO_3$	2.75	Water splitting	141

1.3.1.2 Tantalum Oxide Perovskites

Alkali tantalates and $AgTaO_3$ have band gaps too wide to be able to be used in visible light photocatalysis, however their valence and conduction potentials makes them very efficient in overall water splitting reactions under UV light. Computational studies have demonstrated that partial anionic substitution (N, F, P, Cl, S) may be determinant for visible light absorption, especially when N and P are used. Additionally, doping with Bi, N and magnetic cations such as Mn, Fe and Co have been reported. [168]

- *$AgTaO_3$*

$AgTaO_3$ has a reported band gap of 3.30 eV. However, Nb-doped $AgTaO_3$, with a band gap of 2.9 eV, has been described as a water-splitting photocatalyst under visible light. Overall water splitting was achieved using NiO_x as co-catalyst and a 30% mol Nb-doped $AgTaO_3$. ($NiO_x/AgTa_{0.7}Nb_{0.3}O_3$).[142]

Partial anionic substitution with N introduced discrete mid-gap states while F doping leads to band gap narrowing of the $AgTaO_3$ (from 3.30 eV to 2.9 eV). Compensated co-doping was able to create delocalized levels, increasing both the optical absorption and the charge carrier mobility. As a result, N/F co-doped $AgTaO_3$ exhibited enhanced photocatalytic activity in water splitting compared to undoped $AgTaO_3$.[169]

- *$KTaO_3$*

$KTaO_3$ has a wide band gap of 3.6 eV. The effect of the N, Mo/W pair on the electronic structure of $KTaO_3$ has been studied using DFT. Results showed that the presence of both cationic Mo/W and anionic N resulted in a clean band structure, favouring photoconversion efficiency. The reduction in the band gap by the co-doping enhanced visible light absorption, however, further research needs to be carried out to test its photocatalytic activity. [148]

- *$NaTaO_3$*

$NaTaO_3$ is not active under visible light (E_g = 4.0 eV), however, S-doping has demonstrated to shift its valence band edge upward by 1.35 eV. Partial substitution of O by S, which has the same number of valence electrons as oxygen, does not introduce undesirable holes or defects. Consequently, S-doped $NaTaO_3$ was able to degrade a 60 % of a phenol solution under visible light irradiation for 8 hours. [148] Moreover, Li et al. demonstrated that the band structure of $NaTaO_3$ can be tuned by the amount of dopant. Doping $NaTaO_3$ with P-Mo sharply narrowed its band gap to 2.04 eV. Also, the position of its VB and CB overlap the water redox potential levels, resulting in high photocatalytic efficiency when compared to the undoped $NaTaO_3$.[143]

- *$LiTaO_3$*

$LiTaO_3$ possess a wide band gap of 4.9 eV and exhibits a considerable photocatalytic activity for the reduction of CO_2 in the presence of H_2 under UV light. However, further studies need to be carried out to assess the photocatalytic activity of doped/loaded $LiTaO_3$ under visible light.

1.3.1.3 Niobium Oxide Perovskites

Like alkali tantalum-based photocatalyst, alkali niobates show good photocatalytic activity under UV light. In 1952, Parravano et al. reported the use of alkali niobates, specifically $KNbO_3$ and $NaNbO_3$, and $LaFeO_3$ for CO oxidation.[170] However, modifications on the band structure to enhance the visible light absorption have been explored and reported. [145,146,168]

- *$AgNbO_3$*

$AgNbO_3$ has a reported band gap of ~ 2.8 eV. The narrow band allows for water splitting under visible light. Formation rates for the photocatalytic H_2 in an aqueous methanol solution were 1.7–5.2 µmol H_2 h^{-1} g^{-1}. [171]

- *$CuNbO_3$*

$CuNbO_3$ is a red-colour p-type material with a band gap of 2.0 eV. It has been reported as a photoelectrode. Photocurrent measurements confirmed that the visible-light absorption promoted the generation and separation of electrons-hole pairs and the transfer of the election to the electrolyte, achieving a photon to electron conversion of a 5% at higher incident photon energies. Also, $CuNbO_3$ photocathodes exhibit a stable photocurrent and distinguished resistance to photo corrosion. [145]

- *$KNbO_3$*

$KNbO_3$ has a band gap 3.24 eV of and has been mainly reported in photocatalytic water splitting and dye degradation under UV radiation. The effect of doping with N and W has been reported by Modak et al. Doping with N and W introduced impurity states at the bottom of the conduction band and at the top of the valence band, shifting the band gap to a value of 2.36 eV and improving the visible light driven photoactivity of $KNbO_3$. [146]

- *$NaNbO_3$*

La and Co doping of $NaNbO_3$ has been reported to narrow the band gap from 3.40 eV for pure $NaNbO_3$ to 2.65, 2,70 and 2,74 eV for $(LaCo)_{0.05}(NaNb)_{0.95}O_3$, $(LaCo)_{0.03}(NaNb)_{0.97}O_3$, $(LaCo)_{0.01}(NaNb)_{0.99}O_3$ respectively. The samples were loaded with 0.5 wt% Pt and tested for H_2

evolution from an aqueous methanol solution under visible light. The best sample, $LaCo)_{0.03}(NaNb)_{0.97}O_3$, was able to produce 11.9 μmol of H_2 per hour. [172]

- *$SrNbO_3$*

$SrNbO_3$ has a large band gap of 4.1 eV. However, the partial substitution of O by N results in the formation of the oxynitride $SrNbO_2N$ (E_g = 1.8 eV). This material will synthesised in this Thesis and its photocatalytic properties explored. [173]

Perovskite oxides have shown to have multiple applications as summarised in Table 10. Nevertheless, in most cases the band gaps are too wide to effectively absorb visible light and doping is required in order to narrow their band gap for visible-light driven photocatalysis. Traditionally, most research efforts on oxide compounds have been focused in cationic modifications, giving rise to new complex perovskite materials such as $BaMg_{0.33}Ta_{0.67}O_3$ (widely used in microwave dielectrics).

Table 10. Reported applications of selected oxide perovskite materials.

Applications	Perovskite Material
Multilayer capacitor	$BaTiO_3$
NO_x sensor	$LaFeO_3$
Second harmonic generator	$KNbO_3$
Q-Switch	$LiNbO_3$
P.T.C. Thermister	(Y, Bi) - $BaTiO_3$
Insulator	$SrTiO_3$

However, a less explored approach is the anionic substitution in oxide perovskites. In this context, F^- and N^{3-} have comparable anion sizes to O^{-2} and can be incorporated into the lattice structure without inducing a structural change, giving rise to a new family of materials known as perovskite oxyfluorides and perovskite oxynitrides. The partial substitution of the oxygen anions by similar anions such as F^- and N^{3-} will multilaterally influence the position of the valence band, while maintaining the perovskite framework. In perovskite oxides *ABO_3,* the valence band (VB) is formed by contribution of the *2p* orbitals from the oxygen anion. However, from F < O < N, the atomic 2*p* energy level increases as -17<-14.1<-11.5 eV.[174] When partial substitution occurs, the separations between the O/F and O/N *2p* are too small, resulting in the hybridisation of the two anions' *2p* orbitals. Consequently, when the perovskite oxide is substituted with fluorine atoms (oxyfluoride) the VB will swift downward (broaden band gap), while the substitution with nitrogen atoms (oxynitride) will narrow the optical band gap of the material.

1.3.2 Perovskite Oxynitrides

Perovskite oxides have shown remarkable photocatalytic activity under UV-vis radiation. Partial substitution with N^{-3} results in the formation of perovskite oxynitrides, a novel class of materials of great interest in the photocatalytic field. In 2002, Kasahara et al. reported for the first time the photocatalytic activity of a perovskite oxynitride $LaTiO_2N$ under visible light irradiation. $LaTiO_2N$ (2.1 eV) was able to oxidise H_2O into O_2 and reduce H^+ into H_2 in the presence of a sacrificial electron donor for the reduction (methanol) or acceptor for the oxidation (Ag^+).[175]

The initial quantum efficiency for the water oxidation process was *ca.* 1.5%, and the total O_2 evolved over 43 h was estimated to be 440 μmol (0.02 g $LaTaON_2$) while the initial quantum efficiency for H_2 evolution was estimated to be about 0.15%. Kasahara et al. detected that small amounts of N_2 coevolved with O_2 due to the oxidation of the nitrogen (N^{3-}) in the $LaTiO_2N$ as follows: $3N^{3-}$ + 6 holes (h^+) -> N_2.

Partial substitution of Ca^{2+} for La^{3+} and modification with IrO_2 nanoparticles supressed the self-degradation of the oxynitride and increased O_2 evolution efficiency due to charge carrier separation.[175] $La_{0.75}Ca_{0.25}TiO_{2.75}N_{0.25}$ was also tested and the Ca-modification led to and enhancement of the quantum efficiency from 1.5% for $LaTaON_2$ to *ca.* 5%. [175]

To date, only a limited number of perovskite oxynitrides have been synthesised, however, these are becoming increasingly relevant for photocatalytic applications.[176] Photocatalytic activity under visible light has been reported for *A*TaO_2N (*A*= Ba, Ca, Ce, Eu, Gd, Pr, Sm, Sr, La), $CaNbO_2N$, $SrNbO_2N$, $LaNbON_2$, $LaZrO_2N$, $LaMg_{1/3}Ta_{2/3}O_2N$, $ATiON_2$ (B = Ce, Pr, Nd, Ti), $LaMg_{1/2}Ta1_{/2}O_{5/2}N_{1/2}$.

		A-site																
Site		Li^+	Na^+	K^+	Mg^{2+}	Ca^{2+}	Sr^{2+}	Ba^{2+}	Zn^{2+}	Cd^{2+}	Eu^{2+}	Sc^{3+}	Y^{3+}	Ga^{3+}	In^{3+}	La^{3+}	Pr^{3+}	Nd^{3+}	Sm^{3+}
B-site	Si^{4+}											N	N	N	N	N	N	N	N
	Ge^{4+}											N	N	N	N	N	N	N	N
	Sn^{4+}											N	P	N	N	P	P	P	N
	Ti^{4+}											N	P	N	N	S/P	P	S/P	N
	Zr^{4+}											N	P	N	N	S/P	S/P	S/P	S/P
	Hf^{4+}											N	P	N	N	P	P	P	N
	Mn^{4+}											N	N	N	N	N	N	N	N
	Fe^{4+}											N	P	N	N	P	P	P	P
	Co^{4+}											N	N	N	N	N	N	N	N
	V^{4+}											N	P	N	N	S^b/P	P	S/P	P
	Nb^{4+}											N	P	N	N	P	P	P	N
	Ta^{4+}											N	P	N	N	P	P	P	N
	Mo^{4+}											N	P	N	N	P	P	P	N
	W^{4+}											N	P	N	N	P	P	P	N
	V^{5+}				N	N	N	N	N	N	N	N	N	N	N	N	N	N	N
	Nb^{5+}				N	S/P	S/P	S/P	N	P	S/P	N	N	N	N	S/P	S/P	N	N
	Ta^{5+}				N	S/P	S/P	S/P	N	P	S/P	N	N	N	N	S/P	P	N	N
	Mo^{5+}				N	S^b/P	S^b/P	N	N	P	P	N	N	N	N	P	P	P	N
	W^{5+}				N	P	S/P	N	N	P	S^b/P	N	N	N	N	S^b/P	P	S^b/P	N
	Mo^{6+}	P	P	N	N	N	N	N	N	N	N								
	W^{6+}	P	P	N	N	P	P	N	N	P	P								

Figure 17. Formability of the perovskites ABN_2O and $ABNO_2$. S perovskite oxynitrides synthesised so far, S^b non-stoichiometric perovskites, N non-stable perovskites, P predicted perovskites. Adapted from ref [119].

Table 11. Perovskite oxynitrides reported in the ICSD database to date, their band gaps and photocatalytic activity under visible light.

Material	Band gap (eV)	Photocatalytic Test	Ref
$BaNbO_2N$	1.7	O_2 evolution	117
$BaSc_{1/3}Ta_{2/3}O_{8/3}\ N_{1/3}$	1.8	Test not reported	177
$BaTaO_2N$	1.8	Water splitting	178
$CaNbO_2N$	2.0	Water splitting	117
$CaTaO_2N$	2.4	Water splitting, dye degradation	179
$CeTaON_2$	1.7	Test not reported	180
$CeTiON_2$	2.0	O_2 evolution	181
$EuTaO_2N$	No data	Test not reported	123
$GdTaON_2$	1.8	Test not reported	180
$LaMg_{1/2}Ta1_{/2}O_{5/2}N_{1/2}$	1.9	Water splitting	177
$LaMg_{1/3}Ta_{2/3}O_2N$	1.9	H_2 evolution	182
$LaNbO_2N$	1.6	Water splitting	117
$LaTaON_2$	1.8	Water splitting	183
$LaTiO_2N$	2.1	CO_2 reduction, O_2 evolution	181
$LaVO_{3-x}N_x\ (0 \leq x \leq 1.02)$	No data	Test not reported	184
$LaZrO_2N$	2.8	O_2 evolution	185
$NdTiO_2N$	2.0	O_2 evolution	181
$PrTaON_2$	1.9	Water splitting	180
$PrTiON_2$	2.0	O_2 evolution	181
$SmTaON_2$	2.0	Test not reported	180
$SrMoO_{2.5}O_{0.5}$	No data	Test not reported	186
$SrMoO_{2.6}N_{0.4}$	No data	Test not reported	187
$SrNbO_2N$	1.8	O_2 evolution	117
$SrTaO_2N$	2.1	Water splitting	188
$SrWO_2N$	No data	Test not reported	186

1.3.2.1 Tantalum and Niobium Oxynitride Perovskites

Tantalum and niobium perovskite oxynitrides, $AB(O,N)_3$ (*A* = Ba, Ca, Ce, La, Pr, Sm; *B* = Ta, Nb) are promising candidates for visible light photocatalysis due to their suitable band gaps.

Ebbinghaus et al. reported the photocatalytic properties of CoO_x-loaded nano-crystalline powder perovskite oxynitrides ABO_2N (*A* = Cr, Sr, Ba, La; *B* = Nb, Ta). The oxynitrides were synthesised from hydrothermally obtained oxide precursors and subsequent ammonolysis. Prior to the photocatalytic testing, the perovskite oxynitrides were loaded with the co-catalyst CoO_x, a hole scavenger which prevents electron hole recombination, thus, enhancing the photocatalytic activity of the sample. The samples were tested on their ability to degrade a solution containing methyl orange, a model substance (carcinogenic diazo-compound) which is stable under the chosen reaction conditions photocatalyst. Among all the tested oxynitrides, five of them ($BaTaO_2N$, $CaTaO_2N$, $SrTaO_2N$, $CaNbO_2N$, $SrNbO_2N$) showed high decomposition rates, while $BaNbO_2N$ showed a lower decomposition rate and $LaTaON_2$ showed no activity at all. This was attributed to the unmatched redox potentials of the test reaction with the energies of the valence and/or conduction band of the oxynitride. However, the no activity of the CoO_x:$LaTaON_2$ proved that the co-catalyst does not act as photocatalyst itself.[176]

As observed in Table 12, the oxynitride CoO_x:$SrNbO_2N$ was reported with the highest photocatalytic activity and was able to decompose more than a 25% of a solution containing methyl orange under solely visible light ($\lambda > 420$ nm). This percentage was increased to 29% when UV-vis light ($\lambda > 300$ nm) was used. The second most active photocatalyst was the CoO_x:$CaNbO_2N$, which was able to degrade a 10.5% of the methyl orange solution under solely visible light. The oxynitrides CoO_x:$CaTaO_2N$, CoO_x:$SrTaO_2N$ and CoO_x:$BaTaO_2N$ were able to degrade a 5.13%, 4.72% and 7.46% respectively under solely visible light. As a general trend, the photocatalytic activities increased as the surface area increased (ammonolysis temperature decreases). Thus, lower ammonolysis temperatures, high specific surface areas and band gaps of around 1.9 eV are reported to be key parameters to enhance the photocatalytic activities of reported tantalum and niobium oxynitrides.[176]

Table 12. Thermal stability, band gaps and photocatalytic efficiency of the tested perovskite oxynitrides. Adapted from ref [176]

Sample	Onset temperature of decomposition	Band gap/eV[a]	$\Delta c/c_0$ after 3 h/%[b]		
			$\lambda \geq 300$ nm unloaded samples	$\lambda \geq 300$ nm CoO_x-loaded samples	$\lambda \geq 420$ nm CoO_x-loaded samples
$CaTaO_2N$	410	2.48	1.64	17.47	5.13
$SrTaO_2N$	490	2.16	0.02	6.83	4.72
$BaTaO_2N$	600	1.89	0	9.71	7.36
$LaTaON_2$	320	1.99	0	0	0
$CaNbO_2N$	350	2.16	1.18	15.66	10.54
$SrNbO_2N$	370	1.90	1.29	29.02	25.59
$BaNbO_2N$	600	1.79	0	0.97	0.12

[a] From Kubelka–Munk plots assuming an indirect band gap transition.
[b] Irradiation conditions: 150 W Xe-lamp, 3 h, 200 mg/L catalyst, 50 μM methyl orange.

Seo et al. studied the solar-driven water splitting over a $BaTaO_2N$ photoanode prepared by nitridation of $Ba_5Ta_4O_{15}$.[178] The photoanode was able to generate a photocurrent of 6.5 mA cm^{-2} at 1.23 V_{RHE} , corresponding to a maximum hydrogen-cell solar-to-hydrogen (HC-STH) energy conversion efficiency of 1.4% at 0.88 V_{RHE}.

Oehler et al. reported the decomposition of methyl orange using $CaTaO_2N$ nanocrystals.[179] The oxynitride was obtained by ammonolysis of the $Ca_2Ta_2O_7$ precursor synthesised by solid-state synthesis and the hydrothermal method. The hydrothermally synthesised precursor required a relatively low ammonolysis temperature of 860˚C compared to the solid-state one (>890˚C). Regarding to the photocatalytic activity of the $CaTaO_2N$, the use of CoO_x as co-catalyst resulted in a strong enhancement of the methyl orange decomposition by a factor of 5-10, as previously described in the literature. The hydrothermally synthesised $CaTaO_2N$ loaded with CoO_x was able to degrade a 17.47% (λ > 300 nm) and a 5.13% (λ > 420 nm) of a 50 µM methyl orange solution while its solid-state analogue was able to degrade a 14.70% (λ > 300 nm) and a 3.53% (λ > 420 nm). This reduction in the photocatalytic activity was attributed to the higher particle size of the solid-state synthesised $CaTaO_2N$.

Siritanaratkul et al. reported the photocatalytic activities of the niobium perovskite oxynitrides $CaNbO_2N$, $SrNbO_2N$, $BaNbO_2N$, and $LaNbON_2$ for hydrogen and oxygen evolution of water under visible-light irradiation.[117] The powder oxynitrides were obtained by ammonolysis the oxide precursors previously obtained by the polymeric precursor method. The photocatalytic activities of the niobium oxynitrides was examined in the presence of a sacrificial electron donor such as methanol (H_2 evolution) and an electron acceptor $AgNO_3$ (O_2 evolution). For the hydrogen evolution platinum was loaded as co-catalyst whereas in the O_2 evolution reaction the powders were used as-prepared. Among all the samples, $CaNbO_2N$ showed the highest evolution rates for both H_2 and O_2 evolution, 1.0 µmol h^{-1} and 31.2 µmol h^{-1}, respectively. During the O_2 evolution reaction the Ag^+ cations from the electron acceptor are reduced to metallic Ag, which deposits onto the photocatalyst, blocking the light absorption and the available active sites, gradually reducing its photocatalytic activity. Also, a low level of N_2 evolution was detected (< 2.0 µmol in 5 h) and this was attributed to a slight self-decomposition of the catalyst as previously observed.[189] However, the self-decomposition was not continuous, indicating that the $CaNbO_2N$ powder sample was stable for overall water splitting. The $SrNbO_2N$ sample showed a small but measurable photocatalytic activity for the O_2 evolution reaction of 1.0 µmol h^{-1}, however no H_2 evolution was observed. $BaNbO_2N$ and $LaNbO_2N$ have smaller band gaps (1.6 and 1.7 eV) and therefore absorb a larger part of the solar spectrum, however both samples did not show any photocatalytic activity. A possible explanation is the higher ammonolysis temperatures needed for their synthesis (950˚C for $LaNbO_2N$

and 850˚C $BaNbO_2N$ vs 750˚C for $CaNbO_2N$) which can result in in defect sites in the crystal sites acting as recombination centres for the photogenerated electron-holes.

Hojamberdiev et al. reported the synthesis of $LaTaON_2$ and $PrTaON_2$ and a study of their photocatalytic activities for water-splitting.[190] The $LaTaON_2$ sample was synthesised by classic solid-state, and subsequent ammonolysis of the oxide precursor at 950˚C for 12 h. Alternatively, the $PrTaON_2$ powder was synthesised by a two-step method. First, the oxide precursor was grown by using a flux method. Then, the white oxide precursor powders were ammonolysed at 950˚C for 50 hours. Both powders were loaded with Pt (0.5 % wt.) and CoO_x (2% wt. Co) and tested for visible-light induced H_2 and O_2 evolution, respectively. Results showed that CoO_x:$LaTaON_2$ powders exhibited a higher O_2 evolution rate of 66.9 µmol in 5 hours, compared to 40.9 µmol in 5 h for CoO_x:$PrTaON_2$. The same pattern was observed during the H_2 evolution reaction, Pt-loaded $LaTaON_2$ reached 26.2 µmol within 5 h while the Pt-loaded $PrTaON_2$ only exhibited 18.3 µmol within 5 h. The substitution of the *A* cation La^{3+} by Pr^{3+} results in an enhancement of the tilting of the $Ta(O/N)_6$ octahedral due to the smaller Pr^{3+} cation, leading to a much greater distortion. Consequently, the conduction band of $PrTaON_2$ is slightly narrowed, resulting in a small bang gap that increases the absorption of a larger part of the visible spectrum, expecting a higher photocatalytic activity. However, the longer reaction time required for the synthesis of $PrTaON_2$ presumably contribute to the formation of high intrinsic defects associated with anion vacancies and reduced tantalum species which diminish the higher expected photocatalytic activity.

To date, investigations on the photocatalytic activities of tantalum, niobium and titanium oxynitrides have been limited to powder samples, thus, the use of perovskite oxynitrides films for dye degradation, water-splitting, and CO_2 reduction remains unexplored. In this thesis we will cover this gap in the literature by synthesising niobium, tantalum and titanium perovskite oxynitrides as thin films and assessing their photocatalytic activity for dye degradation.

Table 13. Photocatalytic activities of niobium and tantalum oxynitrides for water-splitting.

Material	Band gap (eV)	H_2 activity	O_2 activity	Ref
$LaTaO_2N$	2	26.2 µmol in 5 h	66.9 µmol in 5 h	[190]
$PrTaON_2$	2	18.3 µmol in 5 h	40.9 µmol in 5 h	[190]
$CaNbO_2N$	3.6	1.0 µmol h^{-1}	31.1 µmol h^{-1}	[117]
$SrNbO_2N$	2.28	0 µmol h^{-1}	1.5 µmol h^{-1}	[117]
$BaNbO_2N$	1.6	0 µmol h^{-1}	0 µmol h^{-1}	[117]
$LaNbO_2N$	1.7	0 µmol h^{-1}	0 µmol h^{-1}	[117]

1.3.2.2 Titanium Oxynitrides Perovskites

Titanium oxynitride perovskites are of great interest since they also show band gaps responsive to visible light and are composed of relatively cheap elements. As mentioned before, in 2002, Kasahara et al. reported for the first time the photocatalytic activity of an oxynitrides, $LaTiO_2N$, a typical oxynitrides of titanium loaded with IrO_2, acting as co-catalyst , was able to oxidise water into O_2 and reduce H^+ to H_2 in the presence of the appropriate sacrificial agents.[175]

Years later, in 2012, Zhang reported a cobalt-modified porous single-crystalline $LaTiO_2N$ for highly efficient water oxidation under visible light.[191] In this work, the expensive IrO_2/RuO_2 co-catalyst were replaced with cheap, earth-abundant cobalt oxide (CoO_x). The oxide precursors were prepared by the polymeric precursor and flux methods and subsequent ammonolysis at 1050˚C, leading to the formation of meso- and microporous $LaTiO_2N$. The oxynitride powders were loaded with CoO_x (2% wt.) by an impregnation method from an aqueous $Co(NO_3)_2$ solution. The optimized CoO_x:$LaTiO_2N$ showed a high quantum efficiency of 27.1 $\pm$ 2.6% at 440 nm.

In 2015, Porter et al. reported the electronic structure and photocatalytic water oxidation activity of *A*$TiNO_2$ *(A* = Ce, Pr, Nd) perovskite oxynitrides. The three materials $CeTiON_2$, $PrTiON_2$ and $NdTiON_2$ showed band gaps in the range of 2.0-2.1 eV, similar to $LaTiO_2N$ (2.1 eV).[181] The samples were impregnated with a 2 % wt. Co and tested for the photocatalytic O_2 evolution over the period of eight hours. The O_2 evolution rates were 5 μmol g^{-1} h^{-1} for $CeTiON_2$, 11 μmol g^{-1} h^{-1} for $PrTiON_2$, 16 μmol g^{-1} h^{-1} for $NdTiON_2$ and 17 μmol g^{-1} h^{-1} for $LaTiO_2N$. Previous studies reported a higher evolution rate for the $LaTiO_2N$ (~ 600 μmol h^{-1}). In large part, this is owed to the change in lamp wattage from 300 W Xe (~ 6 suns) arc lamp to 150 W Xe lamp (~ 0.5 suns) used by Porter et al. This highlights the need of reporting the results as quantum efficiencies, which take into the account the evolution rates and the rate of absorption of incident photons.

Recently, in 2018, Lu et al. reported the selective reduction of CO_2 to CH_4 over $LaTiO_2N$.[192] Based on the detected intermediates, Lu et al. proposed the pathway: $CO_2 \rightarrow COOH^* \rightarrow CO \rightarrow CH_x^* \rightarrow CH_4$. Photocatalytic tests after 8 hours of irradiation and using H_2O as reducing agent showed a CH_4 and CO production rates of 1.51 μmol g^{-1} and 0.28 μmol g^{-1} respectively.

However, compared to $LaTiO_2N$, the heterojunction $0.3Ta_3N_3/LaTiO_2N$ produced higher quantities of CH_4 and CO (2.53 and 11.54 μmol g^{-1}, respectively). The formation of a type-II heterojunction between $LaTiO_2N$ and Ta_3N_5 resulted in an electric field built at the space-charge region of their interface as a result of charge carrier diffusion, resulting in an efficient charge separation (decreased recombination of the photogenerated of electron-holes) which would contribute to an enhancement of the CO_2 photoreduction.

1.4 Scope of the Present Work

The whole thesis is divided into two different blocks. The first part of the present work (Chapter 1 & 2) is dedicated to an introduction to visible light photocatalysts, with a special focus on perovskite materials, reported materials and different photocatalytic tests (**Chapter 1)**, as well as to the synthetic and characterization methods used in this work (**Chapter 2**). The second part of this thesis (Chapters 3, 4, 5 & 6) corresponds to the experimental sections and the following aspects have been addressed:

In **Chapter 3**, the following powdered perovskite oxynitrides $CaTaO_2N$, $SrTaO_2N$, $BaTaO_2N$, $LaTaON_2$, $EuTaO_2N$, $SrNbO_2N$ and $LaNbON_2$ were synthesised by ammonolysis of the oxide precursors obtained via the polymeric precursor method. Different parameters such as reaction times, ammonolysis temperature and ammonia flow were tested in order to obtain the optimal conditions for their future synthesis as thin films. Phase composition and crystal structure of the synthesised powder oxynitrides were determined by XRD and refined using the Rietveld analysis. Optical band gaps were calculated by the Tauc Plot, derived from diffuse reflectance data. Finally, the thermal stability of the samples was also studied using TG analysis.

The optimised synthetic conditions were used to synthesise the mentioned perovskite oxynitrides as thin films in **Chapter 4.** For this, a resin containing the metal cations distributed was dip coated onto substrate (alumina tiles) and calcined in order to burn off the organic framework, obtaining an oxide-precursor thin film. Then, the samples were ammonolysed under ammonia at the conditions described in Chapter 3, obtaining bright orange-yellow-red-brown perovskite oxynitrides. Phase composition and crystal structures were determined using Le Bail refinement. The chemical composition of the thin films was studied using elemental analysis, EDX mapping and XPS while the morphology and microstructure of the thin films were also investigated using SEM.

In **Chapter 5**, the perovskite oxynitride thin films were investigated on their ability to degrade an dichlorophenolindophenol (DCIP) in water under solely visible light. For this, the thin films were loaded with a co-catalyst which acts as hole scavenger to prevent electron-hole recombination during the photocatalytic process. Additionally, perovskite oxynitrides showing the highest degradation rates ($CaTaO_2N$, $SrTaO_2N$, $SrNbO_2N$) were deposited over quartz substrates previously coated with Al_2O_3 via AACVD. Then, an assessment on their ability to degrade a layer of deposited stearic acid was carried out and monitored through FTIR analysis.

Finally, in **Chapter 6**, we proposed a novel technique for the synthesis of a materials library of different perovskite oxynitride compositions using a manual ink-jet printing method and subsequent photocatalytic testing with the goal of screening the most active candidates for scale-

up. Experimentally, we have modified the most active $SrNbO_2N$ thin films from Chapter 5, introducing alkali (Na and K) and earth (Mg) metals into the perovskite structure. The obtained combinations $SrNb_{1-x}M_x(O,N)_3$ (*M* = Na, K and Mg), where x = 0.2-0.8, were manually printed over alumina substrates and phase purity was analysed using GI-XRD. However, this Chapter is incomplete, and further experiments and characterization needs to be carried out in order to understand the effect of the doping of alkaline (Na, K) and alkaline earth (Mg) metals within the perovskite oxynitride structure. Based on prior studies proved metal ion doping as an effective way of enhancing the photocatalytic activity on perovskite oxynitrides, we propose this chapter as part of the future work.[193]

In this context, the original research reported in this thesis sheds new light on the preparation of perovskite oxynitrides as thin films and their ability to be used for self-cleaning applications.

Chapter 2 Experimental and Theoretical Methodology

Preparation Methods

2.1.1 Preparation of Perovskite Oxynitrides

2.1.1.1 Polymeric Precursor Method (PPM)

In 1967, Pechini patented a method for the preparation of thin film capacitors of lead, alkaline earth titanates and niobates via a sol-gel polymerizable complex method making use of citric acid and ethylene glycol.[194] The so-called Pechini route, also called the Polymeric Precursor Method involves the formation of a citrate-complex, which then undergoes polymerization resulting in a transparent resin containing the cations homogeneously distributed within the organic matrix. Soluble carbonates, chlorides or other suitable metal compounds are used as the main source of cations. Citric acid is a cheap, readily available and effective chelating agent, which stabilizes the dissolved cations preventing them from precipitating as hydroxides. The gel formation is induced by the addition of a polyalcohol (e.g. propylene glycol or ethylene glycol) which upon mild heating conditions (150°C) undergoes polyesterification. The resultant polymeric gel with the trapped metal ions can be used for either powder or thin-film synthesis. For the preparation powder samples the resin is calcined in air at 350°C to remove the organic framework, while for thin-film synthesis, the resin is dip coated onto the substrate, followed by the thermal treatment. In both cases the obtained oxide precursor is used for the synthesis of the final oxynitride.

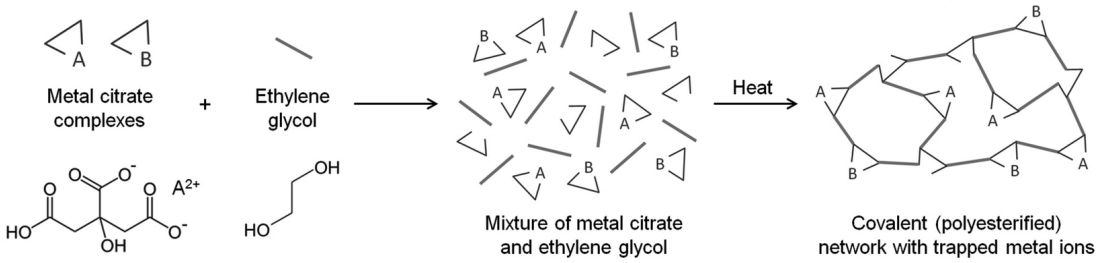

Figure 18 . Schematic representation of the metal-containing resin processing . Adapted from ref .[195]

The Polymeric Precursor Method offers some advantages that are fully exploited in the synthesis of the thin film oxide precursors such as: (1) a precise control of the stoichiometry, (2) different metal cations mixed on an atomic scale, (3) tuning the morphology of the film by

modifying the complexing and dispersing agent ratio and (4) a decrease on the temperature and time of ammonolysis. However, the formation of hard crystallite agglomerates in the original Pechini approach (using the stated molar ratio citric acid to ethylene glycol of 1:4) remains a problem. Thus, uncontrolled agglomerations in the surface can be detrimental to the properties of the final thin films and powders.[196]

To prevent this, it is necessary to optimize the molar ratio of complexing (citric acid) and dispersing agent, ie. EG (ethylene glycol). Figure 19 illustrates the relationship between the different ratios of citric acid:EG and the morphology of formed thin films and its influence.[196] It is noteworthy to mention that an optimal citric acid: EG ratio for the synthesis of a multicomponent powder oxide would be comprised between 4:5 and 6:4 since it comprises the maximum foaming range as well as the maximum viscosity of the gel among all the combinations. These values prevent segregation during the thermal treatment and ensure molecular-scale homogeneity in powder synthesis. However, Pechini (1967) stated a citric acid: ethylene glycol ratio of 1:4 in his original patent. A logical explanation is that the aim of original Pechini patent was the preparation of thin films capacitors, requiring the use of a less viscous resin and absence of foaming during the formation of the organic compositions. Studies conducted by Tai and Lessing (1991) concluded that an excess of EG acts as a barrier to the foaming of the citric acid:EG resins in the Pechini-type processes.[197] Consequently, high concentrations of the polyalcohol are required to obtain smooth thin films and therefore, in this work a ration of 1:11:43 metal/citric acid/propylene glycol is used.

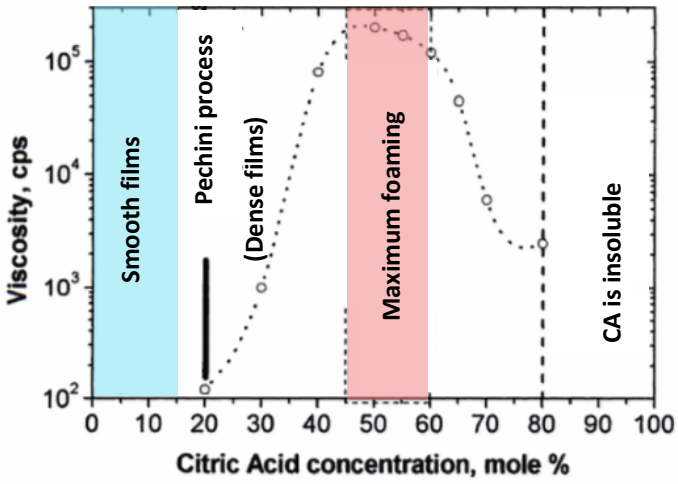

Figure 19. Influence of the citric acid concentration on the gel properties. Adapted from ref.[196]

The described method can be used to synthesize a large number of oxynitride precursors, either as powders or the thin films. Perovskite oxynitrides $AB(O,N)_3$ wherein *A* = Ba, Ca, Eu, La, Sr and *B* = Nb, Ta, Ti can be prepared by direct ammonolysis of the correspondent precursor oxide either amorphous or crystalline.

2.1.1.2 Thermal Ammonolysis

Perovskite oxynitrides are conventionally synthesized by thermal treatment of their oxide precursors under a nitrogen source, preferably, ammonia. Direct nitridation with elemental nitrogen is not used because the high enthalpy of dissociation of the triply bonded N_2 molecule (945.33 kJ mol^{-1}) requires a high activation energy resulting molecular nitrogen (N_2) to be unreactive under atmospheric conditions. Other novel approaches involve the use of cyanamide and urea as nitrogen sources with subsequent heating under N_2 atmosphere for the thermal transformation of metal oxide nanoparticles into ternary metal oxynitrides particles. However, this method was discarded due to the incompatibility of incorporating urea to our thin films.[198] Instead, the use of ammonia (NH_3) under atmospheric pressure offers a feasible, affordable and controlled method for the synthesis of the perovskite oxynitride thin films.

Ammonolysis of the oxide precursors, whether crystalline or amorphous, is carried out by flowing dry ammonia through the reactor tube in a range of 750-1000°C, depending on the nature of the cations *A* and *B* on the oxynitrides. The formation of an oxynitride - $AB(N,O)_3$ – and the overall decomposition of ammonia can be expressed as follows:

$$\text{Oxide precursor} + NH_{3\,(g)} \longrightarrow AB(N,O)_3 + H_2O_{\,(g)}$$

$$NH_{3\,(g)} \longrightarrow 1/2\ N_{2\,(g)} + 3/2\ H_{2\,(g)}$$

Ammonia dissociates into nitrogen and hydrogen at temperatures higher than 500°C and it is suggested to form active nitriding species (N, NH and NH_2) and molecular H_2 on the surface of the oxide.[199] However, the mechanism by which the surface decomposition reactions occurs is not fully understood but it is suggested to adopt the following mechanism by analogy with the nitridation of metals:

$$2NH_{3\,(ads)} \longrightarrow 2NH_{2\,(ads)} + H_2$$

$$2NH_{2\,(ads)} \longrightarrow 2NH_{\,(ads)} + H_2$$

$$2NH_{\,(ads)} \longrightarrow 2\ N_{\,(ads)} + H_2$$

The adsorbed active nitriding species are considered to play a crucial role on the nitridation mechanism, since the N_2 molecules are not effective in nitriding the oxide under the given conditions. The anionic partial exchange between the oxide anions in the lattice and the adsorbed active atomic nitrogen (N) on the surface to give nitride anions results in the release of oxygen. In this context, the abundant surface hydrogen (H_2), result of the combination of two hydrogen atoms released by ammonia molecules on the surface, reacts with the recently removed oxygen atoms

from the oxide, resulting in the formation of water vapour molecules. This step, alongside an overall entropy increase, provides the thermodynamic driving force in the reaction, allowing the active nitrogen atoms to be introduced into the lattice through partial substitution.

However, diatomic nitrogen formed due to the premature dissociation of ammonia affects negatively the efficiency of the formation of the oxynitride phase. In order to minimize the amount of N_2 formed, high flow conditions are preferably required. In this way, speeding up the ammonia flow rate helps to remove the molecular nitrogen and water produced as the renewal of the active nitriding species at the surface sample.

The key processing variables that determine the oxynitride composition during the thermal ammonolysis and need to be considered in order to optimize the purity and reaction rate of the oxynitride phase are:

- *Ammonia Flow*

The percentage (%) of decomposition of ammonia is closely related with the flow rate during the thermal ammonolysis. As observed in Figure 20, at 700˚C and a flow rate of 60 mL min^{-1}, nearly a 49% of NH_3 is decomposed, whereas if we increase the flow rate up to 180 mL min^{-1}, this percentage is reduced to a 10%. Increasing flow velocity provides a higher NH_3 concentration per interval of time, increasing the rate of removal of gaseous by-products and therefore, resulting in a greater nitriding activity. Results in Figure 20 indicate that greater temperatures and slower flow rates enhance the NH_3 dissociation rate, affecting negatively the oxynitride phase formation.

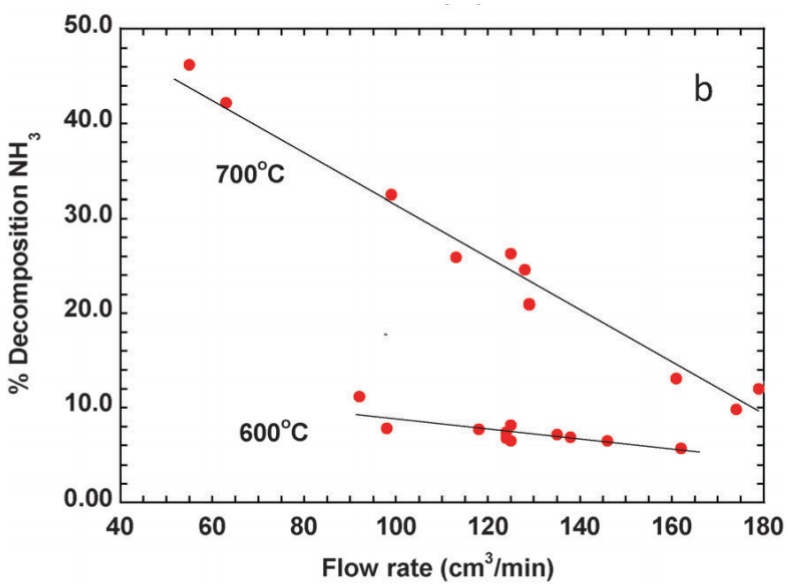

Figure 20. Percentage (%) of decomposition of ammonia as function of the flow rate at 600°C and 700°C. Adapted from ref [26].

- *Sample placement*

Placement of the sample along the reactor contributes to the oxynitride formation. Brophy et al. studied the influence of the sample positioning during the synthesis of $BaTaO_2N$ powders [200] As observed in Figure 21a, the percentage of available ammonia decreases as gas progresses further from the inlet, indicating the importance of sample distribution.

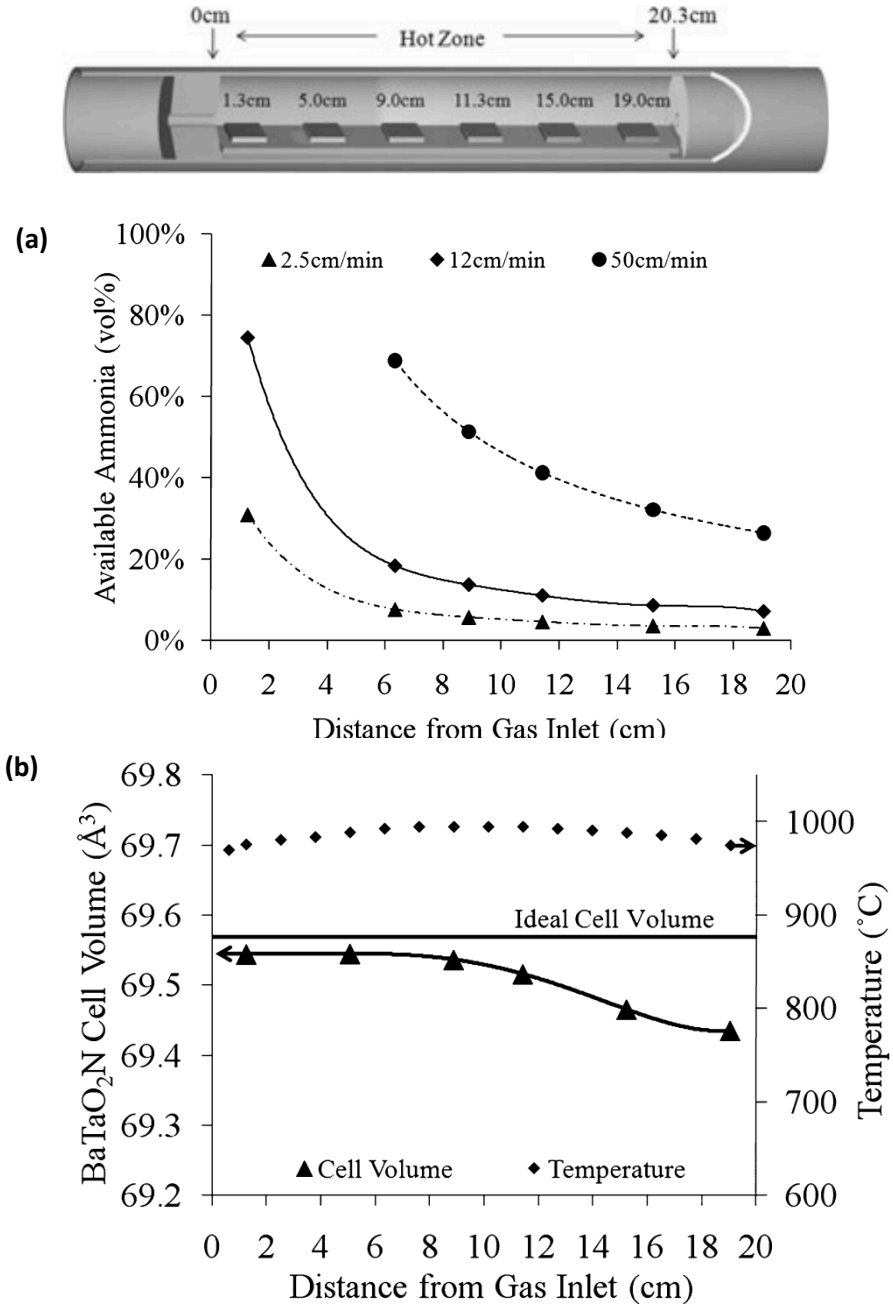

Figure 21. (a) Percentage (%) of available ammonia at 1000˚C as a function of the distance from the ammonia inlet and at three different ammonia flows and **(b)** $BaTaO_2N$ cell volume as a function of the distance from the gas inlet compared with the reported ideal cell volume (1000˚C , 20h, 2.5 $cm^3\ min^{-1}$ NH_3 flow). Adapted from [200].

Moreover, Brophy et al. studied the influence of the sample positioning on the cell volume of the synthesised $BaTaO_2N$ powders. For this, the oxide precursor was ammonised at 1000˚C for 20h, and an ammonia flow rate of 2.5 cm^3 min^{-1}. Samples positioned at 1.3, 5 and 9 cm showed phase purity and similar cell volumes, however, when the distance was increased beyond 9 cm, cell volumes decreased when compared to the reported ideal cell volume and oxide minor phase concentration increased (Figure 21b). Brophy et al. described two primary possible mechanisms for the reported results; first, premature thermal decomposition of NH_3, associated with the reduction in concentration of nitriding species. Second, depletion of NH_3 concentration from upstream sample reactions. The depletion of the NH_3 concentration was investigated by removing the samples at positions 1.3, 5 and 9 cm, leaving only the three downstream samples beyond 9 cm. Results showed matching cell volumes and similar percentages of minor oxide phases for both experiments, indicating that depletion of NH_3 concentration from upstream sample reactions does not occur, while highlighting the importance of placing the samples the first 9 cm.[200]

- *Temperature*

To minimize premature dissociation of NH_3 to N_2 and H_2, it is important to keep the temperatures as low as possible. The upper limitation of temperature during the thermal ammonolysis is defined be the enhanced NH_3 decomposition and instability of the oxynitrides, while the lower limitation of temperature is based on the reaction kinetics of the oxynitride phase formation.[200] Generally, powder niobium and tantalum perovskite oxynitrides have been synthesised in the range of temperatures of 750-1150˚C from their crystalline/amorphous precursors. Results shows that nitridation at temperatures below 750˚C results in incomplete nitridation of the oxynitride phase.[149,176]

- *Reaction times*

Powder niobium, titanium and tantalum perovskite oxynitrides have been reported to require 10-60 hours of thermal ammonolysis for complete phase formation, in most case varying from oxynitride to oxynitride due to their different compositional nature. [176,201]

Based on the previously reported literature mentioned in this section, the key parameters explored in this work will be set as follow:

- Ammonia flow rates in the range of 100 mL and 250 mL min^{-1}
- Samples positioned within the first 8 cm of the reactor
- Temperatures kept as low as possible, in the range of 750 to 1100˚C
- Reaction times of 15 to 60 hours, depending on the oxynitride composition

2.1.2 Thin Film Deposition

2.1.2.1 Dip-coating

The use of perovskite oxynitrides for self-cleaning application requires the material to be deposited in the form of a thin film or coating. In this context, previous work on oxynitrides films produced by expensive techniques such as pulsed laser deposition or magnetron sputtering had been described. The problem remains that these thin film deposition techniques are not ideal for scale up or use in industrial context. Thus, the dip coating technique emerges as an easy and affordable solution for the deposition of oxynitrides as thin films on a large variety of substrates.

Prior to the deposition, the dip coating parameters are set on a computer that controls the dip coater containing a clip holding the substrate. The parameters used for the formation of the thin films described in this work were set as follow; speed up and down of 1 mm sec^{-1}, and immersion time of 30 seconds.

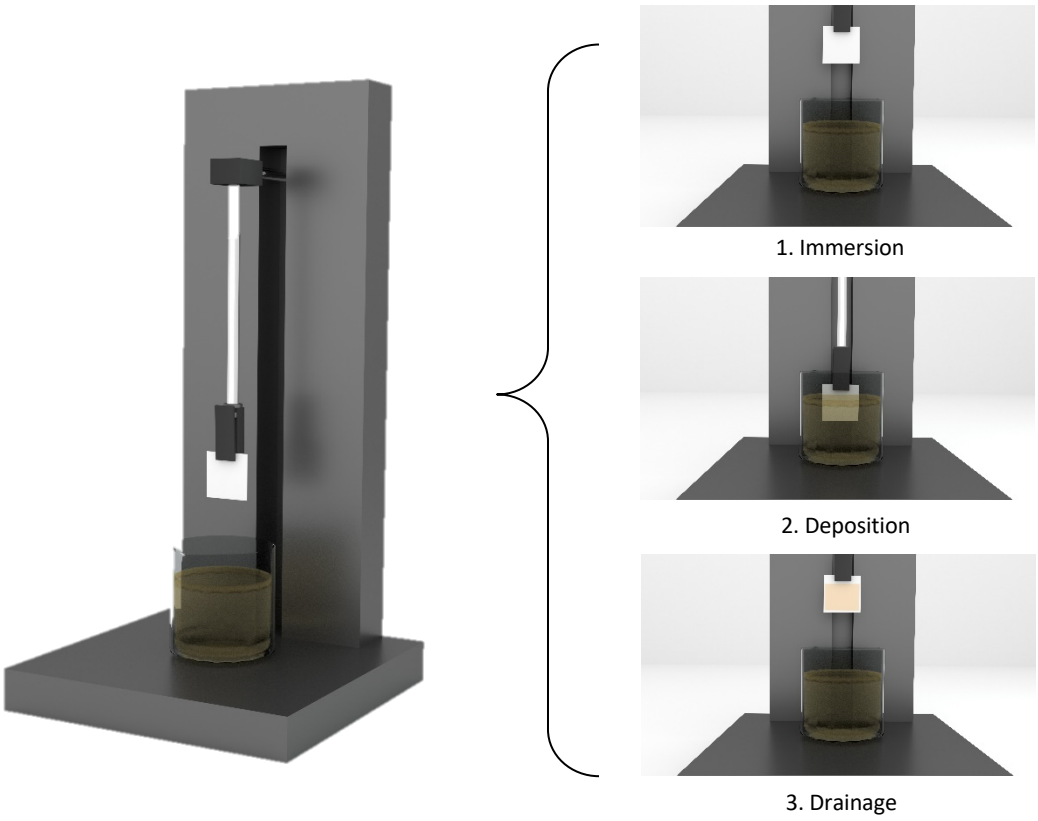

Figure 22. Dip-coater and fundamental stages of sol-gel dip coating.

In a first stage, the substrate is vertically immersed with a constant speed into the coating solution. When the substrate is withdrawn, it entrains the coating liquid. At this point, the excess liquid is drained from the surface resulting in a thin film. The thickness of the deposited thin film is associated to the withdrawal speed and the precursor's concentration. The formation of the thin

film can be broken down into four distinct regions as observed in Figure 23 and these are: (1) the wetting zone, where the formation of the thin films begins, (2) the constant thickness zone, (3) the dynamic meniscus, where the entraining and draining forces are in equilibriums (stagnation point, S) and (4) the static meniscus.

The withdrawal stage during the dip-coating process can be seen as the interaction of the draining and entraining forces. The draining forces are in-charge of drawing the gel away from the substrate and back towards the main solution, while the entraining forces work to retain the gel onto the substrate. The balance between both forces, along with the concentration of the gel, determine the thickness of the thin film.[202]

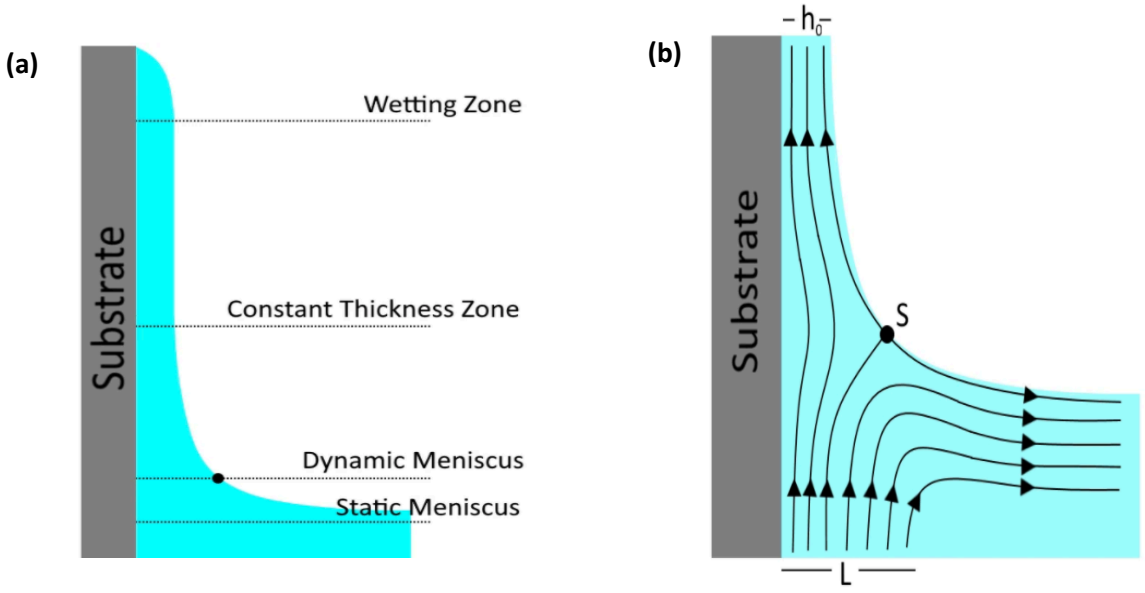

Figure 23. (a) The four distinct regions involved during the dip-coating process: (1) wetting zone, (2) constant thickness zone, (3) dynamic meniscus and (4) static meniscus and **(b)** balance of entraining and draining forces. S corresponds to the stagnation point. Adapted from ossila.com.[202]

Generally, we can assume that lower speeds and low precursors concentrations lead to thinner thin films.[202] Finally, a drying step and a post-thermal treatment are required in order to remove the organic matrix, leading to the oxide precursor.

The thin films prepared in this work were obtained using a lab-made dip-coater with a 1 mm s^{-1} immersion withdrawal speed, and an immersion time of 30 s. In order to improve the atom efficiency, the dip-coating solution (5 mL) was dropped onto 20 mL of tetradecafluorohexane (Sigma-Aldrich, 95%). This innovative approach was developed by Ceratti et al. so that a superficial layer of the dip-coating gel will float on the more dense but inert fluoroalkane and allow dip-coating with the minimum quantity of gel.[203]

2.1.2.2 Aerosol-Assisted Chemical Vapour Deposition (AACVD)

Aerosol-Assisted Chemical Vapour Deposition (AACVD) is also an attractive deposition technique that has gained attention of the academia and industry worldwide due to the control it offers over thin film compositions, coverage and uniformity, even at large scales.[204]

The degradation of stearic acid is easily monitored for transparent samples by FTIR. For this, it was necessary to deposit the perovskite oxynitride thin films over quartz substrates. In a first stage, quartz substrates were protected to prevent the oxynitride from reacting with the quartz, resulting in no formation of the oxynitride phase. In order to emulate the alumina substrates, an Al_2O_3 thin film barrier layer was deposited on the top of the quartz substrate *via* Aerosol-Assisted Chemical Vapour Deposition (CVD), accordingly with the literature.[205] For this, 0.2 g of aluminium acetylacetonate were dissolved in 20 mL of methanol and placed on a 50 mL three-neck round-bottom flask. A piezoelectric device was used in order to generate an aerosol mist, which was subsequently transported into the AACVD reactor by means of an inert carrier gas, in our case, nitrogen. The reactor temperature was set at 500°C and the gas flow to 1 L min^{-1}. The deposited quartz substrates were annealed on air at 1100°C for 10 hours and a 3°C min^{-1} heating ramp.

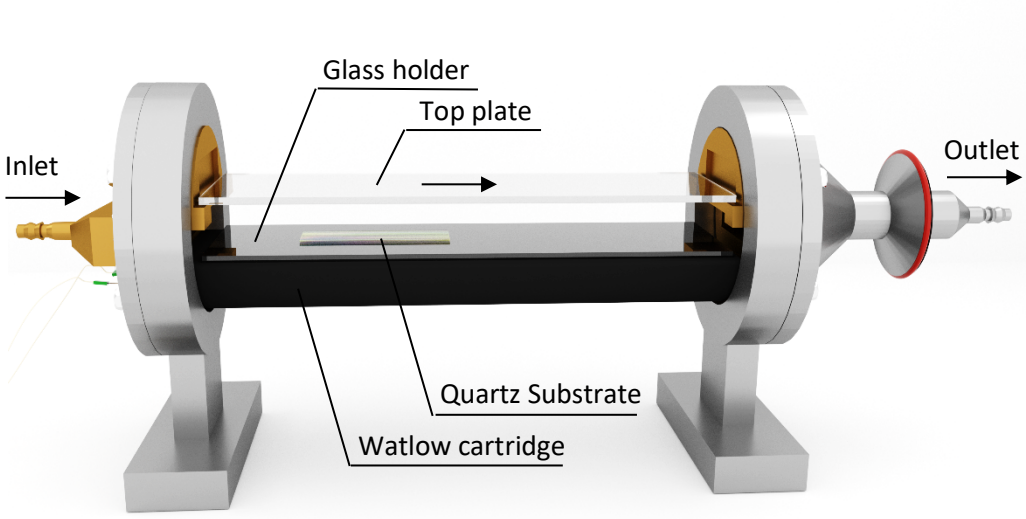

Figure 24. Aerosol-Assisted Chemical Vapour Deposition reactor scheme.

The Figure 24 shows the AACVD reactor rig consists of two stainless steel end supports, inlet and outlet, holding up an open-ended quartz tube (which does not appear in Figure 24). A laminar flow of the aerosol through the chamber was ensured by a brass baffle along with the top plate and the glass support. The glass support was hold over a graphite block containing a Watlow cartridge heater, allowing for the control of the quart substrate temperature by means of a thermocouple.

2.1.3 Ammonolysis Set-Up

The thermal ammonolysis set-up consists of a tube furnace containing a quartz tube connected to a flowmeter that regulates the in-flow from an ammonia cylinder. The quartz tube was fitted with stainless end-caps to prevent any reaction with the ammonia gas. Since the work was carried out under high temperatures, a quartz tube is required instead of a glass one. Alternatively, an alumina tube could be used. The sample is held over a graphite block, which ensures the correct temperature distribution along the substrate. The optimal position of the samples was determined to be the centre of the furnace.

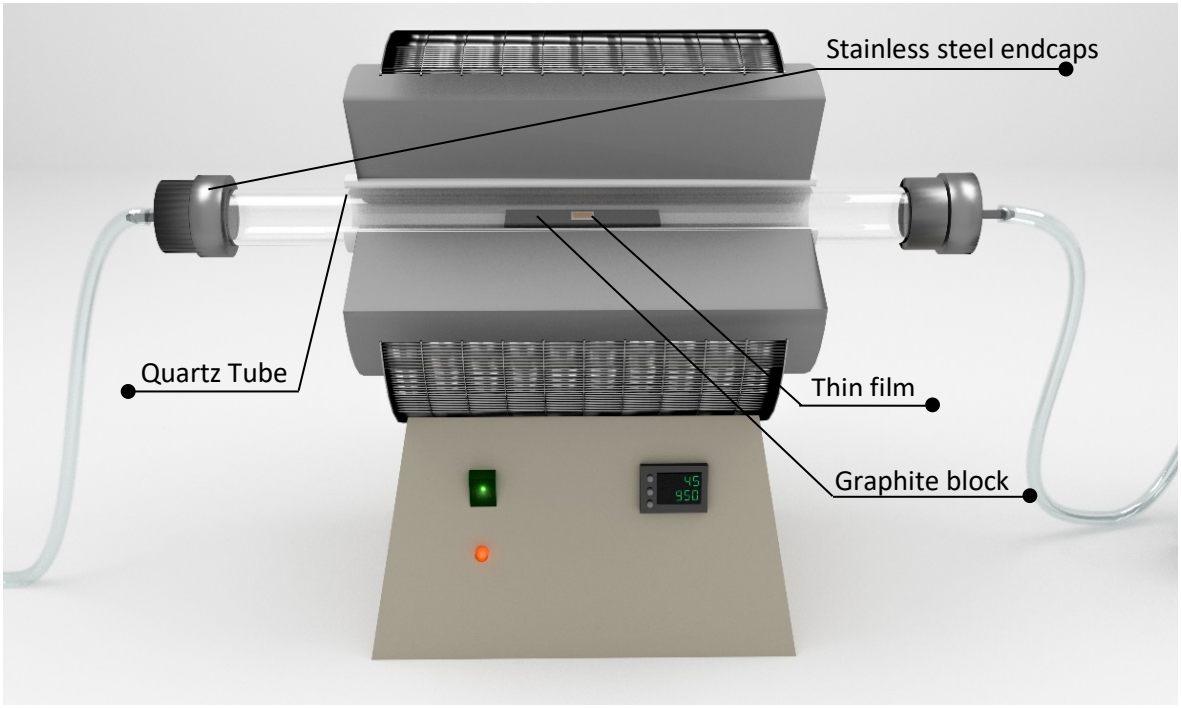

Figure 25. Furnace scheme showing constituent parts of the thermal ammonolysis set-up.

2.1.4 Co-catalyst deposition

The photocatalytic activity of perovskite oxynitrides can be enhanced with the use of cobalt oxide as a co-catalyst.[176] Particles of cobalt oxide (CoO_x) impregnated on the photocatalyst surface provide active centres that can be used for oxidation/reduction reactions and enhance charge carrier separation. Ebbinghaus et al. studied the photocatalytic properties of CoO_x-loaded nano-crystalline powder perovskite oxynitrides. Published results shown that photocatalytic activity of a $SrNbO_2N$ powder sample underwent a strong increase of 30% for the degradation of methyl orange within 3 hours under illumination with solely visible light (≥ 420 nm) by loading the oxynitride with CoO_x co-catalyst.[176]

As shown in Figure 26, two similar pathways are used are used for the deposition of the co-catalysts in this research.

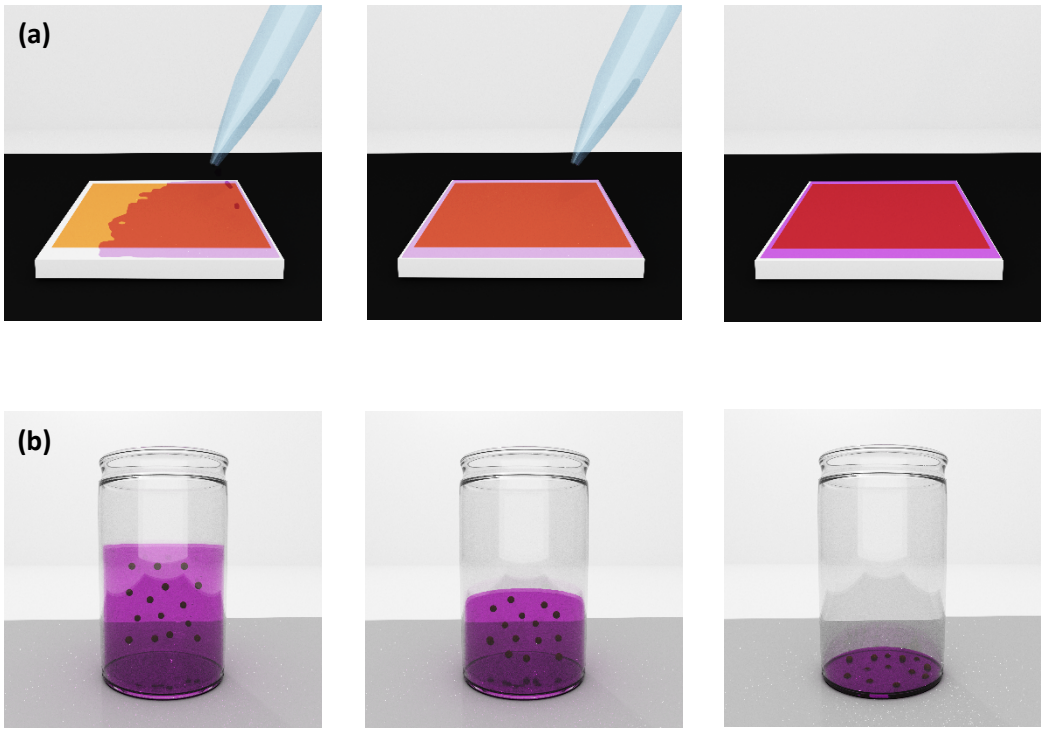

Figure 26. Schematic representation of the different steps during the co-catalyst loading for **(a)** thin films and **(b)** powder samples.

Firstly, the thin films (a) were covered by adding a calculated amount of $Co(NO_3)_2$ dissolved in acetone. Alternatively, powder samples (b) were placed into a vial containing the cobalt nitrate dissolved in the organic solvent. The vial was sonicated in order to ensure complete impregnation of the solution and to avoid aggregation. The thin film dish and the vial were slowly heated (50 °C) until complete evaporation of the solvent, resulting in a homogeneous deposition of the co-catalyst on top of the oxynitride thin films.

For the powders samples tested in this work, the CoO_x values are expressed as % wt. of Co ions and set to a 2 % wt. Co as previously reported in the literature.[176] However, for thin films the co-catalyst concentration was studied at nominal surface concentration of 0.04 – 0.46 μ g cm^{-2}.

The resulting thin films and powder samples were thermally treated under an ammonia flow at 700°C for 60 min, leading to metallic Co-nanoparticles. The active CoO_x co-catalyst was obtained by mild oxidation of the samples in air at 200°C for 1 hour as previously described in the literature.[206]

2.2 Characterization Methods

2.2.1 X-Ray Diffraction (XRD)

X-Ray diffraction is a valuable technique for the identification of unknown crystalline substances as well as for the qualitative and quantitative analysis of described crystalline phases. Crystalline solids can be considered as a periodic arrangement of identical lattice points linked in space by three vectors forming a crystal lattice. X-Ray diffraction experiments can determine the unit cell and the atomic positions within the cell. When X-rays of a given wavelength hit a set of parallel lattice planes (identified with the Miller index) at an angle of θ, every atom within the planes elastically scatters (with no change in energy) the incident radiation in all the directions. Constructive interference occurs when Bragg's Law is obeyed:

$$n\lambda = 2d\ sin\theta$$

where λ is the wavelength of the X, d the interplanar spacing and n is an integer. For a given wavelength and interplanar spacing, d, and setting n = 1, diffraction will occur at a particular θ value.

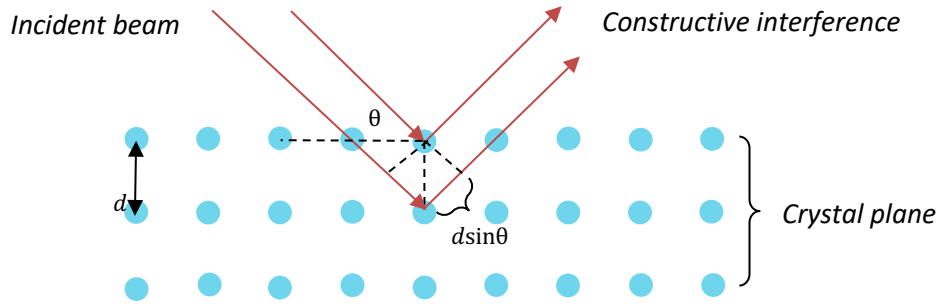

Figure 27. Scheme of the diffraction geometry. $2d$ sinθ represents the path length difference between crystal planes.

The reflected beam depends on the geometric disposition of the atoms within the lattice, thus, every crystalline substance presents its characteristic diffraction pattern (fingerprint). For thin films, grazing incident configuration (GIXRD) is achieved by fixing the incident angle of radiation to values lower than 5°. The GIXRD configuration enables for acquirement of data with a stronger signal from the thin film surface and avoiding (or trying to minimise) the intense signal from the substrate.

2.2.1.1 Thin films

Grazing incident X-ray diffraction patterns were collected by using a Rigaku SmartLab diffractometer equipped with a rotating anode Cu K_a radiation source (45kV - 200mA) and 1D

silicon trip detector. Data were recorded in the angular range of 10°<2θ<80° with a step size of 0.02 and a counting time of 0.1628 min deg^{-1} per data point. Grazing incidence angle was fixed at 1°.

The crystallite sizes (ξ) in nm were estimated by the Scherer's equation as expressed below;

$$\xi = \frac{0.9\,\lambda}{\beta_{hkl}\,cos\theta_{hkl}}$$

where λ the X-ray wavelength, β_{hkl} is the broadening of the hkl diffraction peak at half height of the maximum intensity (FWHM) (radians) and θ_{hkl} is the Bragg angle (degrees).

2.2.1.2 Powders

Powder X-ray diffraction patterns were collected on an X-ray diffractometer Bruker D2 Phaser equipped with a Cu sealed tube ($K_{a1}/(K_{a2})$ source (20kV-10mA), primary and secondary axial Soller slits (2.5°), 0.6 mm divergence slit and a 1D LYNXEYE detector (5° window). A continuous scan mode in the range, 10°<2θ> 80° and a step width of 0.02° and a counting time of 0.1628 min deg^{-1} per data point was selected.

2.2.2 Rietveld Refinement

The characterization of a crystal structure can only be considered complete when the crystallographic parameters are refined using the experimentally obtained diffraction data. In this context, the Rietveld refinement represents a powerful tool for obtaining structural information and the quantitative analysis of phases from an X-ray diffraction pattern. The software performs a series of cyclic calculations of the user-selected parameters (including lattice parameters, preferred orientation and both, shape and peak width) to minimise the difference between the experimental data and a diffraction pattern derived from a given structure model. The Rietveld method consists of an approximation of a calculated line profile to the experimentally obtained X-ray pattern by means of a non-linear least squares fit of a structural model and a non-structural model (profile, parameter, instrumental and spectral), which depends on the angular variation of the linewidths and the peak shape. The intensity at position *i* (y_i) is calculated as:

$$y_i(c) = y_i\,(b) + \sum_k G\,(2\vartheta_i - 2\vartheta_k)\,SM_k\,L_k\,|F_k|^2$$

here $y_i\,(b)$ is the background intensity, L is the Lorentz multiplier, defined by the diffraction geometry, G is the profile peak function, F_k is the structure factor as determined by the crystal structure of the material and *k* represents the Miller indexes *hkl* for a Bragg reflection.

There are four different categories which contribute to the intensities of the experimentally obtained X-ray diffraction patterns and these are:

- *Instrumental factors:* diffractometer efficiency, X-ray intensity from the source, *etc.*
- *Structural factors:* Atomic dispersion factors, structure factor, polarization, multiplicity and temperature.
- *Sample factors:* absorption, size, crystallization and orientation of the crystallites.
- *Measurement factors*: Includes the method for the measurement of the peaks area, the method for the obtention of the background, peaks produced by the $k_{2\alpha}$ radiation and smoothness.

The exhaustive information obtained from the Rietveld analysis allows for the following applications:

- *Quantitative analysis of multi-phase materials*: determination of the proportions of the different phases in the sample by means of their corresponding scale factors (S).
- *Crystal structure refinement*: This method allows to refine cell parameters, atomic positions, thermic factors and atoms occupancy.
- *Microstructural characterisation of the different phases*: determination of the crystallite size, micro-deformations found in the crystal network and preferred orientations.

The Rietveld refinement not only requires a profile function to model the diffraction peaks but also functions that model the full width at half maximum (FWHM), the asymmetry, the preferred orientation, the background, *etc.*

- *Profile Functions:*

The peak description is usually described by three parameters: the peak position, the intensity and the width of the function which is represented by the full width at half maximum (FWHM). The most used symmetric profile functions are defined by the following equations:

$$Gaussian\ (G) = \frac{C_0^{1/2}}{H_i \pi^{1/2}} \cdot \exp\left[-\frac{C_0\ (2\vartheta_k - 2\vartheta_i)^2}{H_i^2}\right]$$

$$Lorentzian\ (L) = \frac{\sqrt{C_1}}{H_i\ \pi} \cdot \frac{1}{1 + \frac{C_1\ (2\vartheta_k - 2\vartheta_i)^2}{H_i^2}}$$

Where H_i represents the full width at half maximum (FWHM) and $C_0 = 4\ ln2$ while $C_1 = 4$.

- *Full Width at Half Maximum (FWHM):*

The full width at half maximum (FWHM) is typically modelled using the following equation:

$$FWHM^2 = U\ tan^2\ \vartheta_i + V \tan \vartheta_i + W$$

Where U, V and W are the refined Caglioti parameters.

- *Preferred Orientation:*

The intensity of the diffraction peaks can be altered by the orientation of the crystallites, which adopt a random orientation or a preferred orientation (tendency of the crystallites to orientate towards a given crystallographic direction). The effects of a preferred orientations are included in the diffraction profile by means of the function $P(\varphi)$, where φ is the acute angle between the scattering vector and the normal of the crystallites.

$$P(\varphi) = e^{-G_1\varphi^2};\ (\varphi) = G_2 + (1 - G_2)e^{-G_1\varphi^2}$$

Where G_1 and G_2 are the refined parameters. G_1 gives information about the degree of preferred orientation for a given direction, while G_2 indicates the proportion of the phases presenting no orientation.

- *Quality of the fit:*

The quality of the refinement depends on finding the best fit between a calculated and experimental pattern; therefore, it is important to have a numerical figure to quantify the quality of the fits and provide insights to how well the model fits the observed data. Different indicators (also called residuals) must be minimised during the refinement and these are:

$$\mathrm{R} = \sum w_i\,[\,y_i(o) - \,y_i(c)]^2$$

Where $y_i(o)$ corresponds to the observed intensity, w_i is the weighted factor assigned in the least square methods, defined as $\sigma_i = \sqrt{N}$, being N the total number of counts registered by the detector.

The Profile Residual (reliability factor, R_p) the Weighted Profile Residual (R_{wp}) quantify the degree of reliability of the fit from a peak's shape point of view:

$$R_p = \frac{\sum|y_i(o) - \,y_i(c)|}{\sum|y_i(o)|}$$

$$R_{wp} = \sqrt{\frac{\sum|y_i(o) - \,y_i(c)|^2}{\sum|w_i\,y_i(o)|^2}}$$

On the other side, the Bragg Residual (R_B) and the Structure Residual (R_F) factor provide information about the reliability of the results from point of views of the unit cell crystallographic data and they are expressed as follow:

$$R_B = \frac{\sum|I_i(o) - I(c)|}{\sum|I_i(o)|}$$

$$R_F = \frac{\sum|F_i(o) - F_i(c)|}{\sum|F_i(o)|}$$

While the Expected Profile Residual (R_{exp}) and the Goodness of fit (χ^2) provide information about the quality of the experimental data and the discrepancy between the theoretical prediction and the experimental data.

$$R_{exp} = \sqrt{\frac{(N - P_1 - P_2)}{\sum w_i \, y_i{}^2 \, (o)}}$$

$$\chi^2 = \sqrt{\frac{\sum|y_i(o) - y_i(c)|^2}{(N - P_1 - P_2)}} = \frac{R_{wp}}{R_{exp}}$$

Where, *N* is the number of observations, P_1corresponds to the number of structural parameters and P_2 the number of profile parameters. Ideally, the value of χ^2 must be slightly higher than one (1) for an optimal refinement.

In this work, X-ray diffraction data was modelled using the GSAS software package, with EXPEGUI graphical interface (Larson and Von Dreele, 2000: Toby 2001) with the aim of identifying the oxynitride phase.

2.2.2.1 Le Bail Refinement

For thin-films, full Rietveld refinement could not be attempted due to the limited number of peaks present in each pattern and the effect of grazing incident geometry on the relative peak intensity. The Le Bail method is used for the decomposition of the diffraction pattern into integrated intensities and subsequent refinement of profile parameters. This technique works especially well with overlapping reflections since the intensity is allocated according to the relative multiplicities that contribute to a particular peak and was used to model the diffraction patterns and extract the lattice parameters and particle size information.

2.2.3 UV-Visible Spectroscopy and Band Gaps

2.2.3.1 Powder Oxynitrides

Measurement of the diffuse reflectance is a widely used and essential sampling tool for the determination of semiconductors materials properties. When the incident radiation is absorbed by

the surface of the sample material, it can be scattered, transmitted and reflected. Considering that the material contains layers in where the crystallites are randomly oriented, the light beam interacts with the particles of the material and it can be scattered to deeper layers via random reflections and dispersions. Diffuse reflectance occurs when the incident radiation is scattered and returned back to the surface to be re-emitted in any possible angle.

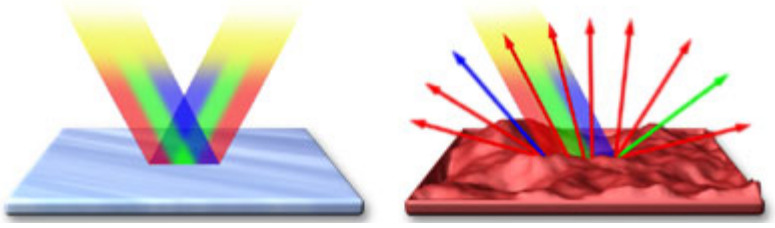

(a) Specular Reflection **(b)** Diffuse Reflection

Figure 28. Illustration of a light beam being reflected on a **(a)** smooth mirror and **(b)** a rough surface. Reproduced from ref.[207]

The UV-Visible spectrometer integrates a white sphere coated with non-absorbent and highly reflective substance, normally barium sulphate, which concentrates the light reflected by the sample on the detector optics.

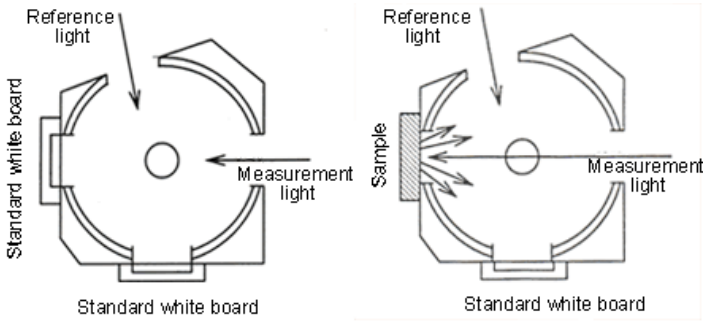

Figure 29. Schematic representation showing the parts of a UV-Visible integrating white sphere. Reproduced from ref.[207]

Firstly, a calibration is performed to adjust a 100% of reflectance by using a reference standard white board with an absorption coefficient equals to zero and it must be a stable material with a high absolute reflectance, such as barium sulphate, Teflon or high purity alumina**.** For the data collection of samples showing small diffuse reflectance, the powder sample is normally ground and mixed with a non-absorbing substance (potassium bromide/iodide), in a ratio sample to matrix between 1 to 5 % wt. Measurement takes place by placing the sample in front of the incident light window. Then, the incident radiation is scattered within the sample and returned to the surface to be collected by the detector. This radiation, known as diffuse reflection, contains the spectral information of the material. It should be noted that the specular reflectance component might

cause changes in the bands as well as in their relative intensity on the diffuse reflectance spectra. These effects are minimised by the sample preparation practices and adjusting the detector position.

2.2.3.2 Band Gap Energy Calculations

The band gap energy of the sample material is calculated by using optical absorbance data plotted with respect to the energy. For this, the raw diffuse reflectance spectrum is converted to the absorbance spectrum by using the Kubelka-Munk equation (Equation 6).

$$F(R) = \frac{(1-R)^2}{2R} \cong \alpha \qquad \text{Equation 6}$$

Tauc (1966), proposed in his studies about the optical properties and electronic structure of amorphous germanium the relation $(\omega^2{}_e{}^2 = h\omega - E_g)^2$ for the determination of the absorption near the edge, which is interpreted as due to indirect transitions (n = 2).[208] Subsequently, Davis and Mott (1970) described a new theoretical model (Equation 7) based on the original Tauc relation, where A is a material specific constant.[209] In order to translate the diffuse reflectance spectra into the absorption spectra, the absorption coefficient (α) is replaced on the David and Mott equation by the Kubelka-Munk function, which is proportional to the absorption coefficient (α). This approach is widely used for the determination of band gaps and the state transition in semiconductors (Equation 7).

$$(\alpha h\nu)^{1/n} = A\,(h\nu - E_g) \qquad \text{Equation 7}$$

$$(F(R)h\nu)^{1/n} = A\,(h\nu - E_g) \qquad \text{Equation 8}$$

According to the Equation 8, h corresponds to the Planck's constant, v is the frequency of vibration, *A* is a proportional constant and E_g is the optical band gap energy. The value of the exponent *n* denotes the nature of the sample transition, then:

- n = 1/2 for direct allowed transitions.
- n= 2 for indirect allowed transitions.
- n= 3/2 for direct forbidden transitions.
- n = 3 for indirect forbidden transitions.

Tauc plots are built by plotting the quantity $(F(R)h\nu)^{1/n}$ on the ordinate *versus* the photon energy (h*v*) on the abscissa. Diffuse reflectance data were collected from the thin films and powders in the wavelength range of 300-900 nm using a Perkin Elmer Lambda 750S spectrometer.

2.2.4 Scanning Electron Microscopy (SEM)

Scanning Electron Microscopy (SEM) is a widely utilised technique that makes use of an electronic microscope for the surface observation and characterization of inorganic and organic materials, providing morphological information of the analysed samples. As opposed to the optical microscopy, which makes uses of photons from the visible spectrum, the electronic microscope generates the image because of the interaction of a projected beam of electrons with a given area from the sample's surface. Therefore, and due to the nature of the electrons (they have shorter wavelengths than visible photons, and the wavelength can be tuned), scanning electron microscopes allow access to spatial resolutions in the range of nanometres.

In the first step, a Field Emission Gun (FEG) generates a beam of primary electrons, which is focused by means of a system of electromagnetic lens, reducing the diameter of the electrons beam. Then, the scanning system guides the focused beam across the sample's surface. The generated primary electrons excite the secondary electrons from the surface, which are ejected and collected by a detector. The microscope can be equipped with a series of detectors that collect the different types of signals generated by the interaction of the primary electrons with the sample and convert them to an electric signal that is subsequently processed by a computer. In Scanning Electron Microscopy (SEM), the detector collects the ejected secondary electrons (SE), thus, the signal of the scattered secondary electrons provides an image of the superficial morphology of the studied sample.

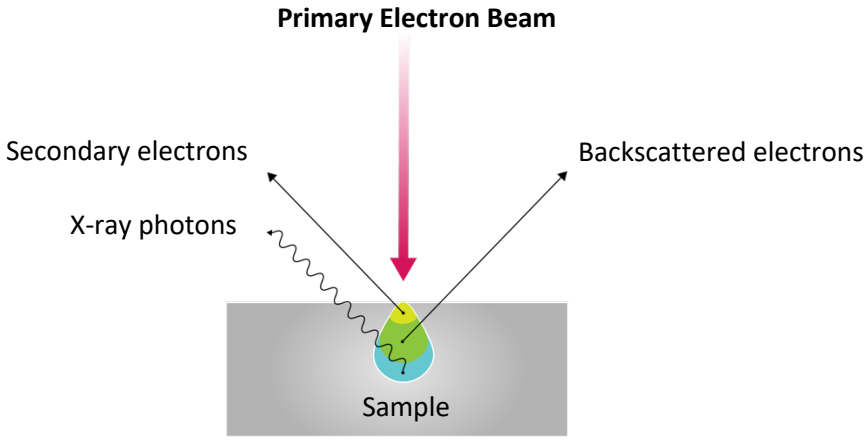

Figure 30. Different signals emitted during the electron bombardment.

Moreover, an X-ray detector can be used to provide information about the chemical composition of the sample constituents. This technique is known as Energy Dispersive Spectroscopy (EDS). SEM images and EDS data were collected by Dr. Alexander Kulak (University of Leeds) using a FEI Nova NanoSEM 450 FEG-SEM operating at 5 kV without coating using a CBS detector and a

working distance of 5 mm. EDX mapping was carried out on the same instrument operating at 18 kV.

2.2.4.1 Energy Dispersive Spectroscopy (EDS)

Electron beams are a type of ionizing radiation. When a beam of primary electrons hits the sample, part of their energy is transferred to the atoms of the sample. Therefore, the primary electrons can excite sample electrons off from the inner shells, leaving a hole behind. Consequently, the atoms remain in an ionised state. In order to recover its original fundamental state, an electron from a higher-energy shell fills the hole (which has a positive charge) emitting characteristic X-rays with an energy equal to the energy difference between the two shells. (Figure 31)

Energy Dispersive Spectroscopy (EDS) fully exploits the fact that each atom has a unique number of electrons that belong to different shells with different energies. Thus, the energy difference between two shells is dependent and characteristic on the atomic number of the element and can be used as a fingerprint of each element, being able to identify the type of elements present in the sample.

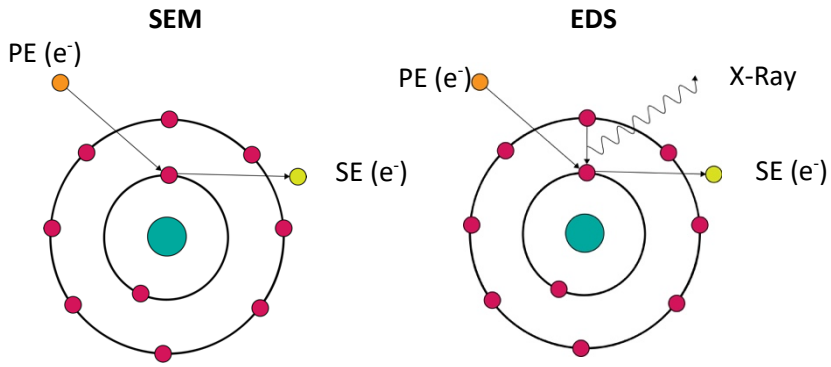

Figure 31. Different electron interactions with sample's atoms.

An Energy Dispersive X-ray detector collects the produced characteristic X-rays, which can be used for either qualitative (mapping showing the elemental distribution) or quantitative (atomic concentration of each element of the sample) analysis. The generated data consists of a spectrum containing the peaks corresponding to all the elements present in the sample. An additional software enables the auto-identification of the characteristic peaks and the calculation of the atomic percentages of each detected element.

2.2.5 X-Ray Photoelectron Spectroscopy (XPS)

X-Ray Photoelectron Spectroscopy (XPS) is a chemical analysis technique widely used for the surface characterization of materials of interest, including inorganic materials, thin films, polymers,

inks, semiconductor and alloys, among others. The collected data provide information about the elemental composition, both qualitative and quantitative, the oxidation states of the elements that make up the samples as well as the empirical formula. In addition, XPS is a non-destructive analysis technique that does not need any specific preparation of the sample (such as coating with a conductive material), being any kind of sample (e.g. inorganic, organic, magnetic, conductive, insulating...) suitable for analysis as long as they are compatible with Ultra High Vacuum.

In a first stage, the substrate is bombarded with a beam of X-rays with well-defined energy. The generated photons (X-rays, with an energy *hv)* interact with the core electrons of the atoms located more superficially in the sample, leading to (due to photoelectric effect) the emission of photoelectrons with a characteristic kinetic energy represented by the following equation:

$$E_k = hv - E_b$$

where E_k is the kinetic energy of the ejected photoelectron collected by the detector, *hv* is the X-ray photon energy and E_b is the electron binding energy.

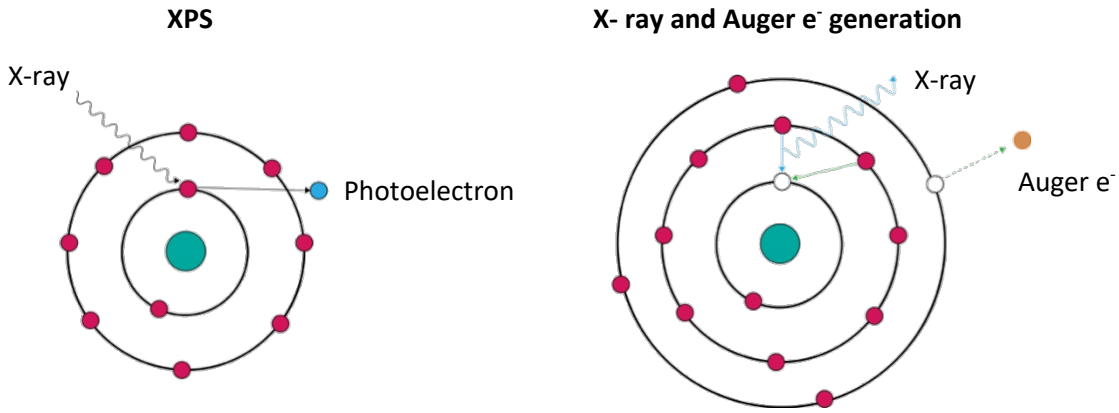

Figure 32. On the left, ejection of a photoelectron in XPS. Right, relaxation process with generation of an X-Ray (blue arrows) and/or emission of an Auger electron (green arrows).

Since the value of *hv* in known, measuring the kinetic energy of the emitted photoelectrons allows to calculate the binding energy, which is characteristic of the element from which the electron is emitted as well as the orbitals wherein the electron is located. Thus, separation of the kinetics energy by the analyser and subsequent plotting of the intensities *versus* the calculated binding energies enables the identification of the type of atom, oxidation state and quantification of the abundance of the elements present near the surface region. Finally, once the photoelectron is ejected from the core, the atom compensates the charge by emitting an Auger electron or a photon in the form of X-ray.

X-ray photoelectron spectroscopy (XPS) was carried out on a Thermo Fisher Scientific K-Alpha instrument, using Al Ka radiation (1486.6 eV), and operated in a constant analyser energy mode. Samples were introduced into the vacuum chamber held at a base pressure of 5×10^{-9} mbar, and the incident X-ray beam focused to a 400-micron spot at the sample surface, which defined the analysis area. Survey spectra and high-resolution spectra were taken with pass energies of 200 and 50 eV, respectively. Charge neutralization was carried out using dual-beam Ar^+ and electron flood gun. Charge correction of spectra was carried out using the adventitious C1s, which was set to a binding energy of 238.6 eV.

2.2.6 Thermogravimetric Analysis (TGA)

The thermogravimetric analysis (TGA) is a method of thermal analysis that measures the weight variation of a sample over the time as temperature changes. TGA provides information about phase transition, absorption, adsorption and desorption; as well as thermic decomposition and solid gas reactions.

Thermogravimetric analysis (TGA) were performed in a Netzsch thermobalance (STA 409) to study the thermal stability and the temperature of decomposition of the synthesised perovskite oxynitrides. The measurements were performed in the temperature range from 25 to 1150˚C with a heating rate of 5˚C min^{-1}, under synthetic air atmosphere, using a gas flow rate of 10 mL min^{-1} and 20-30 mg of oxynitride in an alumina crucible.

2.3 Photocatalytic Testing

2.3.1 Photocatalytic Degradation of DCIP

A technique capable of assessing the photocatalytic activity of self-cleaning thin films involves the photo-induced reduction of a redox dye in presence of a sacrificial electron donor (SED). The redox dye 2,6-dichlorophenolindophenol (DCIP) is an electron acceptor with a redox potential of E^0 (DCIP/dihydro-DCIP) + 0.228 eV at pH= 7 versus SHE, showing a blue colour when oxidised and a colourless form (that is not air-sensitive) when reduced. In agreement with the previous published literature, a solution which makes use of DCIP and glycerol as sacrificial electron donor (SED) was choosen.[210,211]

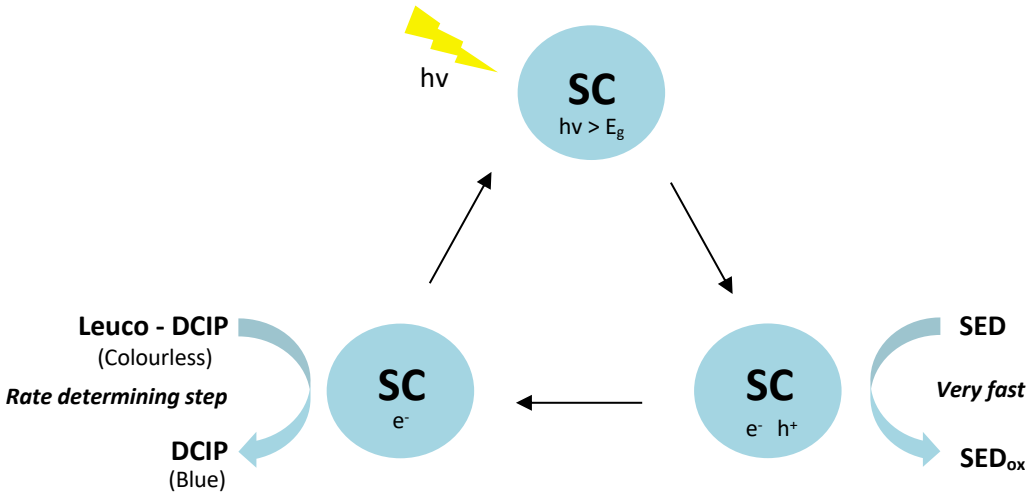

Figure 33. Reaction scheme for the photo-inducted reduction of the ink solution over a semiconductor (SC), where SED/SED_{ox} represents the reduced/oxidised form of the glycerol and the DCIP oxidised blue-colour form and leuco-DCIP reduced colourless form.

The IUPAC defines a sacrificial electro donor (SED) as a molecular entity that acts as the electron donor in a photo-induced electron transfer process and is not restored in a subsequent reduction process but is destroyed by irreversible chemical conversion. In this case, glycerol is used as sacrificial electro donor (SED), which acts as a hole-trap, preventing the electron-hole pairs from recombination and, consequently, being irreversibly oxidised. The photo-oxidation pathway involves the reaction of the formed hydroxyl radicals with the glycerol adsorbed on the photocatalyst surface, yielding the formation of the intermediates; glyceraldehyde, glycoladehyde, glycolic acid and formaldehyde. Finally, though decarboxylation, the intermediates are mineralised to CO_2 and water.

In parallel, photo-generated electrons and H^+ left by the glycerol oxidation reduce the C=O and N- groups of DCIP to C-OH and N-H groups, changing the colour of the solution from blue to colourless.

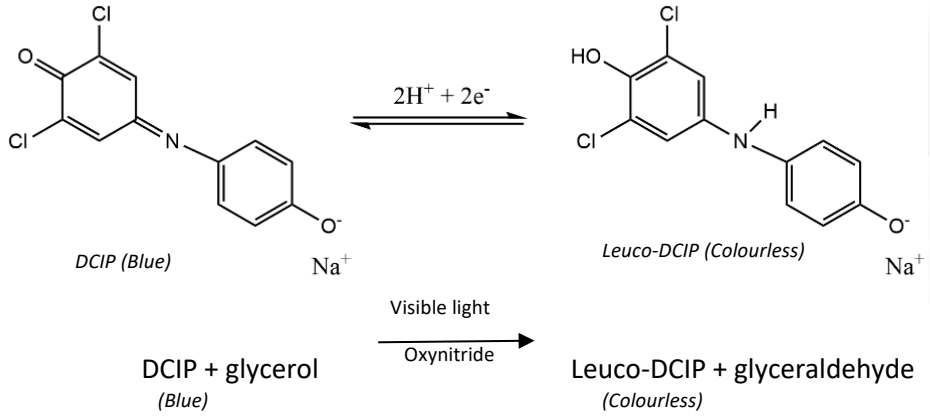

Figure 34. Photo-reduction of 2,6-dichlorophenolindophenol (DCIP) to its reduced colourless form dihydro-DCIP under visible light.

2.3.2 Photodegradation of Stearic Acid

A method that has gained preference over the years for the assessment of the self-cleaning activity of thin films is the stearic acid test, in which a layer of a stearic acid solution is deposited onto the substrate and its degradation is monitored as a function of time. Stearic acid, also known as octadecanoic acid, is a compound of practical interest since it is the type of organic molecule that pollute glasses in kitchens (analogue to grease) and shows exceptional stability under UV/Vis radiation (photolysis) under absence of an effective photocatalyst. For this test, stearic acid can be easily diluted in methanol or chloroform and subsequently deposited onto the photocatalytically-active thin films by means of dip-coating and its degradation monitored by FTIR. Chemically, stearic acid ($C_{17}H_{35}CO_2H$) is a saturated fatty acid containing a long hydrocarbon chain formed by 17 carbon atoms and a carboxyl group at the end, as shown in Figure 35.

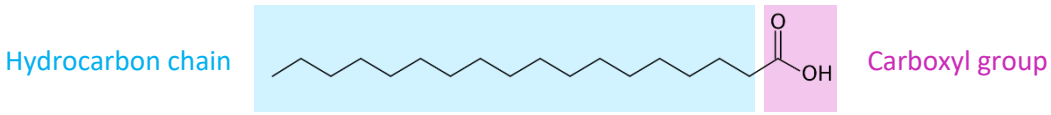

Figure 35. Stearic acid skeletal formula showing the different functional groups.

Previous reports have shown the ability of titanium dioxide to oxidise a wide range of organic contaminants as well as to destroy microbial cells such as *Escherichia coli.* The antibacterial properties rely on the fast decomposition of saturated and unsaturated fatty acids by the titania thin films, which introduces morphological changes in the bacterial cell membrane. This membrane is constituted, among others, of fatty acids, resulting, ultimately in cell death.[214]

The degradation of the stearic acid under the presence of a suitable photocatalyst proceeds via photo-oxidation of the stearic acid molecules in presence of atmospheric oxygen to give CO_2 and water. The equation below shows the overall degradation reaction:

$$CH_3(CH_2)_{16}CO_2H + 26\ O_2 \longrightarrow 18\ CO_2 + 18\ H_2O$$

Fourier-transform Infrared Spectroscopy (FTIR) is an analytical technique used for the identification and study of functional groups in organic molecules. FTIR relies on the fact that the absorption of IR radiation causes a change on the vibrational mode of a molecule and different types of bonds present vibrate at different frequencies resulting in a characteristic and unique spectrum.

This IR spectrum represents the percentage of transmitted light (%T), instead of absorbed light, *versus* frequency (cm^{-1}). Thus, the absorption of IR radiation by a compound on a given wavelength results in a decrease of the radiation transmission (%T), appearing as an absorption band or peak in the spectrum.

Among the major sampling techniques in FTIR, transmission IR was selected due to the nature of the stearic acid test and our samples (coloured transparent thin films deposited over quartz substrates).

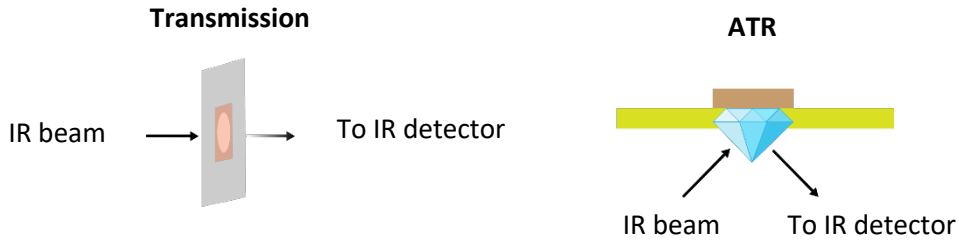

Figure 36. Transmission *versus* Attenuated Total Reflection (ATR).

The photo-degradation of the stearic acid molecules can be monitored *via* transmission FTIR spectroscopy, wherein the peaks corresponding to the asymmetric C-H stretching mode of the CH_3 group, and asymmetric C-H stretch and symmetric C-H stretch of the CH_2 group, appearing at 2958 cm^{-1}, 2923 cm^{-1} and 2853 cm^{-1} respectively.

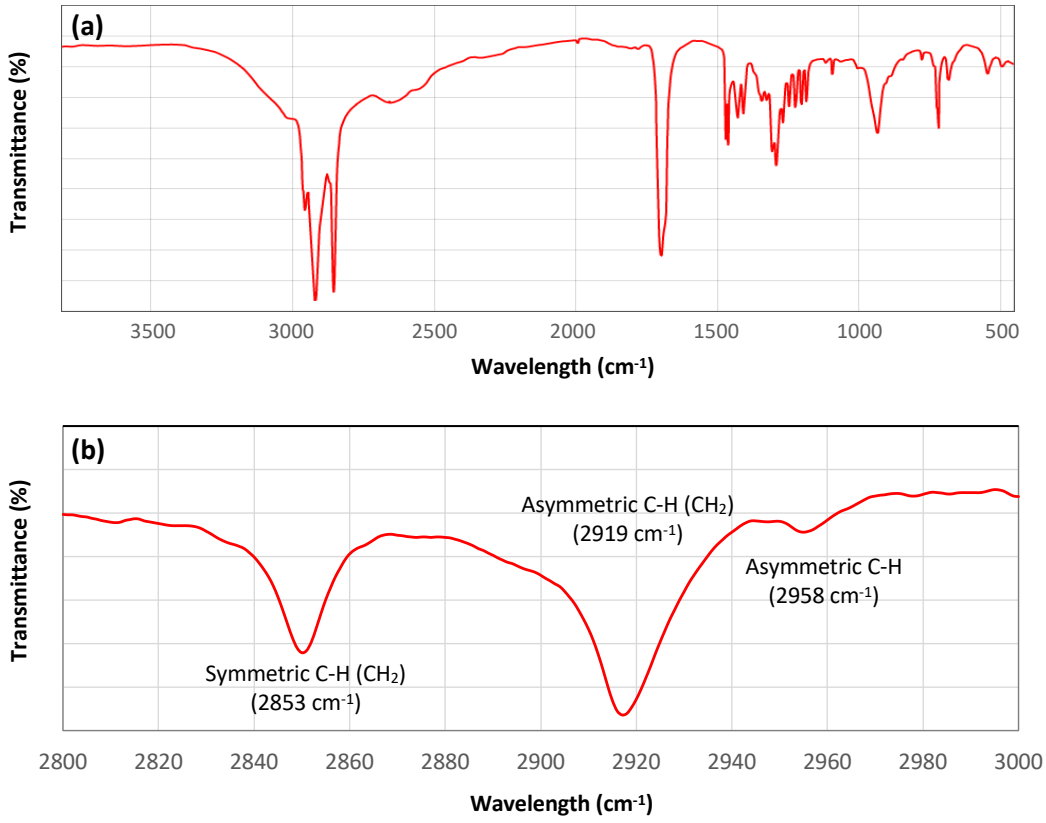

Figure 37. (a) Full FT-IT spectra of stearic acid powder and **(b)** FTIR spectra of a stearic acid thin films deposited over a quartz substrate.

Transmission IR spectra were collected using a Perkin Elmer Spectrum 100 FTIR at a 30 minutes interval up to 180 minutes over the range 3000-2800 cm^{-1}.

Chapter 3 Synthesis and Characterization of Powder Perovskite Oxynitrides

3.1 Introduction

Powder perovskite oxynitrides have been reported to be synthesized using a variety of synthetic routes. The most common and widely used approach is the synthesis of the oxide precursors, whether crystalline or amorphous *via* solid state reactions or soft chemistry routes and subsequent ammonolysis, which makes use of ammonia as reducing agent and source of nitrogen.[26,201] However, novel techniques involving direct incorporation of nitrogen into the perovskite structure using urea or Ta_3N_5/TaON have been explored and reported and will be discussed below.[198]

3.1.1 Solid-state Reactions to Oxynitrides

In ***solid-state routes to oxynitrides***, a complex oxide precursor is prepared from a mixture of solid starting materials which can be binary oxides or their respective carbonates, nitrates or acetonates. The reagents are mixed in a mortar and heated under ammonia at high temperatures for long periods of time.

Chen et al. studied the partial nitrogen loss in $SrTaO_2N$ and $LaTiO_2N$ oxynitride perovskites synthesis by solid-state methods. For this, $Sr_2Ta_2O_7$ and $La_2Ti_2O_7$ were prepared by firing their respective mixtures of $Sr(CO_3)_2$ and Ta_2O_5 and La_2O_3 and TiO_2. Due to the nature of solid-state reactions, annealing temperatures in the range of 1200-1300˚C and several rounds of 10-hours reaction periods with intermittent grinding were needed to obtain the pure oxides. Then, the crystalline oxides precursors were ammonolysed at 980-1000˚C for 90-120 h with intermittent grinding every 10 h, requiring higher temperatures and longer reaction times when compared to the $SrTaO_2N$ and $LaTiO_2N$ obtained *via* soft-chemistry methods. This was attributed to the larger particle size obtained in solid-state reactions.[215]

Flux additives have been used to reduce the reaction temperatures and time in solid-state synthesis of perovskite oxynitrides. The addition of chloride salts such as NaCl, NH_4Cl, $CaCl_2$ and KCl enhance thermal ionic diffusion, providing a molten medium where ionic diffusion occurs faster and therefore, lowering the activation barriers and reducing sintering (smaller particle sizes).[201,216] Rachel et al. studied the effects of flux additives on the synthesis of $CaTaO_2N$, $SrNbO_2N$ and $BaNbO_2N$. For this, they prepared the corresponding ternary oxides $Ca_2Ta_2O_7$, $Sr_2Nb_2O_7$ and BaO-

Nb_2O_5 *via* solid-state reaction. The oxides were ground and mixed with KCl and ammonolysed under flowing ammonia. $CaTaO_2N$, $SrNbO_2N$ and $BaNbO_2N$ were obtained at 950˚C for 18, 36 and 72 h respectively, while the halide-free approach required 36, 54 and 90 h. Thus, flux-assisted ammonolysis required lower temperatures and reactions times.[201]

3.1.2 Alternative Nitrogen Sources

Traditionally, perovskite oxynitrides have been synthesised treating the oxide precursor with ammonia as a nitriding agent under high temperatures. However novel approaches have explored alternative nitrogen sources using urea as nitrogen source instead of gaseous ammonia, reducing the risks associated with the manipulation of toxic gases (e.g. leaks).

Gomathi et al. described a simple urea-base route to ternary metal $CaTaO_2N$, $SrTaO_2N$ and $BaTaO_2N$ oxynitride nanoparticles.[198] The urea route allows to start with a solid mixture of oxides and corresponding carbonates ground with an excess of urea. The solid mixtures were placed in an alumina boat and heated at 950˚C for a short period of time (2 hours) under a N_2 atmosphere. At 250˚C, urea decomposes according to $CO(NH_2)_2 \rightarrow NH_3 + HCNO$, yielding NH_3 which can react with the oxides/carbonates resulting in the formation of the ternary perovskite oxynitrides. The formation of the oxynitrides is suggested to follow the following equation:

$$2\boldsymbol{A}CO_3 + \boldsymbol{B}_2O_5 + 2NH_3 \rightarrow 2\boldsymbol{AB}O_2N + 3H_2O + 2CO_2 \ (\boldsymbol{A}\text{= Sr, Ca, Ba; } \boldsymbol{B}\text{= Ta, Nb})$$

3.1.3 Direct Route to Oxynitrides

Clarke et al. published a high-temperature synthesis of perovskite tantalum oxynitrides. $SrTaO_2N$ and $BaTaO_2N$ were prepared by reaction between the correspondent alkaline earth oxide and TaON at 1500˚C under 1 atm of pure nitrogen gas for a few hours. The reaction is carried out under a nitrogen atmosphere and an inductive-heated metal crucible containing the sample, which enables an atmosphere of pure nitrogen to be maintained above the sample at high temperatures.

In a typical reaction, TaON was prepared by reacting Ta_2O_5 with flowing ammonia at 850˚C. The ammonia was flowed through a vessel containing NH_4OH since, as previously reported, wet ammonia prevents the formation Ta_3N_5.[217] In a second step, the alkaline earth oxides were prepared by thermal decomposition of the carbonate precursors placed in an alumina tube under vacuum. Finally, the precursors were pressed into a pellet in a glove box and loaded into a molybdenum crucible placed inside of a silica tube. The tube was filled with 1 atm of pure nitrogen and heated to 1500˚C. The ternary oxynitrides $SrTaO_2N$ and $BaTaO_2N$ were obtained and their phase purity confirmed by XRD analysis.[218]

Sun et al. reported the direct synthesis of $SrTaO_2N$ from $SrCO_3/Ta_3N_5$. Here, in a first stage, Ta_3N_5 was prepared by the nitridation of Ta_2O_5 at 950˚C for 12 h in flowing ammonia of 50 mL min^{-1}. The obtained nitride was mixed with $SrCO_3$ in acetone with a molar ratio of 1:3 and dried overnight. The powder mixture was fired at a rate of 5˚C min^{-1} under flowing nitrogen (100 mL min^{-1}) and different reaction times were studied. The route proposes thermal decomposition of $SrCO_3$ to SrO and CO_2. Then, the conversion of Ta_3N_5 in presence of CO_2 to TaON, which subsequently reacted with SrO, yielding the oxynitride. The obtained $SrTaO_2N$ showed homogeneous particle size distributions as well as a stoichiometric composition.[219] Subsequent work also carried out by Sun et al. demonstrated the feasibility of this route to also synthesise $BaTaO_2N$ and $CaTaO_2N$.[220]

3.1.4 Soft Chemistry Routes

Soft chemistry methods are those that include solution process steps and include sol-gel routes (e.g. Pechini synthesis), deposition (co-precipitation) from solutions and hydrothermal/ solvothermal synthesis. In case of oxynitride synthesis, these techniques offer the advantage of obtaining the oxide precursor at a lower processing temperature with a high degree of homogeneity and dispersion, enhancing the efficiency of ammonolysis.

3.1.4.1 Hydrothermal/solvothermal Synthesis

The **hydrothermal method** has its origins in Nature and describes the natural occurring processes of action of water at elevated temperatures and pressure, leading to the formation of minerals. This technique was adopted in materials science as a synthesis technique and has been well developed in the last decade due to its versatility. Conceptually, a hydrothermal synthesis is a chemical reaction taking place in water at controlled temperatures below the water boiling point and pressures about 1 bar, while the medium used in a **solvothermal synthesis** is usually an alcohol or any other organic or inorganic solvent.

In a typical hydrothermal/solvothermal synthesis, the precursors (often solutions of simple inorganic compounds such chlorides, nitrates, ands acetates), pH stabilizer and H_2O/solvent are mixed in a sealed vessel (i.e. autoclave) and then heated. The temperature, pressure and time control allows for tuning the crystallization and growth of the particles. Once the reaction is finished the autoclave is cooled down and the material filtrated, washed and dried. In perovskite oxynitride synthesis, the desired oxide is washed and dried in air for subsequent use in ammonolysis.

Oehler et al. reported a comparison of the solid-stated and solvothermal synthesis of $Ca_2Ta_2O_7$ powders.[221] The solvothermal $Ca_2Ta_2O_7$ precursor was synthesised dissolving $TaCl_5$ and calcium nitrate in dry ethanol and then loaded in a Teflon vessel containing a solution of KOH acting

as hydrolysing agent (2-3 g in 80 mL of water). The mixture was heated in an autoclave at 110 °C for 18 hours under stirring. After cooling down, the resulting powder was washed with water, ethanol and acetone and dried. Then, the $Ca_2Ta_2O_7$ was heated in flowing ammonia to obtain the final oxynitride. Highly crystalline $CaTaO_2N$ nanoparticles were obtained and compared to those prepared *via* solid-state. Ammonolysis of the hydrothermal precursor resulted in single crystalline $CaTaO_2N$ nanoparticles while the $CaTaO_2N$ obtained by solid-stated consisted of highly agglomerated microparticles. Hydrothermal $CaTaO_2N$ showed interesting physical properties such as good crystallinity, high specific surface area and low strain. Additionally, the samples showed enhanced photocatalytic activity for methyl orange degradation. Later, Ebbinghaus et al. published a comparison on the photocatalytic properties of nano-crystalline oxynitrides ABO_2N (A= Ca, Sr, Ba, La: B = Nb, Ta) synthesised by the solvothermal method.[176] Their photocatalytic properties will be discussed in the introduction section of Chapter 5.

3.1.4.2 Co-precipitation Method

The **co-precipitation** method, also knowns as polyol-assisted co-precipitation consist of using a weakly binding ligand such as an alcohol (e.g. methanol) at high temperatures to dissolve metal salts and co-ordinate the cations. Then, a hydrolysis agent (e.g. NH_4OH, KOH) is added to initiate a controlled co-precipitation, leading to the crystalline/amorphous oxide. This method has been widely used for the synthesis of metal nanoparticles, but is less established for the synthesis of complex oxides such as the ones used for the perovskite oxynitride synthesis.[222] The described method has the advantage of allowing size control since the methanol acts a surface-capping agent preventing particle agglomerations during the precipitation and resulting in the formation of very small particles. However, there are limitations including a difficult control of the stoichiometry of the precipitated oxide, especially regarding complex oxides, due to the hydrolysis behaviours of the different cations presented in the solution. However, it is possible to find reported in the literature the synthesis of perovskite oxynitrides *via* co-precipitation synthesis and subsequent ammonolysis.

Ebbinghaus et al. reported the synthesis of $LaTi(O,N)_3$ nanoparticles of 10-28 nm diameter from $LaTiO_{3.5}$ obtained via the co-precipitation method and ammonolysis at temperatures between 800°C and 1000°C.[223] For this, they used lanthanum nitrate and titanium tetraisopropoxide (TTIP) as metal precursors, dissolved in diethylene glycol in a closed reaction flask attached to a reflux condenser. In order to avoid an early titanium oxide precipitation (TTIP hydrolyses due to the moisture present in the air), the reaction was carried out in a dry nitrogen atmosphere. To promote the hydrolysis of the cation-DEG complexes, a solution of KOH was used. The precipitated La-Ti amorphous oxide was separated from the solution by centrifugation, washed with acetone several times and dried. Then, it was calcined to burn the organic matrix and form $LaTiO_{3.5}$. Finally, the

crystalline white powder was treated under a NH_3 flow at high temperatures leading to highly crystalline $LaTi(O,N)_3$ nanoparticles which were used for the photocatalytic decomposition of acetone under visible light irritation. This part will be discussed in Chapter 5.

Balaz et al. studied the electronic structure of tantalum oxynitride perovskite photocatalysts and reported the synthesis of $CaTaO_2N$, $SrTaO_2N$ and $PrTaON_2$ by the coprecipitation method.[122] In this case, an equimolar amount of $TaCl_5$ together with the correspondent metal salt, (chlorides) were dissolved in methanol. The metal cations in solution were co-precipitated by adding dropwise a solution of NH_4OH. The use of ammonium hydroxide allows for the co-precipitation of the oxide without adding an extra cation (e.g. K^+ from KOH) which could remain as a dopant in the final oxynitride. The white precipitates were washed, dried, heated in flowing ammonia at 800-850 °C for 18-34 hours to obtain the final perovskite oxynitrides which were used for measurements of their electronic structure.

3.1.4.3 Sol-gel Method

The sol-gel route using citric acid, also known as citrate route or Pechini method has been widely explored and been favoured for the synthesis of the oxide precursors due to its relative simplicity. The **Pechini method** is the most attractive method for the synthesis of nanocrystalline oxides containing multiple cation sites.[196,224] Compared to the methods discussed above, the advantages lie in the steric entrapment of the cations, prevention of segregation and reduction of the problem of diffusion sometimes observed in solid-state synthesis. Generally, a hydroxy-carboxylic acid such as citric acid is used due to its high potential to complex the dissolved metal salts. Then, diols such as ethylene glycol and propylene glycol are used as network builders, leading to the formation of a stable polymerised organic framework. The formation of a polymer resin *via* esterification of the diol allows for a homogeneous distribution of the cations in solution and segregation of multiple phases is inhibited due to the chelation of the cations by the citric acid and subsequent networking due to the polymerization.

Rachel et al. reported the synthesis and analysis of the thermal behaviour of tantalum and niobium perovskite oxynitrides.[201] In the reported work, Ta^{5+} and Nb^{5+} -based oxynitride perovskites of the ABO_2N type (A = Ba, Ca, Sr) were synthesised by ammonolysis of their complex oxide precursors. These precursors were obtained *via* solid-state reaction and by the citric acid route and were, either crystalline perovskites or amorphous xerogels. In a typical Pechini synthesis, the oxide precursors were prepared by dissolving in dry ethanol the corresponding metal salts with $TaCl_5$ and citric acid. Then, propylene glycol was added, and the solution heated at 60°C to promote esterification. Afterwards, the excess solvent was removed on a rotary evaporator. Consequently, the solution became progressively viscous. The resin was oven dried and the organic matrix was

removed by calcining the dried resin at high temperatures, resulting in the white xerogel precursors. For the comparison analysis, crystalline $A_2B_2O_7$-type oxides were obtained by calcining the xerogel precursors at 1000°C for 24 hours. During the thermal ammonolysis, crystalline oxides (prepared by solid state and sol-gel) and xerogels were treated with flowing ammonia to obtain the intended oxynitrides in the temperature range between 600°C and 1000°C for 18 hours. Thereafter, the samples were cooled down to room temperature under a nitrogen atmosphere. Results showed that perovskite oxynitrides prepared from the xerogel precursors obtained by the soft-chemistry method were formed at a rather low temperature and reaction times. Thus, if crystalline oxides are used as starting materials higher temperatures and reaction times were needed until complete formation of the oxynitrides. In order to reduce both, temperature and reaction time, halides were added as mineralisers. However, reaction conditions and excluding the possibility of contamination of the oxynitrides by the alkali fluxes, makes the use of amorphous oxide precursors the most favourable preparation route.

Another example is the formation of $LaTiO_2N$ from an amorphous precursor obtained by the Pechini method. [225] X-ray diffraction data showed that the pure phase oxynitride was obtained only after a 24 hours ammonolysis at 950°C. Morphologically, $LaTiO_2N$ obtained from the xerogel showed typical particles sizes of roughly 20 nm and this is consistent with similar results obtained for different compounds. The specific surface area was also studied by the BET method with nitrogen as adsorbed gas and resulted to be 40 m^2 g^{-1}, which is a value typical for many samples prepared by the Pechini method. The BET isotherm (Figure 38, left) shows a hysteresis between the adsorption and desorption lines.

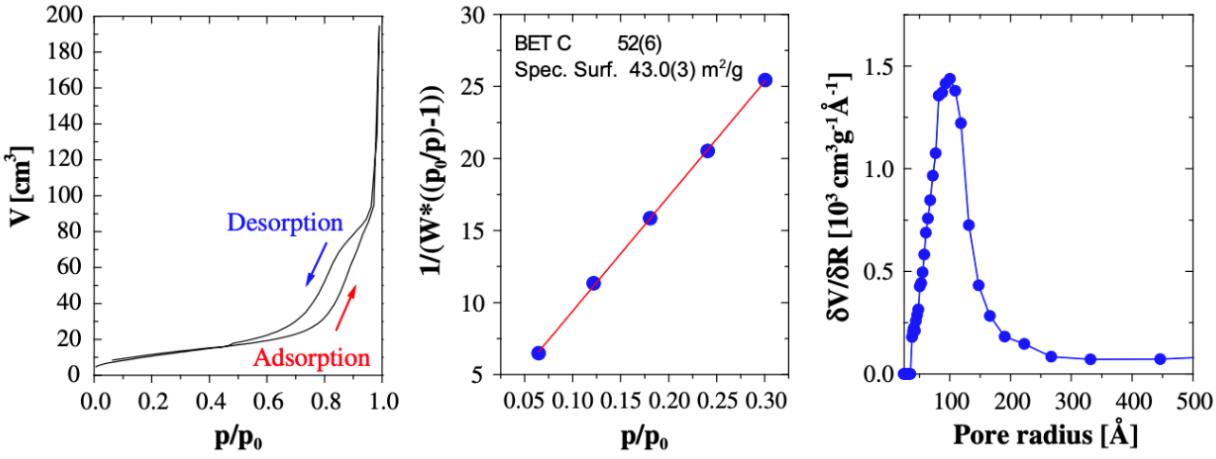

Figure 38. BET isotherm of the $LaTiO_2N$ sample (left), calculated specific surface area (middle) and pore size distribution (right). Adapted from [225].

Regarding porous sample, pore size distribution indicates a pore radius of 100 Å, therefore, the sample can be defined as mesoporous. The large surface area and high porosity favours the gas

exchange during ammonolysis and in turn enhances their reactivity, resulting in shorter reaction times and lower temperatures. Thus, the Pechini method proves that oxynitrides with small particles surfaces and considerable surface areas can be obtained by thermal ammonolysis of the amorphous perovskite oxynitrides under mild conditions.

The described synthetic routes in this section have several advantages and disadvantages, which are summarised in Table 14. The final goal of this project is to synthesise perovskite oxynitrides as thin films, and therefore we require a technique that allows for an easy and convenient deposition of the oxynitride over the desired substrate, in our case, alumina tiles and quartz substrates. In this context, solid-state routes require higher ammonolysis temperatures and longer reaction times which can induce defects that can be detrimental to the photocatalytic activity. On the other side, the co-precipitation method allows for the synthesis of perovskite oxynitrides nanoparticles, which have been successfully used for photocatalytic applications (photocatalytic decomposition of acetone by $LaTiO_2N$ nanoparticles) as described above. However, both routes are indicated for the synthesis of powder oxynitrides since they do not allow for thin film preparation.

Novel routes using alternative nitriding sources such as urea have the disadvantage of not allowing for thin film deposition since they are still a solid-state route ideal for powder synthesis. Consequently, and based on the reported and described literature, the Pechini method is the most interesting approach for the synthesis of our oxynitride powders and thin films, since the obtained resin can be used for the dip-coating deposition onto different substrates. The use of flux additives to reduce reaction times and ammonolysis temperatures is not considered due to the difficulty to add and remove, without contaminating, the oxynitride phase (metal alkali doping).

Additionally, the use of amorphous xerogels has proven to reduce temperature and reaction times as well as results in oxynitrides with higher specific surface areas, making them more suitable for photocatalytic applications that we will discuss in Chapter 5.

Table 14. Advantages and disadvantages of the described synthetic routes for oxynitride preparation.

Synthetic route	Advantages	Disadvantages
Solid-state Reactions to Oxynitrides	• Simplicity	• Higher temperatures and reaction times required • Early ammonia decomposition • Intermediate grinding required sometimes • Only for powders
Alternative Nitrogen Sources to Ammonia	• Reduces exposure to toxic gases	• Higher temperatures and reaction times required • Only for powders
Direct Route to Oxynitrides	• Straightforward • Does not require thermal ammonolysis	• Higher temperatures and reaction times required • Only for powders
Soft Chemistry Routes		
Hydrothermal/Solvothermal synthesis	• Lower temperatures and reaction times required • Homogeneity of the oxide precursors	• Higher temperatures and reaction times required • Only for powders
Co-precipitation Method	• Lower temperatures and reaction times required • Homogeneity of the oxide precursors	• Higher temperatures and reaction times required • Only for powders
Sol-gel Method (Pechini)	• Lower temperatures and reaction times required • Homogeneity of the oxide precursors • Dip-coating	• Lack of size and morphological control [226]

3.2 Experimental

3.2.1 Synthesis of Perovskite Oxynitride Powders

Perovskite metal oxynitride samples *A*Ta(O, N)$_3$ (A= Ba, Ca, Eu, La, Nd, Sr), *A*Nb(O, N)$_3$, (*A*= La, Sr) and $LaTiO_2N$ were synthesized by ammonolysis of their respective oxide precursor. Oxide precursors were prepared *via* the Polymeric Precursor Method (PPM). For this, $TaCl_5$ (0.89 mmol, Sigma-Aldrich, 99.8 %), $NbCl_5$ (0.89 mmol, Sigma-Aldrich, 99 %), or titanium (IV) isopropoxide (TTIP) (0.89 mmol, Sigma-Aldrich, 97%) were dissolved in 6.5 mL of methanol. Then, one of the chemical reagents $BaCO_3$ (1.335 mmol, Sigma-Aldrich, 99.99 %), $Eu_2(CO3)_3$ (0.4895 mmol, Alfa Aesar, 99.99 %), $CaCO_3$ (0.979 mmol, Sigma-Aldrich, 99%), $SrCO_3$ (0.979 mmol, Sigma-Aldrich, 99.99%), $La(NO_3)_3$ $6H_2O$ (0.9078 mmol, Sigma-Aldrich, 99.99 %), or $(CH_3CO_2)_3Nd$ (0.979 mmol, Sigma Aldrich, 99.9%) was added and stirred until complete dissolution. An excess of about 50 mol% Ba, 10 mol% Ca, Eu, Sr and 2 mol% La were used in order to avoid the formation of tantalum rich by-products (Ta_3N_5).[176] Finally, citric acid (19.86 mmol, Fisher) and propylene glycol (76.8 mmol, Sigma-Aldrich, 99.5%) were added to the solution. In our case, we replaced the ethylene glycol originally used in the Pechini synthesis with propylene glycol, a non-toxic alternative. The overall ratio of metal: citric acid: propylene glycol used was 1:11:43. Table 15 summarizes the corresponding amounts of reagents used during the synthesis.

The solutions were then heated at 120 °C for 90 minutes until complete evaporation of the methanol, leading to formation of a transparent resin. The gel containing the metal cations was placed on an alumina boat and heated in air for 1 h at 350˚C, 1h at 650˚C and finally 2 h at 800˚C. At each stage, the heating rate was 10˚C min^{-1}. The heating cycle converted the gel to a metal oxide powder, which was then nitrided by placing the powder on an alumina boat and on a semi-circular carbon block inside a 25 mm diameter-fused silica tube in a tuber furnace, under a flow of ammonia gas.

Depending on the chemical composition, the oxide precursors were ammonized (anhydrous ammonia, BOC, 99,98 %) at temperatures between 850°C and 1000°C, a heating ramp of 3°C min^{-1} and reaction times of 15 hours up to 54 hours. Gas flow was set to 250 mL min^{-1}. Samples were cooled down under an ammonia atmosphere in order to prevent the re-oxidation of the oxynitride.

Table 15. Target oxynitrides list - $AB(N,O)_3$ - with the corresponding amounts in mmol of the *A* metal, *B* metal, citric acid (CA), propylene glycol (PG) and the solvent methanol.

Target Oxynitride	A metal (mmol)	B metal (mmol)	Citric Acid (mmol)	Propylene glycol (mmol)	Methanol (mL)
$BaTaO_2N$	1.335	0.89	13.86	76.8	6.5
$CaTaO_2N$	0.979	0.89	13.86	76.8	6.5
$EuTaON_2$	0.4895	0.89	13.86	76.8	6.5
$LaTaON_2$	0.9078	0.89	13.86	76.8	6.5
$NdTaON_2$	0.979	0.89	13.86	76.8	6.5
$SrTaO_2N$	0.979	0.89	13.86	76.8	6.5
$SrNbO_2N$	0.979	0.89	13.86	76.8	6.5
$LaNbON_2$	0.9078	0.89	13.86	76.8	6.5
$LaTiO_2N$	0.9078	0.89	13.86	76.8	6.5

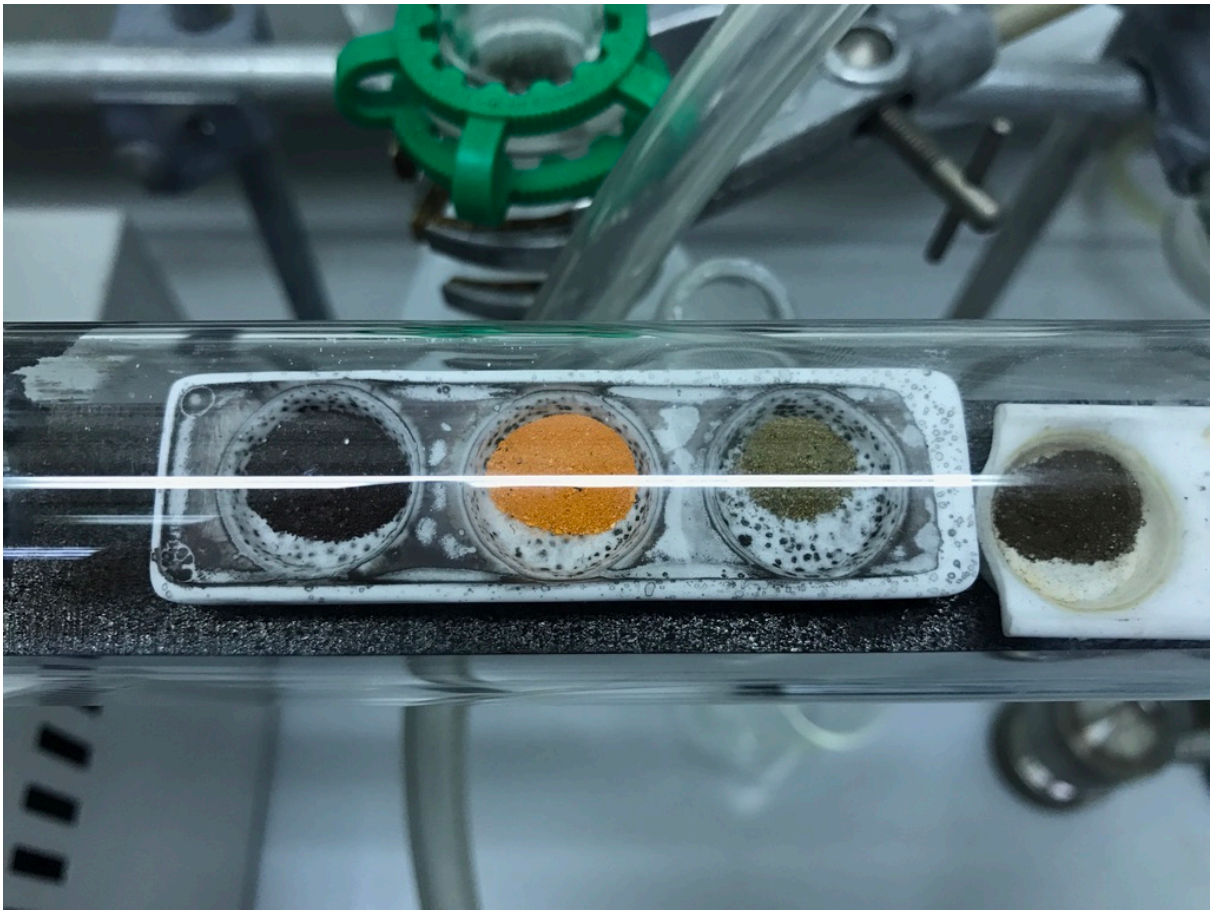

Figure 39. Photographic image showing the alumina boat containing the powder oxynitrides over the semi-circular carbon block and inside the 25-mm diameter-fused silica tube.

3.3 Results and Discussion

Xerogels precursors of the $CaTaO_2N$, $SrTaO_2N$, $BaTaO_2N$, $LaTaON_2$, $EuTaO_2N$, $SrNbO_2N$ and $LaNbON_2$ oxynitrides were obtained via the Pechini synthesis. The metal cations were successfully dissolved in methanol, complexed with citric acid and polymerised by adding propylene glycol. In some cases, hydrolysis of $TaCl_5$ resulted in the formation of hydroxide precipitates, which were re-dissolved by heating up to 100 °C, and when needed, by adding a small amount of acetic acid dropwise. The resins were transparent and viscous like that of honey.

The resins were subsequently heated under air at 350˚C for 1 h, 650˚C for 1 h, and 800˚C for 2 h. This step was carried out in a ventilated furnace room since the first and second step produced a considerable amount of combustion gases due to the burn off, carbon scaffold, which required gas extraction. After overnight cooling, the oxide precursors showed a bright white colour. We did not study the decomposition process of the organic resin during the thermal treatment in air. However, Rachel et al. reported that the oxidation occurs in three major steps, monitored by thermoanalytic measurements.[201]

The first step, also known as “drying”, occurs when the sample is heated under air in the temperature range of 100-200 °C and it is accompanied by the evaporation of water (*m/e* = 18) trapped in the sample. Secondly, the main weight loss occurs in the range between 250 °C and 400 °C. within this temperature the organic matrix is oxidised and converted to CO_2 and water (*m/e* = 44). Finally, a less pronounced weight loss is observed at 600 °C attributed to the combustion of the residual organic matrix and due to the decomposition of bicarbonates.

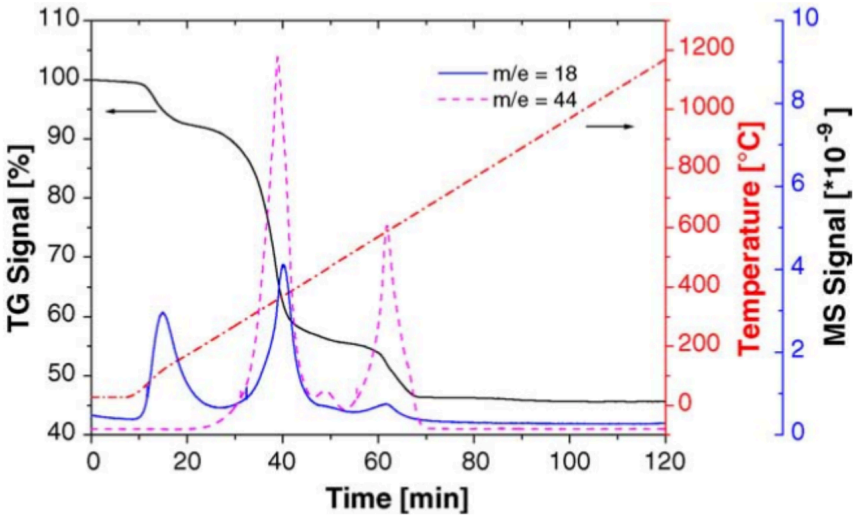

Figure 40. TG curve of the a SrNb-xerogel showing decomposition of the organic framework in air. Reproduced from ref.[201]

Phase pure oxynitrides were obtained via ammonolysis of the oxide precursors for 15-54 h in the range 850- 1000°C and with an ammonia gas flow of 250 mL min^{-1}. Depending on the reported literature, the nature of the oxynitrides and our observations, different temperature reaction times and flow ratios were tested for each sample.

$SrTaO_2N$ and $SrNbO_2N$ were ammonolysed at 850°C during 15 h and an NH_3 flow of 250 mL min^{-1}. The resulting powders showed a bright orange colour for the $SrTaO_2N$ and a brownish colour for the $SrNbO_2N$. Both samples were analysed using XRD and the diffraction patterns showed sharp peaks which match those previously published in the literature. XRD data did not indicate the presence of minor oxide phase and/or impurities such as Ta_3N_5 or niobium oxynitrides NbO_xN_y (Figure 42)

$LaTaON_2$, $LaNbON_2$ and $EuTaO_2N$ were synthesised at 950°C for 15 hours, heating rate of 3°C min^{-1} and an NH_3 flow of 250 mL min^{-1} The powder oxynitrides showed a bright orange colour for the $LaTaON_2$, a darker orange/brown colour for the $LaNbON_2$ and a dark brown colour for the $EuTaO_2N$. The previously reported XRD patterns matched the observed XRD peaks in all samples as seen in Figure 42. Moreover, no minor oxide phases or impurities were observed.

$CaTaO_2N$, $BaTaO_2N$, $LaTiO_2N$ and $NdTaO_2N$ required the higher temperatures during the thermal process as previously described in the literature. $CaTaO_2N$ oxynitride was synthesised at 1000˚C during 15 h, heating rate of 3°C min^{-1} and an NH_3 flow of 250 mL min^{-1}. The oxynitride showed a bright yellow colour and the observed XRD peaks in the diffraction data are in agreement with previously published for the sample. Both oxynitrides, $LaTiO_2N$ and $NdTaO_2N$ were initially ammonolysed at 1000˚C during 15 h and an NH_3 flow of 250 mL min^{-1}. The resulting powders showed pale yellow/white colours. Both samples required longer reaction times since XRD data showed the presence of major oxide phases from the precursors, indicating that the reaction was not completed after 15 hours. Increasing the reaction time from 15 h to 54 h resulted in bright orange powders. Observed XRD data from both samples showed peaks matching those previously published for $LaTiO_2N$ and $NdTaO_2N$.

The $BaTaO_2N$ oxynitride was initially ammonolysed at 1000˚C during 17 h and an NH_3 flow of 250 mL min^{-1}. The oxynitride showed a dark-red bright colour and XRD data showed the presence of the impurity Ta_3N_5. The formation of a minor Ta_3N_5 impurity phase during oxynitride synthesis has been previously reported. Brophy et al. studied the influence of the flow velocity on the formation of Ta_3N_5 during the synthesis of $BaTaO_2N$ via solid-state.[200] The formation of the Ta_3N_5 can be understood as a competition between the solid-state transport and the nitridation process. Higher flow velocities (increasing from 25 mL min^{-1} to 2500 mL min^{-1}) promoted nitridation to binary Ta_3N_5 before solid-state transport process could stabilize mixed anion octahedra.

Following the approach proposed in the literature, we decreased the ammonia flow from 250 mL min^{-1} to 100 mL min^{-1} and increased the % of Ba^{2+} from a 10% to a 50%. Figure 41 shows the XRD data for both reactions, using a 10% excess of Ba^{2+} and a 50% excess of Ba^{2+}. The minor Ta_3N_5 phase was successfully removed by decreasing the ammonia flow, which reduced the nitride reaction, and increasing the excess of available Ba^{2+}.

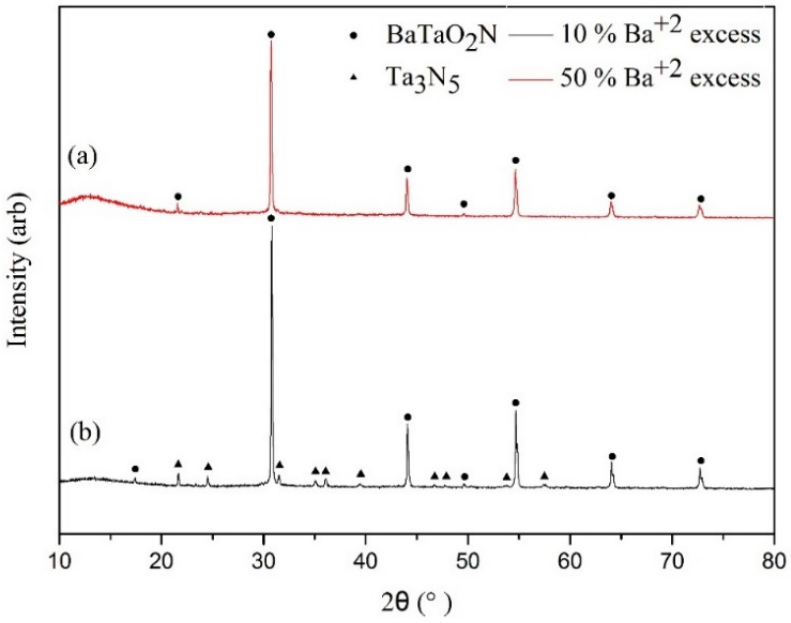

Figure 41. XRD patterns for **(a)** $BaTaO_2N$ synthesised at 1000°C, 17 h, heating rate 3°C min^{-1}, NH_3 flow 500 mL min^{-1} and **(b)** $BaTaO_2N$ synthesised at 1000°C, 15 h, heating rate 3°C min^{-1}, NH_3 flow 250 mL min^{-1}.

An attempt at synthesising $CaNbO_2N$ was unsuccessfully performed. Apparently, at temperatures below 1000 °C, the diffusivity of the constituent ions is not enough for nitridation to completely proceed, while at high temperatures (>1000°C) the synthesis resulted in the formation of a by-product niobium oxynitride phase NbO_xN_y which co-exist in equilibrium with the oxynitride phase. The increase on the intensity of the NbO_xN_y peaks with the temperature suggest the decomposition of the oxynitride phase at high temperatures. In order to avoid the formation of the NbO_xN_y phase, solid-state routes make use of mineralisers such as NaCl/KCl, which facilitates ionic diffusion. However, the limitations of the sol-gel route to incorporate and eliminate mineralisers prevents the synthesis of $CaNbO_2N$.

The X-ray diffraction patterns of the nine oxynitrides (Figure 42) under study revealed sharp characteristic reflections which are in agreement with the single pure perovskite-type phases reported in the literature, indicating that the target oxynitrides were achieved at the given synthesis conditions. As observed in the Figure 42 and according to the Bragg's Law ($n\lambda = 2d \cdot sin\theta$) the

diffraction peaks of the tantalum-containing oxynitrides $ATaO_2N$ shifted to lower 2θ angles when the A-site cation was substituted with cations with higher Shannon radii Ba>Sr>Ta.

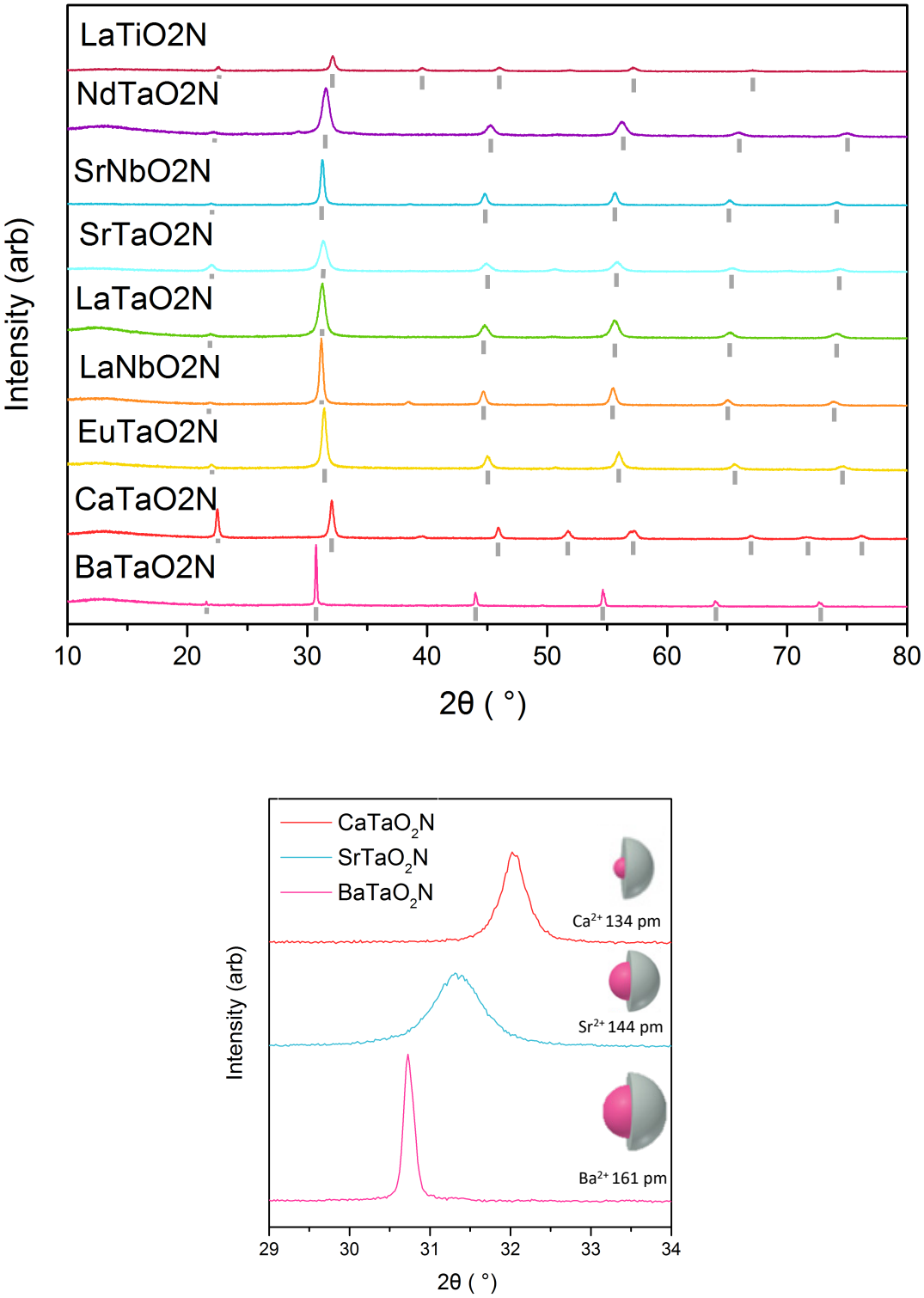

Figure 42. XRD patterns of the powder oxynitrides synthesised *via* Polymeric Precursor Method (PPM) and illustration of the peak shift and broadening at 29-34˚. Shannon radii are indicated for 12-coordinated cations.[121] Grey lines indicate Bragg's peak positions of the oxynitride phase.

In order to confirm the structures and composition of the samples Rietveld refinements of the structures of the nine perovskite oxynitrides samples using the corresponding XRD data was carried out.

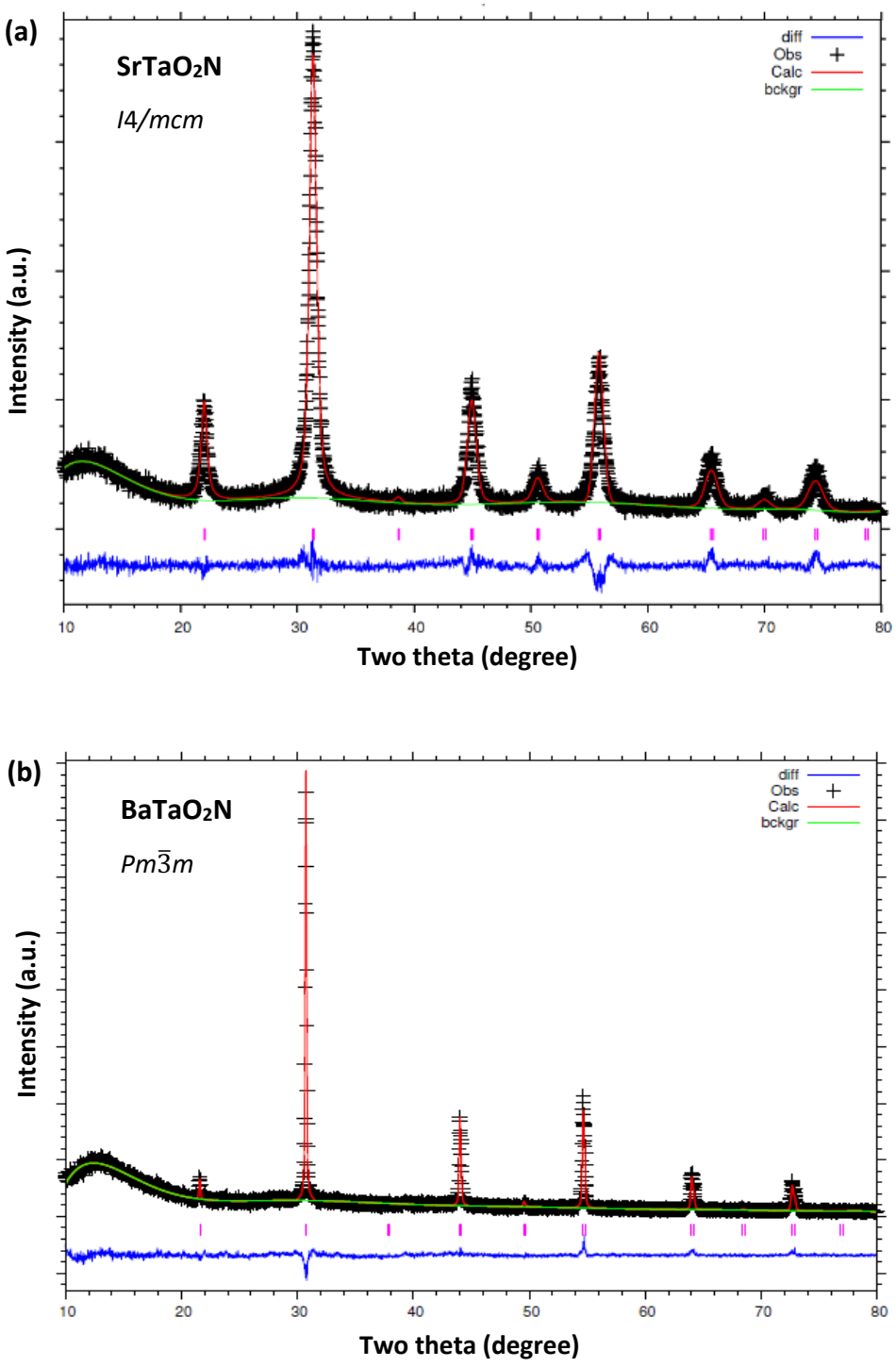

Figure 43. Observed and calculated X-ray diffraction pattern of **(a)** $SrTaO_2N$ and **(b)** $BaTaO_2N$. Obs is observed diffraction data, Calc is the calculated date by the Rietveld Refinement and diff is Obs-Calc. The pink vertical lines denote the standard Bragg's positions.

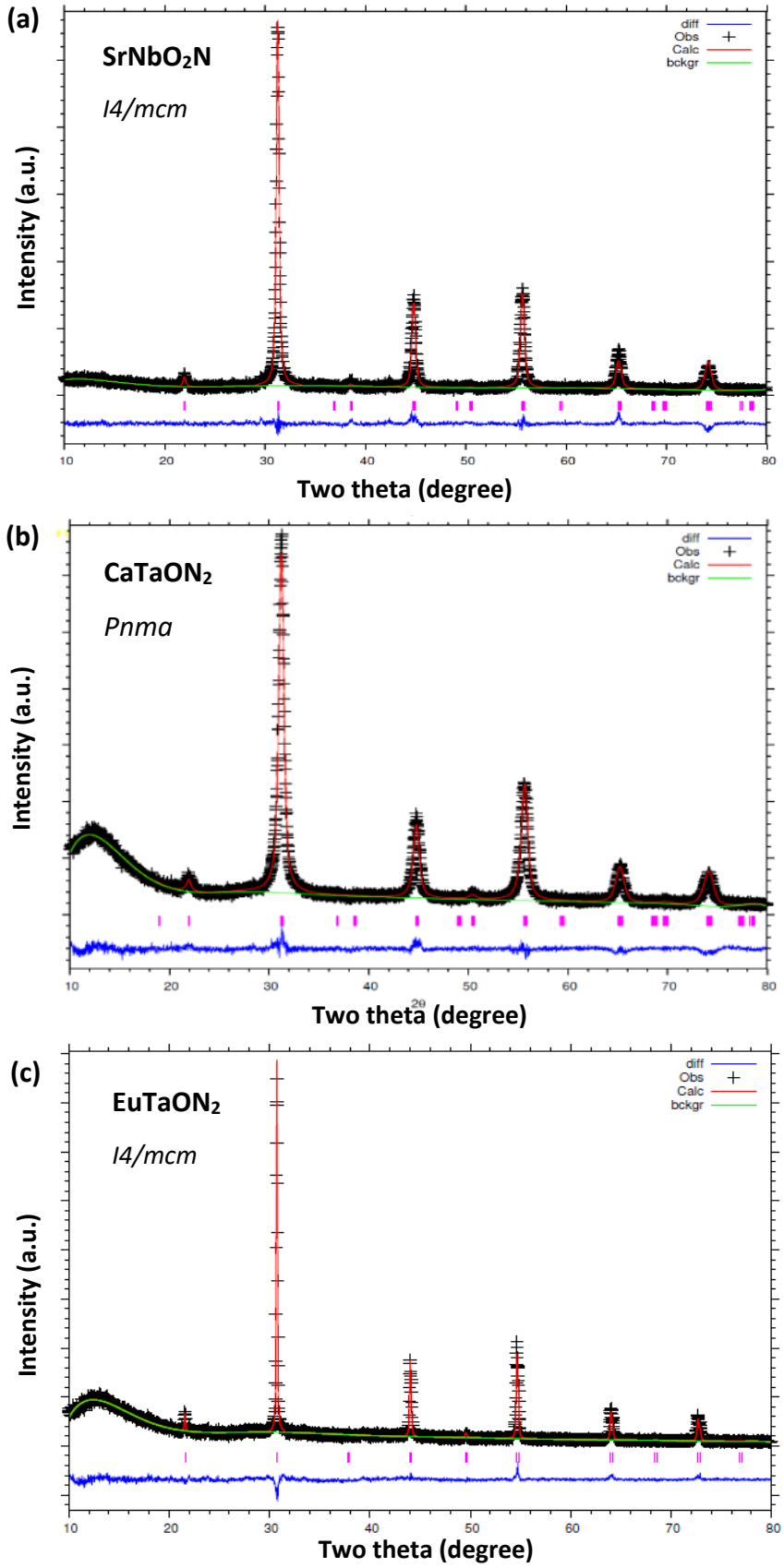

Figure 44. Observed and calculated X-ray diffraction pattern of **(c)** $SrNbO_2N$, **(d)** $CaTaON_2$ and **(c)** $EuTaO_2N$. Obs is observed diffraction data, Calc is the calculated date by the Rietveld Refinement and diff is Obs-Calc. Pink scripts indicate reported position peaks.

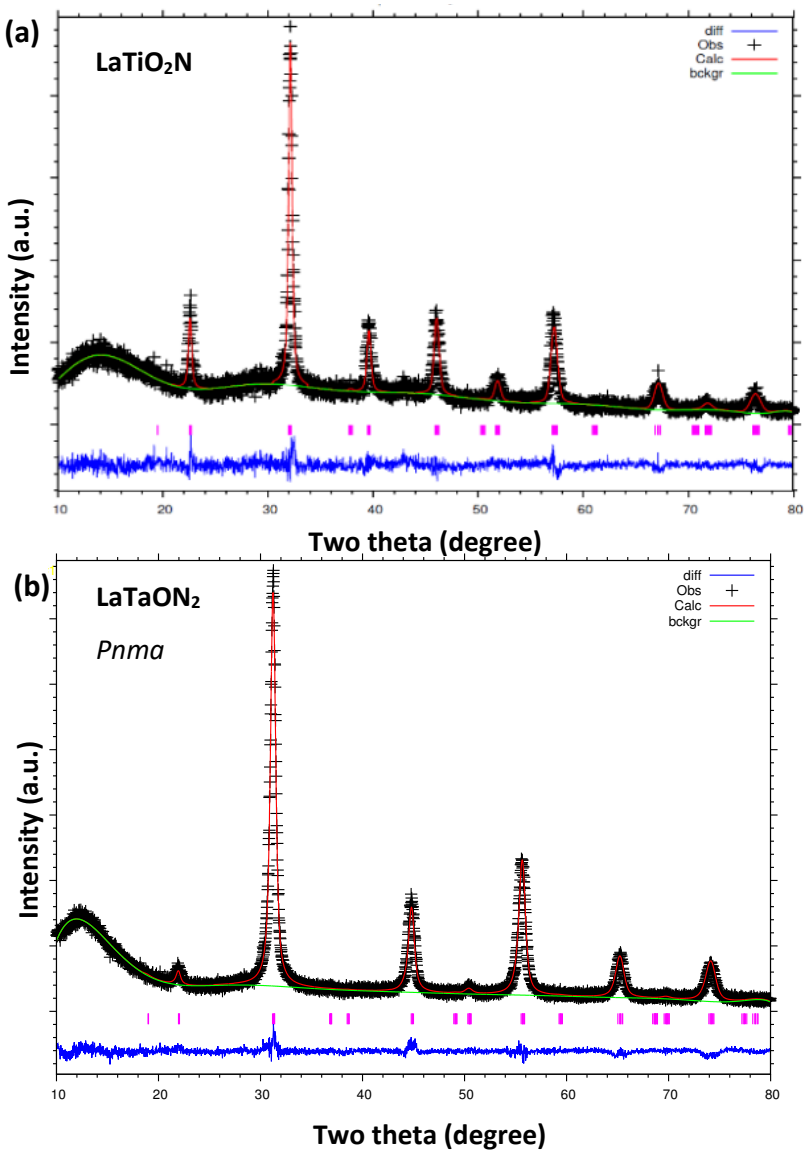

Figure 45. Observed and calculated X-ray diffraction pattern of **(a)** $LaTiO_2N$ and **(b)** $LaNbO_2N$. Obs is observed diffraction data, Calc is the calculated date by the Rietveld Refinement and diff is Obs-Calc. The pink vertical lines denote the standard Braggs positions.

The crystal structures and detailed structural data of $SrTaO_2N$, $CaTaO_2N$, $BaTaO_2N$, $EuTaO_2N$, $SrNbO_2N$, $LaTaON_2$ and $LaTiON_2$ have previously been reported. During the Rietveld refinement, no attempt was made to differentiate the two anions O^{-2} and N^{-3} since they have indistinguishable X-ray scattering factors. The refinement profiles of the perovskite oxynitrides are shown in Figures 43-45, while the crystallographic details are given in Tables 16 and 17.

$SrTaO_2N$, $EuTaO_2N$ and $SrNbO_2N$ were refined on the basis of the tetragonal, *I4/mcm* perovskite-type structure. Orthorhombic $CaTaO_2N$ and $LaTaON_2$ were modelled in the *Pnma* and *Imma* space groups while cubic $BaTaO_2N$ and triclinic $LaTiON_2$ were modelled in the $Pm\bar{3}m$ and *I1* space group, respectively. The distortions present in the perovskites arise from the tilting of the

TaO_6/NbO_6 octahedron to accommodate smaller than ideal ion size in the 12-coordinate site and each niobium oxynitrides was found to be isostructural with its tantalum analogue.

Table 16. Rietveld refinement profiles of the X-ray diffraction data of the powder $SrTaO_2N$, $CaTaO_2N$, $BaTaO_2N$ and $EuTaO_2N$.

	$SrTaO_2N$	**$CaTaO_2N$**	**$BaTaO_2N$**	**$EuTaO_2N$**
2θ range (˚)	10 -80	10 -80	10 -80	10 -80
Space group	*I4/mcm*	*Pnma*	*$Pm\bar{3}m$*	*I4/mcm*
R_{wp} (%)	2.83	4.22	7.15	7.86
χ^2	8.92	7.14	4.34	5.21
a (Å)	5.693(5)	5.566(5)	4.109(4)	5.639(1)
b (Å)	-	7.893(5)	-	-
c (Å)	8.041(4)	5.618(4)	-	7.998(2)
Volume $(Å)^3/Z$	65.15(7)	61.46(8)	69.37(3)	63.58(4)

Table 17. Rietveld refinement profiles of the X-ray diffraction data of the powder $SrNbO_2N$, $LaTaON_2$ and $LaTiON_2$.

	$SrNbO_2N$	**$LaTaON_2$**	**$LaTiO_2N$**
2θ range (˚)	10 -80	10 -80	10 -80
Space group	*I4/mcm*	*Imma*	*I1*
R_{wp} (%)	2.49	4.32	2.82
GOF (χ^2)	3.72	3.28	7.78
a (Å)	5.720(3)	8.084(2)	5.573(3)
b (Å)	-	8.066(3)	7.880(2)
c (Å)	8.105(6)	5.739(2)	5.610(2)
Volume $(Å)^3/Z$	66.29(3)	65.81(8)	61.62(5)

Regarding the cell volumes, all values are in agreements with those previously reported in the literature, except for $EuTaO_2N$, where we observe a smaller than expected unit cell of 2.27% by volume ($V_{expected}$ = 65.09 Å^3 vs $V_{Rietveld}$ = 63.58 Å^3). A possible explanation for this reduced volume can be attributed to increased nitridation towards $EuTaON_2$, with oxidation of the Eu^{2+} to smaller Eu^{3+} ion. This same trend was observed during the Le Bail refinement of the $EuTaO_2N$ thin film in Chapter 4. A similar, but opposite trend was observed in the $SrNbO_2N$ and $SrTaO_2N$ cell volumes. $SrNbO_2N$ cell volume was 1.7% larger than its tantalum analogue. This result was not expected since both, Ta^{5+} and Nb^{5+}, have the same ionic radius (0.64 pm).[121] Again, this can be attributed to a partial reduction of Nb^{5+} to the larger Nb^{3+} (0.72 pm).

The goodness of fit χ^2 were found falling in the range of 3.72-8.92 %, while the overall weighted-profile R-factors (R_{wp}) were found in the range of 2.49-7.86 %, indicating a good fit between the model and the data. In each case, the models account for all the observed Bragg peaks.

The crystallite sizes were estimated by the Scherrer equation during the Rietveld refinement and were found in the range of 20 nm - 109 nm. Oxynitrides synthesised in the range of 850 - 950°C resulted in low crystallite sizes of approximately 20-33 nm. The oxynitride $BaTaO_2N$ was the sample with the highest crystallite size (109 nm), followed by $LaTiO_2N$ (38 nm) and $CaTaO_2N$ (37 nm). The three samples were ammonolysed at the highest temperature of 1000°C and longer reaction times for $CaTaO_2N$ and $LaTiO_2N$ (38 nm) were needed. As a general trend, higher ammonolysis temperatures and reactions times led to higher crystallite sizes due to the effect of sintering. The Table 18 summarises the temperature, reaction time and crystallite sizes of the powder oxynitrides synthesised in this chapter.

Table 18. Temperature, reaction time and crystallite size for the powder oxynitrides synthesised via Polymeric Precursor Method (PPM).

Sample	T (°C)	Time (h)	Crystallite size (nm)
$BaTaO_2N$	1000	17	109
$CaTaO_2N$	1000	15	37
$EuTaO_2N$	950	15	24
$LaTaON_2$	950	15	20
$SrTaO_2N$	850	15	20
$LaNbON_2$	950	15	33
$SrNbO_2N$	850	15	31
$LaTiON_2$	1000	54	38

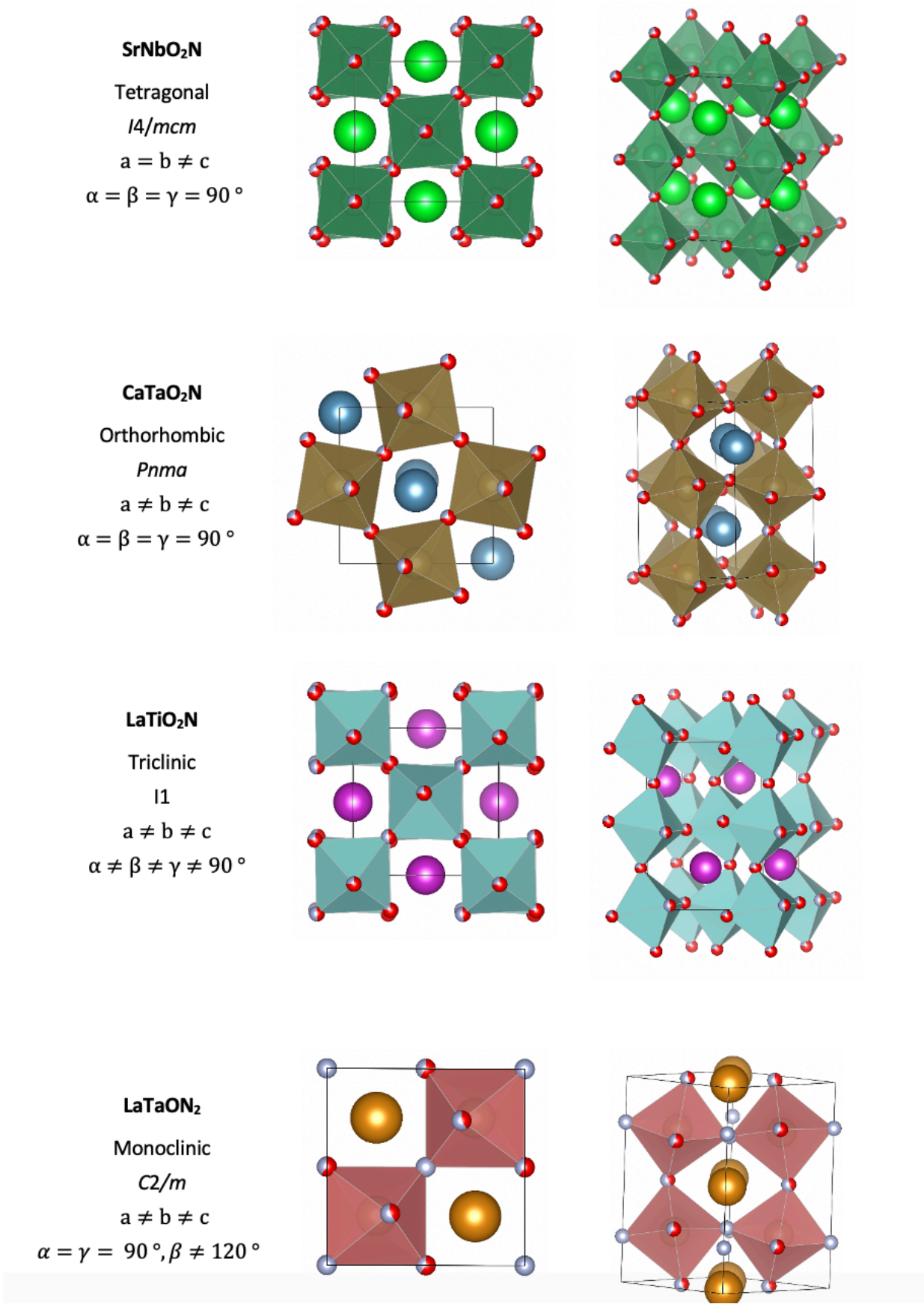

Figure 46. Main structural distortions and crystal parameters observed in perovskites oxynitrides.

3.3.1 UV-Visible Diffuse Reflectance Spectroscopy

Diffuse reflectance spectral data of the synthesized oxynitrides was obtained in the wavelength of 400-900 nm. Later, these data sets were used to create Tauc plots to determine the band gaps. For this, and as previously mentioned in Chapter 2, the raw diffuse spectrum was converted to the absorbance spectrum by using the Kubelka-Munk equation;

$$F(R) = \frac{(1-R)^2}{2R} \cong \alpha$$

Then, the absorption coefficient (α) was replaced in the Davis and Mott equation (based on the original Tauc relation) by the Kubelka-Munk function:

$$(\alpha h\nu)^{1/n} = A\,(h\nu - E_g)$$

Finally, Tauc plots are built by plotting the quantity $(\alpha(R)h\nu)^{1/n}$ on the ordinate *versus* the photon energy ($h\nu$) on the abscissa. Based on prior literature, it was assumed that the band gaps were indirect (n = ½).

For the determination of the band gap energies, we need to take a closer look to the Tauc plot and particularly to the absorption tail, which is defined as the lower region under the optical band gap edge.

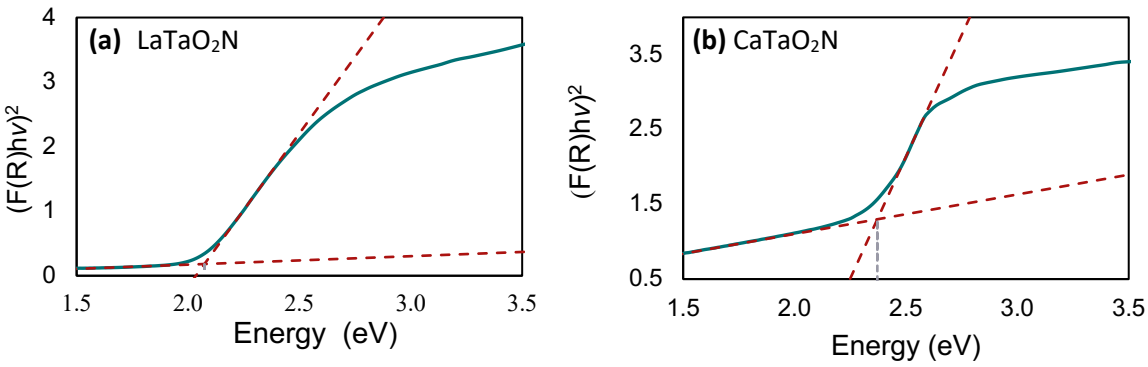

Figure 47. Band gap energies of **(a)** $LaTaO_2N$ and **(b)** $CaTaO_2N$ are found by plotting the Tauc plot and fitting the baseline absorption at the onset. Calculated band gap values for $LaTaO_2N$ and $CaTaO_2N$ are 2.07 e V and 2.37 eV, respectively.

Regarding Tauc plot of $LaTaO_2N$ sample, we assume that the scattering coefficient is constant in the wavelength region measured and the baseline absorption is just above the abscissa (Figure 47a). However, on the $CaTaO_2N$ Tauc plot (Figure 47b) the baseline absorption is above the energy axis and not as flat as it was with the $LaTaO_2N$ sample. For this reason, it is necessary to fit the linear part under the band gap energy level on the onset to find the most accurate value of the band gap.

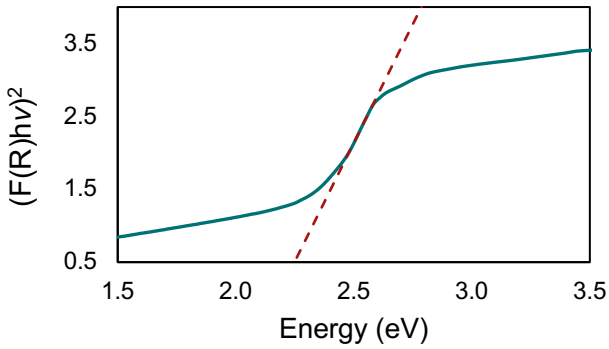

Figure 48. Tauc plot for the $CaTaO_2N$ showing the *y* interception and a band gap value of 2.17 eV.

Comparing both calculated band gap energies for the $CaTaO_2N$ sample, the value determined by extrapolating the band gap linear fit to the abscissa leads to a band gap value of 2.17 eV. On the other hand, the band gap value determined by interception of the fitted baseline with the band gap linear region is calculated to be 2.37 eV. This band gap energy is more in agreement with the value found in the literature (2.4 eV).[179]

The Table 19 summarizes the optical band gaps and colours of the perovskite oxynitrides synthesized so far, which are in a good agreement with the previous literature.[176,201]

Table 19. Calculated band gap energies of *A* = Ba, Ca, Eu, La, Nd, Sr and *B* = Ta, Nb, Ti, perovskite oxynitrides and their reported colours obtained experimentally.

Sample	Experimental Band Gap (eV)[This work]	Reported Band Gap (eV)	Colour
$BaTaO_2N$	1.92	1.89 [176]	Brick red
$CaTaO_2N$	2.37	2.40 [176]	Yellow
$EuTaON_2$	impure	Not reported	Dark grey
$LaTaON_2$	2.07	1.99 [176]	Orange
$NdTaON_2$	impure	Not reported	Orange
$SrTaO_2N$	2.08	2.16 [176]	Orange
$LaNbON_2$	1.68	1.70 [227]	Dark brown
$SrNbO_2N$	1.85	1.90 [176]	Brown
$LaTiO_2N$	2.14	2.10 [191]	Dark brown

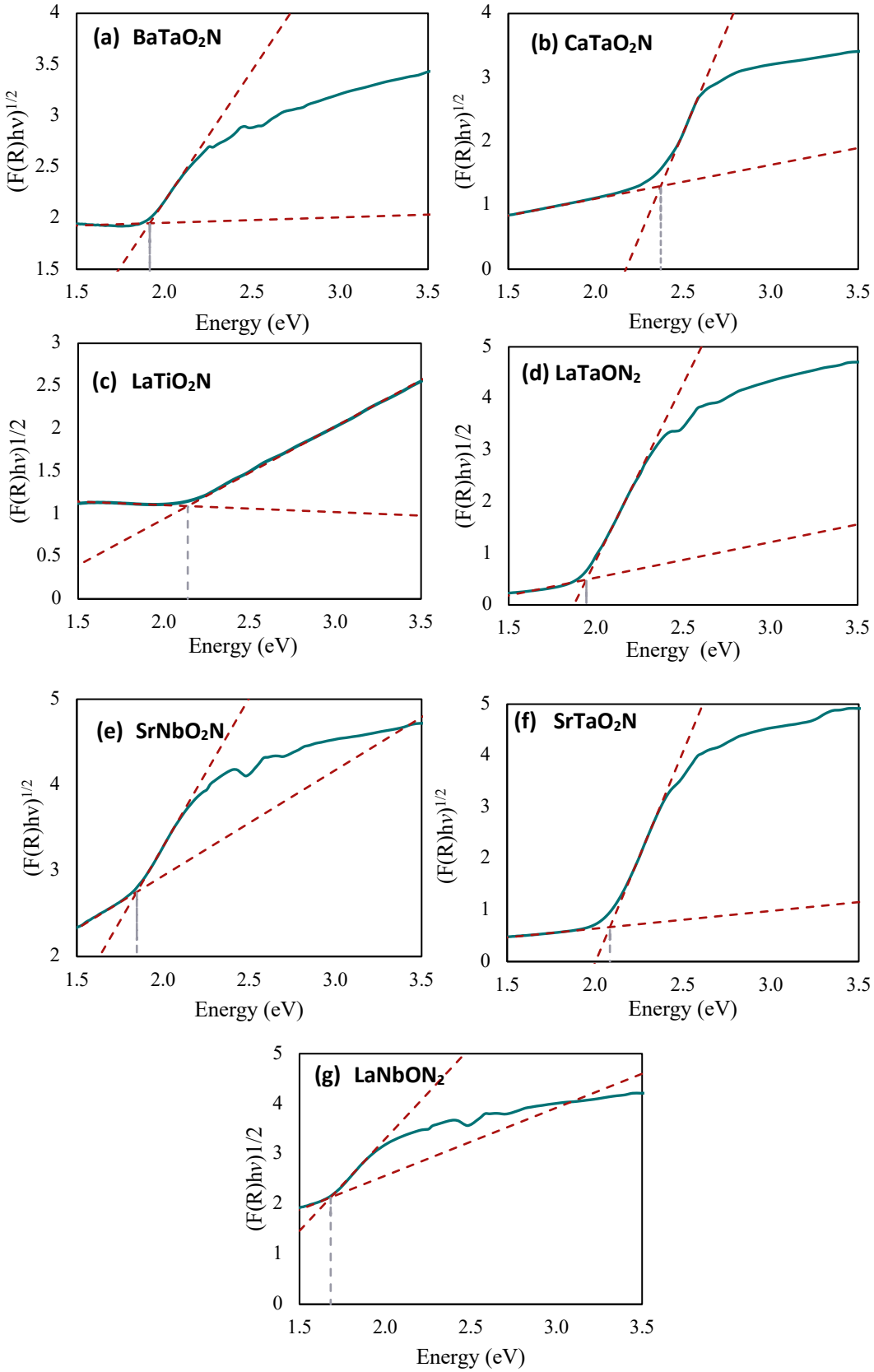

Figure 49. Tauc plots for the correspondent perovskite oxynitrides synthesized in this work.

Colour change in tantalum perovskite oxynitrides *A*TaO_2N can be better understood if the difference in size between the *A*-size cations and their impact on the crystallographic structure are emphasized. The substitution of the *A* cation with another with the same formal charge (+2) but

smaller size produces a change in the colour of the oxynitride which is correlated with a reduction of the crystallographic symmetry. As observed in Figure 50, $CaTaO_2N$ is yellow, while $SrTaO_2N$ is orange and $BaTaO_2N$ is brick red and according to the Shannon radii, for a twelve-coordinated A^{+2} cation the ionic radii are 175 pm, 158 pm and 148 pm for Ba^{2+}, Sr^{2+} and Ca^{2+} respectively. $BaTaO_2N$ possesses a cubic unit cell, $SrTaO_2N$ is tetragonal and $CaTaO_2N$, which contains the larger cation, is orthorhombic with *Pnma* symmetry. These structural distortions of the TaO_4N_2 octaheda resulted in the attempt to accommodate the different size ions into the perovskite unit cell. As a consequence of the distortion induced by cation substitution, the bond angles *B*-(O,N)-*B* are partially altered while the bond lengths *B*-(O,N)-*B* remain constant. As symmetry decreases (cubic > tetragonal > orthorhombic), the overlap between the metal d-orbitals and the O/N-p orbitals decreases (poor overlap), leading to *B*-(O,N)-*B* bonds with less covalent character. [133] Consequently, an impeded overlap results in the reduction of the width of the conduction band, leading to higher optical band gaps and being physically manifested as brighter colours on the oxynitrides (red-orange-yellow). The same effect has been observed with the perovskite niobium oxynitrides $ANbO_2N$.

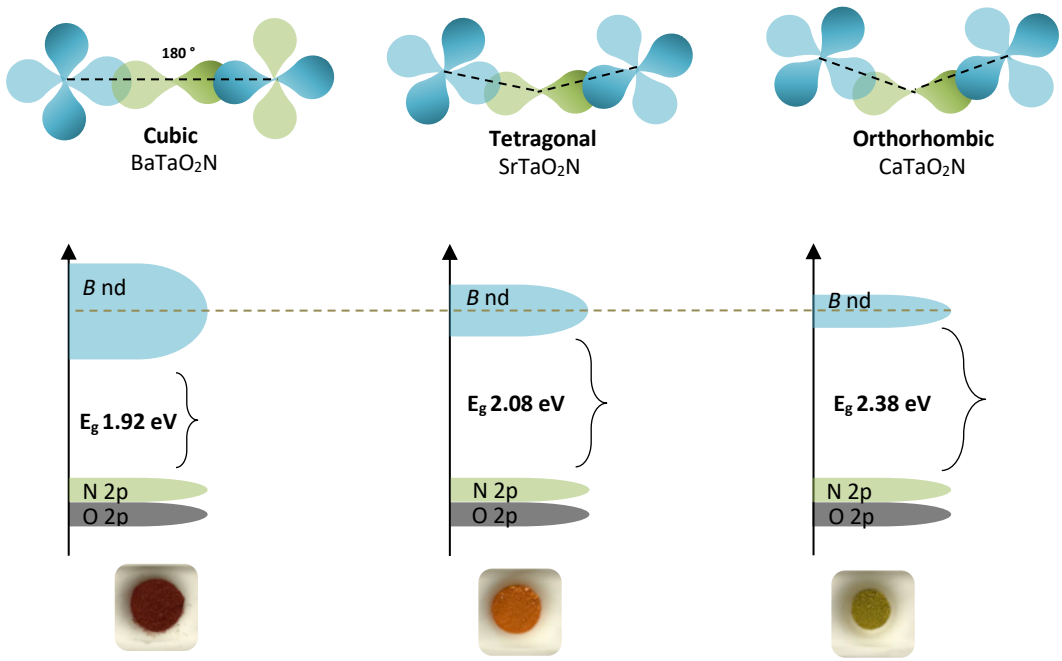

Figure 50. Sketch showing the influence of the *B*-(O,N)-*B* angle on the width of the conduction band. From left to right, better overlap (cubic $BaTaO_2N$, 180 °) results in smaller optical band gaps while decreasing the symmetry (orthorhombic $CaTaO_2N$) leads to a band gap increase. The energetic position of the CV remains unchanged.

However, while $SrTaO_2N$ (2.08 eV) shows a bright orange colour, $SrNbO_2N$ (1.85 eV) is brown. Taking into the account that each niobium oxynitride $ANbO_2N$ is isostructural with their tantalum analogue, the colour difference between both compounds cannot be explained by crystal symmetry

(bond angles) as neither by bond lengths, since Nb^{5+} 12-coordinated has the same ionic radius than Ta^{+5} 12-coordinated (78 pm).[121]

Hence, a plausible explanation for the origin of the color changes is the difference on the electrongativity of the the substituted *B*-cation. Tantalum is a more electropositive transition metal than niobium, thus, the energetic position of the conduction band is displaced upwards leading to wide band gaps. (Figure 51)

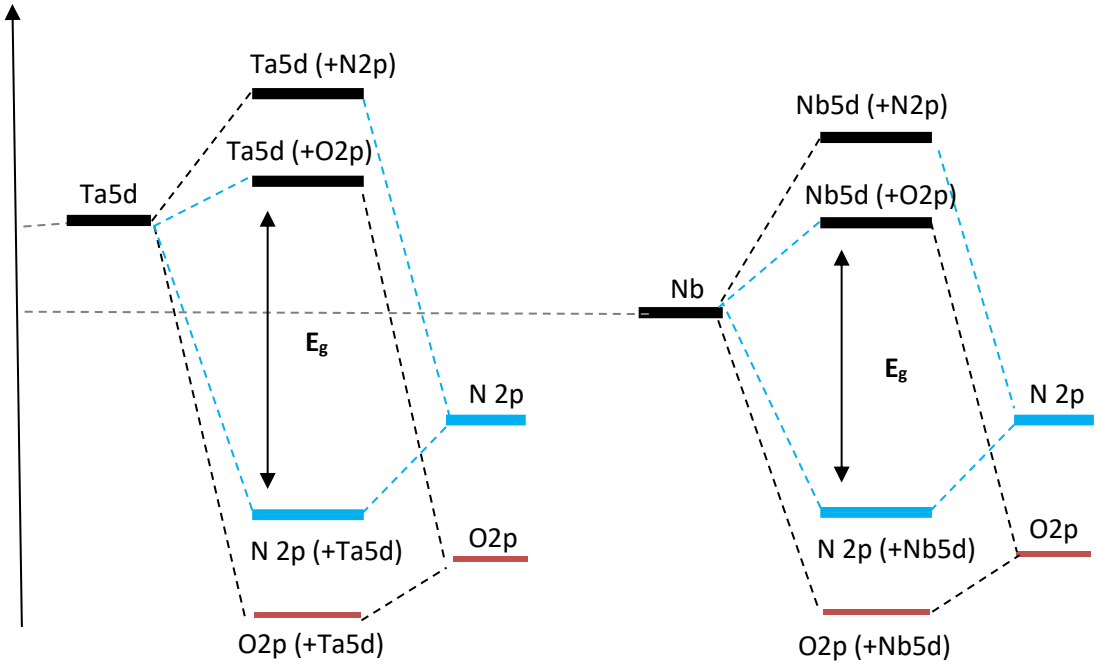

Figure 51. Schematic band structure for the tantalum (left) and niobium perovskite oxynitrides. Increasing the electro positivity of the transition metal results in a wider optical band gap.

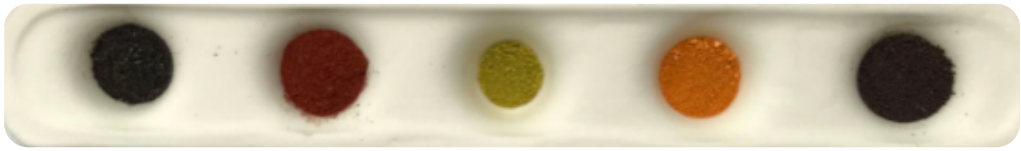

Figure 52. Photographic image of five different perovskite oxynitride powders over an alumina boat. From left to right: $EuTaO_2N$, $BaTaO_2N$, $CaTaO_2N$, $SrTaO_2N$, $LaNbON_2$.

3.3.2 Stability and Thermogravimetric Analysis of the Powder Perovskite Oxynitrides

Because the photocatalyst may be exposed to elevated temperatures and different weather conditions when exposed outdoors, it is important to know their stability under different conditions and the temperature at which the perovskite materials start to decompose.

In order the study the stability of the perovskite oxynitride $SrNbO_2N$, three samples of 100 mg were placed under water, an acidic solution (HCl 1 M) and inside the lab furnace at 100˚C for one month. The XRD data of the three samples did not show any change after a month when compared to the $SrNbO_2N$ sample kept under normal conditions (25˚C, air), thus, indicating the stability of the material under the described conditions

Thermogravimetric analysis was performed on the samples to study the thermal reoxidation of the oxynitrides. The analysis was carried out placing 20-30 mg of powder oxynitride in a Al_2O_3 crucible and heated under synthetic air in the temperature range of 25-1100˚C, with a heating rate of 5˚C min^{-1}.

The re-oxidation process of perovskite type oxynitrides of transition metals with d^0 configuration upon synthetic air follows the equation: [225]

$$ABO_xN_{y\,(s)} + \frac{3y}{4O_2}\,(g) \leftrightarrow ABO_{x+\frac{3y}{2}}\,(s) + \frac{y}{2N_2}\,(g)$$

The nitrogen content (y) can be quantified from the amount of nitrogen evolved and determined from the weight gain (Δm) measured during the reoxidation process and obeys the following equation:

$$y = \frac{\Delta m}{(\frac{3}{2}M\,(O_2) - M(N_2)} \times \frac{M(ABO_{x+\frac{3y}{2}})}{m(ABO_{x+\frac{3y}{2}})}$$

Where $M\,(O_2)$ and $M(N_2)$ are the molar massed to molecular nitrogen and oxygen. $M(ABO_{x+\frac{3y}{2}})$ is the molar mass of the formed oxide and $m(ABO_{x+\frac{3y}{2}})$ its weight. However, this formula has some limitations; both the oxynitride and oxide must be well characterised by XRD. Additionally, powder oxynitrides contain significant amounts of chemically absorbed CO_2 and H_2O, which distort the calculated nitrogen content results. No attempt was made in this section to determine the O/N ratio.

The thermal reoxidation of perovskite-type oxynitrides proceeds *via* the formation of a reoxidation intermediate phase with a higher weight that the oxide phase, as illustrated in Figure 53. [133,201]

At the beginning of the reoxidation process (25-400˚C) a small reduction (around 2%) of weight loss is observed and is attributed to the loss of water present in the oxynitride. As we increase the temperature, the TGA curve shows a characteristic increase in weight attributed to the formation of an intermediate phase with a higher weight than expected for a reoxidation reaction. This weight increase (mass increase of 5-8 %) was observed to start at around 390-450˚C, reaching a maximum at 500-600˚C. Different studies have been published to try to understand the formation of the intermediate phase.[133,201] It was found that the unexpected intermediate weight gain is originated by the retention of bound N_2 in the completely oxidised material, forming intermediate dinitrogen-containing compounds such as *B*-N≡N and *B*-N≡N-*B*, where *B* denotates the *B* metal cation in $AB(O,N)_3$. Finally, at higher temperatures, the N_2 is completely detached and the weight decreases to give the final reoxidation product.

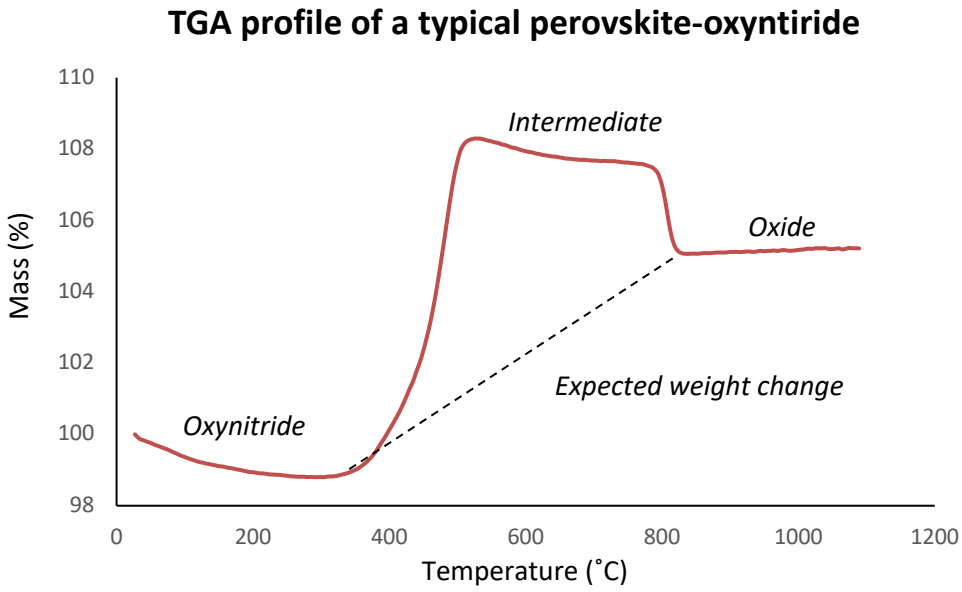

Figure 53. Typical TGA profile of the re-oxidation of a perovskite-oxynitride.

The temperature at which the perovskite oxynitrides start to decompose varies among the different synthesised materials. As an example, $SrNbO_2N$ started to decompose at 450˚C, while $SrNbO_2N$ is stable up to 570˚C and $BaTaO_2N$ and $LaTiO_2N$ start to decompose at 630˚C and 430˚C respectively.

Once the thermogravimetric analysis concluded, the white re-oxidation products were collected and analysed by XRD. The following oxides were identified; $Sr_2Ta_2O_7$, $Sr_2Nb_2O_7$, $LaTaO_4$, $Ba_5Ta_4O_{15}$, $La_2Ti_2O_7$ and $LaNbO_4$ as the peaks observed in the diffraction data are in agreement with those previously published. As mentioned above, the knowledge of the decomposition temperature of the perovskite oxynitrides is essential to decide whether the photocatalyst can be used under given conditions. All the perovskite oxynitrides synthesised in this work showed stability at temperatures below 350˚C.

(a) $SrTaO_2N$

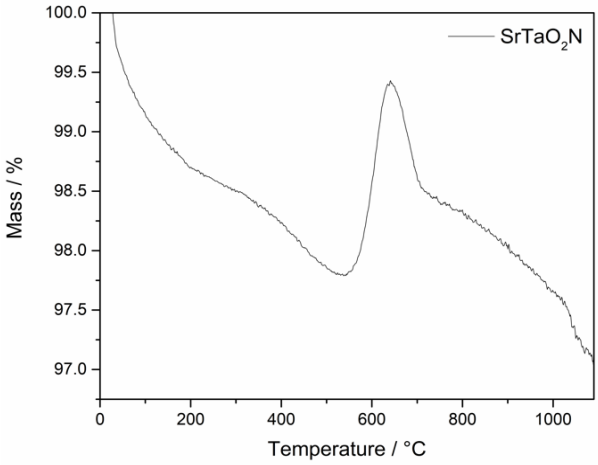

TGA Oxide

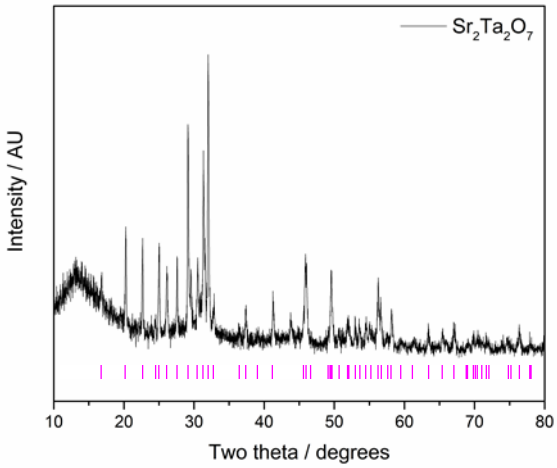

(b) $SrNbO_2N$

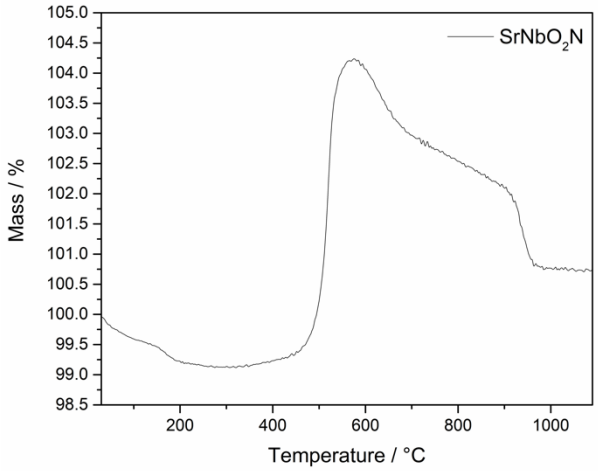

TGA Oxide

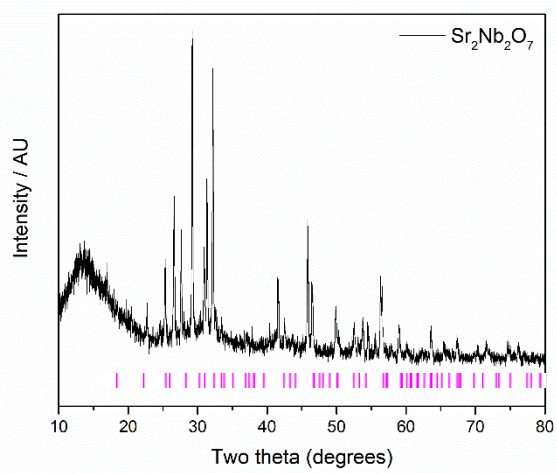

(c) $LaTaON_2$

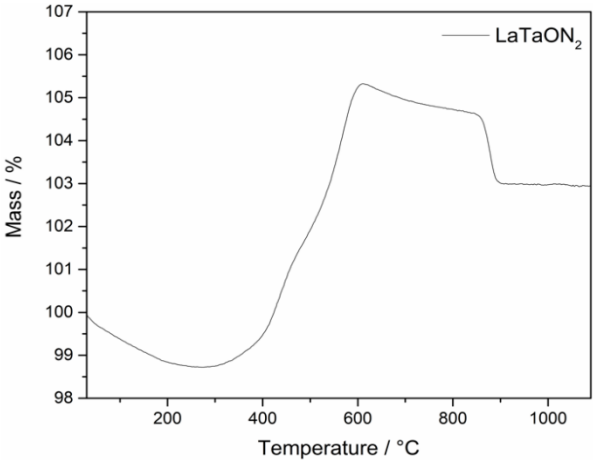

TGA Oxide

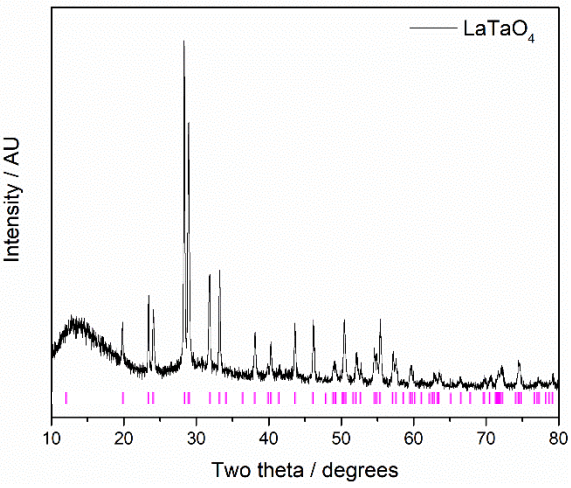

TGA Oxide

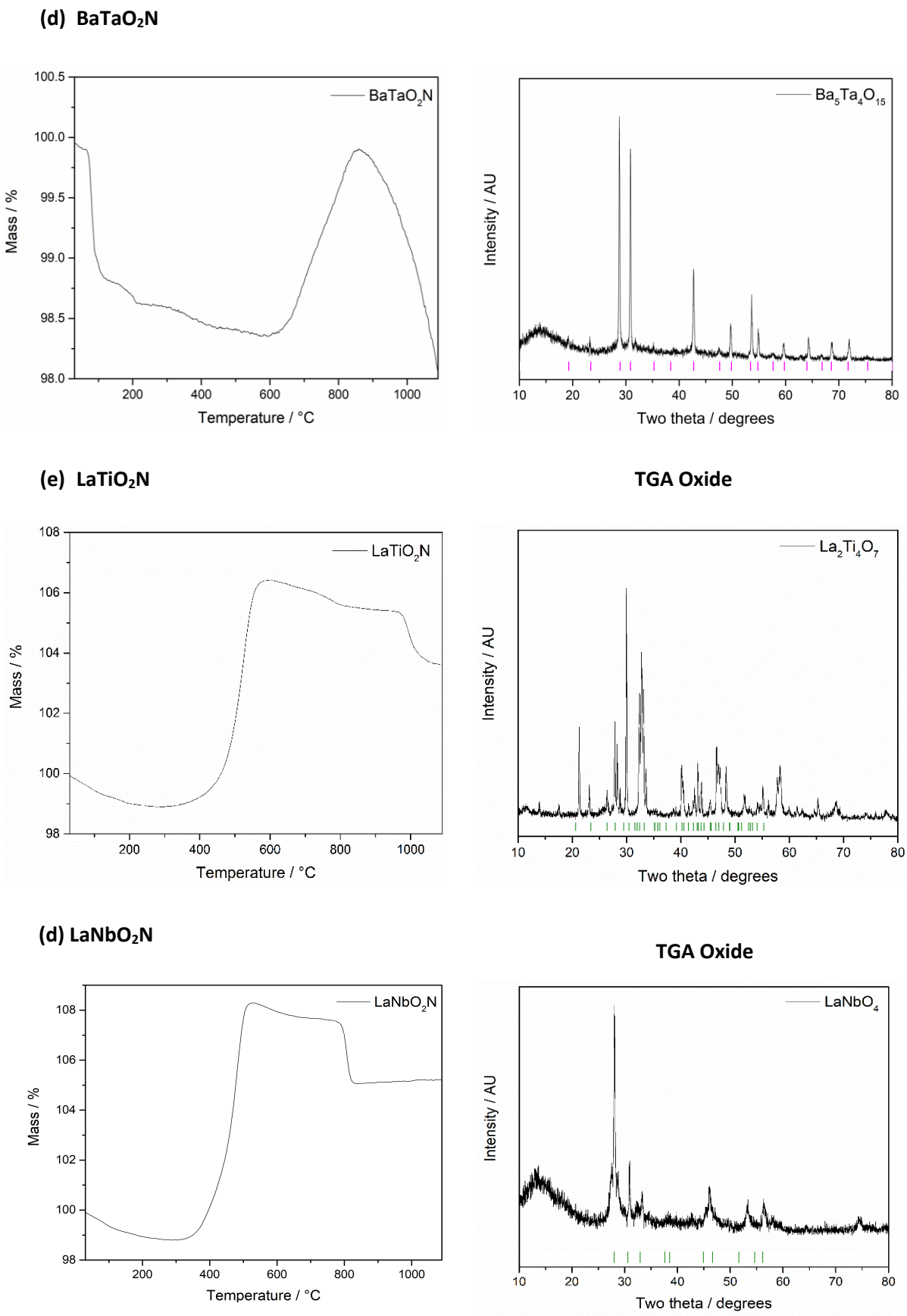

Figure 54. (Left) Thermogravimetric analysis profiles of the different perovskite oxynitrides and (right) XRD patters of the re-oxidation products. Ticks under the XRD patterns indicate reported peak positions for the oxides

Chapter 4 Synthesis and Characterization of Perovskite Oxynitrides as Thin Films

4.1 Introduction

Photocatalysts supported as thin films offer a wide range of benefits compared to those found as powders. The use of suspended powdered catalysts in the medium that contains the target pollutant for degradation can lead to agglomerations that decrease the available surface area, which may result in lower photocatalytic efficiencies. In addition, a major drawback on particulate systems is the expensive filtration technique needed for the optimal separation of the powdered photocatalysts suspension from the treated water for subsequent recycling of the active photocatalysts. This disadvantage would increase the economic demand of the purification process. Alternatively, photocatalysts immobilized as thin films deal with such problems, eliminating the need of separation of particles in suspension and enabling the contaminated water to be treated continuously. In this context, little research has been conducted on the synthesis of tantalum, niobium and titanium perovskite oxynitrides as thin films. In this Chapter, four thin-film deposition methods (pulsed laser deposition (PLD), reactive sputtering, spin coating and dip coating) are reviewed. Also, we establish a route for the deposition of thin films for seven perovskite oxynitrides, $CaTaO_2N$, $SrTaO_2N$, $BaTaO_2N$, $LaTaON_2$, $EuTaO_2N$, $SrNbO_2N$ and $LaNbON_2$, on alumina substrates using dip-coating of a polymer gel to form an amorphous oxide precursor film, followed by ammonolysis.

4.1.1 Pulsed Laser Deposition (PLD)

Pulsed Laser Deposition (PLD) is a physical vapor deposition technique consisting of two major components, an external laser source and a stainless-steel vacuum chamber, which can be positioned direct facing the output laser pulse or at different angles. Inside the chamber, a rotating target, containing the precursor materials and a substrate holder are aligned but separated by 5 cm. The process starts when the incident focusing laser beam hits the target, increasing its temperature resulting in the vaporization of the material. The growth of an ideal thin-film can be affected by particulates and molten globules, which tend to be avoided by controlling different parameters such as vacuum level, laser type, laser repetition rate and laser fluence. Additionally, the thickness of the growth thin-films can be also monitored by adjusting the number of laser pulses on the rotating target, volatising more material which ends up deposited onto the substrate.[228]

The Figure 55 illustrates the Pulsed Laser Deposition (PLD) system set-up and its different parts.

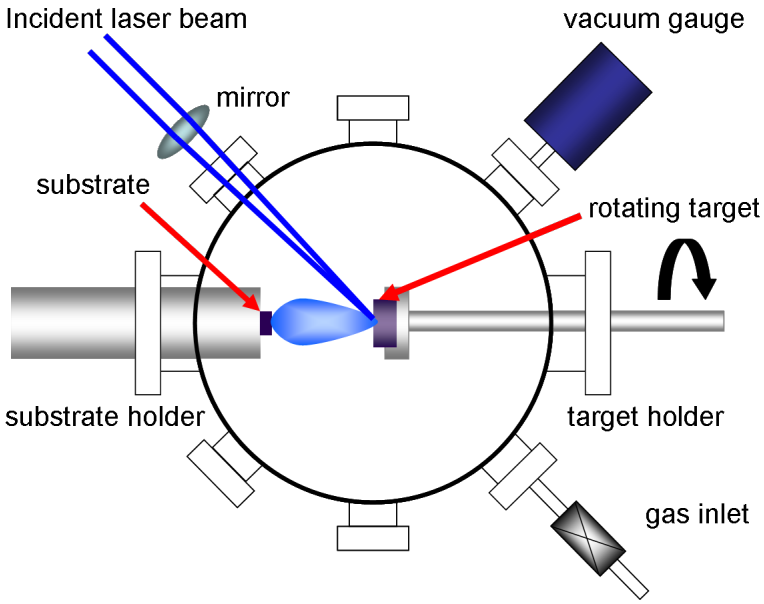

Figure 55. Pulsed Laser Deposition (PLD) system set up. Adapted from [228].

Oka et al. published a study on the possible ferroelectricity of $SrTaO_2N$ epitaxial thin films. The thin films were grown on STO single-crystal substrates, using nitrogen plasma-assisted pulsed laser deposition and a KrF excimer laser (248 nm). A $Sr_2Ta_2O_7$ ceramic pellet prepared by conventional solid-state reaction of Ta_2O_5 and $SrCO_3$ was used as a target. The substrate heated in the temperature range from 500 to 800˚C while the growth rate was controlled by the laser repetition rate (0.2-20 mHz) and pulse energy (4/20 mJ). The $SrTaO_2N$ thin films were successfully synthesised by PLD and ferroelectric behaviour was observed from the piezoresponse force microscope (PFM) measurements.[229]

Kim et al. reported the epitaxial thin-film deposition of the perovskite oxynitride $BaTaO_2N$ and its dielectric properties. The thin-film was deposited on a conducting $SrRuO_3$ buffer layer deposited on a $SrTiO_3$ single-crystal substrate heated to 760˚C. For this, polycrystalline $BaTaO_2N$ powder was prepared *via* solid state by heating a mixture of $BaCO_3$ and Ta_2O_5 at 1000˚C under flowing ammonia and used the target (obtained by hot-isostatic pressing of the powder). For the deposition, a KrF excimer laser (248 nm) was used and a laser repetition rate of 5 mHz. The $BaTaO_2N$ thin-films were successfully synthesised and characterized and exhibited dielectric permittivities.[230]

To the best of my knowledge, perovskite oxynitrides for photocatalytic applications have not been synthesised using PLD. This can be attributed to its relative high cost and the difficulty to scale -up the fabrication of thin films for industrial uses.

4.1.2 Reactive Sputtering Deposition (RSD)

In Reactive Sputtering Deposition (RSD), thin-films of the desired materials are deposited on substrates by sputtering from metallic targets in the presence of a reactive gas usually mixed with an inert working gas (argon). First, the neutral gas is ionized by an external power supply, producing plasma. Then, the target (cathode) is bombarded in a high vacuum by the plasma ions which eject the atoms by momentum transfer from the target. In a final step, the atoms are deposited on the substrate to be coated, resulting in the formation of a thin film.[231]

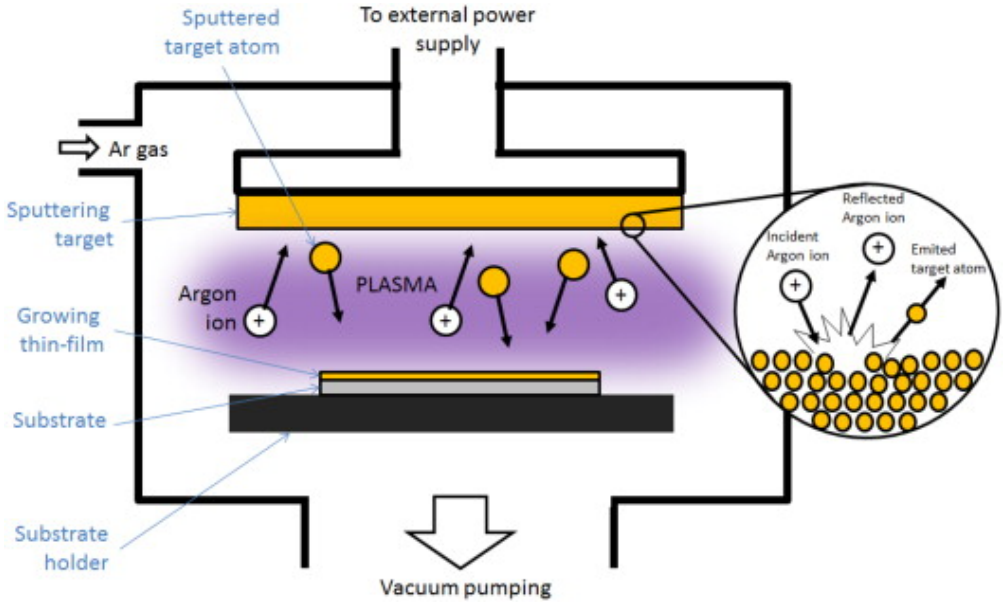

Figure 56. Schematics of the sputtering process. Adapted from [231].

Cohen et al. reported the preparation of oxynitride thin-films of $BaNb(O_yN)_x$ and $BaNb(O_yN_2)_x$ using reactive sputtering from multiphase powder targets. For this, a multiphase target containing Ba_3N_2 and NbN or LaN and NbN were prepared from commercially available powders instead of using a single-phase oxynitride target, due to the difficulty associated with sintering (formation of oxide impurities, cracks *etc)*. Silicon single-crystal wafers were used as substrates. Crystalline $BaNbO_{1.65}N_{1.24}$ was synthesised under a sputtering gas of 70% N_2 + 30% O_2 and showed a crystalline structure with a lattice parameter slightly larger than the reported for the bulk $BaNbO_2N$. However, $LaNbO_{0.29}N_{2.48}$ was amorphous. Both films showed low electronic conductivity.[232]

Photocatalytic active TiO_2 thin-films have been successfully synthesised using the reactive sputtering deposition method, however, complex materials as ternary oxynitrides showed nonstoichiometric in the O:N, indicating the difficulty entrained in the formation process.[232,233] Therefore, taking into the account the high-cost of the technique and the difficulty in scale-up, we will not use the reactive sputtering deposition method for the synthesis of our perovskite oxynitride thin-films.

4.1.3 Spin coating

Spin coatings is a technique widely used to deposit uniform thin films onto a substrate using the centrifugal force of rotation. A small amount of the coating solution is placed at the middle of the rotating substrate, then, the substrate is rotated up to 10,000 rpm to spread the coating solution along the substrate by means of the centrifugal force. In a final stage, the volatile solvent evaporates resulting in the formation of the thin films. The thickness of the coating can be controlled by the viscosity and concentration of the coating solution, as well as higher angular speed of spinning led to thinner thin films.[234]

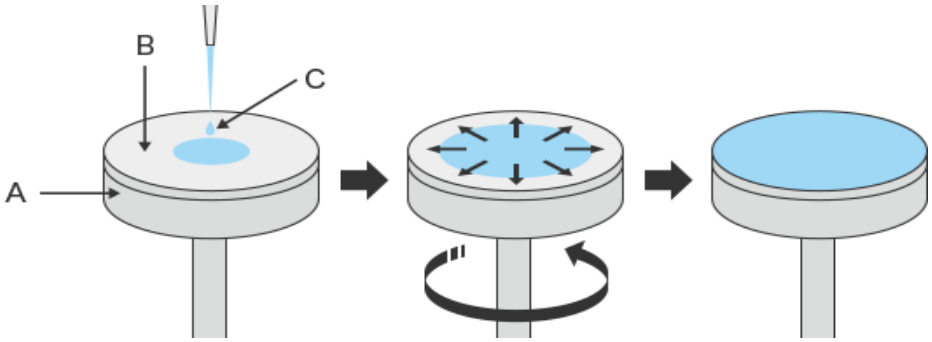

Figure 57. Schematics of the spin-coating process. A: rotating stage, B: target surface and C: coating fluid. Adapted from.[234]

Aguiar et al. reported the synthesis of $Sr_{(1-x)}La_xTi(O,N)_3$ thin-films by spin coating. Thin-films were spin-coated by dropping a small amount of a polymeric precursor containing the metal cations produced by the Pechini Method onto a $SrTiO_3$ (STO) substrate. The viscosity of the solution was tuned to 5 $mm^2\ s^{-1}$ by adding/evaporating water and the rotation speed and spin time were set to 6000 rpm and 30 s, respectively. The obtained thin films were dried as 120˚C for 2 h and calcined at 400˚C for two more hours. Afterwards, the oxide precursor thin-films containing were ammonolysed at 950˚C for 3 h (low rate of 25 mL min^{-1}) in a tube furnace resulting in $Sr_{(1-x)}La_xTi(O,N)_3$ (x= 0, 0.25, 0.5, 0.75 and 1) thin films.[235]

4.1.4 Dip-coating

Dip-coating is an industrial coating technique used to fabricate thin-films based on dipping a substrate into a coating solution (described in detail in Chapter 2). To the best of my knowledge, perovskite oxynitrides have not been synthesised as thin films for photocatalytic applications using the dip-coating method. This technique offers a number of advantages which are summarised and compared with the other three thin film deposition methods in Table 20. The advantages include the use of simple equipment (low cost), reproducibility and uniformity of the obtained thin films, control of the thin films thickness and possibility of scaling-up. For these reasons and to fill the gap in the literature, dip-coating was the chosen technique for deposition of the thin films in this work.

Table 20. Advantages and disadvantages of the four different thin-fil deposition methods reported for perovskite oxynitride thin-film deposition.

Thin-film deposition method	Advantages	Disadvantages
Pulsed Laser Deposition (PLD)	• New technique • Simple and fast	• Formation of particulates on the thin films • High cost • Difficult to scale-up
Reactive Sputtering Deposition	• Uniformity • Low substrate temperatures	• High cost • Target contamination • Difficult to scale-up
Spin Coating	• Simple equipment and low-cost • High consistency of the deposited thin films • Reproducibility and uniformity	• Difficult to scale-up • Size of the substrate • Considerable waste
Dip Coating	• Simple equipment and low-cost • Reproducibility and uniformity • Allows for scale-up • Thin-film thickness control • Highly efficient (minimal waste)	• Traditionally high volume of liquid required

4.2 Experimental

4.2.1 Synthesis of Perovskite Oxynitride Thin Films

The perovskite oxynitrides $CaTaO_2N$, $SrTaO_2N$, $BaTaO_2N$, $LaTaON_2$, $EuTaO_2N$, $SrNbO_2N$, and $LaNbON_2$ were selected based on prior observation, with powder samples, of visible light-activated photocatalysis. For the thin film formation, the gels prepared by the Pechini Method containing the metal cation precursors were used. A gel of appropriate viscosity was formed by re-adding 30 wt % methanol to the original resin and sonicating on an ultrasound bath for 180 s to ensure homogeneity. A layer of the gel was deposited onto a 25 × 25 × 1 mm^3 alumina tile (Almath) using dip-coating, with a 1 mm s^{-1} immersion and withdrawal speed, and an immersion time of 30 s. The dip-coating solution was 5 mL of the gel dropped onto 20 mL of tetradecafluorohexane (Sigma-Aldrich, 95%). This innovative approach was developed by Ceratti et al. so that a superficial layer of the dip-coating gel will float on the more dense but inert fluoroalkane allows dip-coating with the minimum quantity of gel.[203] The tetradecafluorohexane can be decanted and reused. The gel-coated substrates were heated in air for 1 h at 350°C, 1 h at 650°C, and finally 2 h at 800°C. At each stage, the heating rate was 10°C min^{-1}. The heating cycle converted the gel to a metal oxide thin film, which was then nitrided by placing the coated substrate on a semi-circular carbon block inside a 25 mm diameter-fused silica tube in a tube furnace, under a flow of ammonia gas (anhydrous, BOC). Reactions were carried out for 15 h and 17 h for $BaTaO_2N$ at temperatures between 850 and 1000°C based on the previous reaction temperatures optimized in Chapter 3 for the powders, with a heating rate of 3°C min^{-1} and an ammonia flow rate of 250 mL min^{-1} (100 mL min^{-1} for $BaTaO_2N$). The samples were cooled down to room temperature under an ammonia atmosphere.

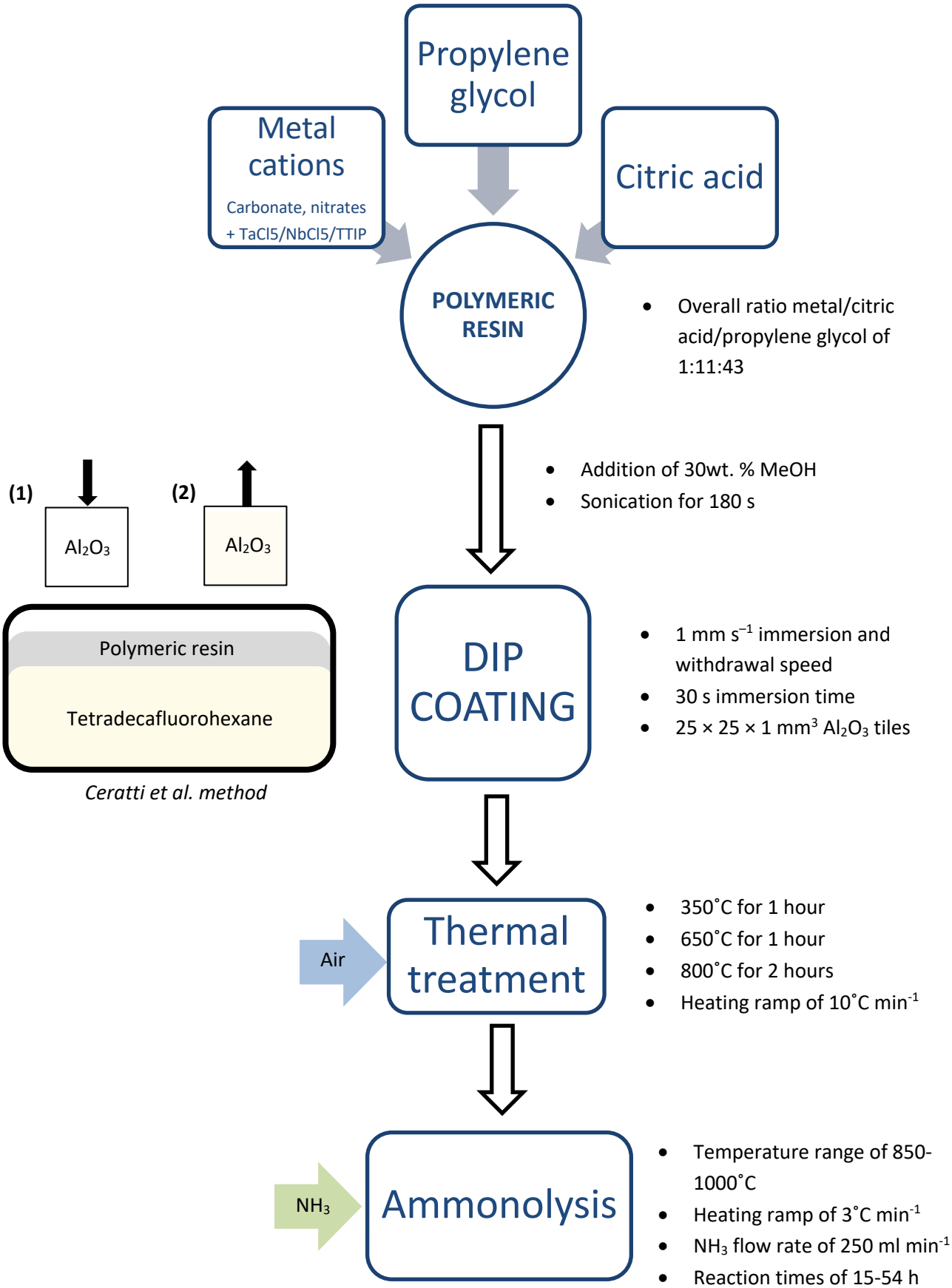

Figure 58. Scheme of the synthetic procedure of the perovskite oxynitrides thin films.

4.3 Results and Discussion

The perovskite oxynitrides $CaTaO_2N$, $SrTaO_2N$, $BaTaO_2N$, $LaTaON_2$, $EuTaO_2N$, $SrNbO_2N$, and $LaNbON_2$ were synthesized by ammonolysis of oxide precursor thin films, deposited onto alumina tiles. Opaque alumina substrates were chosen since they do not react with the oxynitrides at the high temperatures required during ammonolysis. The oxide precursor films were deposited using dip- coating from a resin prepared using the polymerizable complex method. In this approach, known as the citrate gel method (or Pechini Method), the desired cations are chelated with citric acid, and then a polymer is formed through condensation with glycol, thus providing an even distribution of the cations, which can be maintained after dip-coating and calcination of the gel film. [236] The formation of the polymeric resin avoids the segregating of cations that could occur from deposition from solution due to inhomogeneous crystallization rates.

For the thin film dip-coating optimization, different withdrawal speeds were explored. In a first stage, 5 mL of the original gel synthesised in Chapter 3 were deposited into a beaker containing a solution of the heavy fluorinated alkane tetradecafluorohexane, reducing the amount of gel required for dip-coating, and thus, increasing the atom efficiency of the process. Secondly, the alumina substrate was dip-coated into the solution using a high withdrawal speed of 10 mm s^{-1}, obtaining a thick-looking thin film which was thermally treated under air (1h at 350˚C, 1h at 650˚C and 2h at 800˚C) to remove the organic network. After the annealing, thin films were not formed, instead, a powdery deposition was observed. This was probably caused by the high withdrawal speeds and concentration (viscosity) of our original gel solution. A second attempt was made using the same gel but at a lower withdrawal speed of 1 mm s^{-1}. In this case, the thin film was considerably thinner-looking, however, after the annealing, a powder deposition was observed again.

To next step was to reduce the concentration of the original resins, and therefore the thickness of the films. This was achieved by adding a 30% wt. methanol to the resin and sonicating for 180 s to ensure homogeneity. The new gel solution was used to dip-coat the alumina tiles at a speed of 1 mm s^{-1} and an immersion time of 30 s. After the annealing in air, transparent thin films were formed in all cases and could only be observed visually on the substrate with difficulty. The oxide precursor thin films were amorphous as demonstrated by XRD.

Each oxide film was converted to the perovskite oxynitride through high-temperature ammonolysis with a 15-17 h reaction time. Ammonolysis conversion of calcined citrate gels has been successfully demonstrated in the literature for the synthesis of all the target perovskite oxynitrides, although only as powders and not as thin films, at temperatures of 850–1000°C.[149,191,201,206]

The ammonolysis temperatures used for our thin films were adapted from the conditions previously reported and optimized during the synthesis of the oxynitrides as powders in Chapter 3. These were found to be 850°C for $SrTaO_2N$ and $SrNbO_2N$; 950°C for $LaNbON_2$, $EuTaO_2N$, and $LaTaON_2$; and 1000°C for $BaTaO_2N$ and $CaTaO_2N$. After ammonolysis, all seven films were found to be strongly coloured, ranging from straw yellow for $CaTaO_2N$ to red for $BaTaO_2N$ as observed in Figure 59.

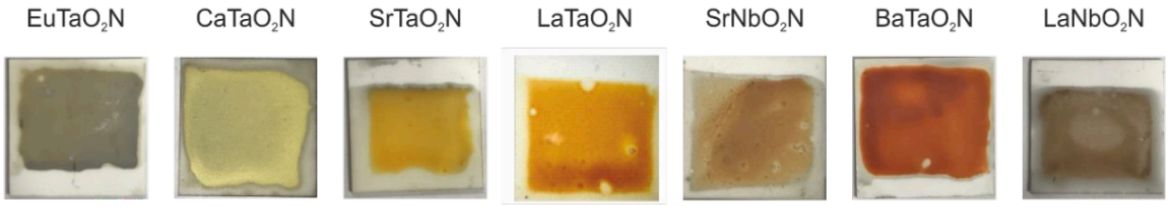

Figure 59. Photography of the synthesised perovskite oxynitride thin films over alumina tiles.

These oxynitride films were subsequently analysed by GI-XRD and UV–Vis spectroscopy. In each diffraction pattern, peaks are observed which can be assigned to either the crystalline alumina phase of the substrate or matched to database patterns of the expected perovskite oxynitride, as shown in Figure 60.

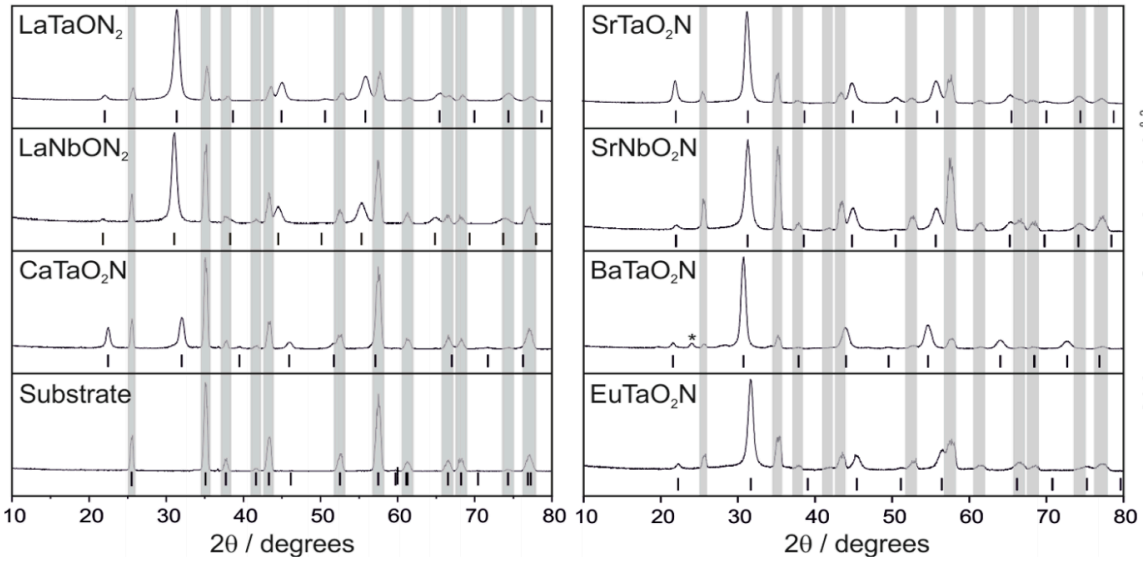

Figure 60. X-ray diffraction patterns of the perovskite oxynitrides thin films deposited onto alumina substrates. Grey bands indicate the position of the peaks corresponding to the alumina substrate; tick marks correspond to the positions of the peaks expected for each of the perovskite phases. Asterisk (*) indicates the impurity phase found in the $BaTaO_2N$ thin film.

Le Bail refinement was used to model the diffraction patterns and obtain the lattice parameters and particle size information for each oxynitride. However, full Rietveld refinement could not be attempted due to the limited number of peaks present in each pattern and the effect of the grazing incident geometry on the relative peak intensity.

First of all, the alumina peaks from the substrate were modelled using the $R\bar{3}c$ space group with a = 5.141 Å and α = 55.54° (grey bars, Figure 60). Then, the perovskite oxynitrides were modelled according to their previously reported crystal structures. The oxynitride $BaTaO_2N$ has been reported to crystallize in the ideal cubic structure, with the $Pm\bar{3}m$ symmetry[149]. Tetrahedral $SrNbO_2N$, $SrTaO_2N$ and $EuTaO_2N$ have been reported to adopt a $I4/mcm$ symmetry.[122,123,149] Finally, orthorhombic $CaTaO_2N$, $LaNbO_2N$ and $LaTaON_2$ have been found to adopt the distorted structure of *Imma* ($LaTaON_2$)[180] or *Pnma* ($CaTaO_2N$, $LaNbO_2N$).[122,227] These small distortions arise from the tilting of the BO_6 in order to accommodate the smaller than ideal ion size in the 12-coordinate sites. In this context, single crystal or high-resolution powder diffraction samples with good crystallinity are required for the different crystal structures to be fully distinguished. Additionally, as mentioned in Chapter 3, N^{3-} anions are not distinguishable from O^{2-} using conventional XRD since both anions have similar scattering factors as both have the same electron density, thus, anion ordering was ignored. As can be seen in Figure 60, peak broadening prevents confirmation of the peak splitting that would identify the different symmetries. Thus, during the refinement, we assumed that the structures adopted by the perovskite thin films were identical to those previously identified in literature.

Using these assumptions, the Le Bail refinement allowed us to model the lattice parameters and particle size broadening for the oxynitride phase of each of the thin films and these are summarised in Table 21. For each sample, the modelled data matched the corresponding perovskite oxynitride Bragg peaks. The weighted R-factor (*wR)* is based upon all data and values were found in the range of 7–12%. The obtained high values are typically indicative of a poor fit, however, this was attributed to the poor fit to the alumina substrate peak, which is made up of very large (2-5 microns) and heterogeneous alumina particles, resulting in a poor fit due to the lack of powder averaging. R_F^2 values corresponding to the perovskite phase only were found in the range of 1.8 - 4.07%, indicative of a good fit between the model and the data (R_F^2 < 5 %).

Table 21. Rietveld refinement results of the perovskite thin films on alumina.

Sample	**Space Groups**	**Lattice parameters (Å)**			**wR (%)** (whole pattern)	**RF²(%)** perovskite phase only	**Volume per formula unit (Å³)**	**Particle size (nm)**
$EuTaO_2N$	*I4/mcm*	5.640(3)	-	7.986(3)	6.90	3.46	63.52(6)	71
$CaTaO_2N$	*Pnma*	5.567(4)	7.885(4)	5.588(4)	10.57	2.27	61.32(9)	119
$SrTaO_2N$	*I4/mcm*	5.691(1)	-	8.035(5)	9.71	2.07	65.05(4)	106
$LaTaON_2$	*Imma*	5.72(2)	8.035(3)	5.721(1)	7.77	1.8	65.75(4)	53
$SrNbO_2N$	*I4/mcm*	5.707(1)	-	8.069(1)	10.31%	3.49%	65.71(3)	27
$BaTaO_2N$	$Pm\bar{3}m$	4.1808(4)	-	-	11.38%	4.07%	69.33(2)	796

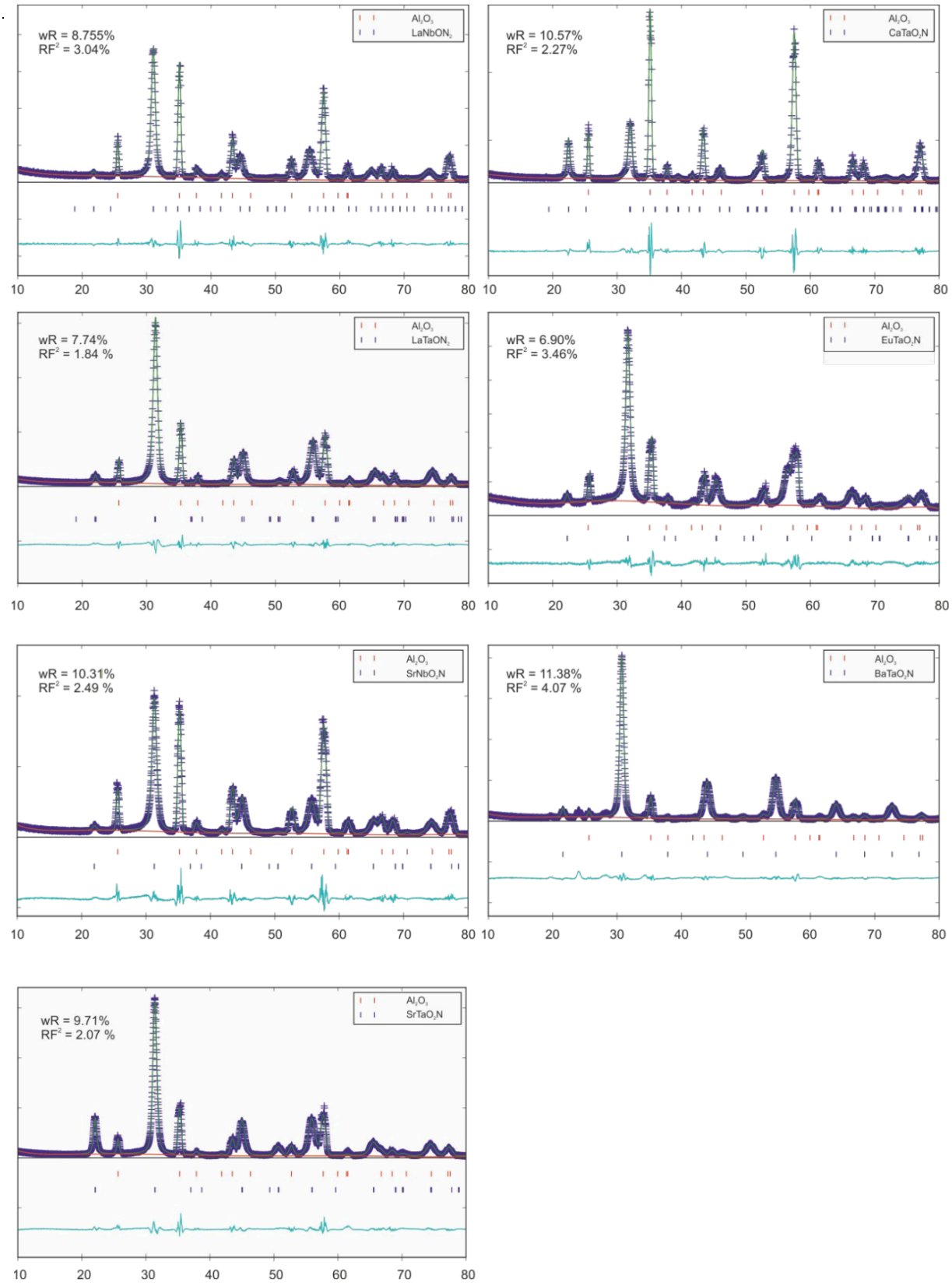

Figure 61. Rietveld refinement of the X-ray diffraction data of the perovskite thin films. The *wR* values are for the whole pattern fit, the RF^2 values are for the phase fit to the oxynitride peaks.

The particle size values determined from the peak broadening produced particles size range of ~30–120 nm with the exception being $BaTaO_2N$ where a much larger particles size of 800 nm were observed. Similar values were found for the powder samples in Chapter 3. In Figure 62, a comparison is made between the cell volume per formula unit for each sample and the volumes previously reported in the literature. For most of the samples, there is a good match between our observed cell volumes and the literature values, with a difference of less than 0.6%, indicative of successful phase formation. The exception is $EuTaO_2N$ where we observe a smaller than expected unit cell of 2.4% by volume. The difference between the experimental cell volume and the reported one was also observed for the powder sample in Chapter 3. $EuTaO_2N$ is a relatively new and underexplored material, with the literature example cited in Figure 60 based on a fully reduced Eu(II) ion. One explanation for the smaller unit cell observed in our film would be due to increased nitridation towards $EuTaON_2$ with some oxidation of the europium to the smaller Eu(III) ion. Overall, analysis of the diffraction data suggests that films of the desired perovskite oxynitride have been formed in all cases.

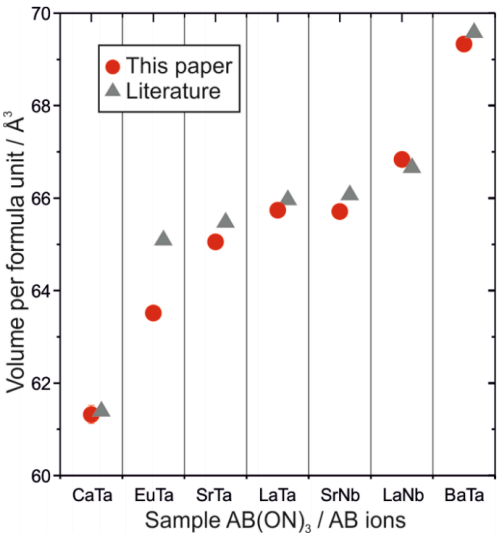

Figure 62. Plot of the volume per formula unit for each of the perovskite phases, red circles labelled *AB*, based on the formula *AB*$(ON)_3$, and comparison to previously published literature values, grey triangles.

4.3.1 UV-Visible Diffuse Reflectance Spectroscopy

The thin films were also analysed using diffuse reflectance spectroscopy, with spectra were recorded on the films in the wavelength range of 400–900 nm. The diffuse reflectance spectra showed absorption of the visible light region as expected for coloured samples. The diffuse reflectance data was converted to absorption spectra using the Kubelka-Munk function as

described in Chapter 2 and 3, then, the absorption coefficient was replaced in the David and Mott equation.

Tauc plots were built by plotting $(\alpha(R)h\nu)^{1/n}$ on the ordinate *versus* the photon energy ($h\nu$) on the abscissa to determine the band gaps and these are illustrated in Figure 64. Based on prior literature, it was assumed that the band gaps were indirect (n= ½).[176]

The following figure compilates the diffuse reflectance spectra for the perovskite oxynitride thin films synthesised in this chapter:

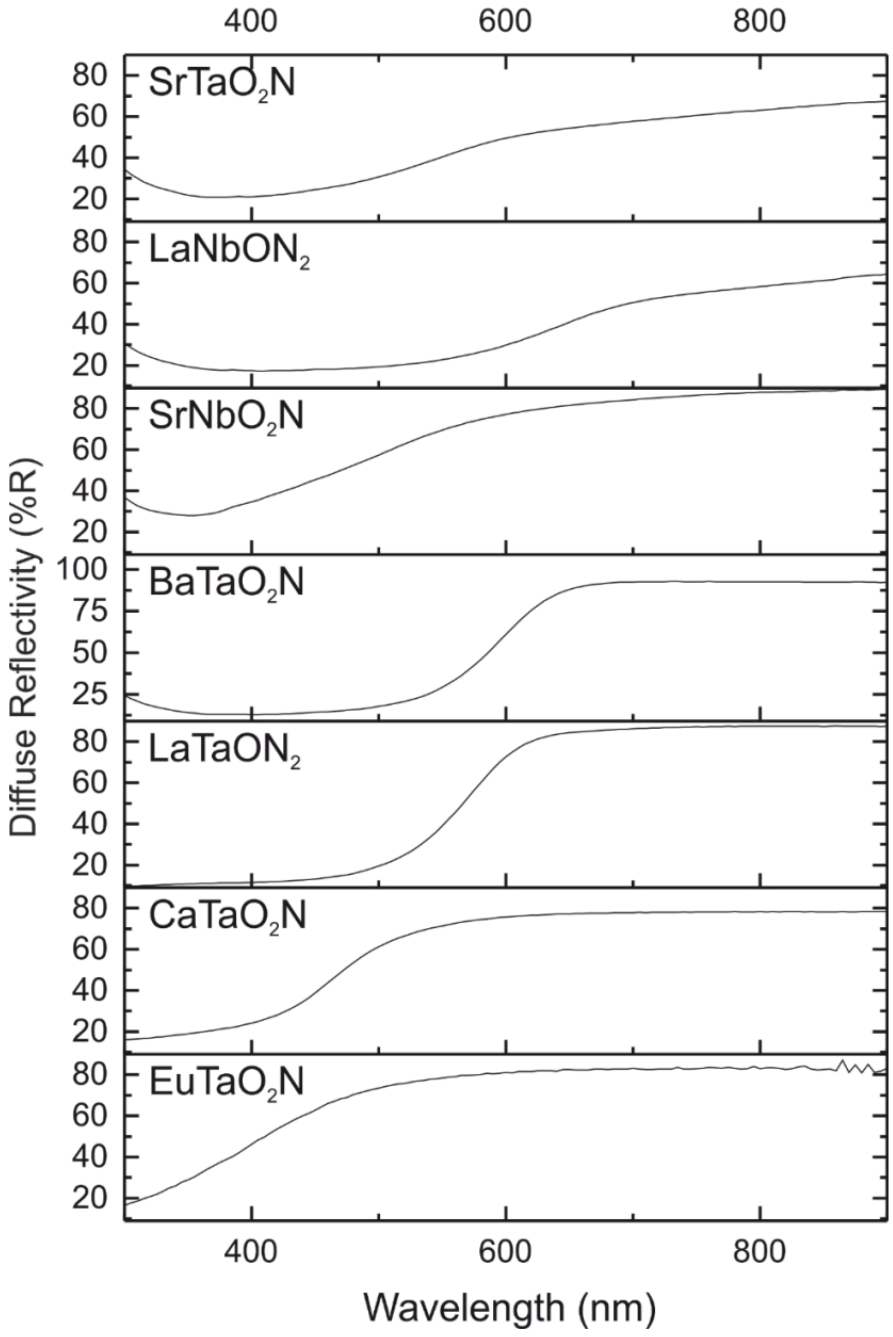

Figure 63. Diffuse reflectance spectra recorded on the perovskite thin films on alumina substrates.

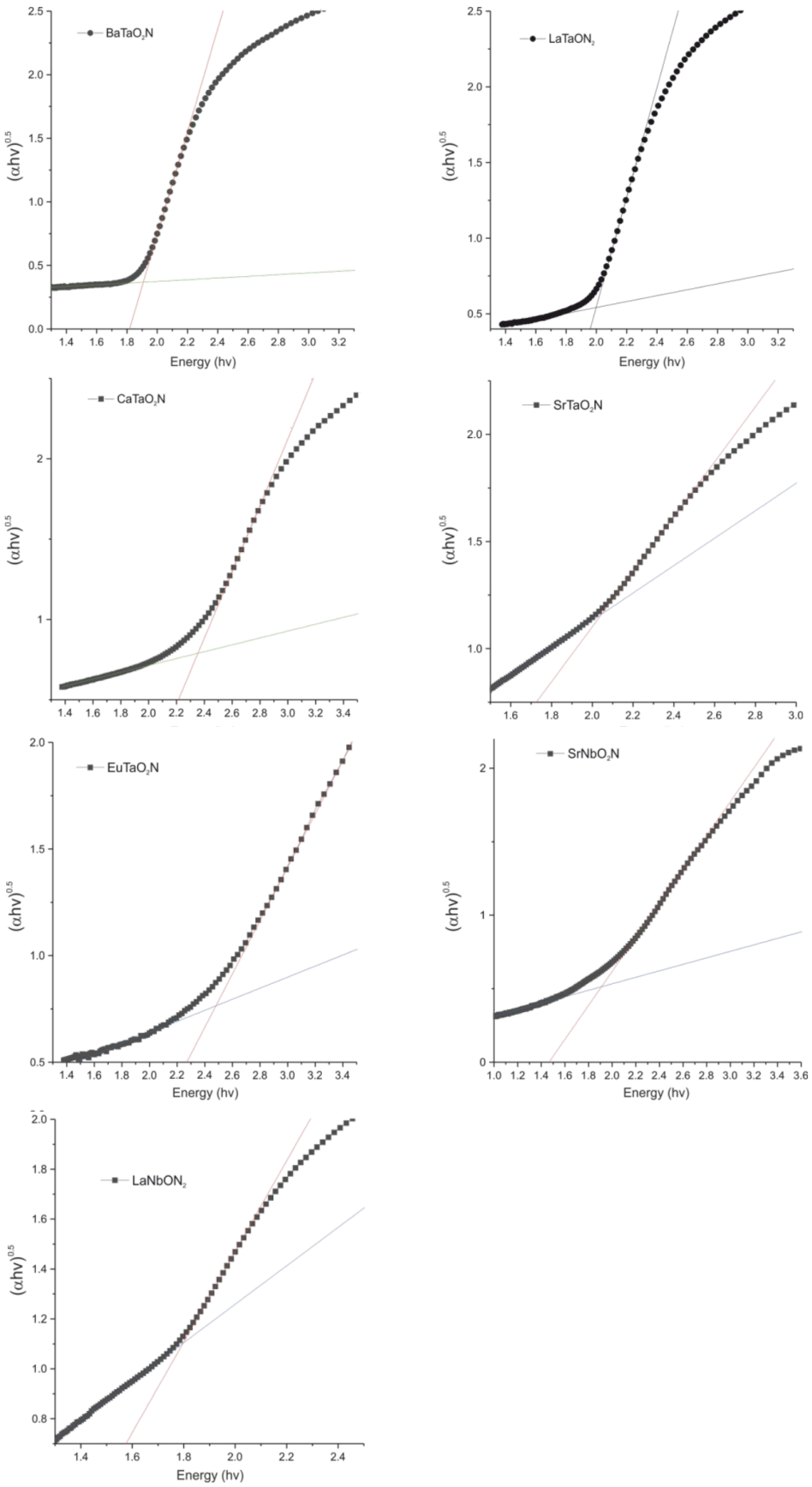

Figure 64. Tauc plots derived from the diffuse reflectance spectra recorded on the perovskite thin films on alumina.

The characterization results, including the bang gaps are summarised in the Table 22.

Table 22. Results of characterization for the perovskite oxynitride films deposited onto alumina.

Sample	Space Groups	Band gap (eV)	Colour	Volume per formula unit (Å^3)	Particle size (nm)
$EuTaO_2N$	*I4/mcm*	2.45(5)	Grey	63.52(6)	71
$CaTaO_2N$	*Pnma*	2.35(5)	Yellow	61.32(9)	119
$SrTaO_2N$	*I4/mcm*	2.05(5)	Orange	65.05(4)	106
$LaTaON_2$	*Imma*	2.00(5)	Orange	65.75(4)	53
$SrNbO_2N$	*I4/mcm*	1.91(5)	Orange	65.71(3)	27
$BaTaO_2N$	*Pm$\bar{3}$m*	1.90(5)	Red	69.33(2)	796
$LaNbON_2$	*Pnma*	1.80(5)	Red-brown	66.83(2)	99

As observed in Figure 65, the obtained band gap values are in agreement with the values previously reported in the literature for the same oxynitrides, except for the $EuTaO_2N$, which band gap value was not found in the literature. Thus, the obtained results confirm the X-ray diffraction analysis and supports our synthetic efforts in obtaining the target oxynitride phases.

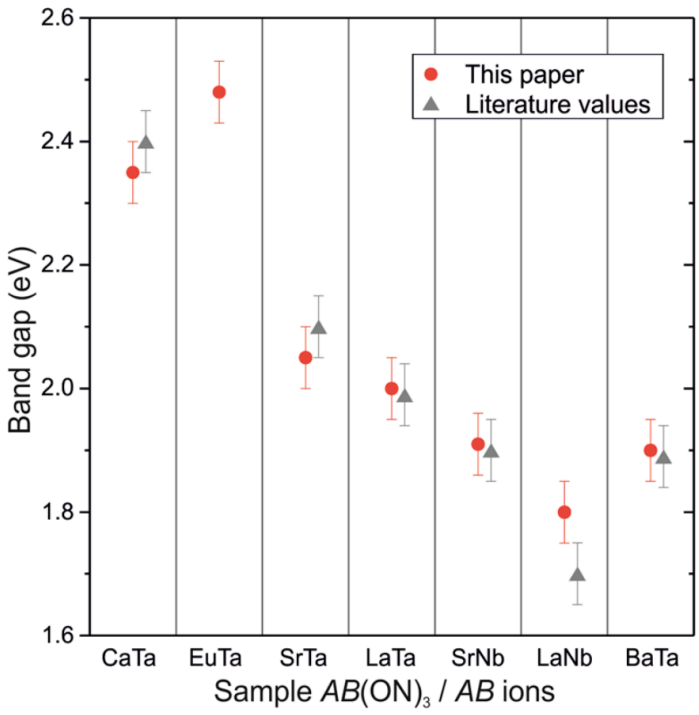

Figure 65. Calculated band gaps for each sample and comparison to previously reported band gaps.

4.3.2 Scanning Electron Microscopy and Elemental Analysis

Investigations on morphological and structural properties of the thin film samples were performed by using scanning electron microscopy with energy dispersive analysis by X-rays (SEM/EDX). To investigate thickness, cross-section SEM micrographs were taken. As observed in Figure 66, the thin films showed a micro-porous or island-like structure. This structure consists of a collection of individual 2-10 µm microplates with variable thickness (200 nm -700 nm) over the alumina substrate. A reason for the formation of the microplates instead of uniform thin films is the stress induced during the combustion/removal of the organic matrix, which led to extensive shrinkage during the pyrolysis. As a general trend, higher amounts of citric acid and propylene glycol increase the probabilities of film-cracking during the thermal process.

Related to the nano-structural details of the thin films, Figure 66 shows different SEM images with different magnifications taken from the $SrNbO_2N$ thin film. The light grey microplates correspond to the oxynitride $SrNbO_2N$ and consists of a porous network of 30-70 nm size grains showing a spherical shape while the dark-grey background corresponds to the alumina substrate.

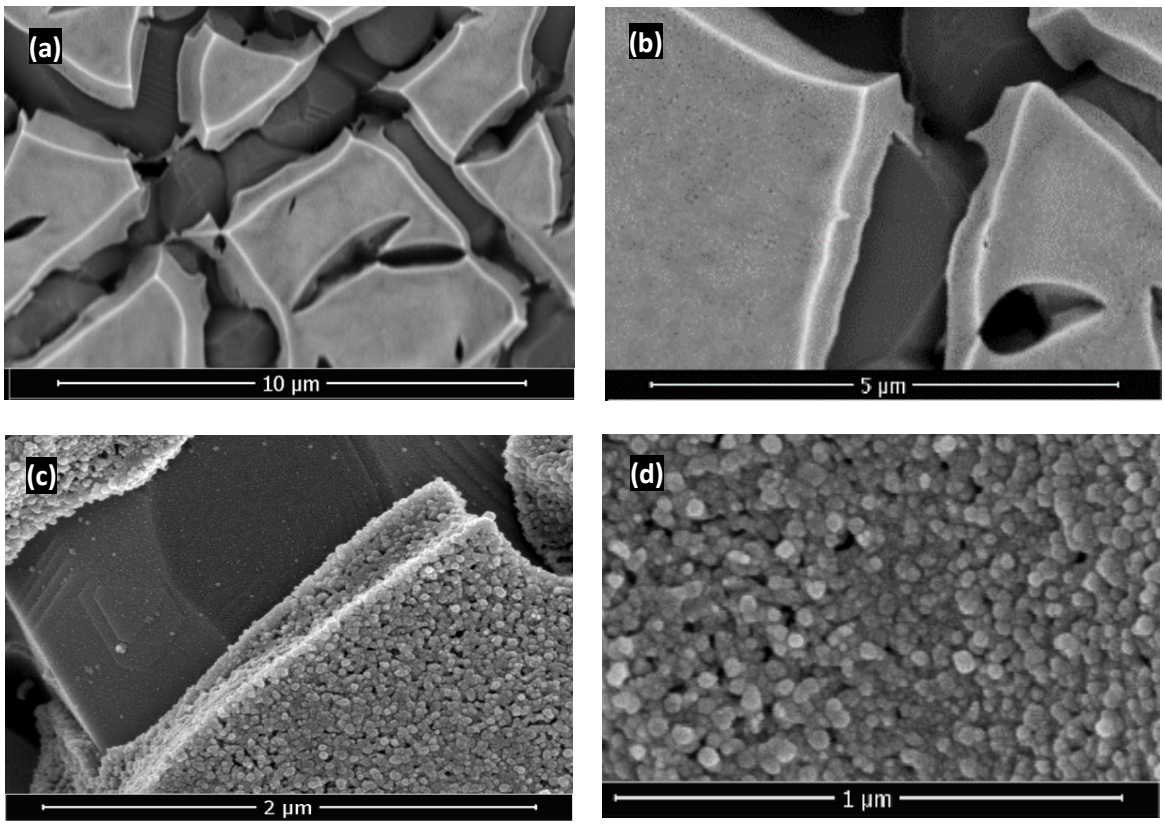

Figure 66. SEM micrographs of the $SrNbO_2N$ thin film at different resolutions. **a-b** showing the micro-porosity of the channel structure and **c-d** the nano-grains shaping the microplates.

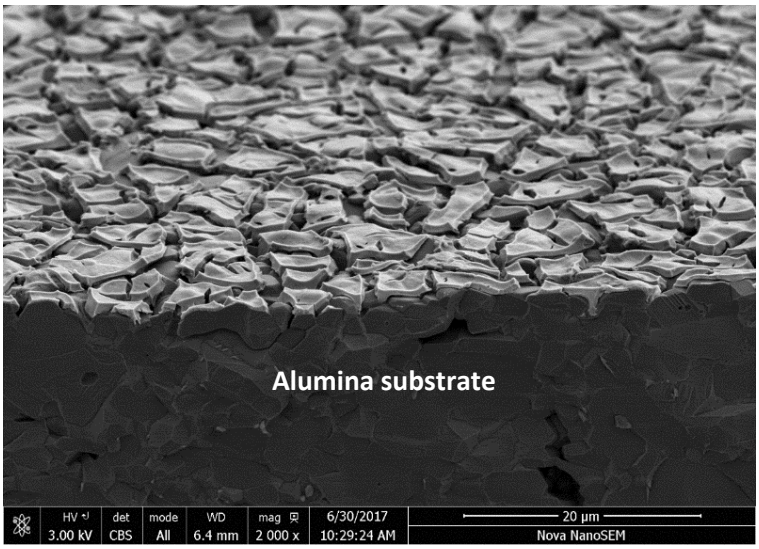

Figure 67. SEM image of the $SrNbO_2N$ thin film showing the channel structure.

The quantitative composition of the $SrNbO_2N$ microplates was analysed and confirmed by cross-sectional elemental analysis. The elemental mapping images indicate that the constituent alumina elements, Al and O are uniformly placed forming the support while the Sr and Nb elements from the oxynitride are mostly located on the substrate surface forming the microplates (Figure 68c-d). On the other hand, the intensity of the O in from the oxynitride in Figure 68d is relatively weak but still noticeable.

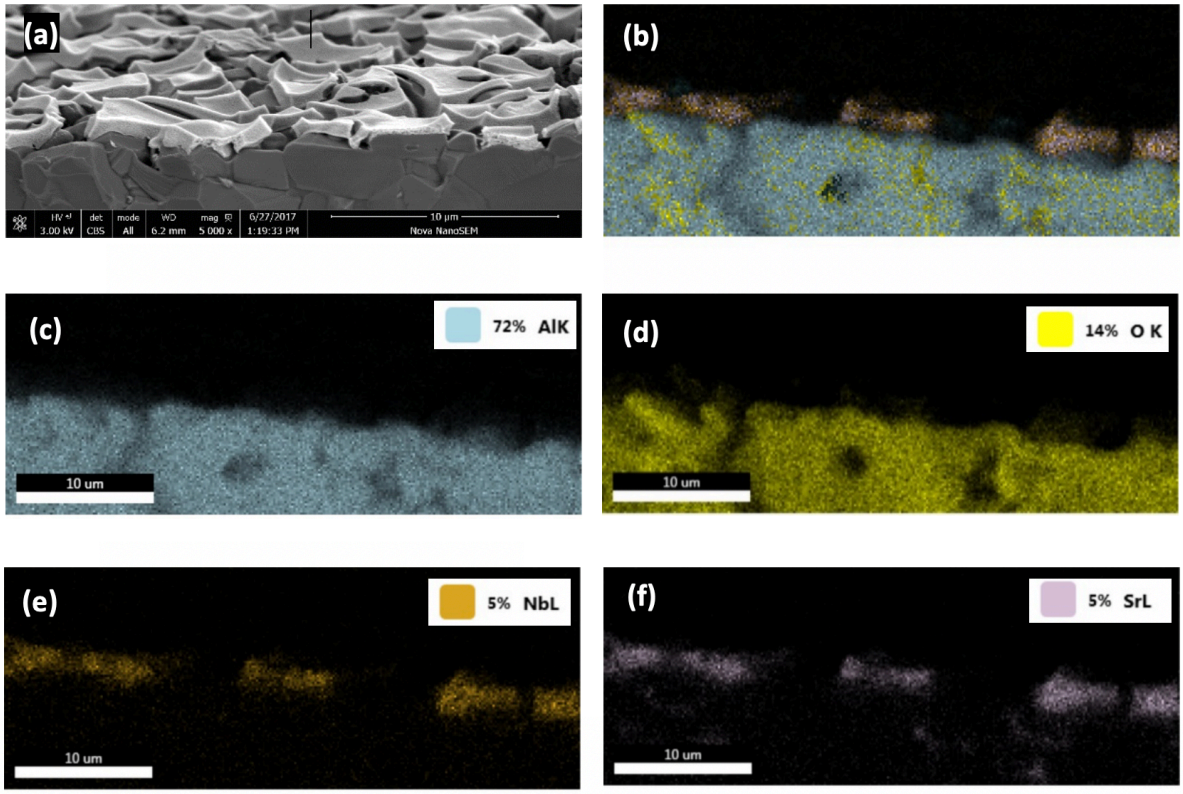

Figure 68. Cross-sectional analysis map of $SrNbO_2N$ showing the relative distribution of Al, O, Nb and Sr elements.

Chapter 5 Photocatalytic Activity of Perovskite Oxynitride Thin Films

5.1 Introduction

Perovskite oxynitrides have been reported as effective photocatalysts for the production of hydrogen from water (water splitting) using visible light.[50,168] More recent reports have shown that perovskite oxynitrides can also photocatalytically degrade dye molecules under visible light irradiation, indicating their potential for water purification applications.[179] In this Chapter, we explore the opportunity of using the $CaTaO_2N$, $SrTaO_2N$, $BaTaO_2N$, $LaTaON_2$, $EuTaO_2N$, $SrNbO_2N$, and $LaNbON_2$ perovskite oxynitrides synthesised in Chapter 4 as thin films for visible light-activated self-cleaning applications.

In the recent years we have seen a widespread commercialization of titanium dioxide films in "self-cleaning" windows where the photocatalyst coating, activated by UV light, photomineralises organic species into water and carbon dioxide and any heteroatoms into water-soluble mineral acids.[55,237] As mentioned in Chapter 1, the mineralization proceeds with absorption of light to form electron–hole pairs that can generate superoxide or hydroxide radicals, both Reactive Oxygen Species (ROS), by reaction with surface bound atmospheric oxygen and water. Evidence was provided by quenching experiments which showed that photocatalytic activity is reduced in the presence of a hole and superoxide scavangers.[238,239] Photocatalytically active titania films can be used for air purification by the removal of VOCs.[240] Additionally, the self-cleaning reaction has also demonstrated antibacterial activity against *E. Coli* by decomposition of the bacterial cell membrane.[214,241]

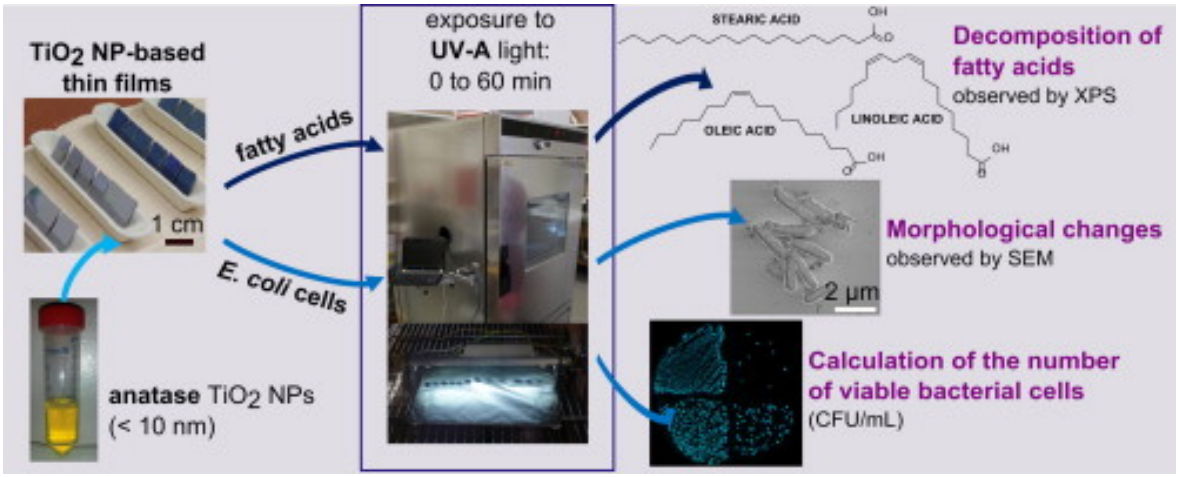

Figure 69. Graphical abstract of the photocatalytic antibacterial and self-cleaning activity of nano-TiO_2-based thin films. Reproduced from ref.[242]

In this context, photocatalyst coatings showing self-cleaning and antibacterial activities under visible light available in enclosed and indoors environments would have a significant commercial value. The key requirement for a visible light-activated photocatalyst is a bandgap smaller than 3 eV so that visible light photons get absorbed but still sufficiently large to retain band edge energies with the necessary oxidizing and reducing power to generate the reactive oxygen species required for self-cleaning.[243]

Dyes are often used for evaluating the photocatalytic properties of photoactive materials, including self-cleaning abilities or as a proxy for contaminated water sources. During dye testing, the photocatalyst is submerged in a solution of the dye and exposed to a light source. The degradation of the dye can be indirectly monitored by measuring the change in the absorbance intensity versus time. Different dyes have been reported in the literature, including rhodamine B, methylene blue, methyl orange, resazurin and dichloroindophenol (DCIP). Among these dyes, methylene blue (MB) is the most commonly used and its degradation has been defined as an ISO standard test, however, a high re-oxidation rate has also been observed.[244,245] Other dyes such as resazurin and DCIP have also been investigated. For example, resarzurin showed the advantage of faster kinetics, while DCIP has a reduced sensitivity to re-oxidation. Generally, dye tests can provide a rapid and convenient method for assessing the photocatalytic ability of a material, but it should be noted that full mineralization of the dye molecule is not typically being observed and therefore it cannot be quantified using spectroscopy.[246] Instead, an initial reduction or oxidation, depending on the dye leads to conversion to a colourless form (Leuco-DCIP in DCIP degradation tests). Further, oxidation can occur for full mineralization, but this is not directly observed by the loss of colour in the solution. In this context, the DCIP degradation test provides rapid assessment of the photocatalytic activity of the thin films, but not a sufficient test for the evidence of self-cleaning behaviour. A more definitive test for thin films is the mineralization of stearic acid, described in section 5.3.3.[246,247]

In this chapter, we report an assessment on the photocatalytic ability of the $CaTaO_2N$, $SrTaO_2N$, $BaTaO_2N$, $LaTaON_2$, $EuTaO_2N$, $SrNbO_2N$, and $LaNbON_2$ thin films synthesised in Chapter 4 to degrade a solution containing DCIP dye. The most active samples are assessed using the stearic acid test, demonstrating full degradation of an organic contaminant under a visible light source.

5.2 Experimental

5.2.1 Photocatalytic Degradation of DCIP

The photocatalytic ability of each co-catalyst-loaded perovskite thin film was initially assessed through decolouration of a dye in the presence of a sacrificial oxidant, with a LS0104 150 W xenon lamp solar simulator as the light source, equipped with a 400 nm cut-off filter. The dye used was 2,6-dichloroindophenol (DCIP, Acros 98+%) and the sacrificial oxidant glycerol (Fisher, reagent grade).[248] The reaction was carried out in a double-jacketed glass vessel with water recirculation at 15°C to prevent heating of the test solution from the light source as shown in Figure 69. The thin-film samples were immersed in 12 mL of an aqueous solution of 5.5×10^{-5} mol dm^{-3} DCIP and 1.26×10^{-2} mol dm^{-3} glycerol and agitated by a magnetic stirrer. The radiation intensity of the solar simulator as measured at the position of the sample was 509 mW cm^{-2}. Dye concentration was monitored by extracting 3.5 mL of aliquots of solution and recording the visible light absorption over the range of 400–800 nm, using a PerkinElmer Lambda 25 spectrometer. Aliquots were then returned to the solution. Prior to starting the test, the immersed samples were kept in the dark until an equilibrium with dye adsorption had been reached, as determined by three-consecutive, constant absorption measurements. Once this was achieved, the solar simulator was switched on, and aliquots were withdrawn at 30 min intervals up to 180 min.

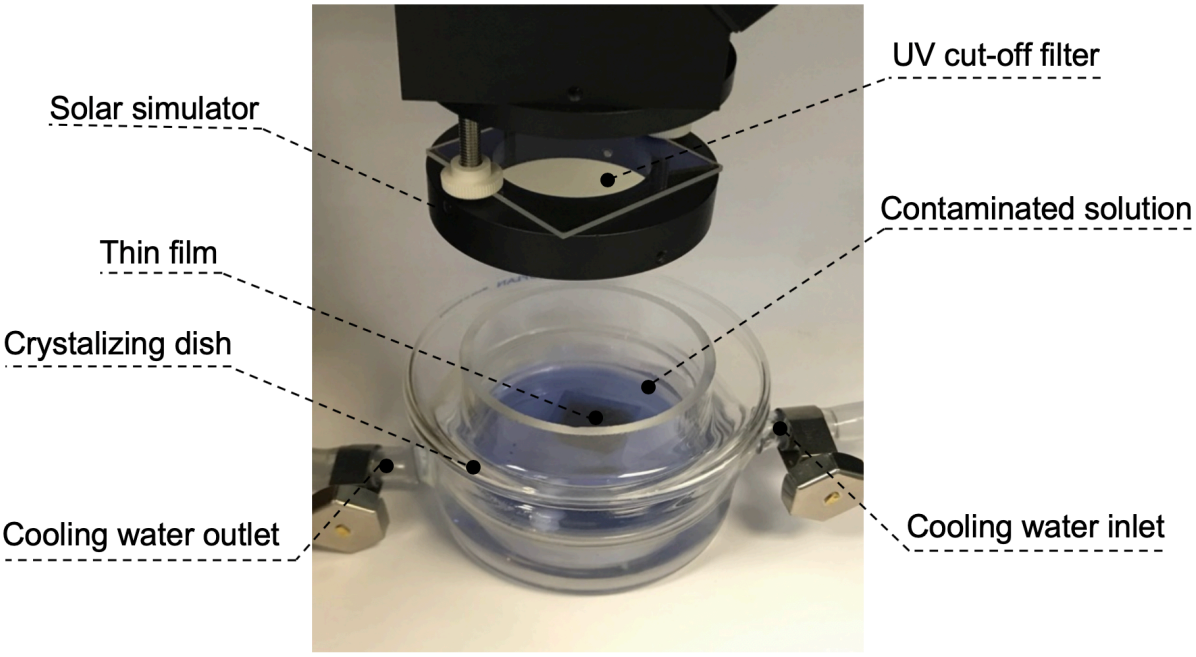

Figure 70. Illustration of the photocatalytic testing set-up.

5.2.1.1 Operational Parameters

- *Concentration of the dye:*

The solution containing the dye and glycerol was prepared as follow; 16 mg of 2,6-dichlorophenolindophenol sodium salt ($C_{12}H_6Cl_2NO_2Na$, 97%, Sigma-Aldrich) dissolved in 0.5 L of distilled water. Subsequently, a solution containing 1.16 g of glycerol (Sigma-Aldrich) in 0.5 L of distilled water was prepared. Both solutions were mixed in equal parts prior to the photocatalytic test. According with the Lambert-Beer Law, the molar absorption coefficient (ε), also called molar absorptivity, is calculated to be 1.52· 10^4 M^{-1} cm^{-1} at $\lambda = 603$ nm. This value was used to calculate the real concentration of the DCIP once the dark adsorption equilibrium of the dye was reached.

Lambert-Beer Law:

$$A = \varepsilon \cdot \ell \cdot [C]$$

Table 23. Absorbance details of a 5.5·10^{-5} M DCIP solution.

Absorbance at $\lambda = 603\ nm$ (A)	**Path length(ℓ)**	**DCIP concentration$[C]$**
0.8354	1 cm	5.5·10^{-5} M

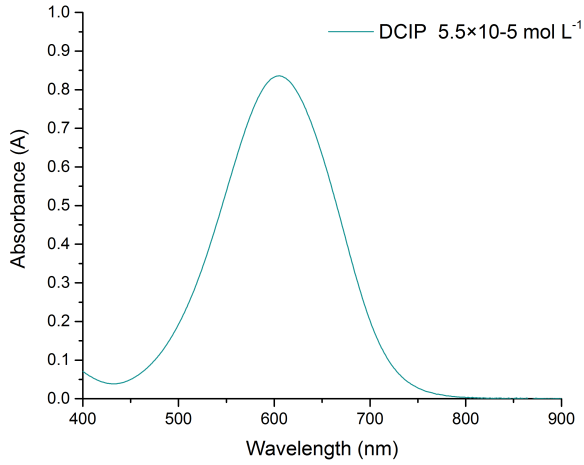

Figure 71. UV-Vis spectra of a 5.5·10^{-5} M DCIP solution.

- *Radiation intensity:*

Irradiance is defined as the amount of radiation received by a surface per unit area and expressed in terms of SI base units of watt per square metre (W/m^2). Experimental studies have shown a correlation between the light intensity and an increasing of the photocatalytic reaction rate, this may be due to the fact that a higher intensity would lead to higher electron-hole pair formation enhancing the photocatalytic efficiency. The radiation intensity (I) was measured by using a radiometer photometer (ILT1400 LOT-Quantum Design, USA) in the range of 250-750 nm, with a sensor with the peak intensity of 5090 W/m^2.

5.2.1.2 Data Interpretation

Photocatalytic decolouration of 2,6-dichlorophenolindophenol (DCIP) under visible light ($\lambda \geq$ 320 nm) was studied to evaluate the photocatalytic activity of the samples. The photo-bleaching efficiency (R, %) of DCIP dye could be calculated as follow;

$$R = \frac{C_o - C}{C_0} \times 100 = \frac{A_o - A}{A_0} \times 100$$

where, at a given wavelength, C_o is initial concentration at time (t) = 0 seconds, C is the value of the concentration (mg/L) after the reaction is finished, A_o corresponds to the initial absorbance at time (t) = 0 seconds and A to the value of absorbance measured after reaction.

Related to reaction on surfaces, many authors and studies showed that the kinetics of the photocatalytic bleaching of organic dyes (if taken to completion) usually proceeds *via* the Langmuir-Hinshelwood (L-H) model, [212,213]

$$r = k\frac{KC}{1 + KC}$$

where r (mg/L · min) represents the initial rate of photobleaching, C the concentration of the reactant, t is the reaction time, k the rate constant of the reaction and K is the adsorption coefficient of the dye in the oxynitride. (Equation 17). When the chemical concentration of the dye is C $\ll 1$, the L-H equation can be simplified and re-written in a form of first order rate law. Hence, the photocatalytic degradation of a DCIP solution on the thin film surface could by described by the formal first-order kinetic equation,

$$ln\frac{C_0}{C} = k_{\ app} \cdot t$$

where $k_{\ app}$ represents the apparent first order rate constant of the photocatalytic degradation and t is the irradiation time. A linear regression of the plot of ln(C_0/C) versus time (t) represents a straight line with a slope that corresponds with the apparent first order rate constant (k_{app}). Accordingly, the initial reaction rate (R_0) (M min^{-1}) is calculated as follow:

$$R_0 = K_{app} \cdot C_0$$

Formal Quantum Efficiency (FQE) is defined as the number of molecules of dye degraded per incident photon. The calculation of the FQE may be used to quantitatively present the photocatalytic activity on films since the values of photobleaching efficiency can be ambiguous to compare results to one another due to the different experimental conditions chosen by different research groups.

$$FQE = \frac{number\ of\ molecules\ degraded/cm^{-2}\ s^{-1})}{incident\ photon\ flux\ (photons\ cm^{-2}\ s^{-1})}$$

The number of molecules of DCIP degraded for a given time and area is estimated by taking the calculated initial rate (R_0) from the lineal regression of the 20-30 % degradation steps, which is consistent to the zero-order kinetics regime, and the corresponding reaction time and thin film surface area. Alternatively, the photon flux (ϕ) is given by the number of incident photons of a certain exposure surface area per unit of time.

$$\phi = \frac{\#\ Photons}{sec}\ \frac{1}{m^2}$$

In the first instance, the total intensity of the polychromatic lamp was fixed to 5090 W m^{-2}. by using a radiometer photometer This experimental value was used for the calculation of the intensity for each wavelength range according to the correspondent output.

Table 24. Xenon Compact Arc Lamp emission spectra. Each row indicates the output, intensity, photon energy and photon flux for the given wavelength range. The summation of all photon flux is the incident photo flux for the range of 250-700 nm.

Wavelength (nm)	Output (%)	Intensity (W m^{-2})	Photon Energy (J)	Photon Flux (Photons sec^{-1} m^{-2})
250-300	2.48	126.6	7.22E-19	1.75E+20
300-350	3.54	180.1	6.11E-19	2.94E+20
350-400	4.57	232.9	5.29E-19	4.39E+20
400-450	5.24	266.9	4.67E-19	5.71E+20
450-500	5.62	286.3	4.18E-19	6.84E+20
500-550	5.21	265.3	3.78E-19	7.01E+20
550-600	5.73	291.6	3.45E-19	8.44E+20
600-650	6.47	329.4	3.17E-19	1.03E+21
650-700	5.65	287.5	2.94E-19	9.77E+20

Additionally, photon energies are obtained by applying the photon energy formula ($E = hc/\lambda$) for each wavelength range average. Finally, the photon flux for a wavelength range corresponds to the quotient of the division of the intensity by the photon energy, being the incident photon flux the summation of all the calculated photon fluxes and with units of photons sec^{-1} m^{-2}. For this case, the incident photon flux is estimated to be 5.725×10^{21} photons sec^{-1} m^{-2}.

5.2.2 Photocatalytic Degradation of Stearic Acid

Photocatalytic testing for the most active samples was conducted using the stearic acid degradation test.[247] Our protocol required transparent samples, so the perovskite films were deposited onto alumina-coated quartz. The alumina coating on the silica acted as a barrier layer to prevent the silica from reacting with the alkali metals in the perovskite thin films, and it was deposited in-house using aerosol-assisted chemical vapor deposition (AACVD) using a previously reported method.[205] For this, 0.2 g of aluminium acetylacetonate (Sigma Aldrich, 99%) were dissolved in 20 mL of methanol and placed in a 50 mL three-necked round-bottom flask. A piezoelectric device was used to generate an aerosol mist of the aluminium precursor solution, which was subsequently transported into the AACVD reactor under a flow of argon gas (BOC, Pureshield).[249] The reactor temperature was set at 500°C and the gas flow to 1 L min^{-1}. After deposition, the alumina-coated silica was annealed in air at 1100°C for 10 h with a 3°C min^{-1} heating rate. The Figure 72 shows the AACVD reactor rig consisted of two stainless steel end supports (inlet and outlet) holding up an open-ended quartz tube. A laminar flow of the aerosol through the chamber was ensured by a brass baffle along with the top plate and the glass support.

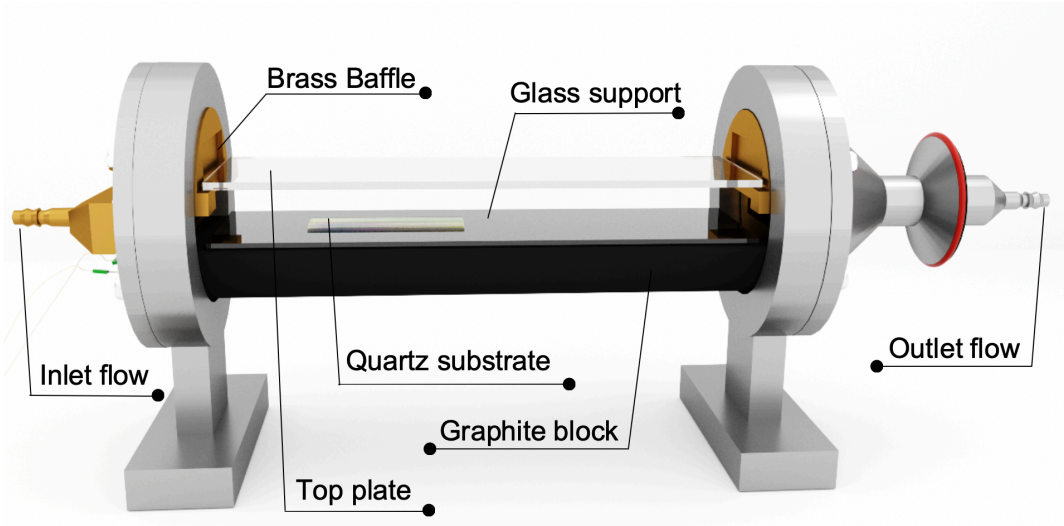

Figure 72. Aerosol-Assisted Chemical Vapour Deposition (AACVD) reactor scheme used for the Al_2O_3 coating of quartz substrates. The reactor does not show the outer sealing quartz tube.

Dip-coating was then used to deposit a thin layer of stearic acid (Fisher Scientific, 98%) onto the samples, from a 0.025 mol dm^{-3} solution of stearic acid in dichloromethane (an immersion time of 30 s, a 1 mm s^{-1} withdrawal speed). IR spectra were collected over the range of 3000–2800 cm^{-1} using a Perkin Elmer 100 FTIR spectrometer where 1 cm^{-1} of the integration of the C–H stretching bands is equivalent to 9.7×10^{15} molecules of stearic acid.[250] A baseline measurement was recorded

on the coated films, and then the samples were placed under the solar simulator described above and removed at regular intervals to recollect the IR spectra to monitor the degradation of the stearic acid layer, up to a total time of 120 min.

5.2.3 Co-catalyst loading

Cobalt oxide co-catalyst particles were deposited onto the thin films to enhance the photocatalytic rates, using a procedure modified from the literature.[206,251] The co-catalyst concentration was studied at nominal surface concentrations of 0.04–0.46 μg cm^{-2}. To load the surface of the film with cobalt oxide co-catalyst particles, a solution of 4.1 × 10^{-5} mol dm^{-3} $Co(NO_3)_2 \cdot 6H_2O$ in acetone was prepared, and aliquots containing the desired amount of cobalt (0.625, 0.25, 0.5, or 0.75 mL) were dropped onto the surface of the thin film. The acetone was allowed to evaporate in air, and then the samples were heated to 700 °C under a flow of 250 mL min^{-1} of ammonia gas for 60 min, leading to metallic Co-nanoparticles. The active CoO_x co-catalyst was obtained by mild oxidation in air at a temperature of 200 °C for 60 min.

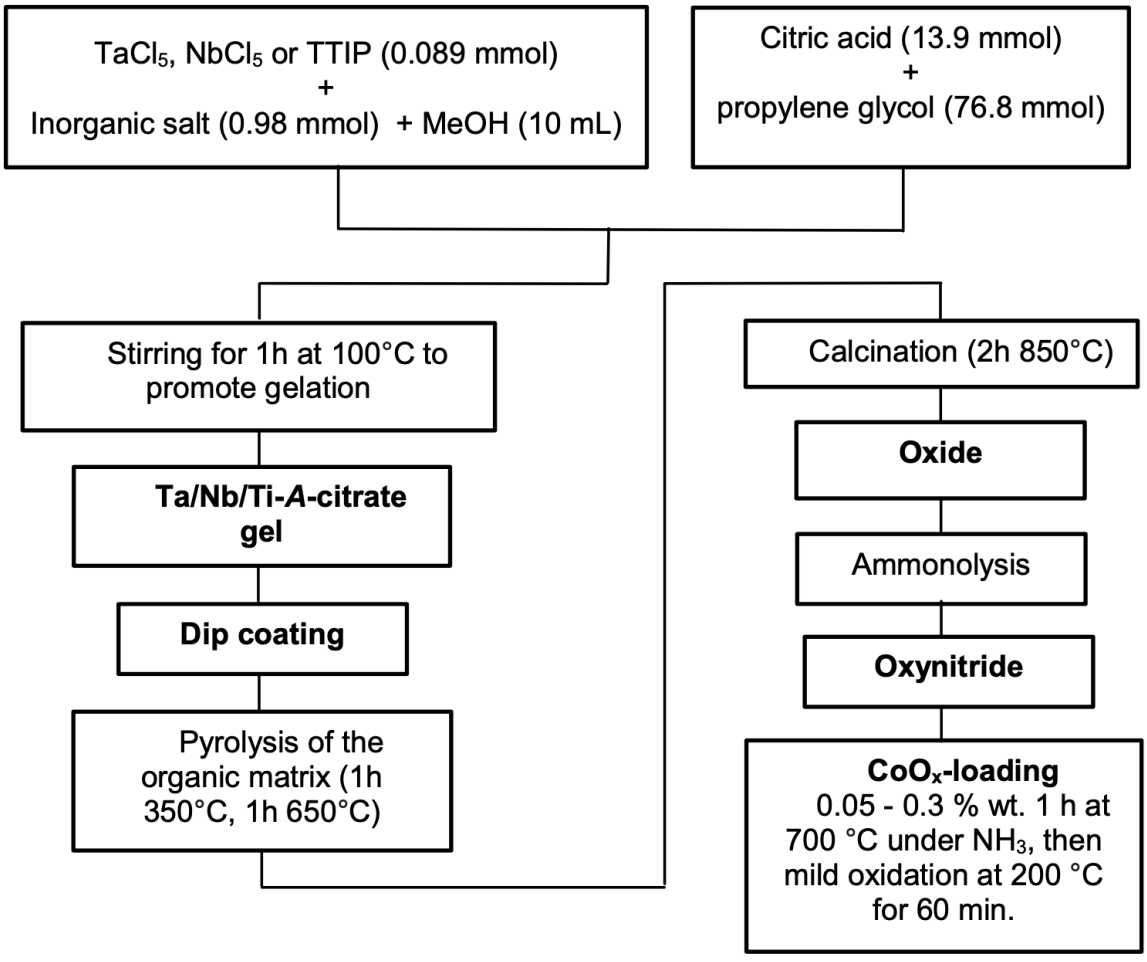

Figure 73. Flow diagram of the preparation of CoO_x-loaded perovskite thin films.

5.3 Results and Discussion

5.3.1 Co-catalyst (CoO_x) Deposition

To initially assess the photocatalytic ability of the perovskite thin films, the DCIP dye test was used,[248] alongside a cobalt oxide co-catalyst to enhance the rate of reaction.[206] Traditionally, CoO_x loading in oxynitride powders is carried out by an impregnation method from aqueous solutions containing the calculated amount of cobalt ions followed by solvent evaporation, heating in ammonia and subsequent mild oxidation of the cobalt nanoparticles. Nevertheless, for thin films, the CoO_x loading involves the deposition of a thin liquid film containing the Co ions on the surface of the alumina substrate and a subsequent heat treatment. Previous groups have reported 2 % wt. Co ions for powder samples. If we assume a 100 nm powder particle size for our oxynitrides, this equates to a particle surface loading of 0.26 μg cm^{-2}. Thus, the initial co-catalyst loading in our samples (cobalt surface density 0.30 μg cm^{-2}) is very similar.

In a first stage, during the CoO_x optimization of the thin films, the solvent chosen containing the cobalt ions was distilled water. However, during drying, an increase in concentration at the edges of the thin films due to evaporation was observed. This described phenomenon is attributed to the Marangoni effect and is the cause of the formation of the 'coffee-ring'. Consequently, in order to ensure a total homogeneity in the deposition of the cobalt it is important to take into the account this spatiotemporal variation in concentration distribution. As previously reported, higher vaporization rates lead to vigorous convective flows (Marangoni flow) inside the liquid thin films that avoid particles to be stuck in the vicinity of the edge of the substrate.[252] A change in the vaporization rate of the solvent by substitution of water by a solvent with a higher evaporation rate such as acetone resulted in a total uniform distribution of the cobalt particles along the substrate as we can observe in Figure 74. Thus, the Marangoni effect caused during evaporation process can be counteracted by changing the nature of solvent.

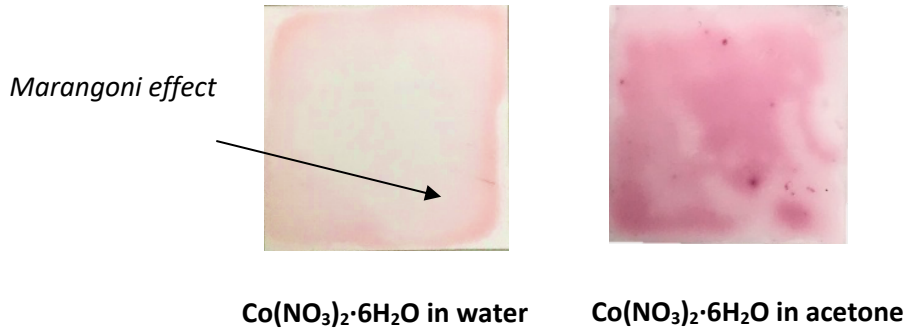

Figure 74. Effect of the nature of solvent minimising the Marangoni effect.

5.3.2 Degradation of DCIP under Visible-Light

The degradation of 2,6-dichlorphenolindophenol (DCIP) in aqueous solution in presence of glycerol acting as sacrificial electron donor (SED) was investigated to evaluate the photocatalytic activity of thin films and powders. In a first stage, and on basis of the results of previous reports showing the photocatalytic activity of CoO_x-loaded $SrNbO_2N$ samples to oxidise MB, a 2 % wt. CoO_x loaded $SrNbO_2N$ powder sample was tested in a vial containing 5 mL of the dye/glycerol solution, the oxynitride and a Teflon stirrer. The initial DCIP solution concentration was $5.5 \cdot 10^{-5}$ M and glycerol $1.26\ 10^{-2}$ M. The amount of tested photocatalyst was 200 mg L^{-1}. The total reaction time was set to 180 minutes. The final concentration of the reduced DCIP was calculated by measuring the absorbance of the sample at 603 nm and was $38 \cdot 10^{-5}$ M, thus a 25 % of DCIP degradation was achieved. This previous photocatalytic test on a CoO_x:$SrNbO_2N$ powder sample proved that the DCIP-based photocatalytic system is valid for assessing the photocatalytic activity of the samples since there is not literature reporting the photocatalytic degradation of DCIP by perovskite oxynitrides.

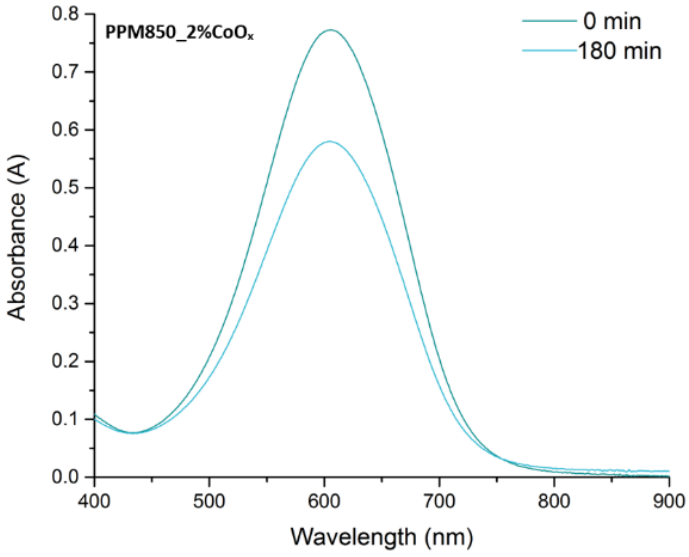

Figure 75. Degradation profile recorded on dye solution containing 200 mg of a 2% wt. CoO_x-loaded $SrNbO_2N$ powder after exposure to solar simulator for 180 minutes.

During thin-film testing, the films were submerged in a solution of DCIP and glycerol and irradiated with a solar simulator equipped with a 400 nm cut-off filter. DCIP is a blue dye that can undergo a two-electron transfer to a colourless form during photocatalysis with the glycerol acting as a sacrificial electron donor. This can be monitored using visible spectroscopy, assuming a Beer–Lambert law relationship between absorption and the concentration of the dye in its coloured, oxidized form. Plots of the concentration of the dye as a function of time during the testing of each oxynitride thin-film are showed in Figure 76.

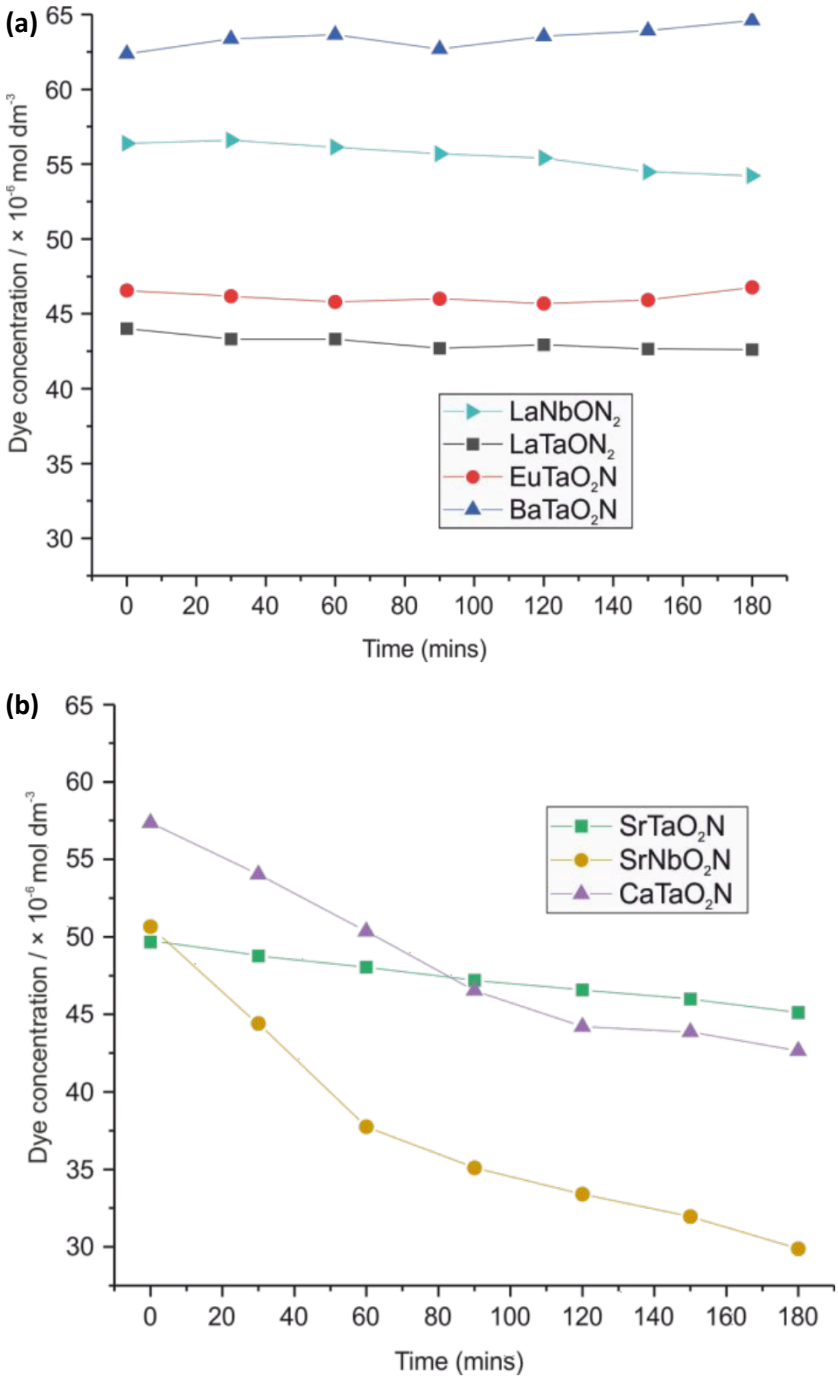

Figure 76. Plots of the DCIP dye concentration as a function of time during the photocatalytic testing of the CoO_x@perovskite thin films on alumina substrate. Dye degradation of CoO_x@perovskite@alumina. **(a)** Non-active samples $LaTaON_2$, $LaNbON_2$, $BaTaO_2N$ and $EuTaO_2N$ and **(b)** active samples $SrTaO_2N$, $CaTaO_2N$ and $SrNbO_2N$.

As observed in Figure 76a, the films of $EuTaO_2N$ and $BaTaO_2N$ showed no significant change in dye concentration over the 180 min test time and therefore seem to be photocatalytically inactive on this timeframe, under visible light irradiation. Small reductions in the DCIP

concentrations of 3-5% after 180 minutes were observed for the CoO_x-loaded films of $LaNbON_2$ and $LaTaON_2$. This percentage increased up to a 9% for the $SrTaO_2N$ sample. $CaTaO_2N$ and $SrNbO_2N$ showed the highest reduction in DCIP concentration of 26 and 46%, respectively. Thus, the CoO_x loaded $SrTaO_2N$, $CaTaO_2N$ and $SrNbO_2N$ thin films were the most active samples reported among all the tested oxynitrides. Previous reports stated that that the photocatalytic dye decolouration of DCIP fits well to the Langmuir-Hinshelwood model (pseudo-first order kinetics).[212] The kinetic parameters were estimated from the linear regression of the initial 33% degradation steps (90 minutes). A plot of $\ln(C_0/C)$ *vs* time leads to a linear diagram which slope equals the apparent first order constant. These are shown for the active samples in Figure 77 with the linear fits used to determine the first-order rate constants, which can be found in Table 25 for the three most active samples.

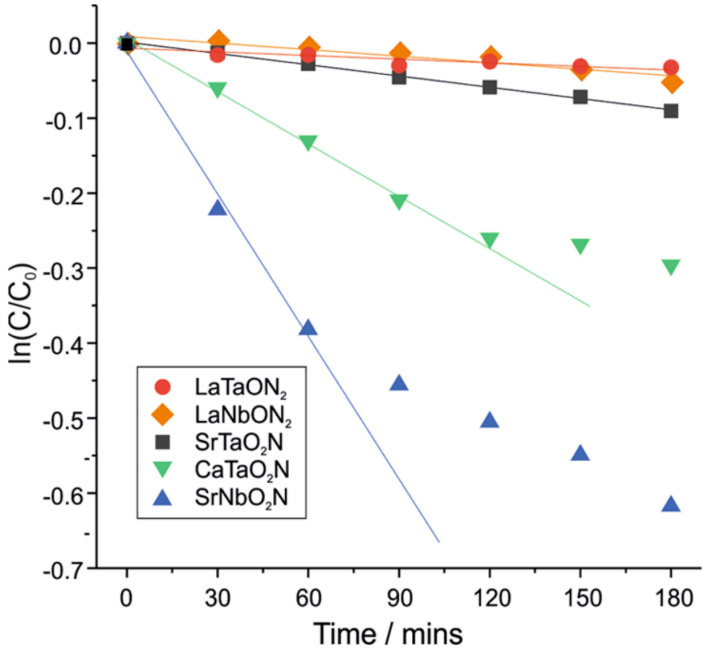

Figure 77. Plots of the ratio of the dye DCIP concentration to initial concentration as a function of time for the photocatalytically active perovskite oxynitride thin films deposited on alumina, with cobalt oxide co-catalyst at surface loading of 30 μg cm^{-2}. Tested using solar simulator with a UV cut-off filter.

Table 25. Summary first-order rate constants for the photocatalytic dye and stearic acid tests for the most active perovskite oxynitride thin films.

The oxynitrides $LaTaON_2$, $LaNbON_2$, and $SrTaO_2N$ showed relatively small first-order rate constants of $1.6(4) \times 10^{-4}$ min^{-1}, $2.3(5) \times 10^{-4}$ min^{-1}, and $5.0(1) \times 10^{-4}$ min^{-1}, respectively. The two most active samples $CaTaO_2N$ and $SrNbO_2N$ have much higher initial rate constants of $24.3(5) \times 10^{-4}$ min^{-1} and $64(5) \times 10^{-4}$ min^{-1}, respectively. However, after 90 minutes, the linear regression did not fit well and exhibited two different regimes showing different kinetics. A plausible reason for

this occurrence is that during the first regime, decolouration of the DCIP dye to the reduced colourless dye (Leuco-DCIP) is occurring and this step is monitored by quantifying the change in the measured absorbances. As reaction progresses, the reduced colourless DCIP can still photocatalytically degrade, reducing the effective rate of decolouration of the primary dye by reducing the number of available electron–hole pairs and occupying active surface sites, explaining the reduction in the rate for the two most active samples where the build-up of by-product leads to competition with the unreacted dye. The DCIP test is therefore a proxy rather than direct test for self-cleaning photocatalysis, but the initial first-order rates are indicative of the relative effectiveness of the samples.

A direct trend between the observed photocatalytic activities and band gaps, particle sizes, reaction temperature or structural properties was not observed. Our most active sample $SrNbO_2N$ has one of the smallest band gaps and crystallite sizes. Indeed, smaller crystallites sizes will result in larger surface areas while a small band gap increases light adsorption, however, it is not clear that these factors are determinative. Prior work reported by Inoue et al., highlighted the importance of controlling the of behaviour of photoexcited electrons and holes in order to achieve high photocatalytic efficiency. Thus, the presence of a local disorder or distortion is essential for an active photocatalyst, to generate a dipole necessary to aid in the separation of electron and holes.[253] This is consistent with our inactive sample $BaTaO_2N$, which does adopt the ideal $Pm\bar{3}m$ structure, whereas at least some activity is observed in the samples adopting distorted structures.

Oehler et al. reported the photocatalytic activity of 2 % wt. CoO_x-loaded niobium and tantalum oxynitrides powders using methyl orange as the test dye and found $SrNbO_2N$, followed by $CaTaO_2N$ to be the most active films, while $SrTaO_2N$ showed a lower photocatalytic acitivity.[176] However, our results vary from these results regarding some of the less active oxynitrides. In particular, Oehler et al. observed a 10% reduction in dye concentration after 3 h for methyl orange with $BaTaO_2N$, however, we did not observe any photocatalytic activity for the same material. On the other side, Oehler et al. found $LaTaON_2$ to be inactive, while our results with DCIP showed a small but still measurable photocatalytic activity after 3 hours. However, for the three most active oxynitrides, $SrNbO_2N$, $CaTaO_2N$, and $SrTaO_2N$ tests conducted with both methyl orange and DCIP dyes are in agreement.

Further DCIP tests were conducted to confirm the ideal CoO_x loading. For this, four $SrNbO_2N$ thin films (identical dip coating parameters), were loaded with 0.04, 0.15, 0.3, and 0.46 μg cm^{-2} of Co ions. No DCIP reduction could be observed upon irradiation of the unloaded $SrNbO_2N$ thin film with solely visible light, in fact, the dye concentration slightly increased with time. This corresponds to a real effect (but not significant) due to evaporation of a small fraction of solvent during the

course of the photocatalytic test, falling within the error of the measurements. As Figure 79 illustrates, loading with CoO_x particles strongly enhanced the photocatalytic activity of the $SrNbO_2N$ thin films, 0.30 μg cm^{-2} of Co ions the amount of co-catalyst showing the higher activity. Additionally, a systematic dependence of the measured photocatalytic activities and the amount of cobalt ions was observed. However, this trend was not followed when the thin film was loaded with a value higher that 0.3 % of Co ions. Further, samples of $CaTaO_2N$, and $SrTaO_2N$ were prepared with targeted co-catalyst loadings of 0.04, 0.15, 0.3, and 0.46 μg cm^{-2} to evaluate if the ideal CoO_x loading varied with the material. The initial first-order rate determined from these tests can be seen in Figure 79 for each sample as a function of co-catalyst loading.

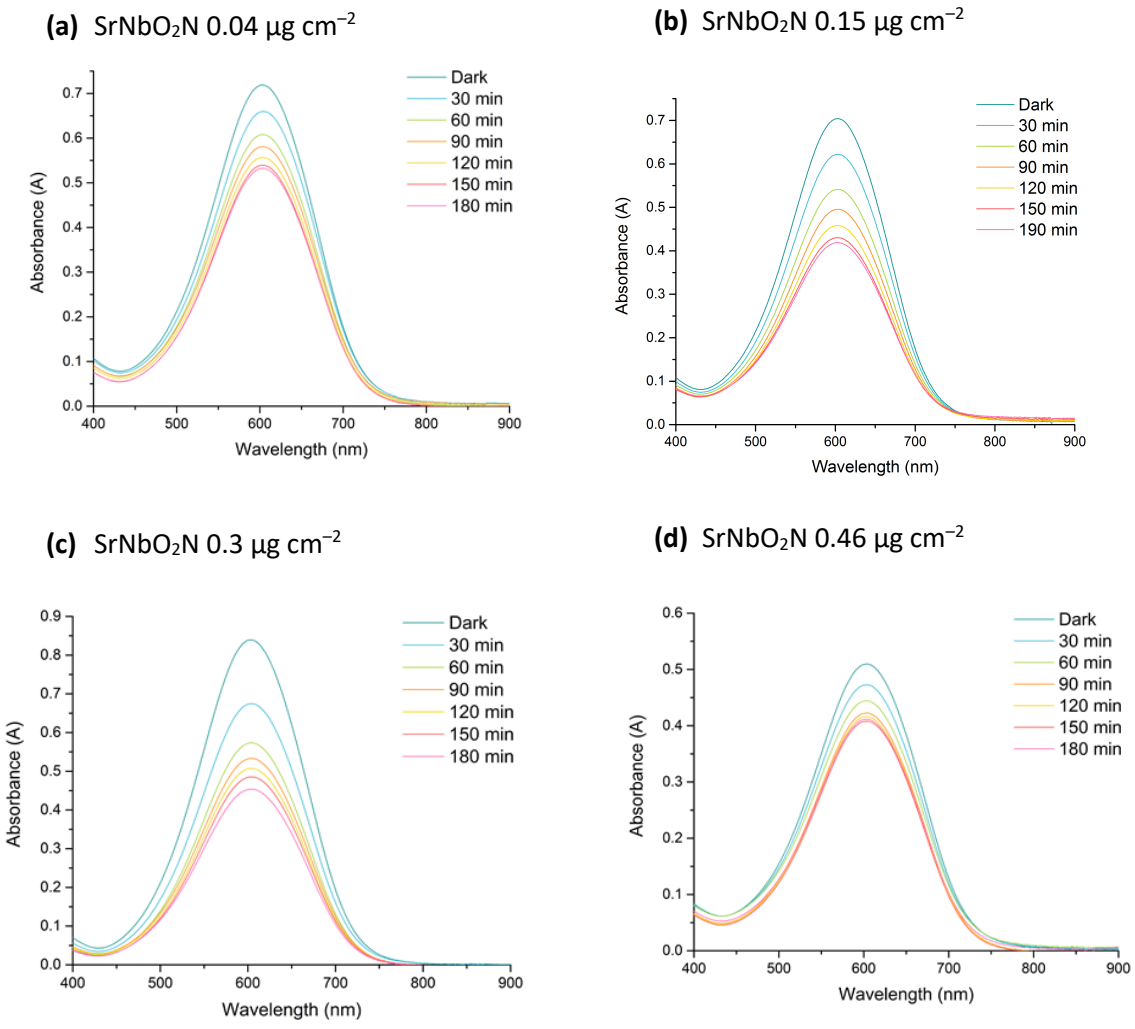

Figure 78. Visible spectral sets of $SrNbO_2N$ (a) 0.04, (b) 0.15, (c) 0.3 and (d) 0.46 μg cm^{-2} of Co ions recorded on DCIP solution aliquots.

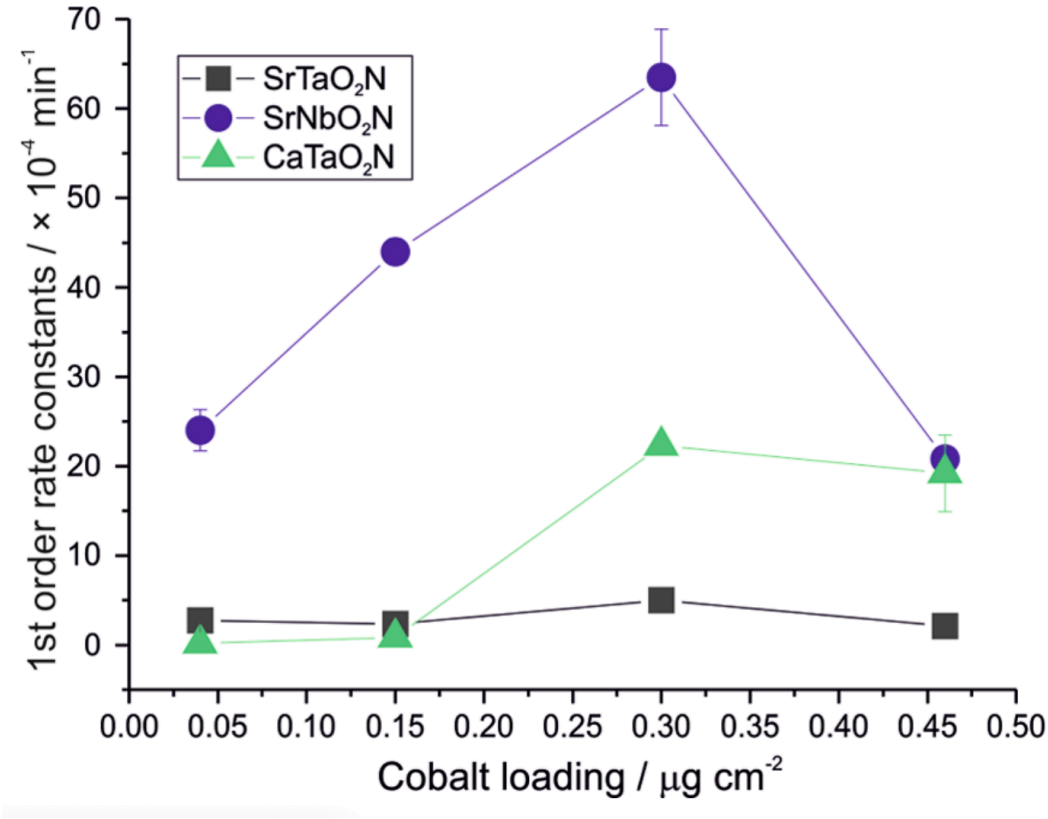

Figure 79. Plots of the initial first-order rate constants for photocatalytic degradation of DCIP dye as a function of cobalt oxide co-catalyst loading for SrNbO2N, CaTaO2N and SrTaO2N thin films on alumina substrates.

Figure 79 shows that for each perovskite oxynitride the 0.3 µg cm^{-2} is the optimum loading. All three samples showed an enhancement of the photocatalytic activity increasing the co-catalyst loading up to 0.3 µg cm^{-2}. However, when the loading was increased to 0.46 µg cm^{-2} a noticeable reduction in the photocatalytic activity was observed. This can be attributed to a minor amount of light reaching the oxynitride thin film, blocked by an excessive amount of cobalt oxide. Thus, co-catalyst loading of 0.3 µg cm^{-2} provided the balance between sufficient active sites without beginning to prevent light from reaching the underlying photocatalyst. It is noteworthy to mention that in all cases the use of a cobalt co-catalyst was required for DCIP degradation. As previously reported, the co-catalyst provided active centres for surface redox chemistry, and allows for surface trapping of holes and electrons, improving the charge carrier separation.

Our most active sample, the CoO_x-loaded $SrNbO_2N$ film was further investigated using SEM, EDX mapping and XPS spectroscopy. As we can see in Figure 80, the thin film is fragmentated into islands of 2–10 µm in size due to shrinkage commonly found in films formed by dip-coating. The film fragments are composed of particles in the order of 30-40 nm, as observed in the higher magnification images. This is consistent with the crystallite sizes of 27 nm determined by XRD. Side-on SEM

Figure 80c), allows an estimation of the overall perovskite film thickness of 450-500 nm.

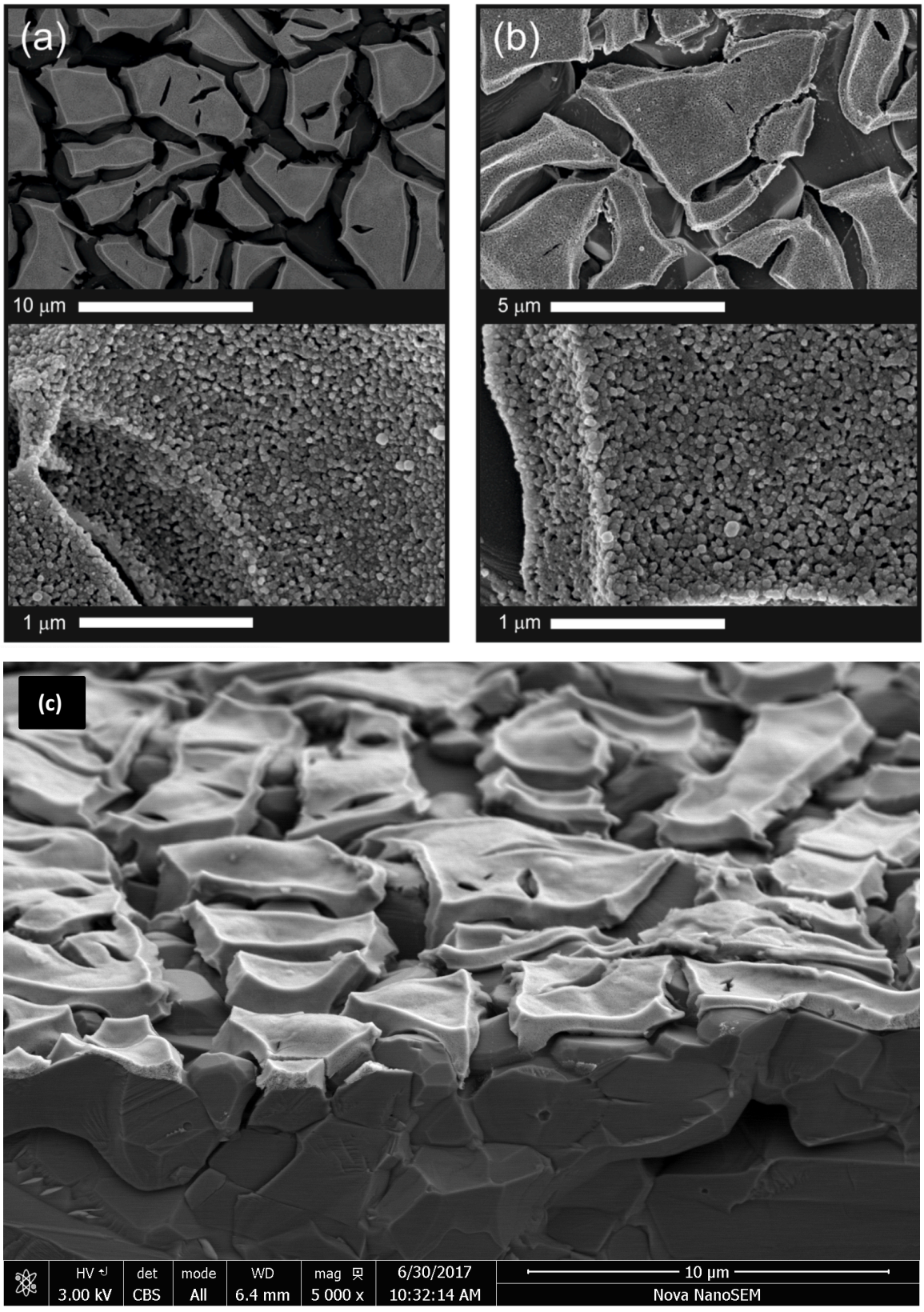

Figure 80. SEM image of the $SrNbO_2N$ thin films **(a)** as deposited **(b)** after deposition of CoO_x co-catalyst particles at 30 µg cm^{-2} and **(c)** side-on as deposited.

After deposition of the CoO_x co-catalyst, the morphology of the film remains unchanged, with the co-catalyst particles not observable at the resolution of the SEM. The presence of the CoO_x is revealed in the EDX mapping (shown in Figure 81). The EDX maps show the distribution of the different elements in the sample. Strontium and niobium ions form the clear shape of the island-type structure, with gaps in the surface due the film shrinkage. The cobalt ions are homogeneously distributed at an even but low concentration across the surface, including in the film gaps, consistent with being deposited after the oxynitride film (Figure 81d). The SEM/EDX therefore confirms the formation of a $SrNbO_2N$ film with a homogeneous surface coverage of cobalt containing particles.

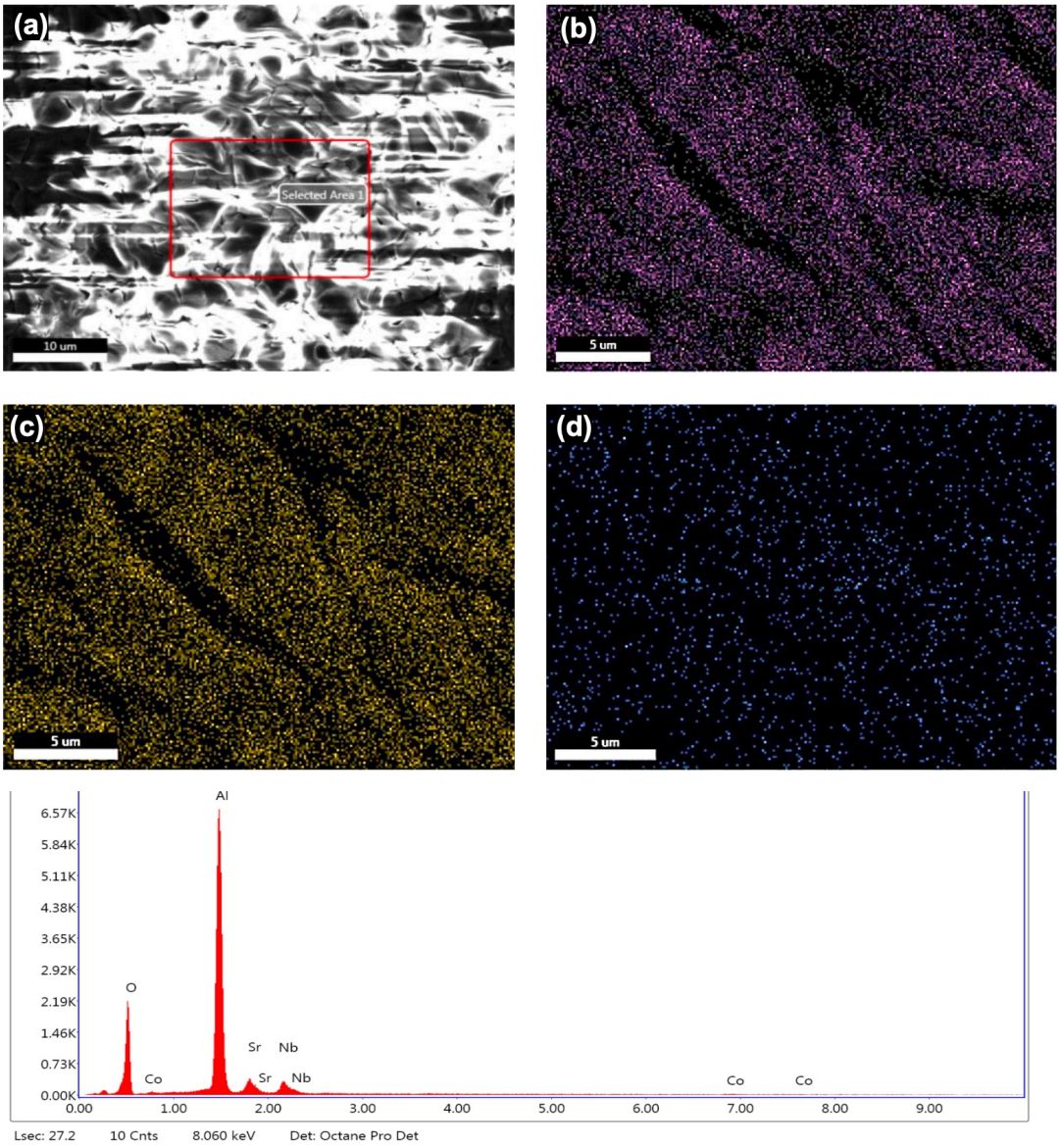

Figure 81. EDX elemental composition and mapping of the SrNbO2N thin film 0.4% wt. Co loaded. Where **(a)** showing $SrNbO_2N$ thin film micrograph undertaken for elemental compositional analysis **(b-d)** presenting elemental maps of Sr, Nb and Co respectively. **(e)** Spectrum investigated for atomic composition showing the elemental weight and atomic percentages in the onset.

X-ray photoelectron spectroscopy (XPS) was used to determinate the composition of the surface of the film. Only strontium, niobium, nitrogen and oxygen were detected in all the samples, along with cobalt co-catalyst. The binding energies of the core-level electrons from constituent elements are shown in Figure 82.

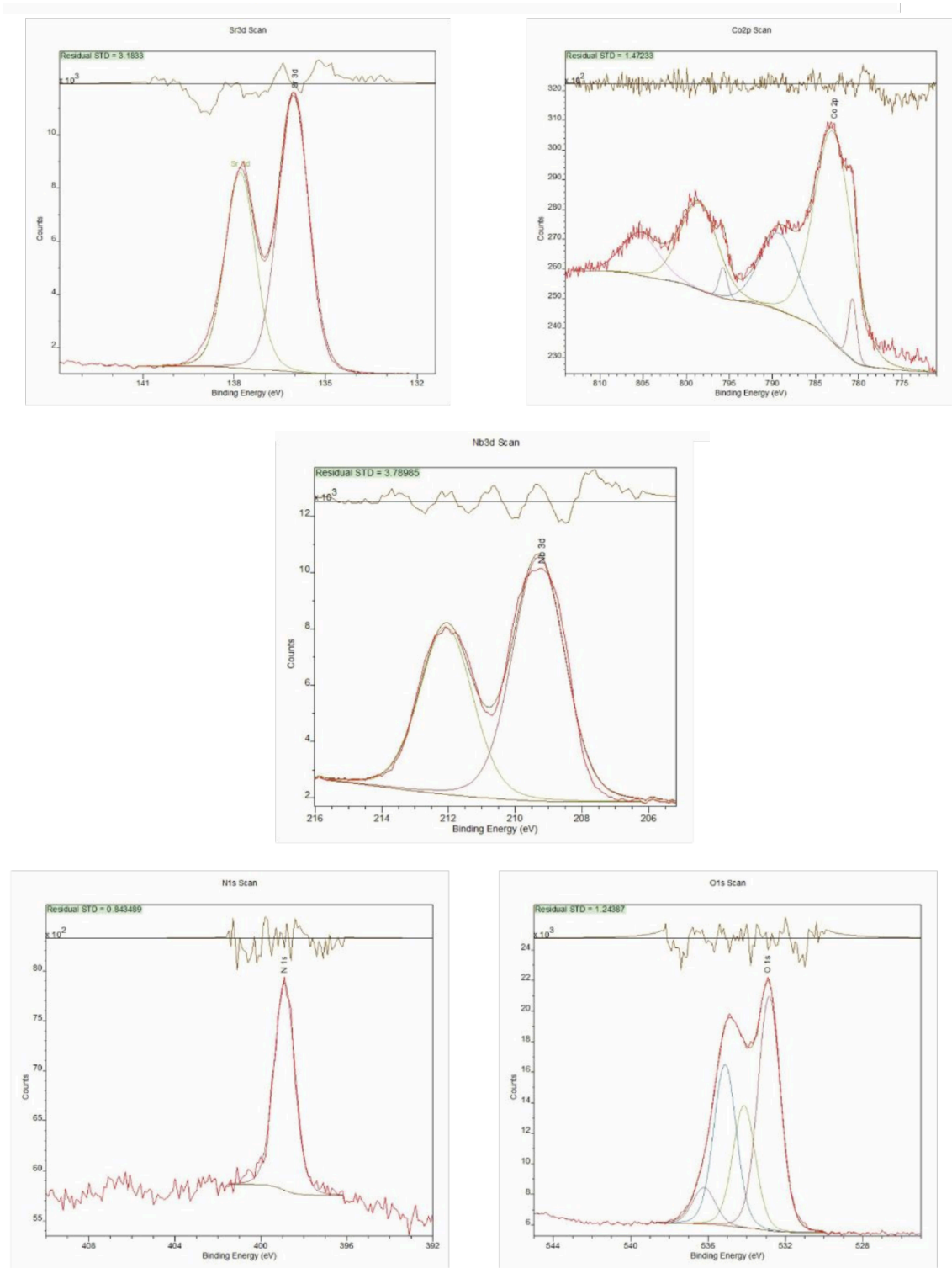

Figure 82. XPS fitting of high-resolution spectra for sample of CoO_x-loaded $SrNb_2N$ deposited onto alumina. Binding energies shown are uncorrected values and must be adjusted for charge correction to adventitious C1s with a binding energy of 284.6 eV by reducing the binding energies by 3.15 eV.

The N 1*s* spectum shows the presence of the nitrogen 1s peak at a very low binding energy of 395.5 eV confirming the presence of anionic N^{3-} settling the lattice substitution during ammonolysis. The nitrogen 1s peak was found at a very low binding energy of 395.5 eV consistent with anionic N^{3-}. Both Nb 3d and Sr 3d could be modelled as single environments. The Nb 3*d* spectra consists of two main $3d^{3/2}$ and $3d^{5/2}$ spin lines. The Nb $3d^{5/2}$ peak was found at 206.1 eV, which lies between the values previously found for Nb^{4+} and Nb^{5+}, based on values reported for NbO_2 (205.0 eV) and Nb_2O_5 (207.1 eV). The Sr 3 $d^{5/2}$ peak was found at 132.9 eV, consistent with Sr^{2+} in SrO.

Due to the similarity of the Co 2*p* spectra, the species CoO and Co_3O_4 are rather difficult to distinguish via XPS by the colocation of the possible Co^{2+} and Co^{3+} peaks and near overlap with Co(0) and the presence of satellite peaks for $Co^{2+/3+}$ As seen in Figure 41a , the Co 2*p* core-levels consist of two main Co $2p_{1/2}$ and Co $2p_{3/2}$, spin-orbital lines. These results suggested that the as-prepared cobalt oxide is mixture of the mixed-valence state of Co^{+2} and Co^{+3} with some unoxidized Co(0) remaining, approximately 6% of the cobalt present. However, it is not possible to distinguish the Co^{2+} and Co^{3+} states.

The interpretation of the O 1*s* spectra was complicated due to the presence of multiple peaks corresponding to the presence of the oxide in the perovskite, oxygen from the alumina tile, the cobalt co-catalyst with multiple Co oxidation states, and organic surface contamination/water absorption. A reasonable fit was obtained by using four overlapping components with fixed FWHM, at 529.7, 531.0, 532.0, and 533.1 eV. The first peak found at 529.7 eV is attributed to the bonding of oxygen to the electropositive strontium and niobium cations. A second peak observed at a higher binding energy of at 531 eV is interpreted to the oxygen bound to the less electropositive cobalt. As observed in the SEM images, the alumina substrate is exposed due to the island-type thin film structure. In this context, the peak observed at the binding energy of 532 eV can be interpreted as originating from the Al_2O_3 exposed in the gaps in the oxynitride film. Finally, the last peak at 533.1 eV is attributed to the presence of hydroxyl species or absorbed water on the surface. An approximate composition of $SrNb_{0.99}O_{2.48}N_{0.45}$ or $SrNb_{0.99}(O,N)_{2.93}$ can be obtained from the adjusted area of the peaks relative to strontium. The obtained composition is consistent with the strontium niobium perovskite oxynitride formula, showing the partial substitution of O^{2-} by N^{3-}. From the obtained formula, a surface oxidation state of +4.3 is calculated for the niobium cation, consistent with the binding energy found for the Nb 3*d* peak being an intermediate oxidation state.

Finally, as decreassing the amount of CoO_x loading from 0.3 to 0 μg cm^{-2} in a set of $SrNbO_2N$ thin film samples, the intensitiy of the unasigned Co^{3+} and Co^{+2} peaks also decreased, as expected.

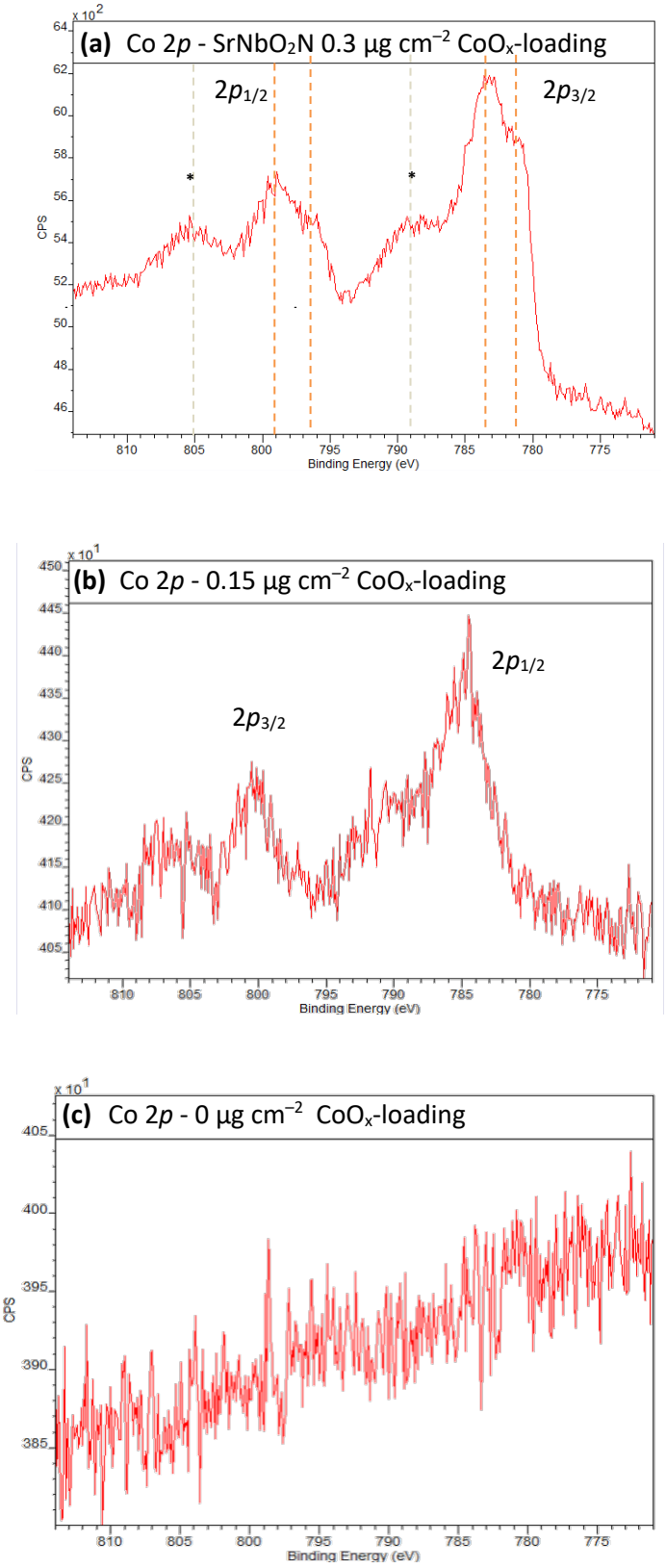

Figure 83. Co 2p XPS spectra of **(a)** 0.3 **(b)** 0.15 and **(c)** 0 µg cm^{-2} CoO_x - loading of $SrNbO_2N$ samples. * satellites.

5.3.3 Degradation of Stearic Acid under Visible-Light

The DCIP dye testing allowed us to identify the most active samples and the optimal co-catalyst loading. However, dye degradation is only a proxy test for self-cleaning; therefore, to confirm the ability of the photocatalyst film to completely mineralize organic contaminants, more convincing stearic acid degradation test was carried out.[247] In order to test the ability of the perovskite oxynitrides to degrade stearic acid it was required the use of a transparent substrate (such as quartz) with the objective of monitoring the degradation of deposited stearic acid molecules *via* transmission FTIR. Quartz substrates can withstand the high-temperature ammonolysis step required for the synthesis. However, unlike alumina, quartz is not inert to the perovskite film and can react with the alkaline earth ions found in the oxynitrides. To overcome this challenge, a layer of aluminium oxide was first deposited onto the quartz substrate using AACVD,[205] and then the perovskite film was deposited on top of this.

As observed in Figure 84, the resulting Al_2O_3 thin films were transparent and iridescent. To measure the adhesion of the thin film, an adhesive tape was applied to the film and subsequently pulled off (Scotch Tape Test). The thin film adhered to the substrate, indicating good adhesion strength.

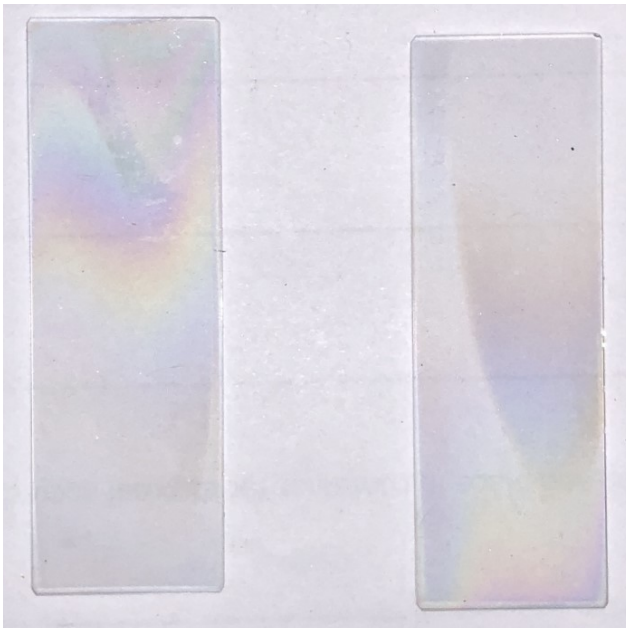

Figure 84. Photography of the Al_2O_3 thin films deposited by AACVD on quartz substrates

The dip-coating deposition over the modified substrates was carried out for $CaTaO_2N$, $SrNbO_2N$, and $SrTaO_2N$. For this, the same gels and dip-coating conditions (1 mm s^{-1}, 30 s immersion time) optimised in Chapter 4 were used for the deposition of the resins onto AACVD Al_2O_3-coated on quartz substrates. However, the adherence of the gel to the AACVD Al_2O_3-coated quartz substrates during the dip-coating process was lower when compared to the solely alumina

substrates. This minor but noticeable change in the gel adhesion is associated to the roughness of the substrate during the dip-coating process. As observed in Figure 84, SEM images show the surface of both substrates, the alumina tiles and the AACVD Al_2O_3-coated quartz substrates, being the surface of the last one noticeably less rough than the alumina tile.

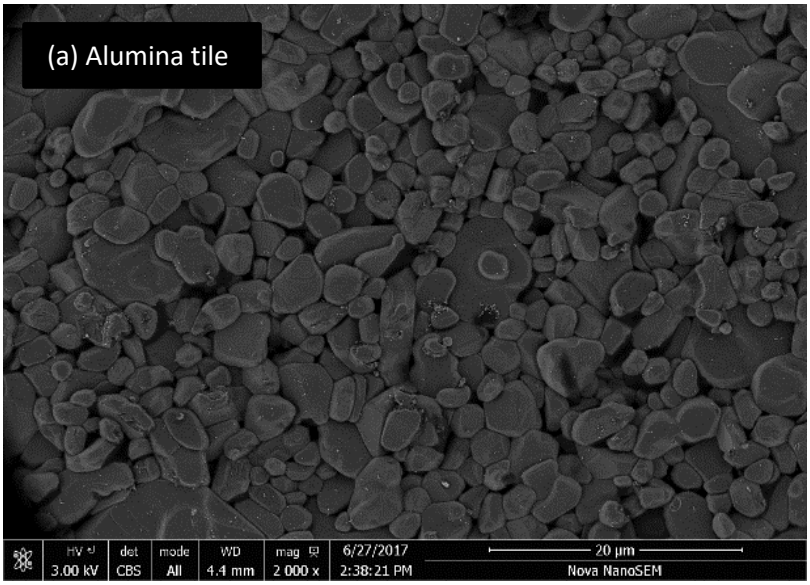

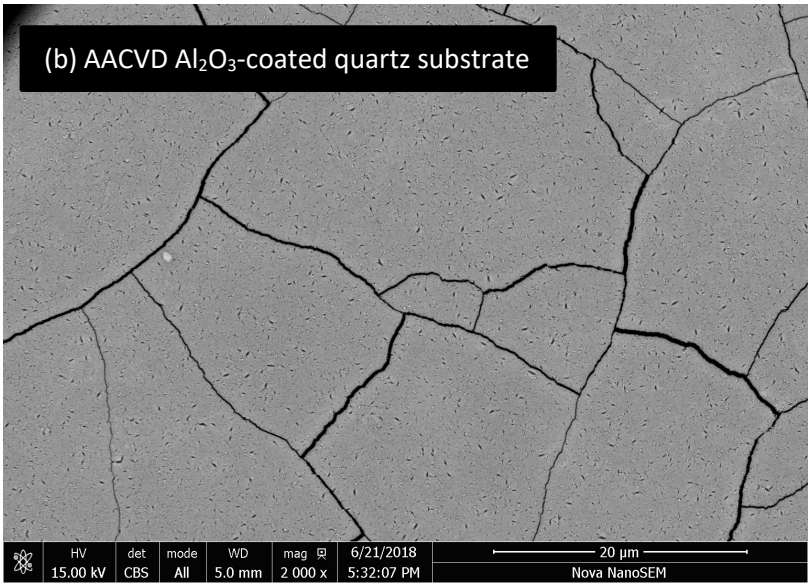

Figure 85. SEM images showing the surface of the (a) alumina tiles and (b) AACVD Al_2O_3-coated quartz substrate.

The coated substrates were annealed in air for 1 h at 350˚C, then 1 h at 650˚C and 2 h at 800˚C, following the same procedure as for the resins deposited on the alumina tiles. The resulting oxide thin films were not physically visible.

In a second stage, the oxide thin films were ammonolysed at 850˚C ($SrTaO_2N$ and $SrNbO_2N$) and 950˚C ($CaTaO_2N$) at a NH_3 flowing rate of 250 mL min^{-1}. After ammonolysis, the three thin films

showed bright colours as expected. The $SrNbO_2N$ was brown, while $SrTaO_2N$ and $SrNbO_2N$ were orange.

$SrNbO_2N$ **$SrTaO_2N$** **$CaTaO_2N$**

Figure 86. Photography of the CaTaO2N, $SrTaO_2N$, and $SrNbO_2N$ thin films deposited onto AACVD Al_2O_3-coated quartz substrates.

XRD was used to confirm the successful formation of these films. The diffraction patterns match with those previously published for the same oxynitrides and are in agreement with the samples synthesised in Chapter 4. The oxynitride was confirmed by Rietveld refinement (Figure 88).

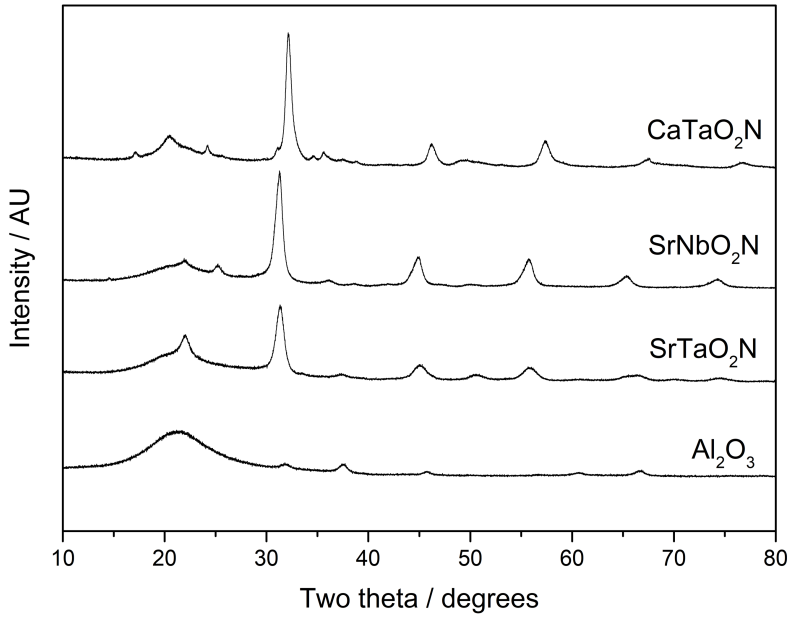

Figure 87. X-ray diffraction spectra of the $CaTaO_2N$, $SrTaO_2N$ and $SrNbO_2N$ thin films deposited over the AACVD Al_2O_3-coated quartz substrates. The X-ray diffraction spectra of the Al_2O_3 thin film is included as a reference.

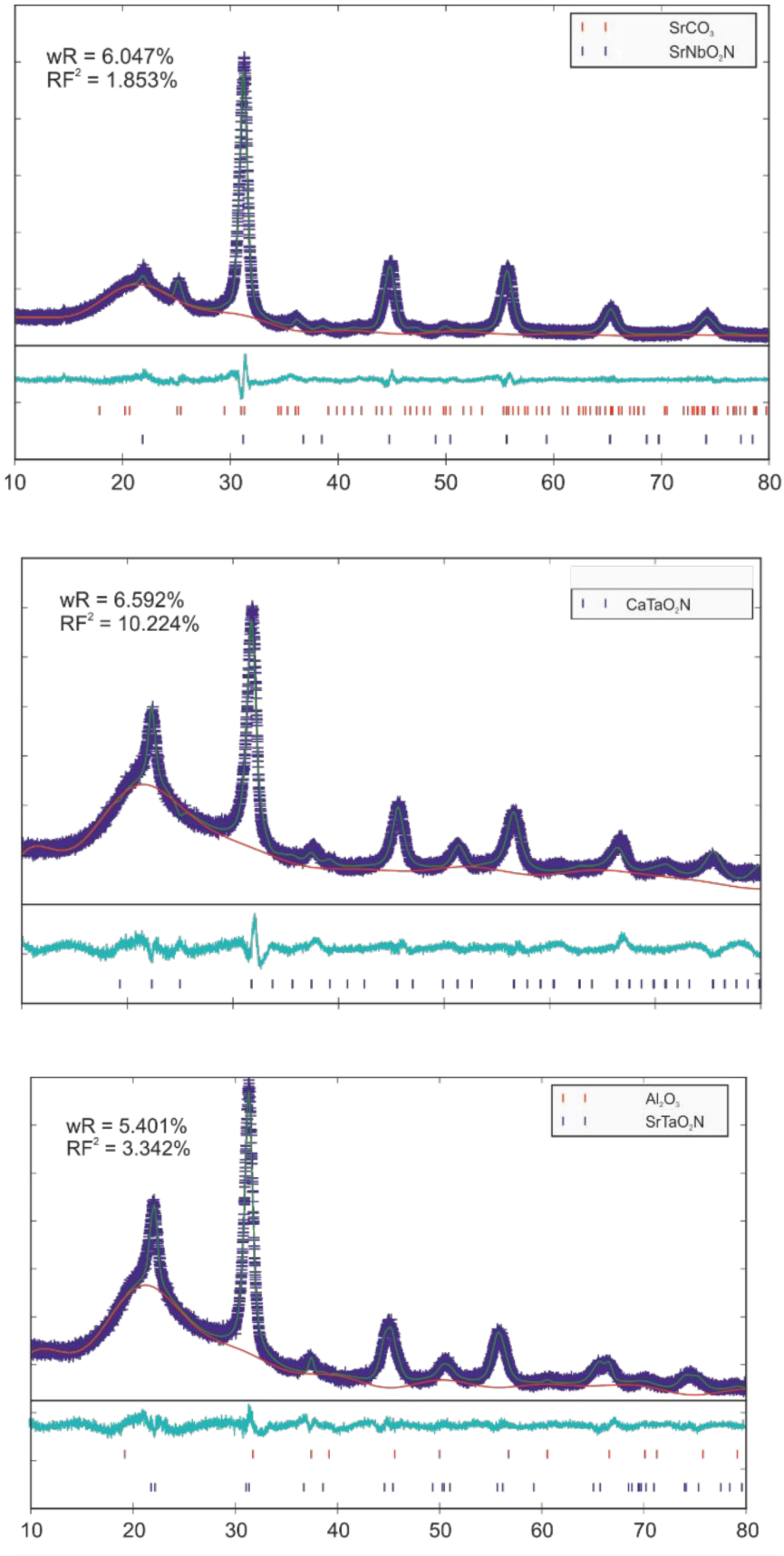

Figure 88. Rietveld refinement of the X-ray diffraction data of the perovskite films on quartz. The wR values are for the whole pattern fit, the RF^2 values are for the phase fit to the oxynitride peaks.

UV–vis transmission spectra were also recorded, and the band gaps reconfirmed for these samples deposited on quartz as 2.43, 2.15, and 1.99 eV for the $CaTaO_2N$, $SrTaO_2N$, and $SrNbO_2N$ samples, respectively, once again within the error of values reported previously in literature.

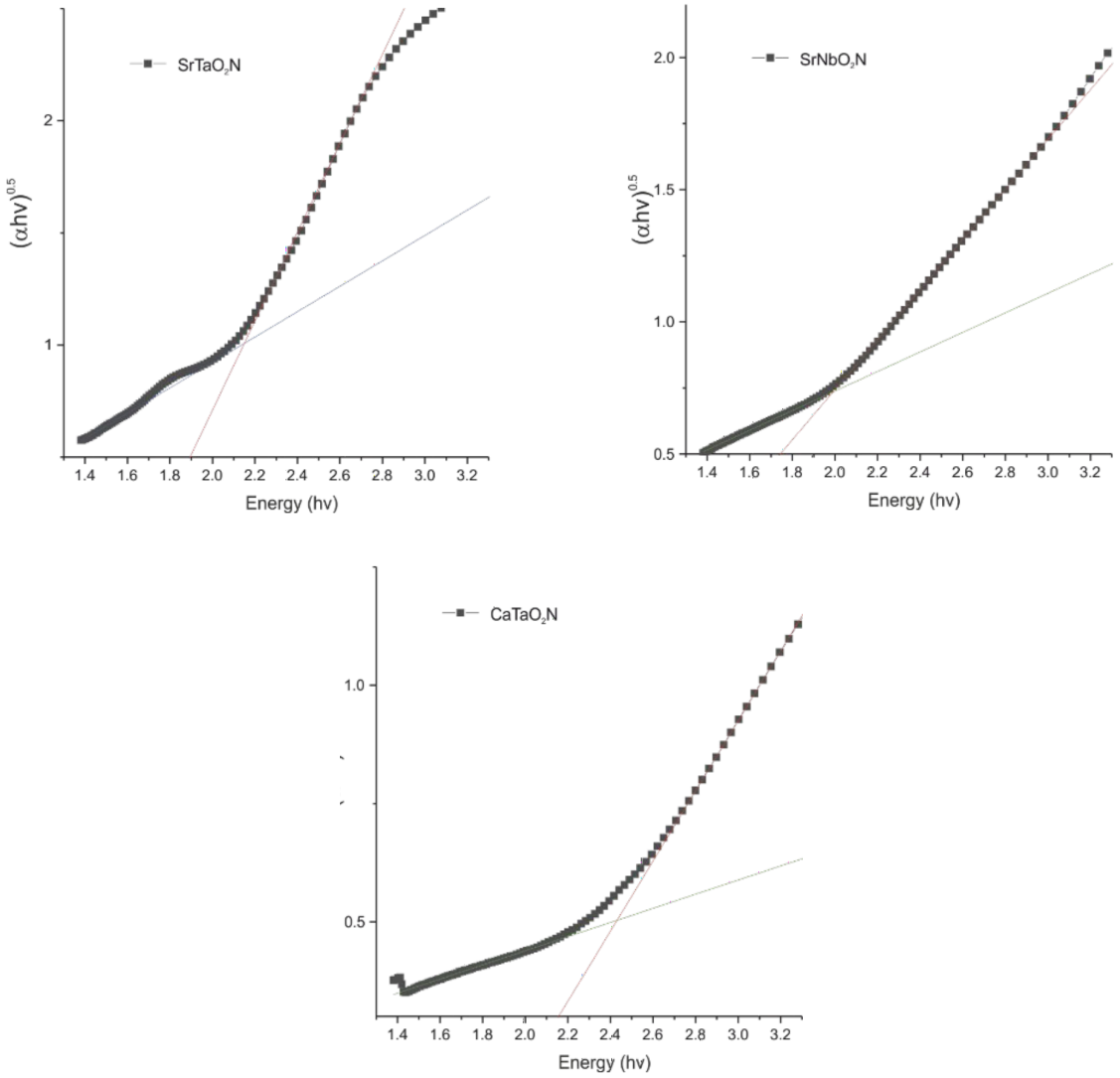

Figure 89. Tauc plots derived from the diffuse reflectance spectra recorded on the perovskite thin films on quartz.

The degradation of stearic acid was carried out by dip-coating a thin layer of stearic acid dissolved in methanol. The initial concentration of the stearic acid thin films was determined by FTIR and was of approximately 1.65×10^{16} molecules cm^{-2}. The thin films were irradiated with the solar simulator for two hours and the degradation of the stearic acid thin film was monitored using FTIR. All samples showed a reduction in the content of stearic acid, proving the self-cleaning properties of the thin films under visible light. Particularly, the $SrNbO_2N$ thin films showed a reduction in the concentration of a 15.4 %, while both $SrTaO_2N$ and $CaTaO_2N$ showed an 8.4 %. The degradation of the stearic acid appears to follow first-order kinetics, thus, plotting the $ln(C/C_0)$ against time allow us for the determination of the degradation rate constants. In this context and

as observed in Figure 90 (bottom right) we obtained the values of 14(2) × 10^{-4} min^{-1} for $SrNbO_2N$, 8(1) × 10^{-4} min^{-1} for $SrTaO_2N$, and 7.8(6) × 10^{-4} min^{-1} for $CaTaO_2N$. These results are in line with the results of the DCIP dye testing, being $SrNbO_2N$ the most active sample.

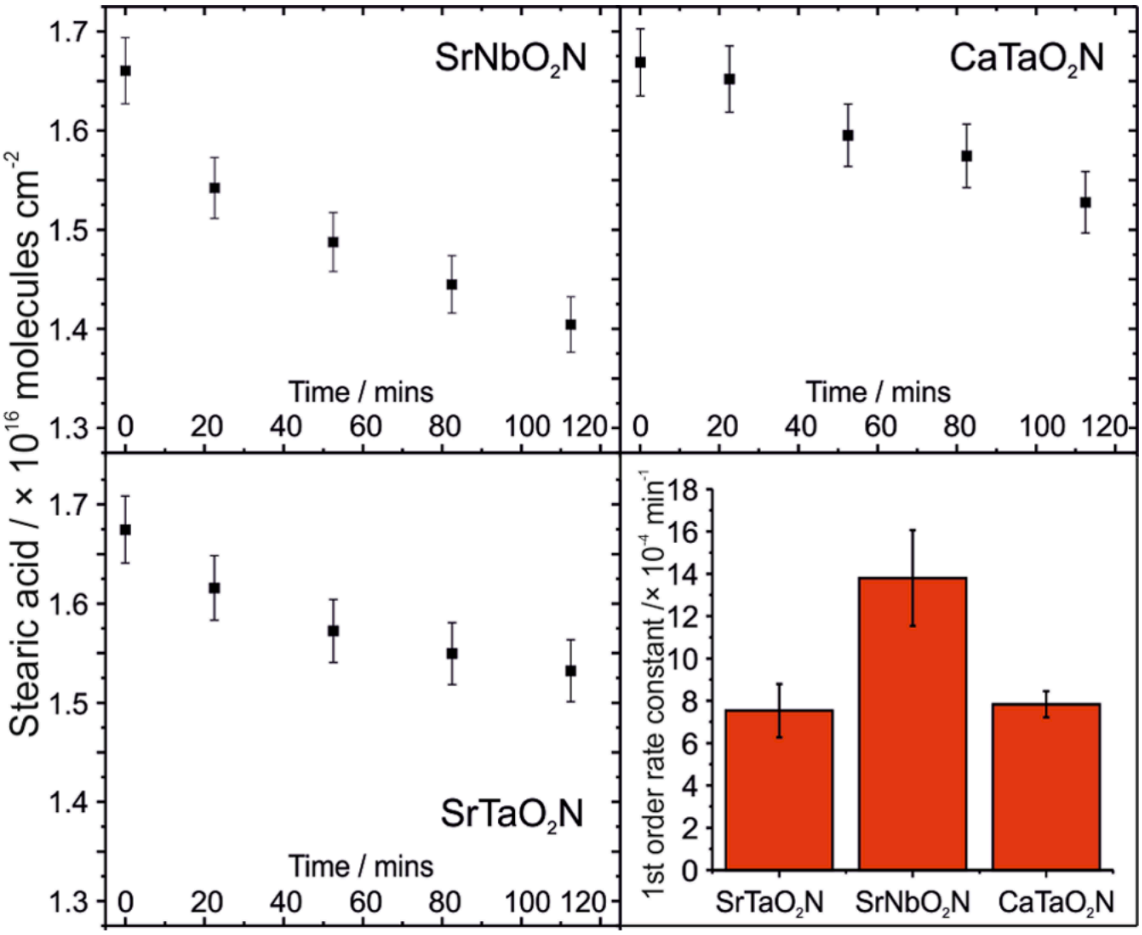

Figure 90. Plots of the stearic acid concentration as a function of time, as assessed using FTIR spectroscopy, for thin films of $SrNbO_2N$, $CaTaO_2N$ and $SrTaO_2N$ on quartz with a CoO_x co-catalyst under solar-simulated light. Bottom right, plot of the first-order rate constant for the stearic acid degradation for each film.

The most active thin film $SrNbO_2N$ showed an initial rate of stearic acid degradation of 5.26 × 10^{13} molecules min^{-1}. Taking into the account the intensity of the solar simulator (5090 W m^{-2}) we obtain a formal quantum efficiency (FQE) of 6.51 × 10^{-7} molecules per photon. However, comparing values of different photocatalytic activities found in the literature is challenging due to the differences in the experimental conditions, including the light source (sometimes not being reported) used and variations in the initial stearic film thickness that can significantly affect reported rates. However, prior work from our group under identical reaction conditions with a film of tantalum oxynitride found an initial rate 2.5 × 10^{13} molecules min^{-1} which is approximately half that observed with the co-catalyst-loaded $SrNbO_2N$ film reported in this thesis.[254]

The 0.3 μg cm^{-2} CoO_x loaded $SrNbO_2N$ film showed the best initial rate among all the samples, exceeding the previously reported rates for visible light photocatalytic degradation of organic species. Previous estimations show an approximate greasy contamination on a surface of 4×10^{-6} g cm^{-2}, thus, using the initial rate of 5.26×10^{13} molecules min^{-1}, we estimate 13.4 hours to completely remove this contamination under conditions of the bright sunlight.

Prior work with visible light degradation of stearic acid on nitrogen and fluorine-doped titanium dioxide has also been reported. Quesada et al. reported nitrogen-doped titania (N-TiO_2). thin films synthesised using atomospheric-preassure chemical vapour deposition (APCVD). [255] The incorporation of nitrogen in titania thin films results in the red shift of the absorption spectrum, resulting in visible light absorption. Alternatively, Park et al. reported the degradation of stearic acid over fluorinated titania (F-TiO_2). If we adjust the reported photocatalytic activities for light intensity, nitrogen-doped titania films exhibited an initial rate of 0.03×10^{13} molecules min⁻1, while fluorinated titania films have a reported rate of 0.2×10^{13} molecules min^{-1}.[256] The smaller rates obtained for the doped titania films can be attributed to a low concentration of the dopants in the TiO_2 allowing for only weak visible light absorption, compared to our coloured perovskite oxynitrides.

Finally, UV-activated titanium dioxide photocatalytic films can also be compared to our perovskite thin films, assuming that films are used in direct sunlight where the UV component is unfiltered. Assuming an intensity of 5 mW cm^{-2} of UV light in the solar spectrum and including an adjustment for the tests carried out typically using UV light alone, we obtain comparable initial rates for titania films in the range of 5×10^{13} and 40×10^{13} molecules min^{-1} cm^{-2}. [258,259] Based on this comparison, the use of TiO_2 thin films is a better choice for self-cleaning applications using direct sunlight due to their higher rates, known non-toxicity, transparency and low cost of TiO_2. However, in situations where little UV light is available, for example for indoor applications such as hospitals, the CoO_x@$SrNbO_2N$ film would be a viable self-cleaning surface.

Chapter 6 Metal Ion Doping of the Perovskite Oxynitrides $SrNbO_2N$.

6.1 Introduction

The active perovskite oxynitrides $SrNbO_2N$, $CaNbO_2N$ and $SrNbO_2N$ have shown that there is room for improvement on the photocatalytic performance under ordinary conditions. The photocatalytic activity displayed by these three perovskite oxynitrides is incommensurate to their strong visible light absorption. This is often attributed to the presence of defects formed during the synthetic process (which requires high temperatures) that cause trapping of the photo-generated carriers and charge recombination.[260]

The introduction of alkaline (Na, K, Li, Rb, Cs) and earth (Mg) metals on nitrides, and oxynitrides can significantly boost their photocatalytic activities.[193,260,261] Previous reports have shown that *M*-doped Ta_3N_5 (*M* = Na, K, Rb, Cs) result in an enhancement of the water splitting activity compared to the non-doped Ta_3N_5.[261] Thus, doping has not only modified the band gaps but also reduced the charge transfer resistance, hence preventing electron-hole recombination, which translates to an improved photocatalytic activity.

Recently, Wu et al. showed that Na-modification of the perovskite oxynitride $SrTaO_2N$ resulted in a boost of the photocatalytic water splitting activity, compared to the non-active pristine $SrTaO_2N$.[260] The introduction of Na^+ into the crystal lattice has an impact on the enhancement of the local Ta-O(N) bond strength as well as a band gap enlargement. The partial replacement of the Ta^{5+} with Na^+ improves the level of covalency of the remaining Ta-(O)N bonds, stabilising the Ta^{5+} against reduction to Ta^{4+}. The described phenomenon results in the formation of less defects levels, which, in turn results in an enhanced photocatalytic activity of the sample.

Additionally, recent work carried out by the same research group proved that doping $BaTaO_2N$ with Ca^{2+} ions also decreased the defect levels and water oxidation reactions were significantly improved in the presence of a co-catalyst compared to the pristine $BaTaO_2N$.[193]

Thus, such modifications using earth and alkali metals, clearly highlights and effective way of tailoring local bond strength and photocatalytic activity of perovskite oxynitrides. Due to the tolerance to structural and compositional modifications of the perovskite structure, this strategy is expected to be extended to other perovskite oxynitrides.

6.1.1 Manual Inkjet Printing

Ink-jet printing is an attractive technique for the deposition of liquid phase materials. In recent years, this technique has gained popularity among industry and scientific applications. Recent advances in the field of ink-jet printing technology include the development of solar cells [262], conductive structures, organic thin film transistors[263] as well as light emitting diodes.[264]

However, the price of the state-of-the-art combinatorial chemistry equipment still remains an economic barrier for most research groups, including this one. As a result, manual ink-jet printing allows reproducing and replicating the work by useing a micropipette and stock metal solutions. These stock metal solutions, also called inks, consist of a solution containing the precursor metals (from salts such as acetates, nitrates or carbonates) dissolved in a solvent, generally methanol or distilled water.

The process comprises the preparation of a series of well-known compositions from stock inks (Na-Ink, Ca-Ink, Nb-Ink, *etc*...) which are subsequently, manually deposited with a micropipette over the desired substrate, ie., 2.5 x 2.5 cm alumina substrates in our case and in the desired ratio. Manual ink-jet printed microarrays can be used for the screening of active photocatalytic materials, as well as for the preparation of a combinatorial material library.

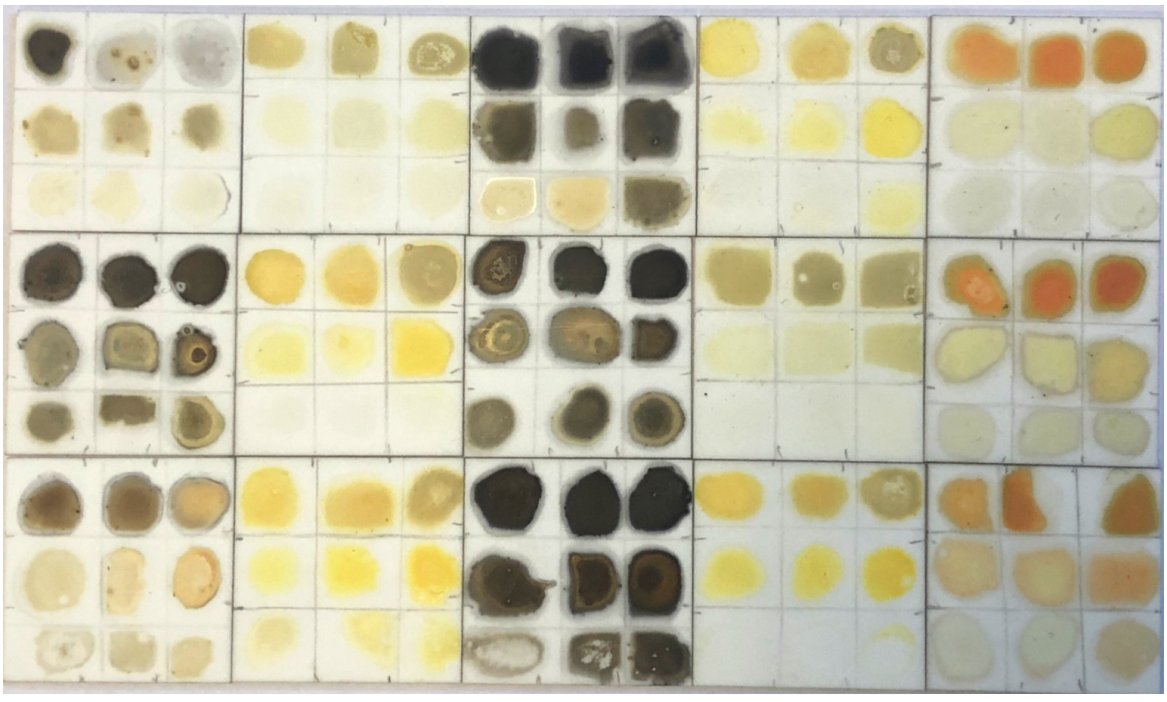

Figure 91. Photograph of a 135 members combinatorial library of perovskite oxynitride materials deposited over 2,5 x 2,5 cm alumina substrates.

This combinatorial approach can lead to the discovery of a number of new photocatalytic active materials with the benefits of reduced material wastage, low cost, scalability, development and selection of phase pure candidates.

In this context, the materials library is analysed using grazing incidence XRD with the goal of confirming the metal doping and formation of the phase pure materials. After GI-XRD, the samples are loaded with a co-catalyst, in our case CoO_x, as previously reported in Chapter 5. Subsequently, each thin-film is split into nine different sections, each of one containing a different composition, and their photocatalytic activities assessed by degradation of DCIP under solely visible-light. Finally, the selected candidates from the materials library can be scaled-up for further characterisation analysis, as well as degradation of stearic acid.

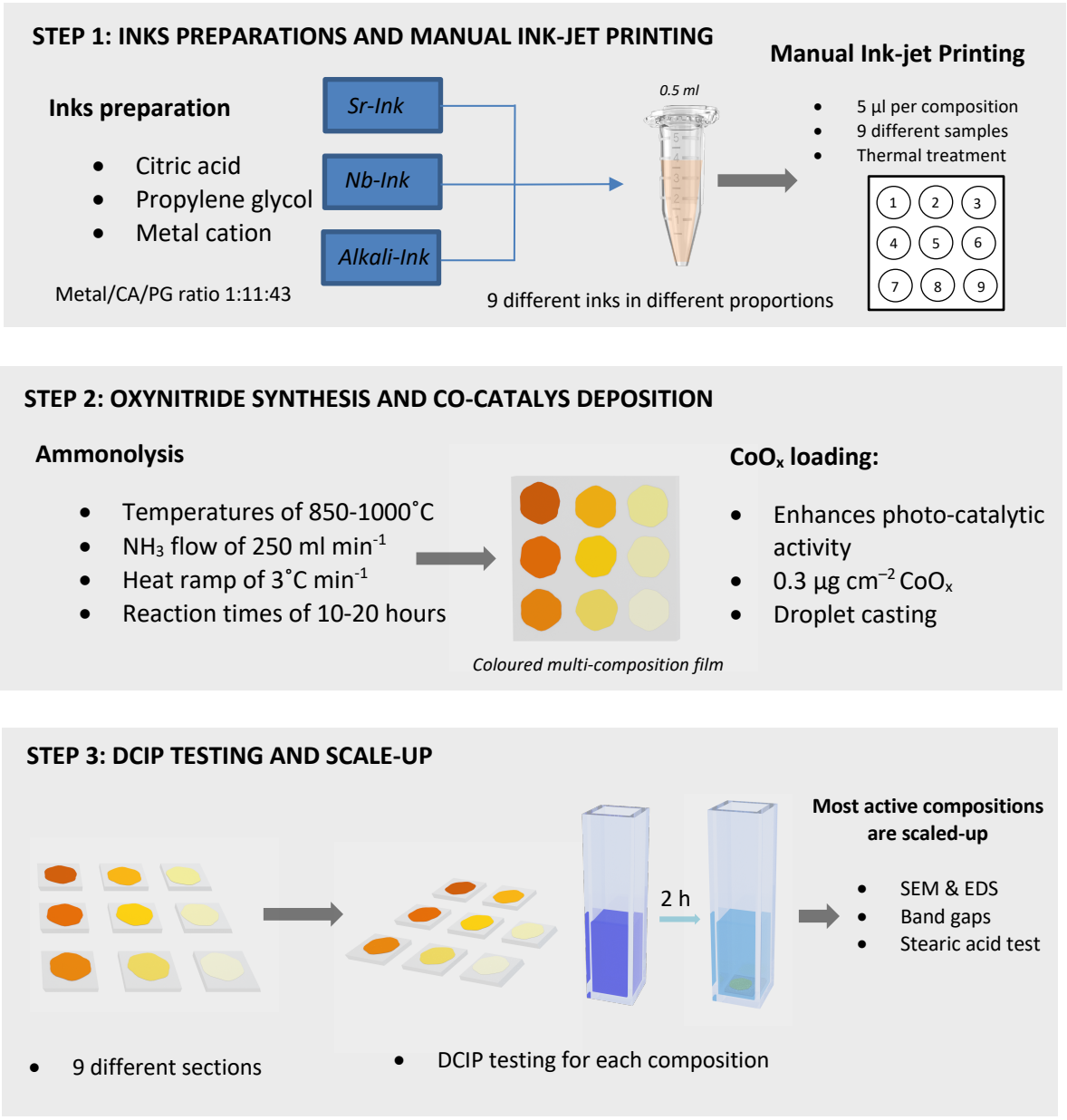

Figure 92. Scheme with the proposed steps for the synthesis and analysis of the materials library.

Due to lack of time, in this chapter we propose an approach for the synthesis of a materials library of different perovskite oxynitride compositions using a manual ink-jet printing method and subsequent photocatalytic testing with the goal of screening the most active candidates for scale-up.

Experimentally, we have modified the most active $SrNbO_2N$ thin film from Chapter 5, introducing alkali (Na and K) and earth (Mg) metals into the perovskite structure. The resulted combinations $SrNb_{1-x}B_x(O,N)_3$ (*B* = Na, K and Mg) where x = 0.2 - 0.8 were manually printed over alumina substrates and phase purity was analysed using GI-XRD.

6.2 Experimental

6.2.1 Synthesis of $SrNb_{1-x}B_x(O,N)_3$ (*B* = Na, K, Mg)

Five individual inks containing 0.89 mmol of the precursor metal ions (Sr, Nb, Na, K, Mg) were prepared via the polymeric precursor method. The amounts of the metal precursor reagents used are indicated as follow:

Ink name	Amount and brand
Sr-Ink	0.13g of $SrCO_3$ (98%, Sigma-Aldrich)
Nb-Ink	0.24 g of $NbCl_5$ (Sigma-Aldrich)
Na-Ink	0.25 g of $Na_2CO_3 \cdot 10H_2O$ (Sigma-Aldrich)
K-Ink	0.146 g of $K_2CO_3 \cdot 6H_2O$ (99%, Sigma-Aldrich)
Mg-Ink	0.19 g of $Mg(Ac)_2 \cdot 4H_2O$ (Sigma-Aldrich)

First, for each ink, the metal precursor reagent was dissolved in 7 mL of deionized water (Na, K, Mg and Sr) and methanol (Nb). Second, 1.28 g of citric acid (CA) were added to the mixture and was magnetically stirred until clear solution. Finally, 2.8 mL of propylene glycol (PG) were added and the solution was heated up to 120°C for 90 minutes to promote the polysterification, resulting in a transparent gel. For the Sr-Ink, 20 drops of 5% HNO_3 were need to re-dissolve the white precipitate. The solutions were brought to a final volume of 10 ml.

Depending on the desired composition, each final solution consists of a calculated amount of the Sr-Ink, Nb-Ink and a *B* metal ion ink (Na, K or Mg) mixed to a total volume of 0.5 mL in an Eppendorf Tube. The Table 27 shows the different amounts of inks used for each composition. The final solutions are sonicated for 180 seconds and 5 µl of each composition are deposited using a micropipette onto the 2.5 x 2.5 cm alumina substrate, resulting in a total of 9 thin films. The thin films were heated in air at 350 °C for 1 hour, 650°C for another hour and at 850°C for 2 hours. The ramp rate was set to 10°C min^{-1}. The alumina tile containing the nine different compositions was ammonolysed for 10-20 hours at a NH_3 flow rate of 250 mL min^{-1} and a ramp rate of 3 °C min^{-1}.

Cobalt oxide co-catalyst particles were deposited onto the tiles at a nominal surface concentration of 0.3 µg cm^{-2} to enhance the photocatalytic rates as previously done in Chapter 5. For this, 0.5 mL of a solution of 4.1×10^{-5} mol dm^{-3} $Co(NO_3)_2 \cdot 6H_2O$ in acetone was dropped onto the surface of the tile containing the different compositions. The acetone was allowed to evaporate in air, and then the samples were heated to 700 °C under a flow of 250 mL min^{-1} of ammonia gas for 60 min, leading to metallic Co-nanoparticles. The active CoO_x co-catalyst was obtained by mild oxidation in air at a temperature of 200 °C for 60 min.

6.2.2 Photocatalytic screening

The photocatalytic screening was achieved by splitting the alumina tiles into nine small sections of 0.5 x 0.5 cm approximately, each one containing a different composition. Each small section was placed at the bottom of a plastic cuvette and immersed in 1.5 mL of an aqueous solution of 5.5×10^{-5} mol dm^{-3} DCIP and 1.26×10^{-2} mol dm^{-3} glycerol. The cuvette was attached to a shaker platform to ensure homogeneity during the reaction. The radiation intensity of the solar simulator as measured at the position of the sample was 509 mW cm^{-2}. Prior to starting the test, the immersed samples were kept in the dark for one hour to achieve the equilibrium with dye adsorption. Once this was achieved, the solar simulator was switched on, and final aliquots were withdrawn at 60 minutes intervals up to 180 min. Aliquots were then returned to the solution.

Table 26. Compositional tables of the *B*-doped $SrNbO_2N$ (*B* = Na, K, Mg).

Composition	Sr-Ink (ml)	Nb-Ink (ml)	Na-Ink (ml)
$SrNb_{0.95}Na_{0.05}(O,N)_3$	0.25	0.0237	0.0125
$SrNb_{0.9}Na_{0.1}(O,N)_3$	0.25	0.225	0.025
$SrNb_{0.8}Na_{0.2}(O,N)_3$	0.25	0.2	0.05
$SrNb_{0.7}Na_{0.3}(O,N)_3$	0.25	0.175	0.075
$SrNb_{0.6}Na_{0.4}(O,N)_3$	0.25	0.15	0.1
$SrNb_{0.5}Na_{0.5}(O,N)_3$	0.25	0.125	0.125
$SrNb_{0.4}Na_{0.6}(O,N)_3$	0.25	0.1	0.15
$SrNb_{0.3}Na_{0.7}(O,N)_3$	0.25	0.075	0.175
$SrNb_{0.2}Na_{0.8}(O,N)_3$	0.25	0.05	0.2

Composition	Sr-Ink (ml)	Nb-Ink (ml)	K-Ink (ml)
$SrNb_{0.95}K_{0.05}(O,N)_3$	0.25	0.0237	0.0125
$SrNb_{0.9}K_{0.1}(O,N)_3$	0.25	0.225	0.025
$SrNb_{0.8}K_{0.2}(O,N)_3$	0.25	0.2	0.05
$SrNb_{0.7}K_{0.3}(O,N)_3$	0.25	0.175	0.075
$SrNb_{0.6}K_{0.4}(O,N)_3$	0.25	0.15	0.1
$SrNb_{0.5}K_{0.5}(O,N)_3$	0.25	0.125	0.125
$SrNb_{0.4}K_{0.6}(O,N)_3$	0.25	0.1	0.15
$SrNb_{0.3}K_{0.7}(O,N)_3$	0.25	0.075	0.175
$SrNb_{0.2}K_{0.8}(O,N)_3$	0.25	0.05	0.2

Composition	Sr-Ink (ml)	Nb-Ink (ml)	Mg-Ink (ml)
$SrNb_{0.95}Mg_{0.05}(O,N)_3$	0.25	0.0237	0.0125
$SrNb_{0.9}Mg_{0.1}(O,N)_3$	0.25	0.225	0.025
$SrNb_{0.8}Mg_{0.2}(O,N)_3$	0.25	0.2	0.05
$SrNb_{0.7}Mg_{0.3}(O,N)_3$	0.25	0.175	0.075
$SrNb_{0.6}Mg_{0.4}(O,N)_3$	0.25	0.15	0.1
$SrNb_{0.5}Mg_{0.5}(O,N)_3$	0.25	0.125	0.125
$SrNb_{0.4}Mg_{0.6}(O,N)_3$	0.25	0.1	0.15
$SrNb_{0.3}Mg_{0.7}(O,N)_3$	0.25	0.075	0.175
$SrNb_{0.2}Mg_{0.8}(O,N)_3$	0.25	0.05	0.2

6.3 Results and Discussion

6.3.1.1 $SrNb_{1-x}M_x(O,N)_3$ (*M* = Na, K, Mg)

The thin films containing different compositions ($SrNb_{1-x}M_x(O,N)$; *M* = Na, K and Mg; x = 0.05-0.8) were obtained by manual ink-jet printing of nine different inks onto the alumina substrate using a micropipette. After manual printing, the thin films were calcined in air, obtaining the white oxide precursors. Then, the films were ammonolysed in order to obtain the final perovskite oxynitride compositions. The multi-composition thin films were analysed using GI-XRD. Each sample was mapped and a screenshot of the thin film containing the nine different compositions allowed us to select nine different analysis points to get nine different diffractograms.

Different reaction times were tested, and each composition was ammonolysed for 10 h and 20 h, except for the Mg^{2+} compositions which was ammonolysed only for 20 h. After ammonolysis all the samples showed bright colours as expected. As observed in Table 28 and Figure 92, the sample containing the lowest amount of doping ion (x= 0.05) showed a brown colour characteristic of the $SrNbO_2N$ thin film. This colour generally diminished to pale brown with increasing proportion of the doping anion. For samples with higher doping proportions, the perovskite structure does not accommodate into the lattice all the metal cations, resulting in the formation of a mixture of perovskite oxynitride and white oxides, which results in brighter compositions.

Table 27. Different synthetic conditions (reaction time and temperature) conditions of the multi-composition $SrNb_{1-x}M_x(O,N)_3$ (*M* = Na, K and Mg) thin films synthesised in this chapter.

		***B* site cation**		
Target	**Reaction Time and Temperature**	**Na^+**	**K^+**	**Mg^{2+}**
$SrNb_{1-x}M_x(O,N)_3$	10 h, 850˚C	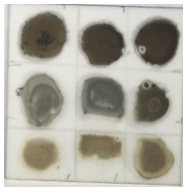	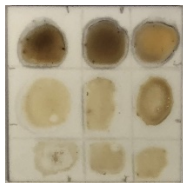	
$SrNb_{1-x}M_x(O,N)_3$	20 h, 850˚C	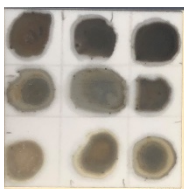	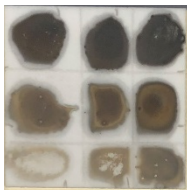	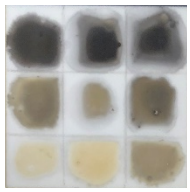

All the different compositions showed the presence of peaks corresponding to the formation of the perovskite structure, as compared with the $SrNbO_2N$ diffractogram. However, XRD data of the solid compositions $SrNb_{1-x}K_x(O,N)_3$ and $SrNb_{1-x}Na_x(O,N)_3$ ammonolysed during 10 h showed the presence of an unassigned phase for all the compositions. Increasing the reaction time to 20 h, the intensity of the unassigned phase diminished, while the peak assigned to the perovskite phase increased in intensity. This can be attributed to the presence of the oxide precursors phase, indicating that 10 h was not enough reaction time for the full transformation into the oxynitride phase. Interestingly, the intensity of this peak was higher as we increase the proportion of the doping cation. Again, we suggest the formation of a complex oxide precursor which is ammonolysed to the oxynitride phase for lower doping metal concentrations, while remaining unconverted for the higher doped samples.

Taking into the account Wei et al. work on doping $BaTaO_2N$ with Ca to form $Ca_{x/3}Ta_{1-x/3}O_{2+y}N_{1-y}$($0 \leq x, y \leq 1$), XRD data of the different solid compositions showed the formation of the perovskite phase for each composition.[193] This is attributed to the existence of the tantalum perovskite oxynitride $CaTaO_2N$. As they increased the proportion of the doping metal (Ca), the perovskite structure was able to accommodate the higher Ca^{2+} percentage, however, DFT calculations carried out by Li et al. showed that the $MgTaO_2N$, Na^+ and K^+ are not formable in the perovskite structure.[119]

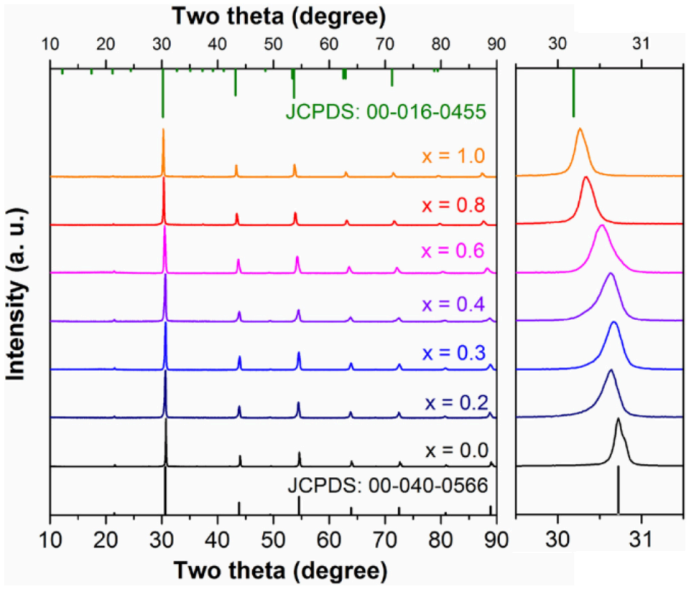

Figure 93. X-Ray powder diffraction patterns of the $Ca_{x/3}Ta_{1-x/3}O_{2+y}N_{1-y}$($0 \leq x, y \leq 1$). Adapted from ref.[193]

Finally, the solid composition $SrNb_{1-x}Mg_x(O,N)_3$, $SrNb_{1-x}Na_x(O,N)_3$ and $SrNb_{1-x}K_x(O,N)_3$ showed phase purity, indicating that the cation has been perfectly allocated into the lattice, within the solid solutions; $SrNb_{1-x}Na_x(O,N)_3$ & $SrNb_{1-x}K_x(O,N)_3$;$0.05 \leq x \geq 0.2$, $SrNb_{1-x}Na_x(O,N)_3$; $0.05 \leq x \geq 0.4$ *and* $SrNb_{1-x}Na_x(O,N)_3$; $x = 0.05 \leq x \geq 0.8$.

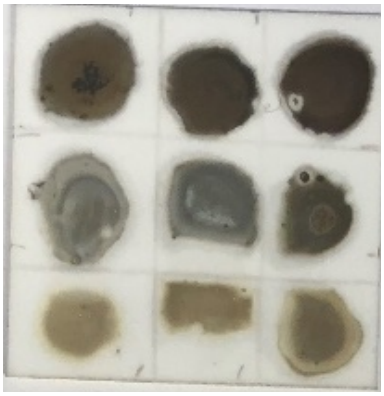

0.05	0.1	0.2
0.3	0.4	0.5
0.6	0.7	0.8

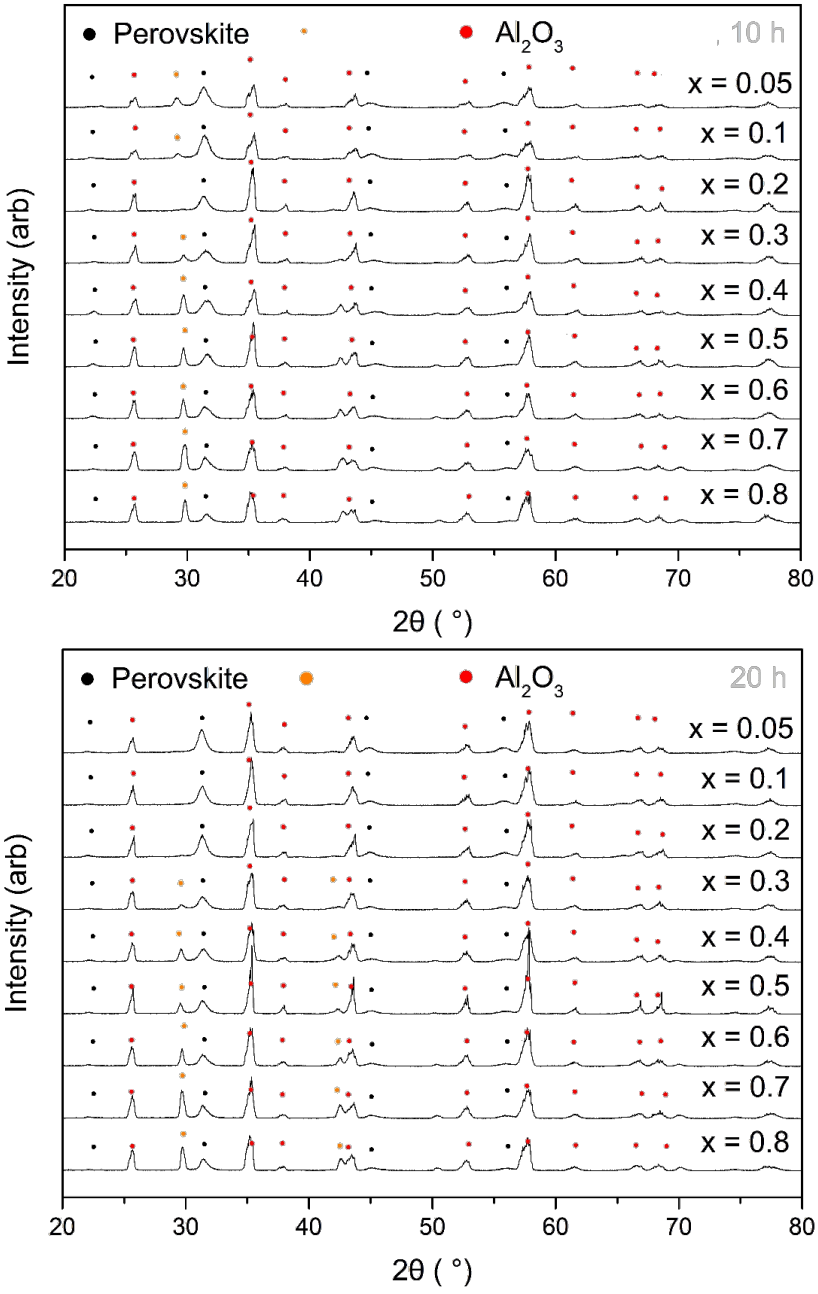

Figure 94. Photographic image of the $SrNb_{1-x}Na_x(O,N)_3$ thin film ammonolysed for 10 hours and grazing incidence X-ray diffraction (GI-XRD) data of the different compositions.

$SrNb_{1-x}K_x(O,N)_3$, where x = 0.05 - 0.8:

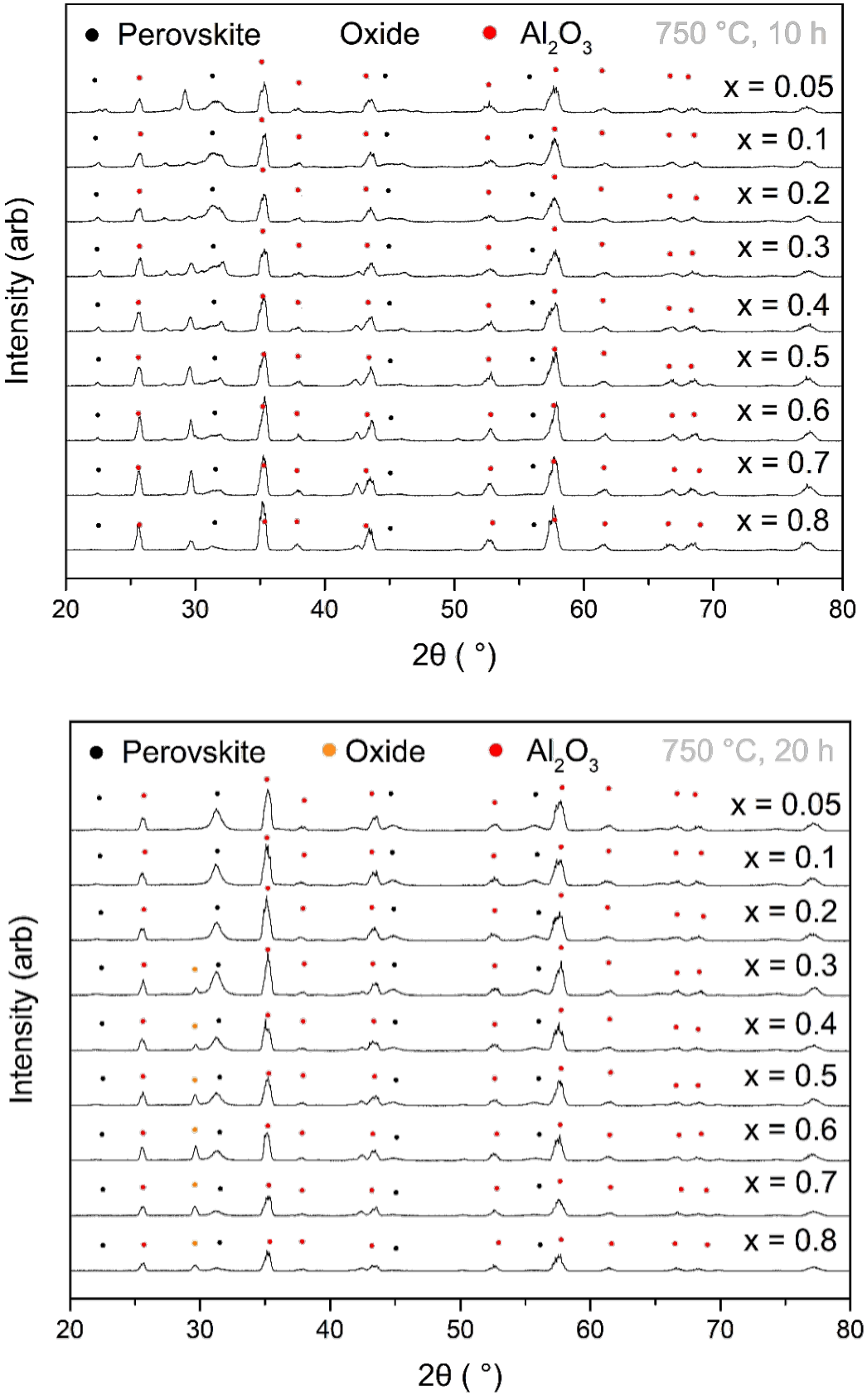

Figure 95. Grazing Incidence X-ray diffraction (GI-XRD) data of the $SrNb_{1-x}K_x(O,N)_3$ compositions.

$SrNb_{1-x}Mg_x(O,N)_3$, where x = 0.05 - 0.8:

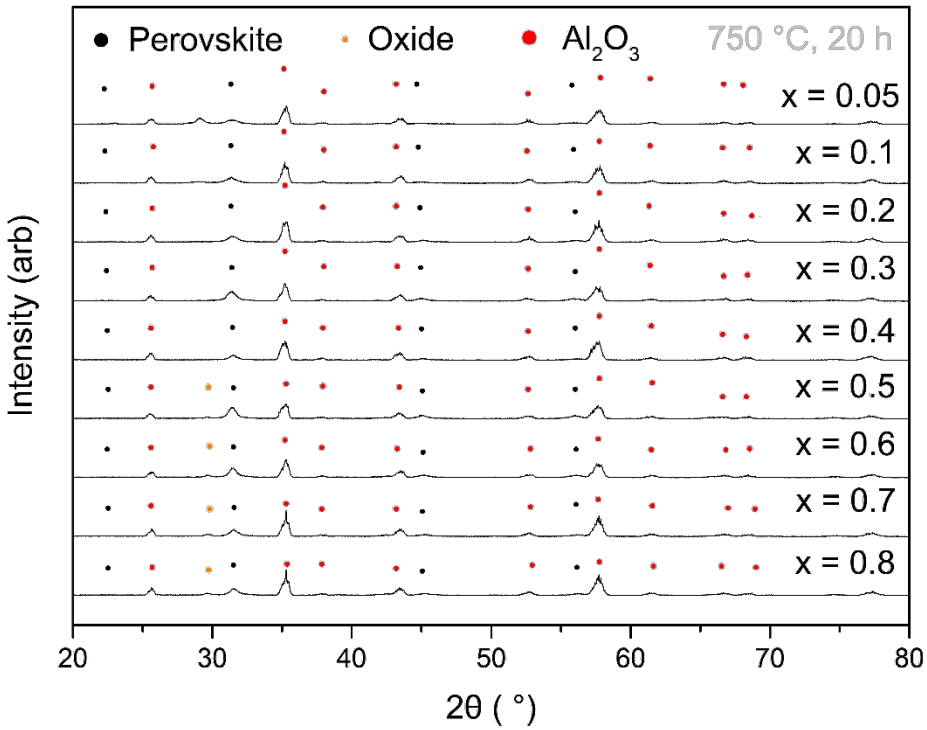

Figure 96. Grazing Incidence X-ray diffraction (GI-XRD) data of the $SrNb_{1-x}Mg_x(O,N)_3$ compositions.

6.3.2 Photocatalytic screening of the $SrNb_{1-x}Na_x(O, N)_3$ solid composition.

An assessment of the photocatalytic activity of the multi-compositional thin films was carried out using the DCIP degradation test under solely visible light. Based on the Langmuir-Hinshelwood, pseudo first-order rate constants were determined by adjusting a linear fit to the plot of the logarithm of the ratio of the dye concentration to initial concentration against time, as previously mentioned in Chapter 5. These obtained values are shown in Figure 97.

Amongst the nine different compositions, the sample containing x = 0.01 showed the highest photocatalytic activity followed by the composition containing x= 0.03, with a first-order rate constants of 30 × 10^{-4} min^{-1} and 24.1 × 10^{-4} min^{-1}, respectively. Surprisingly, samples where x= 0.05 and 0.8 did not show any measurable photocatalytic activity. However, we recommend performing three series of DCIP degradation tests in order to reduce any analytical errors and data variation in order to obtain a reliable value.

Table 28. DCIP degradation profiles of the materials library $SrNb_{1-x}Na_x(O, N)_3$.

(a) x = 0.05

No photocatalytic activity

(b) x = 0.1

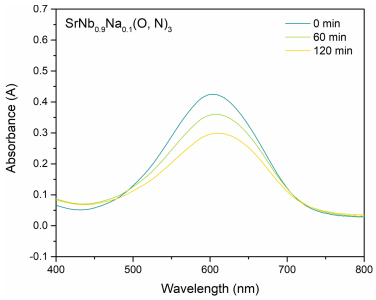

(c) x = 0.2

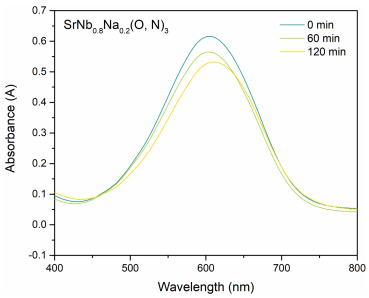

(b) x = 0.3

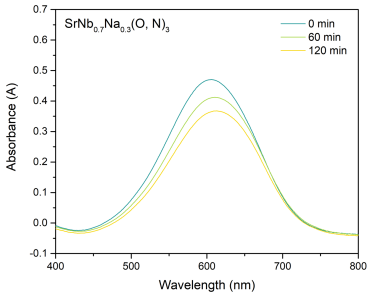

(b) x = 0.4

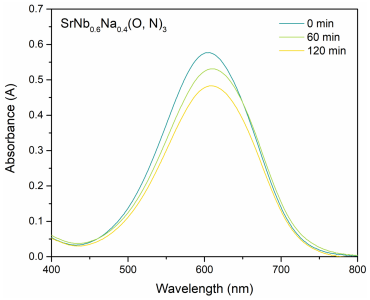

(c) x = 0.5

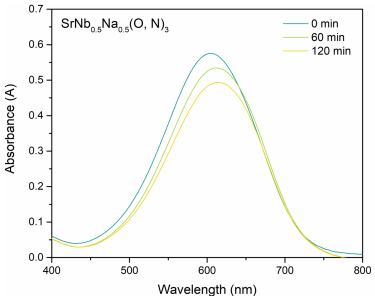

(c) x = 0.6

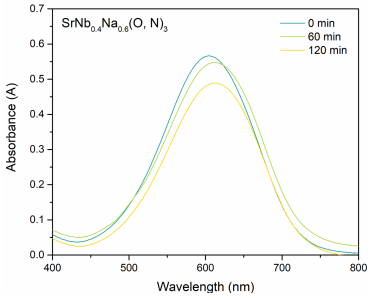

(b) x = 0.7

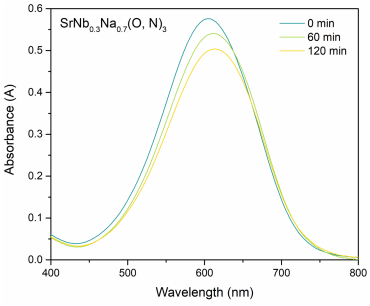

(c) x = 0.8

No photocatalytic activity

The $SrNb_{1-x}K_x(O, N)_3$ thin film was analysed following the same procedure. In this case, all samples revealed considerable photocatalytic activities. The samples containing x = 0.1 and x = 0.2 exhibited the highest first-order rate constants of 17.2 × 10^{-4} min $^{-1}$ and 20.7 × 10^{-4} min $^{-1}$, respectively. In both cases and as a general trend, as we increase the amount of the doping cation, the photocatalytic activities decrease. This can be explained as when increasing the proportion of the metal cation, the perovskite structure is not able to accommodate the K^+ and Na^+ since $SrK(O,N)_3$ and $SrNa(O,N)_3$ have been predicted to not be stable in the perovskite structure.[119] Consequently, as increasing the metal cation content the compositions are composed with two different phases, an oxynitride phase and a white Na^+ and K^+-containing metal oxide with no photocatalytic activity.

At this point, we were not able to demonstrate if the doping resulted in an enhanced photocatalytic activity compared to pure $SrNbO_2N$. This is mainly because the photocatalytic conditions at this stage are different.

Table 29. DCIP degradation profiles of the materials library $SrNb_{1-x}K_x(O, N)_3$.

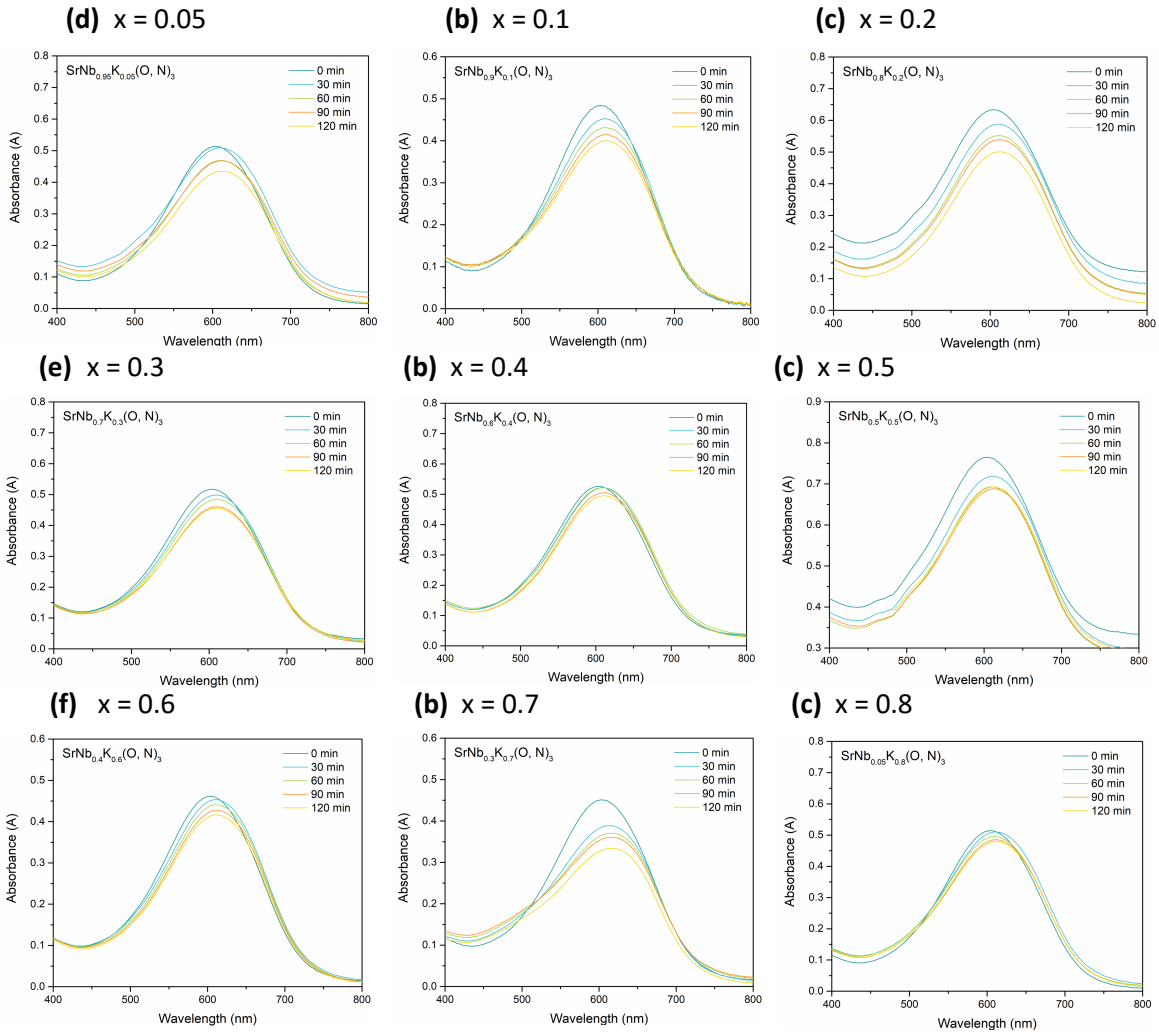

The DCIP degradation tests in Chapter 5 used 12 ml of DCIP/glycerol solution and a photocatalitically active surface area of 6.25 cm^2, while the miniaturised DCIP tests during the photocatalytic screening required only 1.5 ml of DCIP-glycerol solution and an approximate photocatalitically active surface are of 0.16 cm^2. Thus, the photocatalyst screening is a previous step to the scale-up which consist on identifying potential samples with the highest photocatalytic activities for a posterior synthesis and full analysis.

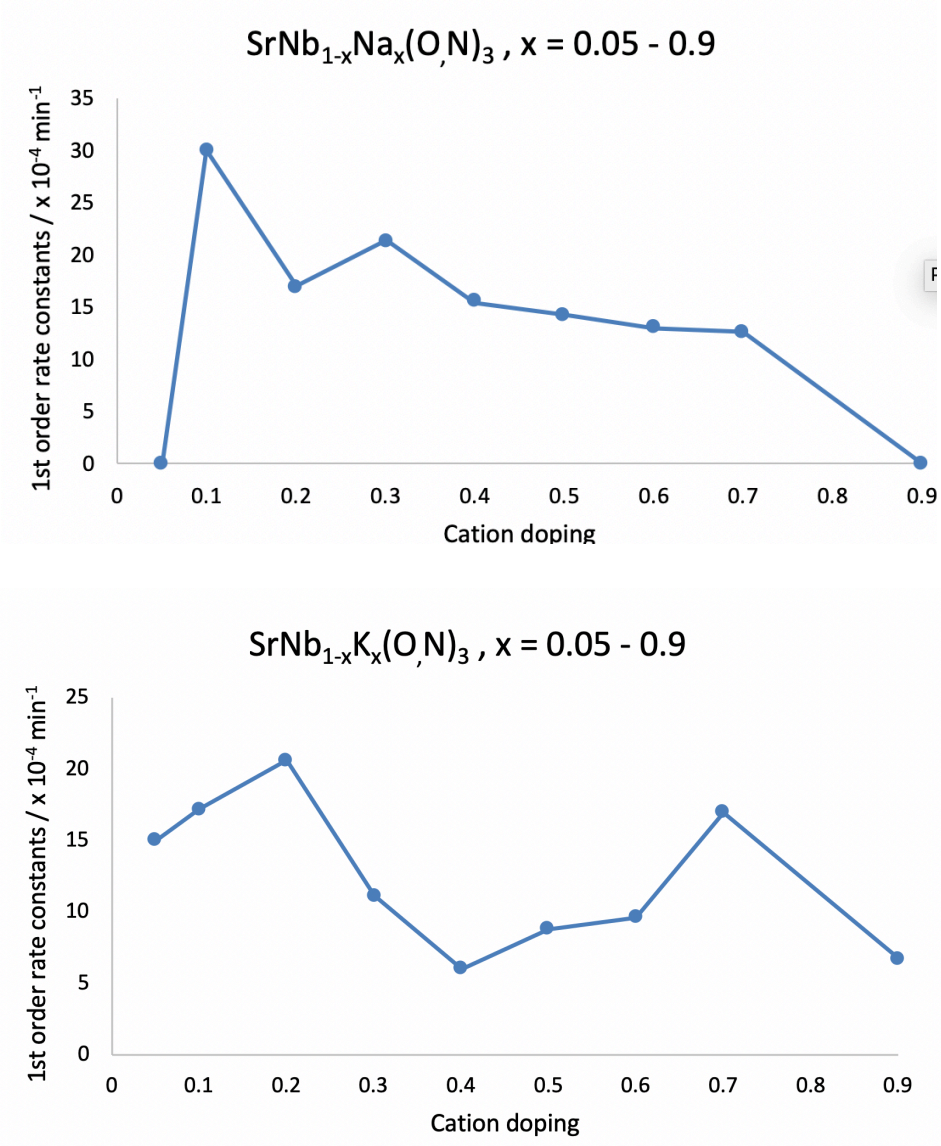

Figure 97. Formal Quantum Yields (FQY) for the composition and **(a)** $SrNb_{1-x}Na_x(O, N)_3$, and **(b)** $SrNb_{1-x}K_x(O, N)_3$ where x = 0.05 – 0.9.

The novel method described in this Chapter allowed us for a fast synthesis of a materials library containing a large amount of different compositions, with a subsequent photocatalytic screening identifying the most active samples, while reducing the amounts of reagents and materials required.

Chapter 7 Conclusions and Future Work

The aim of this thesis was to identify, synthesise and asses the photocatalyst activity of tantalum, niobium and titanium perovskite oxynitrides as thin films. For this we have reported the synthesis of the oxynitrides $CaTaO_2N$, $SrTaO_2N$, $BaTaO_2N$, $LaTaON_2$, $EuTaO_2N$, $SrNbO_2N$, $LaNbON_2$, and $LaTiO_2N$ as powders and as thin films. The photocatalytic activity of each thin films was assessed by dye degradation and the most active samples were tested for stearic acid degradations. Finally, we addressed a method based on the manual ink-jet printing for the synthesis of a materials library and subsequent screening of the different compositions.

The main contributions can be summarised as:

- Synthesis of the perovskite oxynitrides $CaTaO_2N$, $SrTaO_2N$, $BaTaO_2N$, $LaTaON_2$, $EuTaO_2N$, $SrNbO_2N$ and $LaNbON_2$, $LaTiO_2N$ as powders in Chapter 3. The oxide precursor powders were prepared by the polymeric precursor method (Pechini method), making use of citric acid and propylene glycol to promote the formation of a polymer resin containing the metal cations homogenously distributed. Each resin was annealed in air to obtain a white oxide powder precursor. Finally, the samples were converted to the oxynitride phase by partial substitution of the O^{2-} anions by N^{3-}. This step, known as ammonolysis, makes uses of a flow of dry NH_3 flowing through a tube furnace (reactor) promoting nitridation of the oxide precursor. In this context, perovskite oxynitride phase purity was achieved in the temperature range of 850-1000 ˚C, a flowing rate of 250 ml min^{-1}, a heating ramp of 3˚C min^{-1} and reaction time of 10 hours up to 54 hours. Phase purity was confirmed by XRD, Rietveld analysis and DRS spectra were recorder for each sample. Optical band gaps were calculated from the Tauc plot derived from the Kubelka-Munk function and were found in the range of 1.70-2.4 eV. All the perovskite oxynitrides showed bright colours from red ($BaTaO_2N$) to yellow for $CaTaO_2N$ and orange for $SrTaO_2N$. Niobium analogues showed darker colours due to the higher electronegativity of niobium, thus, the energetic position of the conduction band is displaced downwards leading to narrower band gaps.

- The optimised synthetic conditions of the powder perovskite oxynitrides were applied to their synthesis as thin films in Chapter 4. For the formation of the thin films, different deposition methods were studied, but due to its easy and convenient operationality and low cost, dip-coating was chosen. For this, the polymeric resins obtained (Chapter 3) were dip-coated onto 2.5 x 2.5 x 2.5 cm alumina tiles and calcined under air to obtain a white oxide precursor thin film. Each thin film was ammonolysed according to the

synthetic conditions optimised in Chapter 3, resulted in coloured thin films. Oxynitride phase was determined by GI-XRD and confirmed using Le Bail refinement. For each thin film, optical band gap was calculated and compared with the data previously obtained and reported in the literature. Both, XRD refinements and band gaps values confirmed our efforts in synthesising for the first time perovskite oxynitrides as thin films for self-cleaning applications under visible light.

- In order to assess the photocatalytic activities, the perovskite oxynitrides thin films were loaded with a co-catalyst (0.30 μg cm^{2-} of cobalt), which has previously been reported to enhance the rate of reaction. DCIP dye testing allowed us to identify the most active samples and the optimal co-catalyst loading. Among all the samples, the films of $EuTaO_2N$ and $BaTaO_2N$ showed no significant change in dye concentration over 180 mins test time. The $LaNbON_2$ and $LaTaON_2$ showed small reductions in the DCIP concentration of 3-5% after 180 mins. The samples $SrTaO_2N$, $CaTaO_2N$ and $SrNbO_2N$ showed higher reductions of 9, 26 and 46 %, respectively. Assuming the Langmuir-Hinshelwood kinetics model, we obtained relatively small first-order rate constants of 1.6(4) × 10−4 min^{-1}, 2.3(5) × 10^{-4} min^{-1}, and 5.0(1) × 10^{-4} min^{-1} for $LaTaON_2$, $LaNbON_2$, and $SrTaO_2N$, respectively. The two most active samples $CaTaO_2N$ and $SrNbO_2N$ have much higher initial rate constants of 24.3(5) × 10^{-4} min^{-1} and 64(5) × 10^{-4} min^{-1}. The co-catalyst concentration was studied at nominal surface concentrations of 0.04-0.46 μg cm^{-2}, however, for all samples, a co-catalyst loading of 0.3 μg cm^{-2} resulted to be the optimal one providing an equilibrium between sufficient active sites for the degradation to occur without beginning to block the light from reaching the underlying photocatalyst. The most active sample, the $SrNbO_2N$ thin films, was further investigated using SEM and EDX mapping and XPS. SEM images showed the fragmentation of the $SrNbO_2N$ thin film into islands of 2 -10 μm attributed to the shrinkage. Higher magnifications showed that the islands are composed of particles within the range of 30-40 nm, consistent with the crystallite sizes determined by XRD of 27 nm . Additionally, cross-sectional SEM allowed us to estimate the overall thickness of the film of 450-500 nm. The three most active samples $SrTaO_2N$, $CaTaO_2N$ and $SrNbO_2N$ were tested for photocatalytic degradation of stearic acid. The protocol for stearic acid degradation test requires a transparent substrate, for this, quartz substrates were protected by depositing a thin film of alumina by AACVD. This allowed us to dip-coat the resins onto the protected quartz substrate preventing side reactions of the perovskite phase with the quartz during the ammonolysis. The oxynitrides were obtained replicating the synthetic conditions from Chapter 4. The $SrTaO_2N$, $CaTaO_2N$ and $SrNbO_2N$ thin films were able to degrade a 15.4,

8.4 and 8.4 % of the stearic acid film after two h. The degradation of the stearic acid appears to follow first-order kinetics and plots of $ln(C/C_0)$ *vs* time allow for the rate constants to be determined. This analysis gave a value of $14(2) \times 10^{-4}$ min^{-1} for $SrNbO_2N$, $8(1) \times 10^{-4}$ min^{-1} for $SrTaO^2N$, and $7.8(6) \times 10{-}4$ min^{-1} for $CaTaO^2N$. In line with the results from the DCIP dye testing, the $SrNbO_2N$ thin film was the most active sample.

- In Chapter 6 we propose, as part of the future work, a novel and innovative method for the synthesis of a materials library and subsequent screening of the photocatalytic activities of the different constituting compositions. For this, different inks containing a single metal cation are prepared by the polymeric precursor method. Using a micropipette, a calculated amount of each ink is deposited into an Eppendorf Tube and sonicated to ensure homogenization, resulting in a final ink. The materials library is prepared by depositing 5 µl of the final ink solution into the alumina substrate, to a total of nine different compositions. The alumina substrate containing the different compositions are thermally treated in air to obtain the oxide precursors and ammonolysed to obtain the final doped oxynitrides. In our case, and based in the previously reported literature, we reported the doping of our most active oxynitride $SrNbO_2N$ with alkaline (Na, K) and alkaline earth (Mg) metal ions. However, more experiments using different synthetic conditions such as longer reaction times and higher temperatures and further characterisation are required to fully understand the formation of the alkali and alkaline earth doped $SrNbO_2N$.

References

1. Montoya, J. H. *et al.* Materials for solar fuels and chemicals. *Nat. Mater.* **16**, 70–81 (2016).

2. Maeda, K. & Domen, K. Photocatalytic water splitting: Recent progress and future challenges. *J. Phys. Chem. Lett.* **1**, 2655–2661 (2010).

3. Montoya, J. H. *et al.* Materials for solar fuels and chemicals. *Nat. Mater.* **16**, 70–81 (2016).

4. Atkinson, R. Atmospheric chemistry of VOCs and NO(x). *Atmos. Environ.* **34**, 2063–2101 (2000).

5. Finlayson-Pitts, B. J. & Pitts, J. N. Atmospheric chemistry of tropospheric ozone formation: Scientific and regulatory implications. *Air Waste* **43**, 1091–1100 (1993).

6. Chang, X., Wang, T. & Gong, J. CO 2 photo-reduction: insights into CO 2 activation and reaction on surfaces of photocatalysts. *Energy Environ. Sci* **9**, 2177 (2016).

7. Kamat, P. V. & Bisquert, J. Solar fuels. Photocatalytic hydrogen generation. *Journal of Physical Chemistry C* vol. 117 14873–14875 (2013).

8. Paleocrassas, S. N. Photocatalytic hydrogen production: A solar energy conversion alternative? *Solar Energy* vol. 16 45–51 (1974).

9. Ahmed, M. & Xinxin, G. A review of metal oxynitrides for photocatalysis. *Inorg. Chem. Front.* **3**, (2016).

10. Fujishima, A. & Honda, K. Electrochemical photolysis of water at a semiconductor electrode. *Nature* **238**, 37–8 (1972).

11. Zhao, X. *et al.* New insight into the roles of oxygen vacancies in hematite for solar water splitting. *Phys. Chem. Chem. Phys.* **19**, 1074–1082 (2017).

12. Allain, E. *et al.* Transparent mesoporous nanocomposite films for self-cleaning applications. *Adv. Funct. Mater.* **17**, 549–554 (2007).

13. Rathouský, J., Kalousek, V., Kolář, M., Jirkovský, J. & Barták, P. A study into the self-cleaning surface properties - The photocatalytic decomposition of oleic acid. *Catal. Today* **161**, 202–208 (2011).

14. Web of Science. Web of Science Service for UK Education. *wok.mimas.ac.uk* http://wok.mimas.ac.uk/ (2018).

15. Page, K. Photocatalytic thin films: their characterisation and antimicrobial properties. 198 (2009).

16. Binas, V., Venieri, D., Kotzias, D. & Kiriakidis, G. Modified TiO2 based photocatalysts for improved air and health quality. *Journal of Materiomics* vol. 3 3–16 (2017).

17. Mills, A. *et al.* Characterisation of the photocatalyst Pilkington Activ^{TM}: A reference film

photocatalyst? *J. Photochem. Photobiol. A Chem.* **160**, 213–224 (2003).

18. Silva, J. R. *et al.* Light, photosynthetic capacity and growth of papaya (Carica papaya L.): A short review. *Aust. J. Crop Sci.* **13**, 480–485 (2019).

19. Jalvo, B., Faraldos, M., Bahamonde, A. & Rosal, R. Antimicrobial and antibiofilm efficacy of self-cleaning surfaces functionalized by TiO2 photocatalytic nanoparticles against Staphylococcus aureus and Pseudomonas putida. *J. Hazard. Mater.* **340**, 160–170 (2017).

20. Daghrir, R., Drogui, P. & Robert, D. Modified TiO2 for environmental photocatalytic applications: A review. *Ind. Eng. Chem. Res.* **52**, 3581–3599 (2013).

21. Maeda, K. Photocatalytic water splitting using semiconductor particles: History and recent developments. *J. Photochem. Photobiol. C Photochem. Rev.* **12**, 237–268 (2011).

22. Hossain, A., Bandyopadhyay, P. & Roy, S. An overview of double perovskites A2B'B"O6 with small ions at A site: Synthesis, structure and magnetic properties. *Journal of Alloys and Compounds* vol. 740 414–427 (2018).

23. Misra, A. J. *et al.* Doped ZnO nanoparticles impregnated on Kaolinite (Clay): A reusable nanocomposite for photocatalytic disinfection of multidrug resistant Enterobacter sp. under visible light. *J. Colloid Interface Sci.* **530**, 610–623 (2018).

24. Sun, L. *et al.* Antibacterial Activity of Graphene Oxide/g-C3N4 Composite through Photocatalytic Disinfection under Visible Light. *ACS Sustain. Chem. Eng.* **5**, 8693–8701 (2017).

25. Dhakshinamoorthy, A., Asiri, A. M. & García, H. Metal-Organic Framework (MOF) Compounds: Photocatalysts for Redox Reactions and Solar Fuel Production. *Angew. Chemie Int. Ed.* **55**, 5414–5445 (2016).

26. Fuertes, A. Metal oxynitrides as emerging materials with photocatalytic and electronic properties. *Mater. Horizons* **2**, 453–461 (2015).

27. Kudo, A. & Miseki, Y. Heterogeneous photocatalyst materials for water splitting. *Chem. Soc. Rev.* **38**, 253–278 (2009).

28. Li, R. & Li, C. Photocatalytic Water Splitting on Semiconductor-Based Photocatalysts. in *Advances in Catalysis* vol. 60 1–57 (2017).

29. Lee, J. S. Photocatalytic water splitting under visible light with particulate semiconductor catalysts. *Catalysis Surveys from Asia* vol. 9 217–227 (2005).

30. Maeda, K. & Domen, K. Photocatalytic Water Splitting: Recent Progress and Future Challenges. *J. Phys. Chem. Lett.* **1**, 2655–2661 (2010).

31. Peters, G. P. *et al.* Carbon dioxide emissions continue to grow amidst slowly emerging climate policies. *Nature Climate Change* vol. 10 3–6 (2020).

32. Doney, S. C., Fabry, V. J., Feely, R. A. & Kleypas, J. A. Ocean Acidification: The Other CO 2 Problem . *Ann. Rev. Mar. Sci.* **1**, 169–192 (2009).

33. Andersson, A. J. & Gledhill, D. Ocean Acidification and Coral Reefs: Effects on Breakdown, Dissolution, and Net Ecosystem Calcification. *Ann. Rev. Mar. Sci.* **5**, 321–348 (2013).

34. Halmann, M. Photoelectrochemical reduction of aqueous carbon dioxide on p-type gallium phosphide in liquid junction solar cells [5]. *Nature* vol. 275 115–116 (1978).

35. Zeng, S., Kar, P., Thakur, U. K. & Shankar, K. A review on photocatalytic CO2 reduction using perovskite oxide nanomaterials. *Nanotechnology* **29**, 052001 (2018).

36. Kalamaras, E., Maroto-Valer, M. M., Shao, M., Xuan, J. & Wang, H. Solar carbon fuel via photoelectrochemistry. *Catal. Today* **317**, 56–75 (2018).

37. Marszewski, M., Cao, S., Yu, J. & Jaroniec, M. Semiconductor-based photocatalytic CO2 conversion. *Materials Horizons* vol. 2 261–278 (2015).

38. Ma, Y. *et al.* Titanium dioxide-based nanomaterials for photocatalytic fuel generations. *Chemical Reviews* vol. 114 9987–10043 (2014).

39. Lingampalli, S. R., Ayyub, M. & Rao, C. N. R. Recent Progress in the Photocatalytic Reduction of Carbon Dioxide. (2017) doi:10.1021/acsomega.7b00721.

40. Mangrulkar, P. A. *et al.* Photocatalytic Degradation of Phenolics by N-Doped Mesoporous Titania under Solar Radiation. *Int. J. Photoenergy* **2012**, 1–10 (2012).

41. Ong, S. W. D., Lin, J. & Seebauer, E. G. Control of methylene blue photo-oxidation rate over polycrystalline anatase TiO2 thin films via carrier concentration. *J. Phys. Chem. C* **119**, 11662–11671 (2015).

42. Boxi, S. S. & Paria, S. Visible light induced enhanced photocatalytic degradation of organic pollutants in aqueous media using Ag doped hollow TiO2 nanospheres. *RSC Adv.* **5**, 37647–37668 (2015).

43. Tayade, R. J., Kulkarni, R. G. & Jasra, R. V. Photocatalytic degradation of aqueous nitrobenzene by nanocrystalline TiO2. *Ind. Eng. Chem. Res.* **45**, 922–927 (2006).

44. Sun, W. J., Li, J., Yao, G. P., Jiang, M. & Zhang, F. X. Efficient photo-degradation of 4-nitrophenol by using new CuPp-TiO 2 photocatalyst under visible light irradiation. *Catal. Commun.* **16**, 90–93 (2011).

45. Parul, Kaur, K., Badru, R., Singh, P. P. & Kaushal, S. Photodegradation of organic pollutants using heterojunctions: A review. *J. Environ. Chem. Eng.* **8**, 103666 (2020).

46. Wilhelm, P. & Stephan, D. Photodegradation of rhodamine B in aqueous solution via SiO2@TiO2 nano-spheres. *J. Photochem. Photobiol. A Chem.* **185**, 19–25 (2007).

47. Kafizas, A., Mills, A. & Parkin, I. P. A comprehensive aerosol spray method for the rapid photocatalytic grid area analysis of semiconductor photocatalyst thin films. *Anal. Chim. Acta* **663**, 69–76 (2010).

48. Mutalib, M. A. *et al.* Enhancement in photocatalytic degradation of methylene blue by LaFeO3-GO integrated photocatalyst-adsorbents under visible light irradiation. *Korean J.*

Chem. Eng. **35**, 548–556 (2018).

49. Nogueira, A. C. *et al.* Improved Visible Light Photoactivity of CuBi2O4/CuO Heterojunctions for Photodegradation of Methylene Blue and Metronidazole. *J. Phys. Chem. C* **123**, 25680–25690 (2019).

50. Demircivi, P. & Simsek, E. B. Visible-light-enhanced photoactivity of perovskite-type W-doped BaTiO3 photocatalyst for photodegradation of tetracycline. *J. Alloys Compd.* **774**, 795–802 (2019).

51. Wen, X. J. *et al.* Photocatalytic degradation of ciprofloxacin by a novel Z-scheme CeO2–Ag/AgBr photocatalyst: Influencing factors, possible degradation pathways, and mechanism insight. *J. Catal.* **358**, 141–154 (2018).

52. Górska, P., Zaleska, A. & Hupka, J. Photodegradation of phenol by UV/TiO2 and Vis/N,C-TiO2 processes: Comparative mechanistic and kinetic studies. *Sep. Purif. Technol.* **68**, 90–96 (2009).

53. Sharma, A. & Lee, B. K. Rapid photo-degradation of 2-chlorophenol under visible light irradiation using cobalt oxide-loaded TiO2/reduced graphene oxide nanocomposite from aqueous media. *J. Environ. Manage.* **165**, 1–10 (2016).

54. Wang, R. *et al.* Light-induced amphiphilic surfaces [4]. *Nature* vol. 388 431–432 (1997).

55. Mills, A., Hill, G., Bhopal, S., Parkin, I. P. & Neill, S. A. O. '. Thick titanium dioxide films for semiconductor photocatalysis. *J. Photochem. Photobiol. A Chem.* **160**, 185–194 (2003).

56. Sontakke, S., Mohan, C., Modak, J. & Madras, G. Visible light photocatalytic inactivation of Escherichia coli with combustion synthesized TiO 2. *Chem. Eng. J.* **189**–**190**, 101–107 (2012).

57. You, J., Guo, Y., Guo, R. & Liu, X. A review of visible light-active photocatalysts for water disinfection: Features and prospects. *Chemical Engineering Journal* vol. 373 624–641 (2019).

58. Xia, D. *et al.* Enhanced photocatalytic inactivation of Escherichia coli by a novel Z-scheme g-C3N4/m-Bi2O4 hybrid photocatalyst under visible light: The role of reactive oxygen species. *Appl. Catal. B Environ.* **214**, 23–33 (2017).

59. Shenawi-Khalil, S., Uvarov, V., Fronton, S., Popov, I. & Sasson, Y. A novel heterojunction BiOBr/bismuth oxyhydrate photocatalyst with highly enhanced visible light photocatalytic properties. *J. Phys. Chem. C* **116**, 11004–11012 (2012).

60. Zhou, T. *et al.* Post-synthesis modification of a metal-organic framework to construct a bifunctional photocatalyst for hydrogen production. *Energy Environ. Sci.* **6**, 3229–3234 (2013).

61. Sun, D. *et al.* Noble metals can have different effects on photocatalysis over metal-organic frameworks (MOFs): A case study on M/NH2-MIL-125(Ti) (M=Pt and Au). *Chem. - A Eur. J.* **20**, 4780–4788 (2014).

62. Liu, B. *et al.* Visible-light-driven TiO2/Ag3PO4 heterostructures with enhanced antifungal activity against agricultural pathogenic fungi Fusarium graminearum and mechanism insight. *Environ. Sci. Nano* **4**, 255–264 (2017).

63. Rajamanickam, D., Dhatshanamurthi, P. & Shanthi, M. Enhanced photocatalytic efficiency of NiS/TiO2 composite catalysts using sunset yellow, an azo dye under day light illumination. *Mater. Res. Bull.* **61**, 439–447 (2015).

64. Wang, Y., Wu, Y., Yang, H., Xue, X. & Liu, Z. Doping TiO2 with boron or/and cerium elements: Effects on photocatalytic antimicrobial activity. *Vacuum* **131**, 58–64 (2016).

65. Charanpahari, A. *et al.* Enhanced photocatalytic activity of multi-doped TiO 2 for the degradation of methyl orange. *Appl. Catal. A Gen.* **443**–**444**, 96–102 (2012).

66. Santos, D. M. D. L. *et al.* MoS2/Cu/TiO2 nanoparticles: Synthesis, characterization and effect on photocatalytic decomposition of methylene blue in water under visible light. *Water Sci. Technol.* **2017**, 184–193 (2018).

67. Hong, X. *et al.* Hydroxyapatite supported Ag 3 PO 4 nanoparticles with higher visible light photocatalytic activity. *Appl. Surf. Sci.* **258**, 4801–4805 (2012).

68. Ramasamy Raja, V., Rani Rosaline, D., Suganthi, A. & Rajarajan, M. Ultrasonic assisted synthesis with enhanced visible-light photocatalytic activity of NiO/Ag3VO4 nanocomposite and its antibacterial activity. *Ultrason. Sonochem.* **44**, 73–85 (2018).

69. Hu, X. & Hu, C. Selective photocatalytic degradation of azodyes in NiO/Ag 3 VO 4 suspension. doi:10.1002/jctb.2462.

70. Hashemizadeh, S., Biancoli, A. & Damjanovic, D. Symmetry breaking in hexagonal and cubic polymorphs of BaTiO3. *J. Appl. Phys.* **119**, 094105 (2016).

71. Silva, C. G., Luz, I., Llabrés I Xamena, F. X., Corma, A. & García, H. Water stable Zr-Benzenedicarboxylate metal-organic frameworks as photocatalysts for hydrogen generation. *Chem. - A Eur. J.* **16**, 11133–11138 (2010).

72. Sun, D., Liu, W., Qiu, M., Zhang, Y. & Li, Z. Introduction of a mediator for enhancing photocatalytic performance via post-synthetic metal exchange in metal-organic frameworks (MOFs). *Chem. Commun.* **51**, 2056–2059 (2015).

73. He, J. *et al.* A dye-sensitized Pt*UiO-66(Zr) metal–organic framework for visible-light photocatalytic hydrogen production. *Chem. Commun.* **50**, 7063–7066 (2014).

74. Yuan, Y. P. *et al.* Improving photocatalytic hydrogen production of metal-organic framework UiO-66 octahedrons by dye-sensitization. *Appl. Catal. B Environ.* **168**–**169**, 572–576 (2015).

75. Toyao, T. *et al.* Development of a Ru complex-incorporated MOF photocatalyst for hydrogen production under visible-light irradiation. *Chem. Commun.* **50**, 6779–6781 (2014).

76. Dekrafft, K. E., Wang, C. & Lin, W. Metal-organic framework templated synthesis of Fe 2O 3/TiO 2 nanocomposite for hydrogen production. *Adv. Mater.* **24**, 2014–2018 (2012).

77. He, J. *et al.* Significantly enhanced photocatalytic hydrogen evolution under visible light over CdS embedded on metal–organic frameworks. *Chem. Commun.* **49**, 6761–6763 (2013).

78. Lin, R. *et al.* Enhanced photocatalytic hydrogen production activity via dual modification of MOF and reduced graphene oxide on CdS. *Chem. Commun.* **50**, 8533–8535 (2014).

79. Horiuchi, Y. *et al.* Visible-light-promoted photocatalytic hydrogen production by using an amino-functionalized Ti(IV) metal-organic framework. *J. Phys. Chem. C* **116**, 20848–20853 (2012).

80. Toyao, T. *et al.* Efficient hydrogen production and photocatalytic reduction of nitrobenzene over a visible-light-responsive metal-organic framework photocatalyst. *Catal. Sci. Technol.* **3**, 2092–2097 (2013).

81. Shen, L., Luo, M., Huang, L., Feng, P. & Wu, L. A clean and general strategy to decorate a titanium metal-organic framework with noble-metal nanoparticles for versatile photocatalytic applications. *Inorg. Chem.* **54**, 1191–1193 (2015).

82. Nasalevich, M. A. *et al.* Co@NH2-MIL-125(Ti): Cobaloxime-derived metal-organic framework-based composite for light-driven H2 production. *Energy Environ. Sci.* **8**, 364–375 (2015).

83. Fu, Y. *et al.* An Amine-Functionalized Titanium Metal-Organic Framework Photocatalyst with Visible-Light-Induced Activity for CO2 Reduction. *Angew. Chemie* **124**, 3420–3423 (2012).

84. Sun, D. *et al.* Studies on photocatalytic CO2 reduction over NH 2-uio-66(Zr) and its derivatives: Towards a better understanding of photocatalysis on metal-organic frameworks. *Chem. - A Eur. J.* **19**, 14279–14285 (2013).

85. Wang, D., Huang, R., Liu, W., Sun, D. & Li, Z. Fe-based MOFs for photocatalytic CO2 reduction: Role of coordination unsaturated sites and dual excitation pathways. *ACS Catal.* **4**, 4254–4260 (2014).

86. Sun, D. *et al.* Construction of a supported Ru complex on bifunctional MOF-253 for photocatalytic CO2 reduction under visible light. *Chem. Commun.* **51**, 2645–2648 (2015).

87. Li, R. *et al.* Integration of an inorganic semiconductor with a metal-organic framework: A platform for enhanced gaseous photocatalytic reactions. *Adv. Mater.* **26**, 4783–4788 (2014).

88. Wang, S. & Wang, X. Photocatalytic CO2 reduction by CdS promoted with a zeolitic imidazolate framework. *Appl. Catal. B Environ.* **162**, 494–500 (2015).

89. Wang, S., Lin, J. & Wang, X. Semiconductor-redox catalysis promoted by metal-organic frameworks for CO2 reduction. in *Physical Chemistry Chemical Physics* vol. 16 14656–

14660 (Royal Society of Chemistry, 2014).

90. Liu, Q. *et al.* ZIF-8/Zn2GeO4 nanorods with an enhanced CO 2 adsorption property in an aqueous medium for photocatalytic synthesis of liquid fuel. *J. Mater. Chem. A* **1**, 11563–11569 (2013).

91. Lyu, H. *et al.* An Al-doped SrTiO3 photocatalyst maintaining sunlight-driven overall water splitting activity for over 1000 h of constant illumination. *Chem. Sci.* **10**, 3196–3201 (2019).

92. Fernández-Ibáñez, P. *et al.* Solar photocatalytic disinfection of water using titanium dioxide graphene composites. *Chem. Eng. J.* **261**, 36–44 (2015).

93. Cruz-Ortiz, B. R. *et al.* Mechanism of photocatalytic disinfection using titania-graphene composites under UV and visible irradiation. *Chem. Eng. J.* **316**, 179–186 (2017).

94. Yang, X. *et al.* Fabrication of P25/Ag3PO4/graphene oxide heterostructures for enhanced solar photocatalytic degradation of organic pollutants and bacteria. *Appl. Catal. B Environ.* **166**–**167**, 231–240 (2015).

95. Shim, J., Seo, Y. S., Oh, B. T. & Cho, M. Microbial inactivation kinetics and mechanisms of carbon-doped TiO2 (C-TiO2) under visible light. *J. Hazard. Mater.* **306**, 133–139 (2016).

96. Ananpattarachai, J., Boonto, Y. & Kajitvichyanukul, P. Visible light photocatalytic antibacterial activity of Ni-doped and N-doped TiO2 on Staphylococcus aureus and Escherichia coli bacteria. *Environ. Sci. Pollut. Res.* **23**, 4111–4119 (2016).

97. Milošević, I. *et al.* Synthesis and characterization of fluorinated anatase nanoparticles and subsequent N-doping for efficient visible light activated photocatalysis. *Colloids Surfaces B Biointerfaces* **171**, 445–450 (2018).

98. Stan, M. *et al.* Photocatalytic, Antimicrobial and Biocompatibility Features of Cotton Knit Coated with Fe-N-Doped Titanium Dioxide Nanoparticles. *Materials (Basel).* **9**, 789 (2016).

99. Eswar, N. K. R., Ramamurthy, P. C. & Madras, G. Novel synergistic photocatalytic degradation of antibiotics and bacteria using V-N doped TiO2 under visible light: The state of nitrogen in V-doped TiO2. *New J. Chem.* **40**, 3464–3475 (2016).

100. Zheng, X. *et al.* Photocatalytic disinfection performance in virus and virus/bacteria system by Cu-TiO2 nanofibers under visible light. *Environ. Pollut.* **237**, 452–459 (2018).

101. Guo, L., Shan, C., Liang, J., Ni, J. & Tong, M. Bactericidal mechanisms of Au@TNBs under visible light irradiation. *Colloids Surfaces B Biointerfaces* **128**, 211–218 (2015).

102. Xu, J., Wang, Z. & Zhu, Y. Enhanced Visible-Light-Driven Photocatalytic Disinfection Performance and Organic Pollutant Degradation Activity of Porous g-C3N4 Nanosheets. *ACS Appl. Mater. Interfaces* **9**, 27727–27735 (2017).

103. Ouyang, K. *et al.* Metal-free inactivation of E. coli O157:H7 by fullerene/C3N4 hybrid under visible light irradiation. *Ecotoxicol. Environ. Saf.* **136**, 40–45 (2017).

104. Zhang, C. *et al.* Visible-light-driven, water-surface-floating antimicrobials developed from

graphitic carbon nitride and expanded perlite for water disinfection. *Chemosphere* **208**, 84–92 (2018).

105. Ma, S., Zhan, S., Jia, Y., Shi, Q. & Zhou, Q. Enhanced disinfection application of Ag-modified g-C3N4 composite under visible light. *Appl. Catal. B Environ.* **186**, 77–87 (2016).

106. Gao, B. *et al.* Enhanced visible-light-driven photocatalytic performance of AgNbO3 cubes with a high-energy (001) facet. *J. Phys. Chem. Solids* **135**, 109083 (2019).

107. Lin, T. *et al.* Boron- and phenyl-codoped graphitic carbon nitride with greatly enhanced light responsive range for photocatalytic disinfection. *J. Hazard. Mater.* **358**, 62–68 (2018).

108. Wang, R. *et al.* Mechanism insight into rapid photocatalytic disinfection of Salmonella based on vanadate QDs-interspersed g-C3N4 heterostructures. *Appl. Catal. B Environ.* **225**, 228–237 (2018).

109. Hu, Z., Shen, Z. & Yu, J. C. Converting Carbohydrates to Carbon-Based Photocatalysts for Environmental Treatment. *Environ. Sci. Technol.* **51**, 7076–7083 (2017).

110. Zhang, B., Zou, S., Cai, R., Li, M. & He, Z. Highly-efficient photocatalytic disinfection of Escherichia coli under visible light using carbon supported Vanadium Tetrasulfide nanocomposites. *Appl. Catal. B Environ.* **224**, 383–393 (2018).

111. Lemanov, V. V., Sotnikov, A. V., Smirnova, E. P., Weihnacht, M. & Kunze, R. Perovskite CaTiO3 as an incipient ferroelectric. *Solid State Commun.* **110**, 611–614 (1999).

112. Polinger, V., Garcia-Fernandez, P. & Bersuker, I. B. Pseudo Jahn-Teller origin of ferroelectric instability in BaTiO3 type perovskites: The Green's function approach and beyond. *Phys. B Condens. Matter* **457**, 296–309 (2015).

113. King, G. & Woodward, P. M. Cation ordering in perovskites. *J. Mater. Chem.* **20**, 5785–5796 (2010).

114. Woodward, P. M. Octahedral Tilting in Perovskites. I. Geometrical Considerations. *Acta Crystallogr. Sect. B Struct. Sci.* **53**, 32–43 (1997).

115. Glazer, A. M. The classification of tilted octahedra in perovskites. *Acta Crystallogr. Sect. B Struct. Crystallogr. Cryst. Chem.* **28**, 3384–3392 (1972).

116. Howard, C. J. & Stokes, H. T. Group-Theoretical Analysis of Octahedral Tilting in Perovskites. *Acta Crystallogr. Sect. B Struct. Sci.* **54**, 782–789 (1998).

117. Siritanaratkul, B., Maeda, K., Hisatomi, T. & Domen, K. Synthesis and photocatalytic activity of perovskite niobium oxynitrides with wide visible-light absorption bands. *ChemSusChem* **4**, 74–78 (2011).

118. Marchand, R., Pors, F. & Laurent, Y. Préparation et caractérisation de nouveaux oxynitrures à structure perovskite. (1986).

119. Li, W., Ionescu, E., Riedel, R. & Gurlo, A. Can we predict the formability of perovskite oxynitrides from tolerance and octahedral factors? *J. Mater. Chem. A* **1**, 12239 (2013).

120. Dabrowski, B. *et al.* Tolerance factor rules for Sr1-x-yCaxBayMnO3 perovskites. *J. Solid State Chem.* **170**, 154–164 (2003).

121. Shannon, R. D. Revised effective ionic radii and systematic studies of interatomic distances in halides and chalcogenides. *Acta Crystallogr. Sect. A* **32**, 751–767 (1976).

122. Balaz, S., Porter, S. H., Woodward, P. M. & Brillson, L. J. Electronic Structure of Tantalum Oxynitride Perovskite Photocatalysts. *Chem. Mater.* **25**, 3337–3343 (2013).

123. Motohashi, T. *et al.* Structural phase transition in the perovskite-type tantalum oxynitrides, Ca1-xEuxTa(O,N)3. *Mater. Res. Bull.* **44**, 1899–1905 (2009).

124. Kumar, N., Sundaresan, A. & Rao, C. N. R. Rare earth niobium oxynitrides, LnNbON2−δ (Ln=Y, La, Pr, Nd, Gd, Dy): Synthesis, structure and properties. *Mater. Res. Bull.* **46**, 2021–2024 (2011).

125. Yashima, M. *et al.* Imma perovskite-type oxynitride LaTiO2N: structure and electron density. *Chem. Commun.* **46**, 4704 (2010).

126. Yang, M. *et al.* Anion order in perovskite oxynitrides. *Nat. Chem.* **3**, 47–52 (2011).

127. Kim, Y.-I. & Woodward, P. M. Band Gap Modulation of Tantalum(V) Perovskite Semiconductors by Anion Control. *Catalysts* **9**, 161 (2019).

128. Yang, M. *et al.* Anion order in perovskite oxynitrides. *Nat. Chem.* **3**, 47–52 (2011).

129. Kubo, A., Giorgi, G. & Yamashita, K. Anion Ordering in CaTaO2N: Structural Impact on the Photocatalytic Activity. Insights from First-Principles. *Chem. Mater.* **29**, 539–545 (2017).

130. Attfield, J. P. Principles and applications of anion order in solid oxynitrides. *Crystal Growth and Design* vol. 13 4623–4629 (2013).

131. Habu, D., Masubuchi, Y., Torii, S., Kamiyama, T. & Kikkawa, S. Crystal structure study of dielectric oxynitride perovskites La1-xSrxTiO2+xN1-x (x=0, 0.2). *J. Solid State Chem.* **237**, 254–257 (2016).

132. Jansen, M. & Letschert, H. P. Inorganic yellow-red pigments without toxic metals. *Nature* **404**, 980–982 (2000).

133. Aguiar, R. *et al.* The vast colour spectrum of ternary metal oxynitride pigments. *Dye. Pigment.* **76**, 70–75 (2008).

134. Upadhyay, S. *et al.* Enhanced photoelectrochemical response of BaTiO 3 with Fe doping: Experiments and first-principles analysis. *J. Phys. Chem. C* **115**, 24373–24380 (2011).

135. Qin, Y., Wang, G. & Wang, Y. Study on the photocatalytic property of La-doped CoO/SrTiO3 for water decomposition to hydrogen. *Catal. Commun.* **8**, 926–930 (2007).

136. Qu, Y. *et al.* Facile preparation of porous NiTiO 3 nanorods with enhanced visible-light-driven photocatalytic performance. *J. Mater. Chem.* **22**, 16471–16476 (2012).

137. Pei, J. *et al.* Hierarchical CaTiO3 nanowire-network architectures for H2 evolution under

visible-light irradiation. *J. Alloys Compd.* **806**, 889–896 (2019).

138. Qu, Y., Zhou, W. & Fu, H. Porous Cobalt Titanate Nanorod: A New Candidate for Visible Light-Driven Photocatalytic Water Oxidation. *ChemCatChem* **6**, 265–270 (2014).

139. Gao, B., Kim, Y. J., Chakraborty, A. K. & Lee, W. I. Efficient decomposition of organic compounds with FeTiO3/TiO2 heterojunction under visible light irradiation. *Appl. Catal. B Environ.* **83**, 202–207 (2008).

140. Shamshi Hassan, M., Amna, T. & Khil, M. S. Synthesis of High aspect ratio CdTiO3 nanofibers via electrospinning: Characterization and photocatalytic activity. *Ceram. Int.* **40**, 423–427 (2014).

141. Li, R., Zhao, Y. & Li, C. Spatial distribution of active sites on a ferroelectric PbTiO3 photocatalyst for photocatalytic hydrogen production. *Faraday Discuss.* **198**, 463–472 (2017).

142. Li, M. *et al.* Photocatalytic hydrogen generation enhanced by band gap narrowing and improved charge carrier mobility in AgTaO3 by compensated co-doping. *Phys. Chem. Chem. Phys.* **15**, 16220–16226 (2013).

143. Li, S. *et al.* Highly efficient NaTaO3 for visible light photocatalysis predicted from first principles. *Sol. Energy Mater. Sol. Cells* **149**, 97–102 (2016).

144. Abuk, S. C. ¸ & Mamedov, A. *A Study of the LiN bO 3 and LiT aO 3 Absorption Edge*. *Tr. J. of Physics* vol. 22 (1998).

145. Joshi, U. A., Palasyuk, A. M. & Maggard, P. A. Photoelectrochemical investigation and electronic structure of a p-type CuNbO3 photocathode. *J. Phys. Chem. C* **115**, 13534–13539 (2011).

146. Modak, B. & Ghosh, S. K. Improving KNbO3 photocatalytic activity under visible light. *RSC Adv.* **6**, 9958–9966 (2016).

147. Ali, R. F. & Gates, B. D. Synthesis of Lithium Niobate Nanocrystals with Size Focusing through an Ostwald Ripening Process. *Chem. Mater.* **30**, 2028–2035 (2018).

148. Grabowska, E. Selected perovskite oxides: Characterization, preparation and photocatalytic properties-A review. *Applied Catalysis B: Environmental* vol. 186 97–126 (2016).

149. Kim, Y.-I., Woodward, P. M., Baba-Kishi, K. Z. & Tai, C. W. Characterization of the Structural, Optical, and Dielectric Properties of Oxynitride Perovskites AMO 2 N (A) Ba, Sr, Ca; M) Ta, Nb). doi:10.1021/cm034756j.

150. Gao, L., Li, Z. & Liu, J. Facile synthesis of Ag3VO4/β-AgVO3 nanowires with efficient visible-light photocatalytic activity. *RSC Adv.* **7**, 27515–27521 (2017).

151. Nishimura, K., Yamada, I., Oka, K., Shimakawa, Y. & Azuma, M. High-pressure synthesis of BaVO3: A new cubic perovskite. *J. Phys. Chem. Solids* **75**, 710–712 (2014).

152. Jellite, M. *et al.* Investigation of LaVO3 based compounds as a photovoltaic absorber. *Sol. Energy* **162**, 1–7 (2018).

153. Shpanchenko, R. V. *et al.* Synthesis, structure, and properties of new perovskite PbVO3. *Chem. Mater.* **16**, 3267–3273 (2004).

154. Yoshida, T., Kobayashi, M., Yoshimatsu, K., Kumigashira, H. & Fujimori, A. *Correlated electronic states of SrVO 3 revealed by angle-resolved photoemission spectroscopy*.

155. Yuan, Z. *et al.* Sunlight-activated AlFeO3/TiO2 photocatalyst. *Sci. China, Ser. B Chem.* **49**, 67–74 (2006).

156. Dhanasekaran, P. & Gupta, N. M. Factors affecting the production of H 2 by water splitting over a novel visible-light-driven photocatalyst GaFeO 3. *Int. J. Hydrogen Energy* **37**, 4897–4907 (2012).

157. Hu, R. *et al.* Photocatalytic activities of LaFeO3 and La2FeTiO 6 in p-chlorophenol degradation under visible light. *Catal. Commun.* **29**, 35–39 (2012).

158. Freeman, E. *et al.* $PrFeO_3$ Photocathodes Prepared Through Spray Pyrolysis. *ChemElectroChem* **7**, 1365–1372 (2020).

159. Wang, M. & Wang, T. Structural, Magnetic and Optical Properties of Gd and Co Co-Doped YFeO3 Nanopowders. *Materials (Basel).* **12**, 2423 (2019).

160. Takei, T. *et al.* Photocatalytic activities of various pentavalent bismuthates under visible light irradiation. *J. Solid State Chem.* **184**, 2017–2022 (2011).

161. Ma, Z., Wu, K., Sun, B. & He, C. Band engineering of AgSb1-xBixO3 for photocatalytic water oxidation under visible light. *J. Mater. Chem. A* **3**, 8466–8474 (2015).

162. Chambers, S. A., Kaspar, T. C., Prakash, A., Haugstad, G. & Jalan, B. Band alignment at epitaxial BaSnO3/SrTiO3(001) and BaSnO3/LaAlO3(001) heterojunctions. *Appl. Phys. Lett.* **108**, 152104 (2016).

163. Liu, Q., Jin, F., Li, B. & Geng, L. Structure and band gap energy of CaSnO3 epitaxial films on LaAlO3 substrate. *J. Alloys Compd.* **717**, 55–61 (2017).

164. Lee, C. W. *et al.* Simple synthesis and characterization of SrSnO 3 nanoparticles with enhanced photocatalytic activity. *Int. J. Hydrogen Energy* **37**, 10557–10563 (2012).

165. Maeda, K. Rhodium-doped barium titanate perovskite as a Stable p-type semiconductor photocatalyst for hydrogen evolution under visible light. *ACS Appl. Mater. Interfaces* **6**, 2167–2173 (2014).

166. Tan, H. *et al.* A facile and versatile method for preparation of colored TiO2 with enhanced solar-driven photocatalytic activity. *Nanoscale* **6**, 10216–10223 (2014).

167. Gao, B., Kim, Y. J., Chakraborty, A. K. & Lee, W. I. Efficient decomposition of organic compounds with FeTiO3/TiO2 heterojunction under visible light irradiation. *Appl. Catal. B Environ.* **83**, 202–207 (2008).

168. Kanhere, P. & Chen, Z. A review on visible light active perovskite-based photocatalysts. *Molecules* **19**, 19995–20022 (2014).

169. Irie, H. & Ni, L. *To cite this article: Hiroshi Irie and Lei Ni*. *Meet. Abstr* (2013).

170. Parravano, G. Ferroelectric Transitions and Heterogenous Catalysis. *J. Chem. Phys.* **20**, 342–343 (1952).

171. Arney, D., Hardy, C., Greve, B. & Maggard, P. A. Flux synthesis of AgNbO3: Effect of particle surfaces and sizes on photocatalytic activity. *J. Photochem. Photobiol. A Chem.* **214**, 54–60 (2010).

172. (PDF) Band-Gap Engineering of NaNbO 3 for Photocatalytic H 2 Evolution with Visible Light. https://www.researchgate.net/publication/275472204_Band-Gap_Engineering_of_NaNbO_3_for_Photocatalytic_H_2_Evolution_with_Visible_Light.

173. Gerard Tobías, † *et al.* Anion Ordering and Defect Structure in Ruddlesden−Popper Strontium Niobium Oxynitrides. (2004) doi:10.1021/IC049236K.

174. Oka, D. *et al.* Strain Engineering for Anion Arrangement in Perovskite Oxynitrides. *ACS Nano* **11**, 3860–3866 (2017).

175. Asako Kasahara, † *et al.* Photoreactions on LaTiO2N under Visible Light Irradiation. (2002) doi:10.1021/JP025961+.

176. Oehler, F. & Ebbinghaus, S. G. Photocatalytic properties of CoOx-loaded nano-crystalline perovskite oxynitrides ABO2N (A = Ca, Sr, Ba, La; B = Nb, Ta). *Solid State Sci.* **54**, 43–48 (2016).

177. Kim, Y. Il & Woodward, P. M. Syntheses and characterizations of complex perovskite oxynitrides LaMg1/3Ta2/3O2N, LaMg1/2Ta1/2O5/2N1/2, and BaSc0.05Ta0.95O2.1N0.9. *J. Solid State Chem.* **180**, 3224–3233 (2007).

178. Seo, J. *et al.* Solar-Driven Water Splitting over a BaTaO2N Photoanode Enhanced by Annealing in Argon. *ACS Appl. Energy Mater.* **2**, 5777–5784 (2019).

179. Oehler, F., Naumann, R., Köferstein, R., Hesse, D. & Ebbinghaus, S. G. Photocatalytic activity of CaTaO2N nanocrystals obtained from a hydrothermally synthesized oxide precursor. *Mater. Res. Bull.* **73**, 276–283 (2016).

180. Cordes, N. & Schnick, W. Ammonothermal Synthesis of Crystalline Oxonitride Perovskites LnTaON2 (Ln=La, Ce, Pr, Nd, Sm, Gd). *Chem. - A Eur. J.* **23**, 11410–11415 (2017).

181. Porter, S. H. *et al.* Electronic structure and photocatalytic water oxidation activity of R TiNO2 (R = Ce, Pr, and Nd) perovskite nitride oxides. *Chem. Mater.* **27**, 2414–2420 (2015).

182. Pan, Z. *et al.* Application of LaMg1/3Ta2/3O2N as a hydrogen evolution photocatalyst of a photocatalyst sheet for Z-scheme water splitting. *Appl. Catal. A Gen.* **521**, 26–33 (2016).

183. Zhang, L. *et al.* Photoelectrochemical water oxidation of LaTaON2 under visible-light irradiation. *Int. J. Hydrogen Energy* **39**, 7697–7704 (2014).

184. Antoine, P. *et al.* Transport properties of the new perovskite-type LaVO3⇔xNx Oxynitrides. *Mater. Sci. Eng. B* **5**, 43–46 (1989).

185. Black, A. P. *et al.* New rare earth hafnium oxynitride perovskites with photocatalytic activity in water oxidation and reduction. *Chem. Commun.* **54**, 1525–1528 (2018).

186. Fawcett, I. D., Ramanujachary, K. V. & Greenblatt, M. Synthesis, structure and properties of the oxynitrides SrWO2N AND SrMoO2.5N0.5. *Mater. Res. Bull.* **32**, 1565–1570 (1997).

187. Logvinovich, D. *et al.* Synthesis, Mo-valence state, thermal stability and thermoelectric properties of SrMoO3-xNx (x>1) oxynitride perovskites. *J. Solid State Chem.* **180**, 2649–2654 (2007).

188. Fu, J. & Skrabalak, S. E. Enhanced Photoactivity from Single-crystalline SrTaO2N Nanoplates Synthesized by Topotactic Nitridation. *Angew. Chemie Int. Ed.* (2017) doi:10.1002/anie.201708645.

189. and, K. M. & Domen*, K. New Non-Oxide Photocatalysts Designed for Overall Water Splitting under Visible Light. (2007) doi:10.1021/JP070911W.

190. Hojamberdiev, M. *et al.* Elucidating the impact of A-site cation change on photocatalytic H2 and O2 evolution activities of perovskite-type LnTaON2 (Ln = la and Pr). *Phys. Chem. Chem. Phys.* **19**, 22210–22220 (2017).

191. Zhang, F. *et al.* Cobalt-Modified Porous Single-Crystalline $LaTiO_2N$ for Highly Efficient Water Oxidation under Visible Light. *J. Am. Chem. Soc.* **134**, 8348–8351 (2012).

192. Lu, L. *et al.* Surface chemistry imposes selective reduction of CO2 to CO over Ta3N5/LaTiO2N photocatalyst. *J. Mater. Chem. A* **6**, 14838–14846 (2018).

193. Wei, S., Zhang, G. & Xu, X. Activating BaTaO 2 N by Ca Modifications and Cobalt Oxide for Visible Light Photocatalytic Water Oxidation Reactions. *Appl. Catal. B Environ.* (2018) doi:10.1016/j.apcatb.2018.06.017.

194. M.P.Pechini. Method of Preparing Lead and Alkaline Earth Titanates and Niobates and Coating Method Using the Same To Form a Capacitor. (1967).

195. Danks, A. E., Hall, S. R. & Schnepp, Z. The evolution of 'sol–gel' chemistry as a technique for materials synthesis. *Mater. Horiz* **3**, 91–112 (2016).

196. Sakka, S. Handbook of sol-gel science and technology: processing, characterization, and applications. *Choice Rev. Online* **42**, 42-5885-42–5885 (2005).

197. Tai, L. W. & Lessing, P. A. Modified Resin Intermediate Processing Of Perovskite Powders .2. Processing For Fine, Nonagglomerated Sr-Doped Lanthanum Chromite Powders. *J. Mater. Res.* **7**, 511–519 (1992).

198. Gomathi, A., Reshma, S. & Rao, C. N. R. A simple urea-based route to ternary metal oxynitride nanoparticles. *J. Solid State Chem.* **182**, 72–76 (2009).

199. Hellwig, A. & Hendry, A. *Formation of barium-tantalum oxynitrides*. *JOURNAL OF*

MATERIALS SCIENCE vol. 29
https://link.springer.com/content/pdf/10.1007%2FBF00356510.pdf (1994).

200. Brophy, M. R., Pilgrim, S. M. & Schulze, W. A. Synthesis of BaTaO2N powders utilizing NH3 decomposition. *J. Am. Ceram. Soc.* **94**, 4263–4268 (2011).

201. Rachel, A. *et al.* Tantalum and niobium perovskite oxynitrides: Synthesis and analysis of the thermal behaviour. *Thermochim. Acta* **438**, 134–143 (2005).

202. Dip Coating Theory | Dip Coating Thin Films, Complete Guide. https://www.ossila.com/pages/dip-coating-theory-film-thickness.

203. Ceratti, D. R., Louis, B., Paquez, X., Faustini, M. & Grosso, D. A New Dip Coating Method to Obtain Large-Surface Coatings with a Minimum of Solution. *Adv. Mater.* **27**, 4958–4962 (2015).

204. Marchand, P., Hassan, I. A., Parkin, I. P. & Carmalt, C. J. Aerosol-assisted delivery of precursors for chemical vapour deposition: Expanding the scope of CVD for materials fabrication. *Dalt. Trans.* **42**, 9406–9422 (2013).

205. Ponja, S. D., Parkin, I. P. & Carmalt, C. J. Synthesis and material characterization of amorphous and crystalline (α-) Al_2O_3 via aerosol assisted chemical vapour deposition. *RSC Adv.* **6**, 102956–102960 (2016).

206. Maegli, A. E. *et al.* Enhancement of Photocatalytic Water Oxidation by the Morphological Control of LaTiO2N and Cobalt Oxide Catalysts. *J. Phys. Chem. C* **118**, 16344–16351 (2013).

207. Diffuse Reflectance Measurement – UV-Vis Spectrophotometers |Shimadzu. https://www.ssi.shimadzu.com/products/uv-vis-spectrophotometers/diffuse-reflectance-measurement.html.

208. J. Tauc; R. Grigorovici; A. Vancu. Optical properties and eletronic structure of amorphous germanium. *Phys. stat. sol.* vol. 15 627–637 (1966).

209. Davis, E. a. & Mott, N. F. Conduction in non-crystalline systems V. Conductivity, optical absorption and photoconductivity in amorphous semiconductors. *Philos. Mag.* **22**, 0903–0922 (1970).

210. Mills, A., Wang, J., Lee, S.-K. & Simonsen, M. An intelligence ink for photocatalytic films. *Chem. Commun.* **0**, 2721 (2005).

211. Kafizas, A., Adriaens, D., Mills, A. & Parkin, I. P. Simple method for the rapid simultaneous screening of photocatalytic activity over multiple positions of self-cleaning films. *Phys. Chem. Chem. Phys.* **11**, 8367–8375 (2009).

212. Platt, N. J. *et al.* Order of magnitude increase in photocatalytic rate for hierarchically porous anatase thin films synthesized from zinc titanate coatings. *Dalt. Trans.* **46**, (2017).

213. Mills, A., Wang, J. & Mcgrady, M. Method of Rapid Assessment of Photocatalytic Activities of Self-Cleaning Films. doi:10.1021/jp063577x.

214. Sunada, K., Watanabe, T. & Hashimoto, K. Studies on photokilling of bacteria on TiO 2 thin film. *J. Photochem. Photobiol. A Chem.* **156**, 227–233 (2003).

215. Chen, D. *et al.* Partial nitrogen loss in SrTaO2N and LaTiO2N oxynitride perovskites. in *Solid State Sciences* vol. 54 2–6 (Elsevier Masson SAS, 2016).

216. Kodera, M. *et al.* Effects of flux synthesis on SrNbO 2 N particles for photoelectrochemical water splitting †. (2016) doi:10.1039/c6ta00971a.

217. Dabirian, A., Van't Spijker, H. & Van De Krol, R. Wet ammonia synthesis of semiconducting N:Ta2O5, Ta3N5 and β- TaON films for photoanode applications. in *Energy Procedia* vol. 22 15–22 (2012).

218. Clarke, S. J., Hardstone, K. A., Michie, C. W. & Rosseinsky, M. J. High-Temperature Synthesis and Structures of Perovskite and n) 1 Ruddlesden-Popper Tantalum Oxynitrides The perovskite-and K 2 NiF 4-structure group 5 oxynitrides SrTaO. (2002) doi:10.1021/cm011738y.

219. Sun, S. K., Motohashi, T., Masubuchi, Y. & Kikkawa, S. Direct synthesis of SrTaO2N from SrCO3/Ta3N5 involving CO evolution. *J. Eur. Ceram. Soc.* **34**, 4451–4455 (2014).

220. Sun, S. K., Masubuchi, Y., Motohashi, T. & Kikkawa, S. Direct synthesis of nearly single-phase BaTaO2N and CaTaO2N powders. *J. Eur. Ceram. Soc.* **35**, 3289–3294 (2015).

221. Oehler, F., Naumann, R., Köferstein, R., Hesse, D. & Ebbinghaus, S. G. Photocatalytic activity of CaTaO2N nanocrystals obtained from a hydrothermally synthesized oxide precursor. *Mater. Res. Bull.* **73**, 276–283 (2016).

222. Flores-Gonzalez, M. A. *et al.* Preparing nanometer scaled Tb-doped Y2O3 luminescent powders by the polyol method. *J. Solid State Chem.* **178**, 989–997 (2005).

223. Aguiar, R., Kalytta, A., Reller, A., Weidenkaff, A. & Ebbinghaus, S. G. Photocatalytic decomposition of acetone using LaTi(O,N)3 nanoparticles under visible light irradiation. *J. Mater. Chem.* **18**, 4260 (2008).

224. Brinker, C. J., Frye, G. C., Hurd, A. J. & Ashley, C. S. Fundamentals of sol-gel dip coating. *Thin Solid Films* **201**, 97–108 (1991).

225. Ebbinghaus, S. G. *et al.* Perovskite-related oxynitrides - Recent developments in synthesis, characterisation and investigations of physical properties. *Progress in Solid State Chemistry* vol. 37 173–205 (2009).

226. Dimesso, L. Pechini Processes: An Alternate Approach of the Sol–Gel Method, Preparation, Properties, and Applications. in *Handbook of Sol-Gel Science and Technology* 1–22 (Springer International Publishing, 2016). doi:10.1007/978-3-319-19454-7_123-1.

227. Logvinovich, D. *et al.* Synthesis, Crystal Structure and Optical Properties of LaNbON2 . *Zeitschrift für Anorg. und Allg. Chemie* **636**, 905–912 (2010).

228. Wang, K. Laser Based Fabrication of Graphene. in *Advances in Graphene Science* (InTech,

2013). doi:10.5772/55821.

229. Oka, D. *et al.* Possible ferroelectricity in perovskite oxynitride SrTaO2N epitaxial thin films. *Sci. Rep.* **4**, 1–6 (2014).

230. Kim, Y. Il *et al.* Epitaxial thin-film deposition and dielectric properties of the perovskite oxynitride BaTaO2N. *Chem. Mater.* **19**, 618–623 (2007).

231. Pessoa, R. S. *et al.* Plasma-assisted techniques for growing hard nanostructured coatings: An overview. in *Anti-Abrasive Nanocoatings: Current and Future Applications* 456–479 (Elsevier Inc., 2014). doi:10.1016/B978-0-85709-211-3.00018-2.

232. Cohen, Y. & Riess, I. Preparation of oxynitride thin films of BaNb(OyN)x and LaNb(OyN2)x using reactive sputtering from multiphase powder targets. *Mater. Sci. Eng. B* **25**, 197–202 (1994).

233. Tavares, C. J. *et al.* Reactive sputtering deposition of photocatalytic TiO2 thin films on glass substrates. *Mater. Sci. Eng. B Solid-State Mater. Adv. Technol.* **138**, 139–143 (2007).

234. Spin Coating | Coating & Dispensing Methods | Coating & Dispensing Technology | KEYENCE America. https://www.keyence.com/ss/products/measure/sealing/coater-type/spin.jsp.

235. Aguiar, R., Weidenkaff, A., Schneider, C. W., Reller, A. & Ebbinghaus, S. G. Synthesis and properties of oxynitrides (La,Sr)Ti(O,N)3 thin films. *Progress in Solid State Chemistry* vol. 35 291–298 (2007).

236. KAKIHANA, M. Synthesis of high-performance ceramics based on polymerizable complex method. *J. Ceram. Soc. Japan* **117**, 857–862 (2009).

237. Mills, A., Wang, J., Lee, S.-K. & Simonsen, M. An intelligence ink for photocatalytic films. (2005) doi:10.1039/b501131k.

238. Ye, L., Su, Y., Jin, X., Xie, H. & Zhang, C. Recent advances in BiOX (X = Cl, Br and I) photocatalysts: Synthesis, modification, facet effects and mechanisms. *Environmental Science: Nano* vol. 1 90–112 (2014).

239. Wu, D. *et al.* Visible-light-driven BiOBr nanosheets for highly facet-dependent photocatalytic inactivation of Escherichia coli. *J. Mater. Chem. A* **3**, 15148–15155 (2015).

240. Peral, J., Domènech, X. & Ollis, D. F. Heterogeneous Photocatalysis for Purification, Decontamination and Deodorization of Air. *J. Chem. Technol. Biotechnol.* **70**, 117–140 (1997).

241. Kikuchi, Y., Sunada, K., Iyoda, T., Hashimoto, K. & Fujishima, A. Photocatalytic bactericidal effect of TiO2 thin films: Dynamic view of the active oxygen species responsible for the effect. *J. Photochem. Photobiol. A Chem.* **106**, 51–56 (1997).

242. Joost, U. *et al.* Photocatalytic antibacterial activity of nano-TiO2 (anatase)-based thin films: Effects on Escherichia coli cells and fatty acids. *J. Photochem. Photobiol. B Biol.* **142**, 178–

185 (2015).

243. Takata, T., Tanaka, A., Hara, M., Kondo, J. N. & Domen, K. Recent progress of photocatalysts for overall water splitting. *Catal. Today* **44**, 17–26 (1998).

244. Mills, A. & Wang, J. Photobleaching of methylene blue sensitised by TiO2: An ambiguous system? *J. Photochem. Photobiol. A Chem.* **127**, 123–134 (1999).

245. Mills, A., Hill, C. & Robertson, P. K. J. Overview of the current ISO tests for photocatalytic materials. *J. Photochem. Photobiol. A Chem.* **237**, 7–23 (2012).

246. Mills, A. & McFarlane, M. Current and possible future methods of assessing the activities of photocatalyst films. *Catal. Today* **129**, 22–28 (2007).

247. Sawunyama, P., Jiang, L., Fujishima, A. & Hashimoto, K. Photodecomposition of a Langmuir-Blodgett film of stearic acid on TiO2 film observed by in situ atomic force microscopy and FT-IR. *J. Phys. Chem. B* **101**, 11000–11003 (1997).

248. Mills, A. & McGrady, M. A study of new photocatalyst indicator inks. *J. Photochem. Photobiol. A Chem.* **193**, 228–236 (2008).

249. Rees, K., Lorusso, E., Cosham, S. D., Kulak, A. N. & Hyett, G. Combining single source chemical vapour deposition precursors to explore the phase space of titanium oxynitride thin films. *Dalt. Trans.* **47**, 10536–10543 (2018).

250. Mills, A. & Wang, J. Simultaneous monitoring of the destruction of stearic acid and generation of carbon dioxide by self-cleaning semiconductor photocatalytic films. *J. Photochem. Photobiol. A Chem.* **182**, 181–186 (2006).

251. Maegli, A. E. *et al.* Perovskite-type LaTiO2N oxynitrides for solar water splitting: Influence of the synthesis conditions. *Energy Procedia* **22**, 61–66 (2011).

252. Ueno, I. & Kochiya, K. Effect of evaporation and solutocapillary-driven flow upon motion and resultant deposition of suspended particles in volatile droplet on solid substrate. *Adv. Sp. Res.* **41**, 2089–2093 (2008).

253. Inoue, Y. Photocatalytic water splitting by RuO2-loaded metal oxides and nitrides with d0- and d10 -related electronic configurations. *Energy Environ. Sci.* **2**, 364–386 (2009).

254. Cosham, S. D., Celorrio, V., Kulak, A. N. & Hyett, G. Observation of visible light activated photocatalytic degradation of stearic acid on thin films of tantalum oxynitride synthesized by aerosol assisted chemical vapour deposition. *Dalt. Trans.* **48**, 10619–10627 (2019).

255. Quesada-Cabrera, R. *et al.* On the apparent visible-light and enhanced UV-light photocatalytic activity of nitrogen-doped TiO2 thin films. *J. Photochem. Photobiol. A Chem.* **333**, 49–55 (2017).

256. Park, J. S. & Choi, W. Enhanced remote photocatalytic oxidation on surface-fluorinated TiO 2. *Langmuir* **20**, 11523–11527 (2004).

257. Dunnill, C. W. *et al.* Nanoparticulate silver coated-titania thin films-Photo-oxidative

destruction of stearic acid under different light sources and antimicrobial effects under hospital lighting conditions. *J. Photochem. Photobiol. A Chem.* **220**, 113–123 (2011).

258. Quesada-Cabrera, R., Sotelo-Vazquez, C., Darr, J. A. & Parkin, I. P. Critical influence of surface nitrogen species on the activity of N-doped TiO2 thin-films during photodegradation of stearic acid under UV light irradiation. *Appl. Catal. B Environ.* **160**–**161**, 582–588 (2014).

259. Platt, N. J. *et al.* Order of magnitude increase in photocatalytic rate for hierarchically porous anatase thin films synthesized from zinc titanate coatings. *Dalt. Trans.* **46**, 1975–1985 (2017).

260. Wu, F., Sun, X., Liu, G. & Xu, X. Actualizing efficient photocatalytic water oxidation over $SrTaO_2N$ by Na modification. *Catal. Sci. Technol.* **7**, 4640–4647 (2017).

261. Kado, Y. *et al.* Enhanced water splitting activity of M-doped Ta3N5 (M = Na, K, Rb, Cs). *Chem. Commun.* **48**, 8685 (2012).

262. Wang, W., Su, Y. W. & Chang, C. H. Inkjet printed chalcopyrite CuInxGa1-xSe2thin film solar cells. *Sol. Energy Mater. Sol. Cells* **95**, 2616–2620 (2011).

263. Kawase, T., Shimoda, T., Newsome, C., Sirringhaus, H. & Friend, R. H. Inkjet printing of polymer thin film transistors. *Thin Solid Films* **438**–**439**, 279–287 (2003).

264. Zhou, L. *et al.* Inkjet-Printed Small-Molecule Organic Light-Emitting Diodes: Halogen-Free Inks, Printing Optimization, and Large-Area Patterning. *ACS Appl. Mater. Interfaces* **9**, 40533–40540 (2017).